

QUANTIFICATION AND CHARACTERISATION OF MULTI-SCALE GREENHOUSE GAS EMISSIONS USING IN SITU OBSERVATIONS

A THESIS SUBMITTED TO THE UNIVERSITY OF MANCHESTER FOR THE
DEGREE OF DOCTOR OF PHILOSOPHY IN THE FACULTY OF SCIENCE AND
ENGINEERING

2022

PATRICK A. BARKER

DEPARTMENT OF EARTH AND ENVIRONMENTAL SCIENCES

Contents

Abstract	6
Declaration	8
Copyright.....	10
Acknowledgements	12
Introduction Part 1: Climate Change and Greenhouse Gases	14
1.1. Climate change.....	16
1.1.1. Natural climate change	16
1.1.2. Anthropogenic climate change	22
1.2. Methane	29
1.2.1. Atmospheric abundance and temporal variability	30
1.2.2. Isotopic signature.....	31
1.2.3. Sources, sinks, and budget.....	36
1.3. Nitrous oxide	43
1.3.1. Atmospheric abundance and temporal variability	44
1.3.2. Isotopic signature.....	45
1.3.3. Sources, sinks, and budget.....	46
Introduction Part 2: Emission Quantification and Instrumentation.....	51
2.1. Current measurement networks and infrastructure.....	51
2.2. Emission quantification techniques	54
2.2.1. Flux chambers	54
2.2.2. Eddy covariance	56
2.2.3. Mass balance	57
2.2.4. Emission ratios and emission factors.....	60
2.2.5. Process modelling.....	62
2.2.6. Inversion modelling.....	63
2.3. GHG measurement techniques.....	64
2.3.1. The Beer-Lambert law and infrared spectroscopy	64
2.3.2. Cavity enhanced absorption spectroscopy	66
2.3.3. Cavity ring-down spectroscopy	68
2.3.4. Other techniques	68
2.4. Thesis outline	69

Manuscript 1: Airborne measurements of fire emission factors for African biomass burning sampled during the MOYA campaign.....	72
Manuscript 2: Airborne quantification of net methane and carbon dioxide fluxes from European Arctic wetlands in Summer 2019.....	74
Manuscript 3: Measurement of recreational N₂O emissions from an urban environment in Manchester, UK.....	76
Conclusions and future work	78
6.1. Conclusions	79
6.1.1. Biomass burning.....	79
6.1.2. Arctic wetlands.....	80
6.1.3. Urban emissions	81
6.2. Future directions	82
6.2.1. Biomass burning.....	82
6.2.2. Arctic wetlands.....	84
6.2.3. Urban emissions	85
6.3. Closing remarks and outstanding research questions.....	86
6.4. Published work	89
6.4.1. Published	89
6.4.2. In review	91
References	92
Appendix	119
A.1. Supplementary material to Manuscript 1	119
A.1.1. Comparison of peak integration and regression method for emission factor calculation.....	124
A.2. Supplementary material to Manuscript 2	129
A.2.1. CH ₄ isotope analysis.....	130
A.2.2. CH ₄ flux upscaling.....	130
A.2.3. N ₂ O flux threshold.....	131
A.3. Supplementary material to Manuscript 3	137
A.3.1. Extended temporal analysis	138
A.3.2. Flux estimation using dispersion modelling	140

Word Count: **73,991**

Abstract

Methane (CH_4) and nitrous oxide (N_2O) are the second and third most important greenhouse gases in terms of contribution to anthropogenic climate forcing, with the atmospheric abundances of these gases increasing to this day. The uncertainties in the individual sources and sinks of these gases remain poorly constrained, partly due to the lack of precise and accurate top-down greenhouse gas flux quantification and the discrepancy between top-down and bottom-up emission estimates. This thesis examines the use of in situ greenhouse gas measurements to quantify or otherwise characterise emissions from sources from a wide range of spatial scales, helping to constrain top-down estimates for CH_4 and N_2O emission sources.

Two aircraft-based measurement studies are presented within this thesis, both using the Facility for Airborne Atmospheric Measurements (FAAM) research aircraft. The first of these case studies was focused on biomass burning emissions of greenhouse gases from biomass burning in northern sub-Saharan Africa. Fire plumes were sampled in Senegal in March 2017 and Uganda in January/February 2019 as part of the Methane Observations and Yearly Assessments (MOYA) project. Emission factors (in g emitted per kg of dry fuel burnt) were calculated for carbon dioxide (CO_2), CH_4 , and carbon monoxide (CO) for both locations, as well as for N_2O in Uganda. Strong positive linear correlation was found between CH_4 emission factor and combustion efficiency of the fires for both locations. However, the slope of this linear relationship was significantly different between the two regions, which is likely a result of differences in biomass fuel composition. The second aircraft-based study focused on CH_4 flux quantification from European arctic peatlands. A single research flight was carried out in July 2019, where a wide area of Fennoscandian mixed peatland and forest was surveyed. Area-normalised CH_4 fluxes were positively correlated with peatland area within three subsections of the survey area. The observed fluxes were significantly higher than those reported by a series of biogeochemical process models, which may be partially accounted for by the higher temporal coverage of the models, as well as the presence of riverine and lake CH_4 emissions not accounted for by the models.

The final case study presented in this thesis is a departure from the aircraft-based work of the previous chapters, focusing on ground-based measurements of N_2O in an urban environment in Manchester, UK. A year of continuous N_2O measurements were made from October 2020 to October 2021 along with other atmospheric trace gases, aerosols, and meteorological parameters. Discrete enhancements in N_2O were observed with no co-emission of any other atmospheric pollutants. Temporal profiles of N_2O mole fraction showed clear nocturnal enhancements between 18:00 and 02:00, with significantly higher enhancements during weekend nocturnal periods. This suggested the presence of a significant source of N_2O from its use as a recreational substance.

Finally, future directions for the studies presented in this thesis are discussed. For the aircraft-based studies, the use of additional measurements such as in situ observations (Unpiloted Aerial Vehicles), satellite remote sensing retrievals, and ground-based eddy covariance flux towers are discussed. As for the ground-based N_2O study, the use of an atmospheric dispersion model to determine fluxes of N_2O , as well as the possibility of upscaling the study to provide a nationwide emission estimate are explored.

Declaration

I declare that no portion of the work referred to in the thesis has been submitted in support of an application for another degree or qualification of this or any other university or other institute of learning.

Copyright

The author of this thesis (including any appendices and/or schedules to this thesis) owns certain copyright or related rights in it (the “Copyright”) and s/he has given the University of Manchester certain rights to use such Copyright, including for administrative purposes.

Copies of this thesis, either in full or in extracts and whether in hard or electronic copy, may be made only in accordance with the Copyright, Designs and Patents Act 1988 (as amended) and regulations issued under it or, where appropriate, in accordance with licensing agreements which the University has from time to time. This page must form part of any such copies made.

The ownership of certain Copyright, patents, designs, trademarks and other intellectual property (the “Intellectual Property”) and any reproductions of copyright works in the thesis, for example graphs and tables (“Reproductions”), which may be described in this thesis, may not be owned by the author and may be owned by third parties. Such Intellectual Property and Reproductions cannot and must not be made available for use without the prior written permission of the owner(s) of the relevant Intellectual Property and/or Reproductions.

Further information on the conditions under which disclosure, publication and commercialisation of this thesis, the Copyright and any Intellectual Property and/or Reproductions described in it may take place is available in the University IP Policy (see <http://documents.manchester.ac.uk/DocuInfo.aspx?DocID=24420>), in any relevant Thesis restriction declarations deposited in the University Library, the University Library’s regulations (see <http://www.library.manchester.ac.uk/about/regulations/>) and in the University’s policy on Presentation of Theses.

Acknowledgements

First of all, I'd like to give special thanks to my supervisors Grant and Martin for their constant support and optimism in my research (especially when I was perhaps less confident!), and for allowing me to take real ownership of my project. I'd also like to thank Joe for helping me get to grips with instrument work early on, and for his invaluable advice throughout my PhD. Thanks also to those past and present in the Grant Allen group; Jacob, Adil, Amy, Han, and Prue, for their support throughout. Stéphan and Tom also deserve a special mention for all their help on and off the aircraft. I'd also like to thank NERC for funding my research as part of the Earth Atmosphere and Ocean Doctoral Training Partnership, and also to the MOYA project and all those involved.

I'm also especially grateful to my friends and colleagues in CAS and the EAO DTP, as well as all those friends that have put up with me during the highs and lows of my PhD. Finally, I'd like to thank my family, who have always taken an interest in my work, and have been an unending source of encouragement throughout.

Chapter 1

Introduction Part 1: Climate Change and Greenhouse Gases

The Earth's atmosphere is vital for the existence of all life on the planet. It forms a key reservoir in many elemental cycles that are crucial for supporting life, as well as filtering out ultraviolet radiation from the sun which poses a significant risk to terrestrial organisms. Activities of living organisms have resulted in direct and indirect changes to the composition of the atmosphere for millennia, however the onset of the industrial revolution in ca. 1750 AD marked the start of deliberate large-scale emissions of greenhouse gases (GHGs) to the atmosphere. Substantial GHG emissions have persisted up to the present day, and the subsequent impacts on Earth's climate will remain for many hundreds of thousands of years or may even be irreversible unless substantial mitigation strategies are implemented promptly.

Water vapour (H_2O) is both the most abundant GHG in the atmosphere and the largest contributor to the global greenhouse effect, however atmospheric abundances of water vapour have significant local and regional variability, and anthropogenic activity does not have a direct impact on the abundance of water vapour in the atmosphere. Variability in water vapour atmospheric abundance is instead a consequence of the anthropogenic greenhouse effect rather than a cause of it, as increasing temperatures from anthropogenic GHG emission lead to increased liquid water evaporation and hence an increase in water vapour abundance. Water vapour often exacerbates and reinforces the climate effects of anthropogenic GHG emission, but is not considered to be a direct contributor to the anthropogenic greenhouse effect, and is therefore typically excluded from such discussions. On the other hand, the next three most abundant GHGs: carbon dioxide (CO_2), methane (CH_4), and nitrous oxide (N_2O) contribute significantly to the global greenhouse effect and all have direct anthropogenic emission sources, such as from fossil fuels, fertilisation of agricultural land, and biomass burning (Le Quéré et al., 2018; Reay et al., 2012; Andreae, 2019). These anthropogenic emission sources have perturbed the natural cycle of these gases through the Earth system within the carbon and nitrogen

cycles, resulting in increasing atmospheric abundance up to the present day. Despite having a smaller overall contribution to the global greenhouse effect than CO₂, methane and nitrous oxide are significantly more potent GHGs on a per-molecule basis. Furthermore, methane has a far shorter atmospheric lifetime of 9.1 years on average in comparison the highly variable CO₂ lifetime of 5 – 200 years, so mitigation strategies targeting methane emission reduction are likely to have a more immediate effect on reducing anthropogenic warming, as methane will be removed from the atmosphere within a short timescale.

This thesis focuses on in situ observation of both natural and anthropogenic sources of methane and nitrous oxide; the second and third most abundant greenhouse gases respectively (excluding water vapour). There is an urgent need to better quantify sources of methane and nitrous oxide due to their increasing abundance in the atmosphere, their potency as GHGs, and the potential for more rapid climate remediation with a relatively modest reduction in methane emissions. 2021 was a record year for methane and nitrous oxide global increase (NOAA, 2021a, b), and individual source emission estimates currently still have significant uncertainties associated with them. In situ GHG measurements are often used to constrain current source estimates and reduce the uncertainty of these, this work in particular addresses how in situ “top-down” GHG measurements can be used for vital intercomparison and validation of process-based “bottom-up” emission estimates.

The work presented here will first describe natural and anthropogenic climate change and the greenhouse effect, key sources and sinks of methane and nitrous oxide (Chapter 1), and the major measurement techniques used for estimating emissions of these gases (Chapter 2). Following this, published work from two aircraft-based in situ measurement campaigns will be described, the first of which is focused on GHG emissions from African biomass burning and calculation of fire emission factors (Chapter 3). The second describes GHG emissions from peatlands in Arctic regions of northern Sweden and Finland (Chapter 4). The final piece of published work presented in Chapter 5 of this thesis is a departure from the aircraft-based studies of the previous two chapters, the third manuscript describes ground-based long-term measurements of urban nitrous oxide emissions and the identification of a potential recreational nitrous oxide source from the qualitative analysis of measurements.

1.1. Climate change

The term ‘climate change’ as is colloquially understood is the recent increase in global mean temperature as a consequence of sustained GHG emission to the atmosphere from the onset of industrial revolution to the present day. However Earth’s climate has undergone natural and predictable changes in the past, these natural climate variations occur on timescales of years to hundreds of thousands of years and can be predicted with high accuracy. Long-term natural climate variations over the span of many millennia pose little threat to terrestrial life, as living organisms are able to adapt to changing climate conditions over these timescales. Shorter-term climate variations can result in localised disruptions to food chains and a higher prevalence of extreme weather events, but often the change to the climate is modest, and any threat to life is minimal. In contrast to this, anthropogenically-driven climate change has resulted in a likely global average temperature increase anomaly between 0.8 – 1.2 °C since the pre-industrial era and 2017 (Allen et al., 2018). Humanity will be unable to naturally adapt to global temperature increase on such a timescale, and future warming will lead to a higher probability of extreme weather events, large-scale food chain disruptions, and displacement of citizens and higher numbers of climate refugees (Sommer and Schad, 2015; Mann et al., 2017; Chodur et al., 2018).

1.1.1. Natural climate change

The Earth’s climate has experienced constant naturally-occurring change over the span of the entire history of the planet. One of the most significant phenomena that has resulted in cyclical climate change and the presence of distinct climatic periods over at least the past 800,000 years are Milankovitch cycles. Milankovitch cycles are the natural variations in the Earth’s movement around the sun and about its own axis, which result in variability of solar radiation reaching Earth and hence have a cyclical impact on Earth’s climate (Hays et al., 1976). Milankovitch cycles are commonly divided into four major classes of orbital movement: axial precession, axial obliquity, orbital eccentricity, and apsidal precession. Axial precession refers to the gradual change in the direction of Earth’s axis of rotation relative to fixed stars over a period of approximately 26,000 years. This results in variability of seasonal extremes in the northern and southern hemisphere and the “swapping” of hemispheric seasons with time of year. Axial obliquity is the approximate 2° variability in the angle of the Earth’s axis of rotation relative to the orbital

plane which exists in a 40,000-year cycle. Increases in Earth's axial tilt result in higher insolation during summer months in both hemispheres, this results in enhanced seasonality during periods of increasing axial tilt. Conversely, periods of decreasing axial tilt lead to overall milder conditions, with cooler summers and warmer winters in both hemispheres. Orbital eccentricity is the variation in the ellipticity of Earth's orbit around the sun. Earth's orbit transitions from a more circular orbit to a more elliptical orbit and back again over the course of approximately 100,000 years. Increases in the ellipticity of Earth's orbit lead to seasons where solar irradiance of Earth is decreased due to the planet being physically further away from the sun, this has the potential to reduce temperatures in a cyclical fashion. Apsidal precession is the gradual rotation of the Earth's orbital ellipse over a 112,000 year period, this cycle leads to changes in the relative lengths of summer and winter periods. Both apsidal and axial precession combine to give a total precession cycle with a 23,000 year period (Lourens, 2021).

Milankovitch cycles are believed to be partially responsible for transitions between glacial and interglacial climate periods. Studies involving Antarctic ice core data, in which air trapped in ice sheets or glaciers can be analysed by drilling out a vertical column, give direct information on paleoclimate records from up to 800,000 years in the past (Lambert et al., 2008). Historical records of the $^{18}\text{O}/^{16}\text{O}$ ratio of H_2O (known as $\delta^{18}\text{O}$) and $^2\text{H}/^1\text{H}$ ratio ($\delta^2\text{H}$) from ice core samples can be used as accurate proxies for past temperature. This occurs due to isotopic fractionation in water upon evaporation from oceans and precipitation. Evaporated water is relatively depleted in heavier isotopes, whereas precipitation preferentially removes heavier isotopes. As both precipitation and evaporation are temperature-dependent, the ratio of heavy to light isotopes of water in ice cores (which themselves originate from ancient polar precipitation) can be used as a proxy for historical temperature.

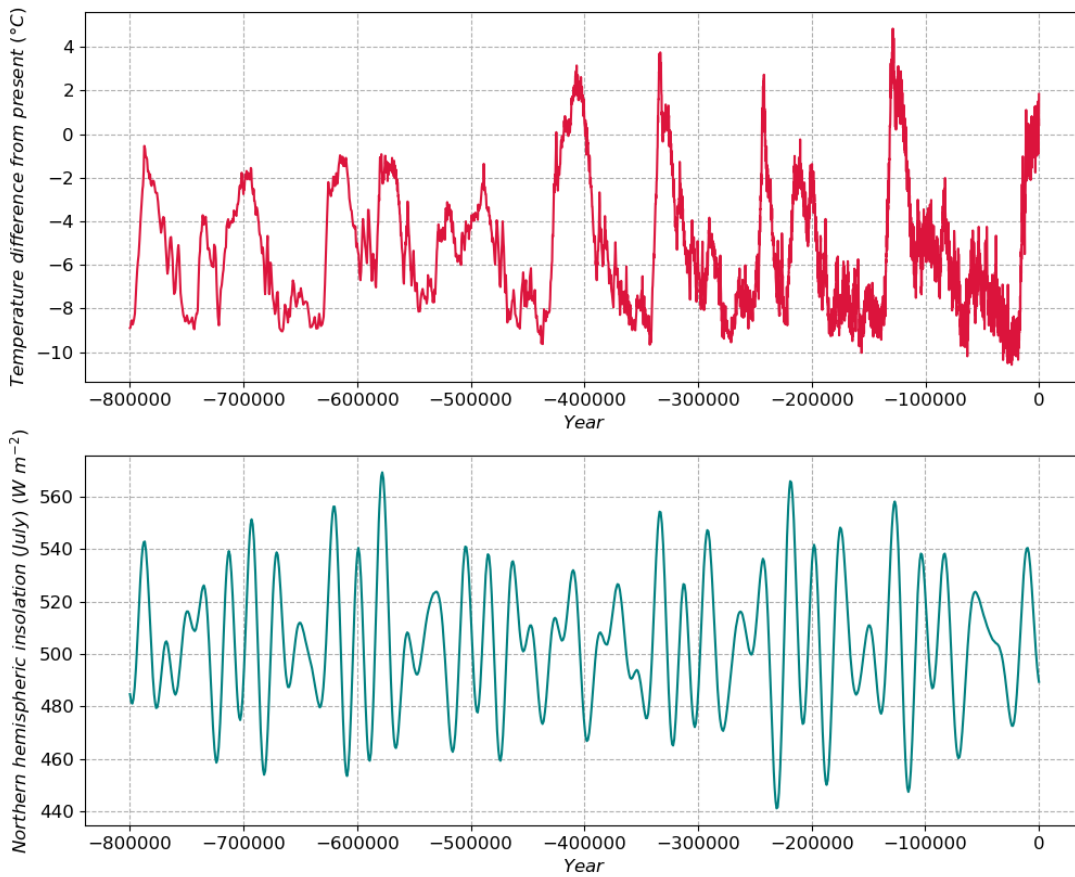


Figure 1.1: Temperature anomaly from the present day (top) and estimated July insolation at the northern hemisphere (bottom) over the past 800,000 years. Data are taken from ice core samples from the EPICA Dome C site in East Antarctica (Lambert et al., 2008).

Figure 1.1 shows temperature anomaly from the present day (inferred from $\delta^2\text{H}$) and estimated changes in northern hemispheric insolation over the past 800,000 years determined from ice core samples taken from the EPICA Dome C drilling site in Antarctica (Jouzel et al., 2007). The historical temperature anomaly from the top panel of fig. 1.1 shows an approximate 100,000-year cycle of short higher temperatures (interglacial periods) followed by longer periods of lower temperature (glacial periods) (Berger et al., 2005). The glacial-interglacial cycle suggests that it is primarily driven by the orbital eccentricity cycle, of which both exhibit a 100,000-year period, yet the changes in irradiance as a result of the eccentricity cycle are far too small to produce the observed glacial-interglacial climate cycle (Imbrie et al., 1993; Lisiecki, 2010). In contrast, changes in axial obliquity result in significant variations in northern hemispheric insolation, exhibiting a 40,000-year cycle with peak irradiance at higher tilt angles. The variation in northern hemispheric insolation in the bottom panel of fig. 1.1 appear to have minimal influence on climatic changes, with the 100,000-year glacial-interglacial cycles

being the dominant feature of the paleoclimatic record. These observations therefore suggest that Milankovitch cycles alone cannot fully describe historical climatic trends, as eccentricity cycles accompanied by relatively small changes in irradiance appear to result in significant climate cycles, whereas larger changes in irradiance from obliquity cycles appear to have a minimal effect on climate variability.

A possible explanation for the 100,000-year glacial-interglacial cycle is the presence of positive climate feedbacks, which may help to sustain glacial and interglacial periods, with Milankovitch cycles providing the initiating conditions for a glacial or interglacial period. Axial obliquity impacts on insolation have been found to affect atmospheric CO₂ abundances, likely due to algal uptake of CO₂ in oceans or ocean mixing (Lear et al., 2016). Increased CO₂ lags slightly behind the temperature increase during interglacial periods, hence changes in CO₂ abundance may help drive the glacial-interglacial cycle, with changes in insolation simply facilitating the start of the transition between the periods (Shackleton et al., 2000; Sigman and Boyle, 2000; Ganopolski et al., 2016). In addition to CO₂ abundances, there is evidence that the higher albedo associated with increased ice cover during glacial periods may help to sustain the cooler glacial periods (Willeit and Ganopolski, 2018). It is believed that a 100,000-year cycle of such feedback processes, independent of Milankovitch cycles, may be the cause of the glacial-interglacial cycle, yet the exact mechanisms for CO₂ variability in a cyclical fashion are still poorly understood (Marsh et al., 2014).

In addition to climate feedbacks, alternative hypotheses exist that attempt to explain the glacial-interglacial cycle. One such theory has proposed that extra-terrestrial dust or meteoroids attenuate solar irradiance during an elliptical orbit, hence explaining the link between glacial-interglacial cycles and orbital eccentricity (Muller and MacDonald, 1995; Kortenkamp and Dermott, 1998), yet there has been little recent research into this hypothesis. Recent research has suggested that a combination between the precession cycle and orbital eccentricity results in a 100,000-year cycle in hemispheric ice cover, which may initiate the transition to a glacial period (Lee et al., 2017). Despite the variety of hypotheses that have been proposed for glacial-interglacial cyclic behaviour, there is still no consensus on a definitive explanation for the cycle.

As of the present day, the Earth's climate is currently in an interglacial period and has been for approximately the past 12,000 years. However, temperatures are currently

increasing beyond the trend of glacial-interglacial cycles. Figure 1.2 shows the variability in CO_2 , CH_4 , and N_2O mole fraction over the past 800,000 years from ice core samples. The 100,000-year glacial-interglacial temperature cycle can be seen clearly in CO_2 mole fraction, and to some extent in CH_4 mole fraction. However, recent years have seen the highest mole fractions of all three of these GHGs in 800,000 years, well beyond their natural variability as a result of Milankovitch cycles. Anthropogenic emission of GHGs is currently driving increasing warming following a 2000-year period of gradual cooling (Kaufman et al., 2009). The continued temperature increase due to anthropogenic GHG emission could result in permanent perturbation of this natural climate cycle, with sustained warming as long as GHG emissions persist at the current rate (Caccamo and Magazù, 2021).

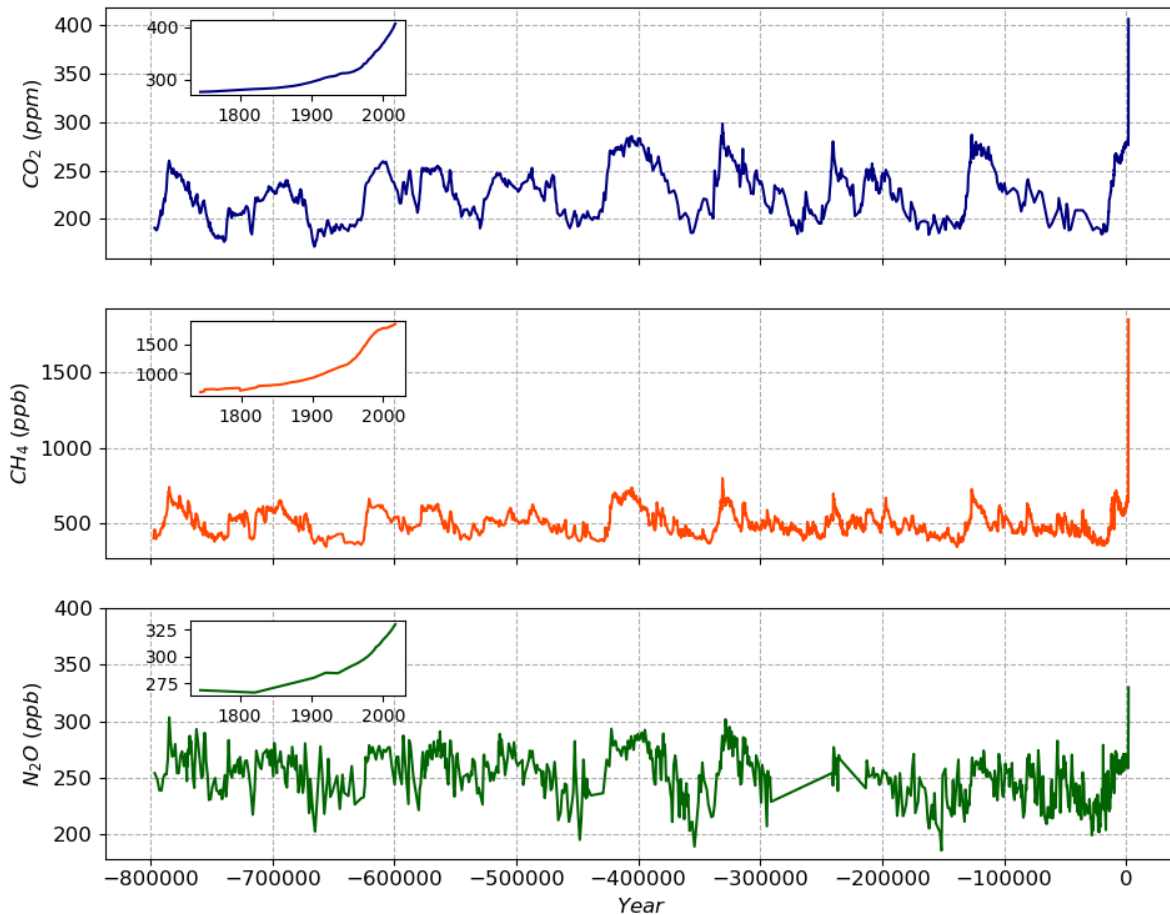


Figure 1.2: Mole fractions of CO_2 (blue) CH_4 (orange), and N_2O (green) from 800,000 BC to 2017 AD. Historical data are obtained from the EPICA Dome C ice core air records (Lambert et al., 2008). 20th and 21st century data are obtained from a latitudinally-distributed range of sources, including the Mauna Loa Observatory (Hawaii), Cape Grim (Australia), and the Shetland Islands (UK) (NOAA, 2021a).

In addition to longer term natural climate cycles existing over periods of tens or hundreds of thousands of years, other natural cyclical climate variations exist that vary over much smaller timescales such as over years or decades. The most prominent and widely studied short-term cyclical climate phenomenon is the El Niño Southern Oscillation (ENSO), which occurs in and over the equatorial Pacific Ocean. ENSO involves the breakdown of strong westerly trade winds travelling from the east coast of South America towards the west coast of Southern Asia (Philander et al., 1983). The normal behaviour of these trade winds results in movement and accumulation of warmer surface-level ocean waters from the western Pacific towards the east near Indonesia and the presence of colder waters towards the west. This results in convective circulation between the east and west Pacific (known as the Walker cell). El Niño conditions involve lower intensity westerly trade winds, which allow the accumulated warmer waters in the east to drift back eastwards across the Pacific leading to inversion of the original westerly trade winds to an easterly direction. El Niño events are typically short-lived and are often followed by a La Niña period; normal conditions that are exaggerated to an extent, with stronger westerly trade winds leading to upwelling and distribution of deeper colder waters from the west to east, leading to cooler temperatures around the equatorial Pacific (Timmermann et al., 2018). Despite ENSO existing in the southern pacific, the impacts of this phenomenon are felt across the entire globe. El Niño periods often result in warmer, wetter conditions across South America and South-East Asia and higher likelihood of severe storms and rainfall across the southern United States. La Niña periods lead to much cooler and drier conditions in South-East Asia (Ropelewski and Halpert, 1986; Davey et al., 2014). The global climatic effects of ENSO have significant repercussions on human activities. For example El Niño events can lead to poorer fishing yields, increased incidence of flooding, and lower crop yields in North and South America (Bakun and Broad, 2003; Ward et al., 2014; Anderson et al., 2017).

The ENSO cycle occurs with a frequency of approximately 2 – 7 years, with intensity varying widely between individual cycles (Trenberth and Shea, 1987). Current modelling capabilities allow for the prediction of El Niño and La Niña events 6 – 12 months before they begin, which is important for pre-empting and mitigating the effects these events have on human activities. However, research has found that approximately 43% of all extreme ENSO events since 1525 have occurred in the 20th century, suggesting that anthropogenic climate change has increased the risk of dramatic climate-related natural

disasters from extreme ENSO events (Gergis and Fowler, 2009). Furthermore, there is evidence that climate variations from ENSO events may be becoming more frequent with increasing warming, which adds further difficulty in predicting potentially catastrophic weather events resulting from anthropogenic climate change (Urban et al., 2000).

1.1.2. Anthropogenic climate change

The most significant mechanism relevant to anthropogenically-influenced climate change is the greenhouse effect. Despite the greenhouse effect occurring naturally within the atmosphere due to the natural presence of GHGs in the atmosphere as part of Earth's elemental cycles, human activities have exacerbated the total greenhouse effect by the continued emission of GHGs to the atmosphere. The greenhouse effect can be described by the balance between incoming solar electromagnetic radiation, outgoing radiation from Earth's surface, and absorption by atmospheric chemical species.

The sun provides almost all of Earth's energy in the form of infrared, visible, and ultraviolet electromagnetic radiation. The peak wavelength, λ , of top of atmosphere solar irradiance is ~504 nm; well within the visible portion of the electromagnetic spectrum. The solar radiation reaching Earth's surface is attenuated by absorption and scattering by atmospheric gases and aerosols, as well as reflection by clouds, hence ground level insolation is of lower intensity than at the top of the atmosphere. Around 70% of incoming solar radiation is absorbed by Earth's atmosphere and surface, with the remaining 30% being reflected or re-emitted back into space (Trenberth et al., 2009). Earth's surface is significantly cooler than the surface of the sun (approximately 287 K on average compared to 5778 K for the sun). The lower surface temperature of the Earth results in the emitted radiation being shifted to longer wavelengths than the incoming solar radiation absorbed by Earth's surface. Radiation emitted from Earth ranges between $\lambda = 3 - 100 \mu\text{m}$, which is in the infrared portion of the electromagnetic spectrum. Figure 1.3a illustrates the difference in emission wavelength of the sun and the Earth due to temperature as idealised black bodies with complete absorption of all electromagnetic radiation. In reality, a very small net percentage (17%) of the radiation emitted by the Earth is radiated back out into space. The majority of the Earth's emitted infrared radiation is absorbed by GHGs in the atmosphere and re-radiated as heat, which increases the temperature of the atmosphere and the Earth's surface.

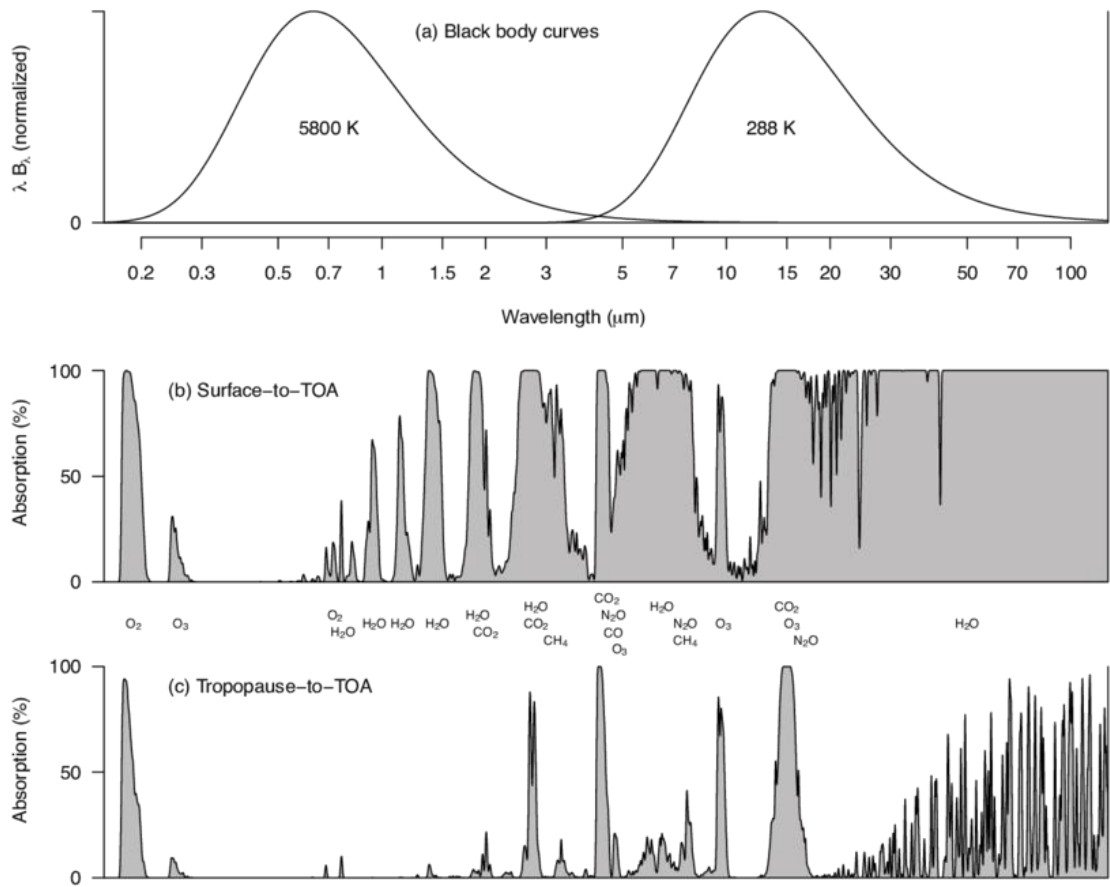


Figure 1.3. (a) Normalized black body curves for 5800K (the approximate emission temperature of the Sun) and 288K (the approximate surface temperature of the Earth). (b) Representative absorption spectrum of the Earth's atmosphere for a vertical column from the surface to space, assuming the atmosphere to be a homogeneous slab. (c) The same but for a vertical column from the tropopause ($\sim 11\text{km}$) to space. Figures and captions obtained from Goessling and Bathiany. (2016).

Figures 1.3b and 1.3c show the atmospheric absorption spectra for a vertical column taken from the entire atmosphere (b), and from the tropopause upwards (c). It can be seen that infrared absorbing GHG species such as H_2O , CO_2 , CH_4 , N_2O , CO , and O_3 all have significant bands of absorption within the infrared spectral region for a total atmospheric column. However, many of these absorption bands are non-existent or at much lower intensity when the troposphere is excluded from the atmospheric column, illustrating the high infrared absorption primarily occurring in the troposphere, resulting in the greenhouse effect directly affecting and being affected by Earth's surface.

GHGs are able to absorb infrared radiation due to their molecular structure and bonding. Quantised (discrete) vibrational and rotational energy levels exist within

molecular species, and the energy of the infrared (IR) radiation is of a similar magnitude to the energy required for a transition from a ground to excited vibrational energy level in a molecular species. Vibrational excitation of molecules in this way results in increased kinetic energy of said molecules, resulting in more frequent collisions with surrounding molecules and hence resulting in a temperature increase. Specific selection rules exist for a molecule to be “IR-active”; molecules must undergo a change in dipole moment (distribution of electric charge across the molecule) upon vibration. It is for this reason that homonuclear diatomic molecules within the atmosphere (such as N_2 and O_2) are IR-inactive, as vibrational bond stretching does not change the dipole moment across the molecule. Therefore N_2 and O_2 , the highest-abundance gaseous components of the atmosphere, make zero contribution to the greenhouse effect and are not GHGs. Atmospheric trace gases such as H_2O , CO_2 , CH_4 , N_2O , CO , and O_3 all involve a change in dipole moment in one of their vibrational modes and are therefore IR-active. It is worth noting that some GHGs such as CO_2 and CH_4 do not have a permanent dipole moment in their ground states due to their symmetrical structure. It is only upon an asymmetrical vibration that the instantaneous dipole moment changes to be non-zero, resulting in IR-activity. These IR-active GHGs absorb incident solar infrared radiation and infrared radiated from Earth’s surface, then re-radiate this thermal radiation back to Earth’s surface and to the surrounding air, resulting in surface and air temperature increases. The greenhouse effect is necessary for the existence of life as we know it on Earth, as it maintains the Earth’s mean surface temperature at $14\text{ }^\circ\text{C}$. Without the presence of any greenhouse effect Earth’s mean surface temperature would be $-18\text{ }^\circ\text{C}$.

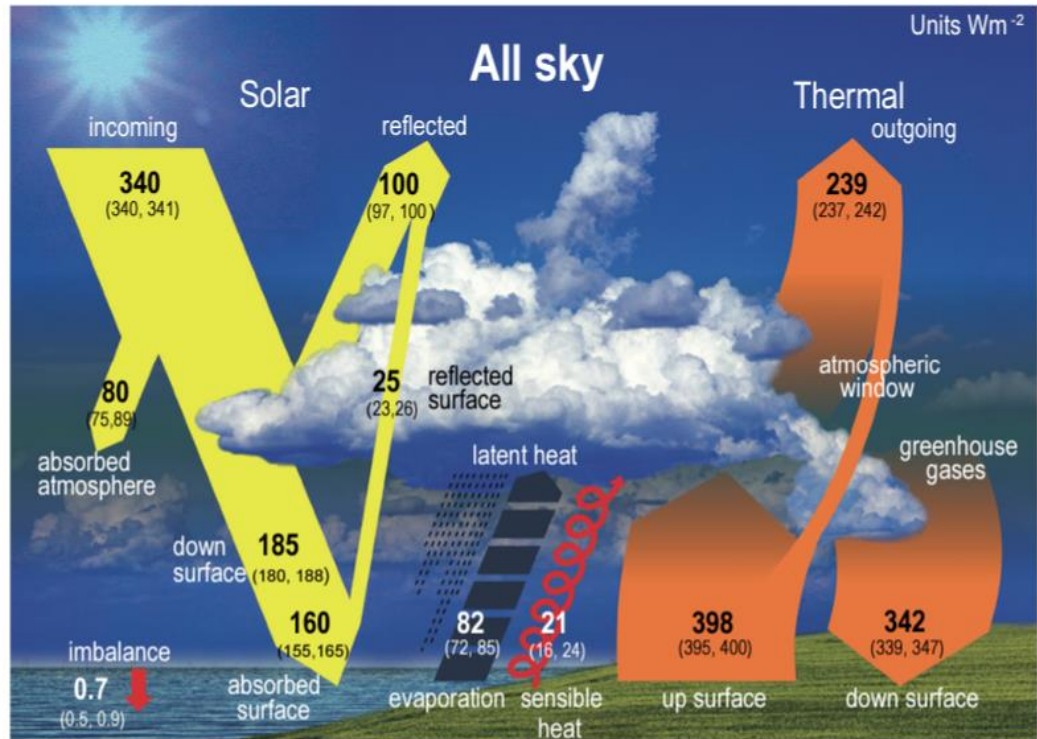


Figure 1.4: Schematic representation of the global mean energy budget of the Earth. Numbers indicate best estimates for the magnitudes of the globally averaged energy balance components in $W m^{-2}$ together with their uncertainty ranges in parentheses (5–95% confidence interval), representing climate conditions at the beginning of the 21st century.

A schematic representation of Earth's energy budget is illustrated in figure 1.4, which highlights the relative contributions of different atmospheric constituents on Earth's energy budget. For example, clouds exhibit both positive and negative effects on Earth's energy budget. Cloud cover results in reflection of short-wave radiation back into space due to their high reflectivity (albedo), accounting for a $100 W m^{-2}$ energy removal from the Earth system. In addition to their reflection of solar radiation, undersides of clouds absorb surface-reflected infrared radiation and emit this energy to colder cloud tops (Ramanathan et al., 1989). Despite the presence of these antagonistic effects, the reflection of long-wave radiation dominates, and clouds have a net negative effect on Earth's energy budget and have a cooling effect, yet the balance between these radiative processes, and hence uncertainty in their contribution to energy balance, have been shown to be related to the phase of water within the cloud (Matus and L'Ecuyer, 2017). The thermal radiation absorbed and radiated by GHGs accounts for $342 W m^{-2}$ energy increase, which is larger than the mean incoming solar energy to the Earth system (340

W m^{-2}). As mentioned previously, the large contribution of GHGs to Earth's energy budget is evident in the current mean surface temperature of $14\text{ }^{\circ}\text{C}$, as opposed to $-18\text{ }^{\circ}\text{C}$ in the absence of GHGs

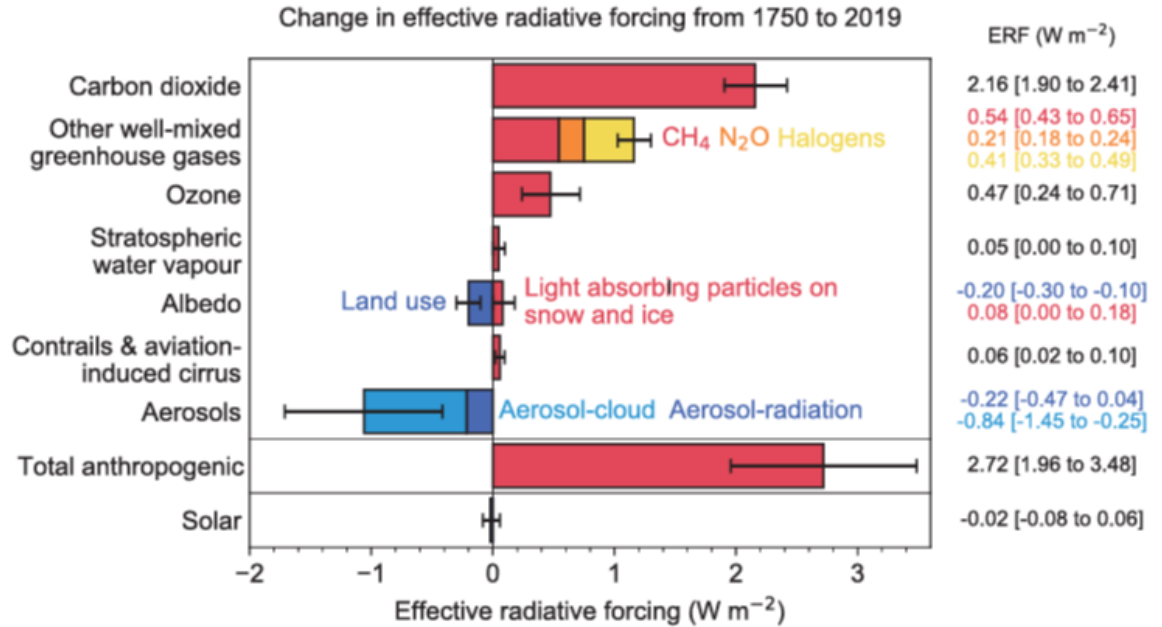
It can be seen that there is an almost-perfect balance between incoming solar radiation and outgoing reflected solar radiation and thermal radiation. In the absence of anthropogenic climate perturbation, Earth's energy balance exists in this steady-state with mean balance of incoming and outgoing radiation, yet the effect of anthropogenic forcing from increasing GHG and aerosol abundance results in a widening of the energy imbalance between incoming and outgoing radiation. The perturbation of Earth's energy budget as a result of changing atmospheric constituents can be used as a metric to assess the impact of human and natural activity on climate change.

The contributions of individual atmospheric constituents to the radiation budget of Earth are commonly quantified as Radiative Forcings (RF). RFs are defined as the net change an atmospheric component has on the energy budget of the Earth system as a whole, measured in W m^{-2} (IPCC, 2021a). RF changes can easily be used to derive an estimated surface temperature change as a result of anthropogenic activity, and hence provide a quantifiable link between GHG abundances and climate change. The anthropogenic RF change budget from 1750 – 2019 is shown in figure 1.5.

Figure 1.5 clearly shows that CO_2 has the largest positive RF impact of any single atmospheric component due to its large increase in atmospheric abundance since the industrial revolution, accounting for $+2.2\text{ W m}^{-2}$ mean RF increase from 1750 – 2019. CH_4 follows as the next largest GHG contributor to positive RF, followed by N_2O . Both of these gases have a higher per-molecule potency as GHGs than CO_2 , but atmospheric abundance increases of CH_4 and N_2O have been more modest than the increase in CO_2 in this timeframe. Halocarbons (CFCs and HCFCs) represent a greater mean contribution to positive RF than N_2O , but the bar in figure 1.5 is comprised of many individual halocarbon compounds, all with small atmospheric abundances and small individual contributions to positive RF despite being highly potent GHGs on a per-molecule basis. HFCs, PFCs and SF_6 are extremely potent GHGs as with halocarbons, but atmospheric abundances have not increased significantly enough for them to contribute largely to positive RF. Tropospheric O_3 has increased in abundance in the post-industrial era. Secondary production of O_3 occurs within the NO_x cycle in the presence of hydrocarbons

and sunlight (i.e. in polluted air) (Fishman and Crutzen, 1978). Increased O₃ abundance therefore results in a positive change in RF of +0.47 W m⁻² on average.

Figure 1.5: Change in effective radiative forcing (ERF) from 1750 to 2019 by contributing forcing agents (carbon dioxide, other well-mixed greenhouse gases (WMGHGs), ozone, forcing agents (carbon dioxide, other well-mixed greenhouse gases (WMGHGs), ozone,



stratospheric water vapour, surface albedo, contrails and aviation-induced cirrus, aerosols, anthropogenic total, and solar). Solid bars represent best estimates, and very likely (5–95%) ranges are given by error bars. Non-CO₂ WMGHGs are further broken down into contributions from methane (CH₄), nitrous oxide (N₂O) and halogenated compounds. Surface albedo is broken down into land-use changes and light-absorbing particles on snow and ice. Aerosols are broken down into contributions from aerosol–cloud interactions (ERF_{aci}) and aerosol–radiation interactions (ERF_{ari}). Volcanic aerosol is not included due to the episodic nature of volcanic eruptions. Figure and caption are obtained from the IPCC sixth assessment report (IPCC, 2021)

The presence of aerosol results in both warming and cooling effects, yet the net effect of aerosols is a mean reduction in radiative forcing of -1.06 W m⁻². Atmospheric aerosols act as Cloud Condensation Nuclei (CCN) increasing cloud cover as a consequence, increasing albedo and hence reflected solar radiation. Aerosol precursor species such as NH₃ and SO₂ lead to the formation of nitrate and sulphate aerosol respectively, which in turn contribute to the aforementioned aerosol-cloud interactions. Additionally, aerosols interact with incoming solar radiation by direct absorption or scattering, modifying the Earth's radiation balance directly. This is shown as aerosol-radiation interactions in fig. 1.5. The extent and dynamics of aerosol-radiation interactions is currently poorly

understood, resulting in large uncertainties in its contribution to radiative forcing (Chandra and Paul, 2019). Black Carbon (BC) is a unique case with aerosols as it results in an increase in RF in contrast to the aerosol-cloud and aerosol-radiation interactions previously mentioned. BC deposited on snow reduces the effective albedo of the snow cover, meaning that less solar radiation is reflected back to space and more is absorbed by the Earth's surface, leading to a positive RF change.

Anthropogenic components of the atmosphere clearly exhibit both positive (warming) RF and negative (cooling) RF. However the impact of anthropogenic activity has led to a net positive change in RF, with the net effective RF change from all anthropogenic components estimated to be between $+1.96$ and $+3.48 \text{ W m}^{-2}$ (IPCC, 2021a). A significant proportion of the net positive RF change since 1750 is due to increased atmospheric abundance of CO_2 , with increasing CH_4 and N_2O also accounting for notable positive RF perturbations. It is worth noting that when compared to the total energy budget contribution of GHGs (fig. 1.4), the perturbation due to increasing GHG abundance is relatively small (approximately 0.5 – 1 % of the total GHG contribution). Despite this, small energy budget increases from anthropogenic GHG emissions result in non-negligible mean temperature increases and hence climate change that will be too rapid for humanity to naturally adapt to. A considerable challenge with assessing and predicting the current and future extent of anthropogenic climate change is the uncertainty in RF change estimates, which directly propagate to uncertainty in the temperature impact of increasing GHG abundance. RF perturbations must be understood to a higher level of precision to allow for effective guidance on climate change mitigation (i.e. how much do GHG concentration increases and hence emissions need to be reduced by to limit global warming to 1.5°C ?). For this reason, the uncertainty in global GHG budgets must be reduced, and top-down and bottom-up emission estimates must be reconciled, and this can be achieved in part by in situ study of poorly understood and climate sensitive GHG sources.

1.2. Methane

Methane (CH_4) is a hydrocarbon molecule which is the second most significant GHG behind CO_2 in terms of contribution to overall greenhouse effect in the atmosphere. Atmospheric abundance and growth rate of methane are notably smaller than CO_2 , yet CH_4 is approximately 84 times more effective at trapping infrared radiation than an equal mass of CO_2 over a 20-year time period, which make it a more potent GHG than CO_2 on a per-molecule basis. However CH_4 drops to being only 28 times more potent than CO_2 over a 100-year timescale, reflecting the relatively short mean tropospheric lifetime of 9.1 years for CH_4 (IPCC, 2021a). Individual GHGs differ in their infrared absorbing ability and potency for several reasons. A GHG that absorbs infrared in spectral regions with little overlap with absorptions of other atmospheric constituents will have a greater infrared-absorbing ability. Additionally, if absorption occurs over a wider spectral range, then the potency of the GHG will be greater. This section will describe how the atmospheric abundance of CH_4 has changed over recent decades, the major sources and sinks, and the global atmospheric methane budget.

1.2.1. Atmospheric abundance and temporal variability

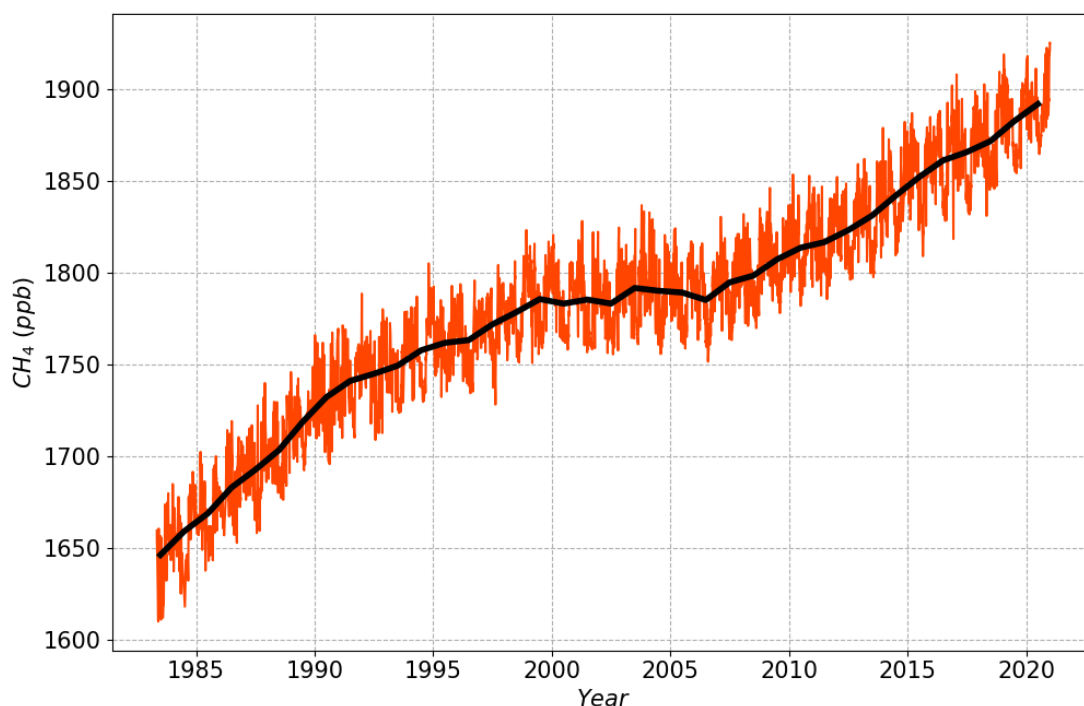
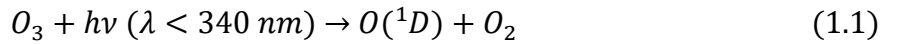


Figure 1.6: CH₄ mole fraction from May 1983 to December 2020 measured from flask samples taken from the Mauna Loa Atmospheric Observatory, Hawaii. The orange plot shows weekly CH₄ mole fraction data, while the black line shows the yearly rolling average CH₄ mole fraction (NOAA, 2021a).

The mean atmospheric abundance of CH₄ has increased from 772 ppb in pre-industrial times to a global average concentration of 1891 ppb as of April 2021 as seen in figures 1.2 and 1.6 (IPCC, 2021b; NOAA, 2021a). It can be seen from figure 1.6 that while there has been a clear increase in CH₄ mole fraction since 1983, the rate of growth has not remained constant over the whole period. Atmospheric CH₄ abundance over the past 37 years has shown steady growth of +11.8 ppb year⁻¹ on average from 1983 up to approximately 1991, after which the CH₄ growth rate slowed to +5.1 ppb year⁻¹ until 1999. Between 1999 and 2007, atmospheric CH₄ growth stagnated and yearly-averaged CH₄ mole fractions remained relatively constant during this period, with decreases in abundance seen in some years. However following 2006, CH₄ growth resumed at a comparable rate to before the period of stagnation (+7.9 ppb year⁻¹). In addition to the variability in CH₄ growth, there is clear intra-year variability in CH₄ with local minima in northern hemispheric summer months and local maxima in northern hemispheric autumn/winter.

Seasonal and interhemispheric variability in CH₄ abundance is driven by a combination of source and sink behaviours. Oxidation by OH is the primary sink mechanism for tropospheric CH₄, and OH is formed by the photolysis of O₃ and subsequent reaction of an excited oxygen radical (O(¹D)) with H₂O as shown in equations 1.1 and 1.2 (Stone et al., 2012), therefore OH abundance is positively correlated with the amount of ultraviolet (UV) irradiation from the sun. Hence CH₄ abundances are lowest in summer months when OH abundance is high, and the majority of CH₄ removal by OH occurs in the tropics (Canty and Minschwaner, 2002). The chlorine (Cl) radical also acts as an important tropospheric chemical sink of CH₄, yet its influence on seasonal CH₄ variability is poorly understood (Strode et al., 2020). Seasonal CH₄ variability is more pronounced in the northern hemisphere varying by ~25 ppb over the course of a year, as opposed to a less prominent seasonal cycle of ~15 ppb per year in the southern hemisphere. This interhemispheric difference is due to the higher proportion of CH₄ sources in the northern hemisphere, as higher surface emissions typically occur during northern hemispheric winter (Khalil and Rasmussen, 1983; Crevoisier et al., 2013).



1.2.2. Isotopic signature

The 1999 – 2007 stagnation in CH₄ growth has yet to be fully accounted for, however several hypotheses have been proposed for this change in CH₄ growth. In order to further understand CH₄ source and sink behaviour during the growth variability over the past ~40 years, the isotopic ratio of ¹³CH₄ to ¹²CH₄ (known as δ¹³C-CH₄) can be used to identify relative contributions of individual sources to atmospheric CH₄ growth. δ¹³C-CH₄ can be calculated using equation 1.3 and is often reported in permil (‰). δ¹³C isotopic ratios are reported relative to a known reference material of which the δ¹³C ratio is known to a high degree of precision and accuracy.

$$\delta^{13}\text{C}\text{H}_4 = \left(\frac{\left(\frac{^{13}\text{C}\text{H}_4}{^{12}\text{C}\text{H}_4} \right)_{\text{sample}}}{\left(\frac{^{13}\text{C}}{^{12}\text{C}} \right)_{\text{reference}}} - 1 \right) \times 1000 \text{ ‰} \quad (1.3)$$

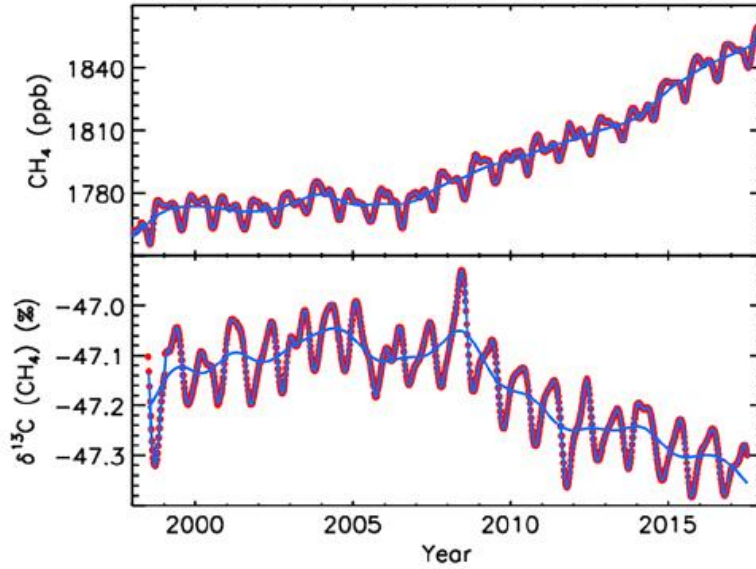


Figure 1.7: Atmospheric CH_4 at Earth's surface in the remote marine troposphere. Upper panel shows globally averaged surface atmospheric CH_4 at weekly resolution (red and blue) and deseasonalised trend (blue), 2000–2017. Lower panel as above, but for globally averaged surface atmospheric $\delta^{13}\text{C}\text{-CH}_4$. The x axis tick marks denote the 1st of January of the year indicated. Figure and caption are from Nisbet et al. (2019), and original data are from NOAA (2021a).

Prior to 1996, the growth in atmospheric CH_4 abundance was accompanied by an increasing $\delta^{13}\text{C}\text{-CH}_4$ isotopic ratio, meaning that the CH_4 emitted to the atmosphere was somewhat enriched in ^{13}C . The increase in $\delta^{13}\text{C}\text{-CH}_4$ stopped after 1996, with the isotopic ratio remaining constant at approximately -47.2 ‰ during the 1999–2007 stagnation period. Unexpectedly, upon resumed growth in CH_4 abundance from 2006 onwards, the $\delta^{13}\text{C}\text{-CH}_4$ isotopic ratio began decreasing over time meaning that relatively ‘lighter’ CH_4 was being emitted to the atmosphere (Schaefer et al., 2016). The stable isotopic ratio from 1999–2007 and subsequent decrease in $\delta^{13}\text{C}\text{-CH}_4$ is shown in figure 1.7. The isotopic ratio of CH_4 emitted from different sources can differ notably and can often be used to assist source identification and apportionment. For example, biogenic CH_4 produced from wetland environments is depleted in ^{13}C relative to background with $\delta^{13}\text{C}\text{-CH}_4$ values in the range of -50 to -70 ‰ . On the other hand, thermogenic methane sources such as from

fossil fuel combustion are ^{13}C enriched relative to background, having a -25 to -35 ‰ $\delta^{13}\text{C}\text{-CH}_4$ range. Biomass burning tends to produce ^{13}C -enriched CH_4 , but $\delta^{13}\text{C}\text{-CH}_4$ values vary between -15 to -30 ‰ due to differing photosynthetic pathways (C3 and C4) of vegetation burnt leading to different isotopic fractionation of ^{13}C (Chanton et al., 2000; Dlugokencky et al., 2011). The $\delta^{13}\text{C}\text{-CH}_4$ signatures from different source categories are illustrated in figure 1.8. It has therefore been proposed that the 1999 – 2007 stagnation period and renewed CH_4 growth since was due to a reduction in fossil fuel ^{13}C -enriched CH_4 emissions, along with a subsequent increase in ^{13}C -depleted wetland emissions driving the renewed growth. This pattern of source behaviour would explain the shift in isotopic ratio towards lighter CH_4 following the stagnation period (Dlugokencky et al., 2009, Kirschke et al., 2013).

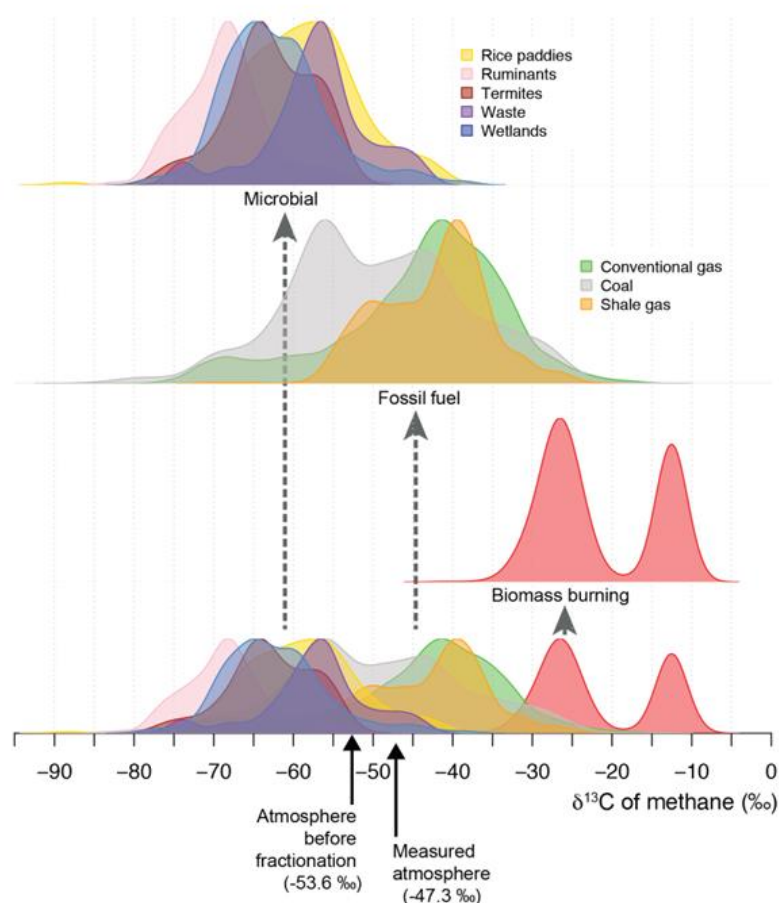


Figure 1.8: Normalized probability density distributions for the $\delta^{13}\text{C}\text{-CH}_4$ of microbial, fossil, and biomass burning sources of methane. The flux-weighted average of all sources produces a mean atmospheric $\delta^{13}\text{C}\text{-CH}_4$ of ~ -53.6 ‰, as inferred from measured atmospheric $\delta^{13}\text{C}\text{-CH}_4$ and isotopic fractionation associated with photochemical methane destruction. Figure and caption from Sherwood et al. (2017).

The hypothesized variability in source behaviour inferred from isotopic ratio changes is supported by literature. Bousquet et al. (2013) used an atmospheric inversion model encompassing in situ flask CH₄ measurements, an atmospheric chemical transport model, and the use of isotope ratio data to constrain different CH₄ source variabilities during this period, a significant reduction in fossil fuel CH₄ flux was found preceding and during the period of stagnation. Furthermore, Dlugokencky et al. (1994) also identified that a reduction in anthropogenic fossil fuel emissions may be the driver for CH₄ growth decrease in the early 1990s.

Despite clear evidence of a change in the balance of CH₄ emission sources during the 1999 – 2006 stagnation period, there is also evidence of a notable change in OH abundance during this period which may have contributed to the stalling in CH₄ growth. Prinn et al. (2005) examined measurements of CH₃CCl₃ mole fraction, which is commonly used as a proxy for OH abundance as CH₃CCl₃ almost exclusively reacts with OH. Prinn et al. found that OH abundance reached a minimum between 1997 and 1999 immediately preceding the stagnation period, this was likely due to higher CO abundance from strong wildfires and unusually strong El Niño conditions. Following 1999, OH abundance increased significantly, which would theoretically have contributed to the halting in CH₄ growth. Furthermore, recent inversion modelling research has found that the 1999-2006 stagnation period likely occurred due to increasing sources being counterbalanced by a significant increase in OH. Atmospheric transport of CH₄ to the tropics where OH abundances are higher, as well as higher atmospheric temperature increasing reactivity were also found to be minor factors influencing CH₄ growth suppression (McNorton et al., He et al., 2020).

As seen in figure 1.7, the post-2006 renewed CH₄ growth was accompanied by a decrease in $\delta^{13}\text{C-CH}_4$, suggesting a significant change in the nature of CH₄ sources and/or sinks in comparison to the pre-1999 growth. Recent studies using global wetland process models (McNorton et al., 2016; Oh et al., 2022) have found that a post-2006 increase in wetland emissions is the dominant factor in the increasing CH₄ abundance from 2006 onwards, with particular emphasis on arctic wetland emission increases as a result of accelerated warming in northern latitudes (Schuur et al., 2015). A shift towards ¹³C-depleted biogenic emission sources would explain the observed post-2006 decline in $\delta^{13}\text{C-CH}_4$, yet other studies suggest that changing wetland emissions are not solely responsible for the post-2006 trends in CH₄ growth. Inversion modelling studies (Worden

et al., 2017; Thompson et al., 2018) have identified a post-2006 increase in fossil fuel emissions, with a reduced emphasis on increased wetland emissions. A concurrent increase in ethane (C_2H_6) with post-2006 CH_4 also suggests that an increase in fossil fuel emissions have been a significant contributor to recent CH_4 growth (Franco et al., 2016; Angot et al., 2021). Despite these observations, a dominant fossil fuel CH_4 source post 2006 would be accompanied by an increase in $\delta^{13}C-CH_4$, as opposed to the observed shift towards lower $\delta^{13}C-CH_4$. Recent research has attributed the recent isotopic trends to a subsequent decrease in biomass burning emissions alongside an increase in fossil fuel emissions, wherein the lower emission of highly ^{13}C -enriched CH_4 from biomass burning offsets the higher emission of moderately enriched fossil fuel CH_4 , accounting for the observed trend in isotopes.

In addition to source behaviour, changes in CH_4 sinks have been proposed as a significant contributor to the post-2006 growth. Inversion modelling of OH via CH_3CCl_3 proxy by Rigby et al. (2017) found a high (64 – 70%) probability that OH decreases contributed to post-2006 CH_4 . This in turn also explains the increased C_2H_6 abundance from a sink perspective, as C_2H_6 is primarily removed from the atmosphere by OH. Despite this, the Rigby et al. (2017) research highlights the considerable uncertainties associated with their OH inversion, and states that a definitive conclusion on the relative impact of source and sink behaviour on post-2006 CH_4 growth could not be made at the level of uncertainty of the inversion. Similarly, a recent inversion study by Turner et al. (2017) found that a decrease in OH abundance and, unexpectedly, a concurrent decrease in emissions was the most likely scenario for post-2006 CH_4 growth. Yet this study, as with the Rigby et al. (2017) study, suffers from significant inversion uncertainties, hence resulting in significant uncertainty in post-2006 CH_4 source-sink behaviour.

In summary, it is likely that a combination of OH abundance increase and reduction in fossil fuel emissions were both important drivers for the stabilisation in CH_4 abundance between 1999 and 2006, yet the balance between these two factors remains poorly understood and there is still debate as to which was the dominant driver of CH_4 stagnation (Nisbet et al., 2016; McNorton et al., 2018). The subsequent CH_4 growth from 2006 is less clear, with evidence for both changes in source behaviour and a decrease in the OH sink. In order to better understand recent trends in CH_4 abundance and to help predict future trends, individual source budgets must be understood to a higher degree of precision and accuracy. This will allow global and regional inversion modelling studies

to attribute global CH₄ abundance changes to sources and sinks to a higher degree of certainty. A combination of in situ studies of target regions alongside global inversion and process-based modelling will help reduce the uncertainty in our estimates of CH₄ emissions, and may allow us to better understand the temporal variability in CH₄ over recent years.

1.2.3. Sources, sinks, and budget

CH₄ sources can be categorised into three major groups based on the nature of how CH₄ is produced. Biogenic CH₄ is produced via biological activity, namely through the conversion of organic matter to CH₄ (fermentation) by methanogenic microorganisms (Schoell, 1988). The largest biogenic CH₄ source is methanogenic activity in wetland systems, where anoxic conditions in wetland soils lead to fermentation of organic matter to CH₄ as opposed to respiratory production of CO₂ in more oxygenated soils (Bridgman et al., 2013). Other biogenic CH₄ sources include enteric fermentation in ruminant animals such as cows and sheep (Johnson and Johnson, 1995), and fermentation associated with waste treatment (Daelman et al., 2012). Thermogenic CH₄ is produced geologically through the action of high temperature and pressure in carbonaceous sediments deep within the Earth's crust (Etiope and Sherwood, 2013). Almost all thermogenic CH₄ is emitted via the anthropogenic exploitation of natural gas deposits for use as a fossil fuel. CH₄ emissions from this source often occur as a result of 'planned' venting of natural gas to the atmosphere which is often accounted for by emission inventories. 'Fugitive' emissions from natural gas infrastructure can also occur via leakage from improperly sealed pipelines or storage vessels. The final CH₄ source category is pyrogenic emissions which refer to CH₄ produced via combustion processes (Le Fevre, 2017). Biomass burning, fossil fuel combustion and biofuel combustion are all significant sources of pyrogenic CH₄. As previously discussed in section 1.2.1, the three CH₄ source categories produce CH₄ with differing carbon isotopic ratios due to isotopic fractionation in photosynthetic and methanogenic processes. Differences in isotopic signature which can be used as a powerful tool for differentiating between CH₄ source types.

Table 1.1 displays the estimated CH₄ budget of sources and sinks between 2000 and 2017 reported by Saunio et al. (2020). CH₄ source estimates are reported using two approaches; the "bottom-up" approach estimates emissions using process-based models,

where intrinsic parameters associated with specific CH₄ source processes are compiled in computational models to estimate CH₄ emission. For example, biogeochemical models using soil moisture, organic carbon content, and temperature can estimate wetland CH₄ emission, and models using prior emission inventory data can be used for fossil fuel CH₄ emission estimates. The “top-down” approach involves using direct atmospheric measurements of trace gases in order to estimate CH₄ emissions, for the data in table 1.1, top-down emission estimates are often calculated via atmospheric inversion, where atmospheric observations of CH₄ are combined with an atmospheric chemical transport model in order to determine CH₄ emission.

As can be seen from table 1.1, the top-down approach is unable to resolve emission estimates for individual specific source types and can only provide source and sink estimates from broad categories of sources (“land sources”, or “fossil fuels”). Bottom-up methods can estimate sources and sinks from individual source sub-categories. This is due to the spatial and temporal overlap of atmospheric CH₄ observations that top-down models are based upon. Individual source activities cannot be easily disentangled from atmospheric measurement datasets, whereas bottom-up modelling estimates methane output using process-based data for individual source activities, which allows estimation of CH₄ sources/sinks from individual processes.

Table 1.1: The estimated global CH₄ budget between 2000 and 2017, with CH₄ emission sources and sinks reported in units of Tg CH₄ year⁻¹. Top-down and bottom-up approaches are both used to estimate sources and sinks. Values in square brackets represent the minimum and maximum source values as reported by literature. Data are obtained from Saunio et al., (2020).

Period of time	Saunio et al. (2020)					
	2000–2009		2008–2017		2017	
Approaches	Bottom-up	Top-down	Bottom-up	Top-down	Bottom-up	Top-down
Natural sources						
Wetlands	147 [102–179]	180 [153–196]	149 [102–182]	181 [159–200]	145 [100–183]	194 [155–217]
Other natural sources	222 [143–306]	35 [21–47]	222 [143–306]	37 [21–50]	222 [143–306]	39 [21–50]
Other land sources	209 [134–284]					
Freshwaters ^a	159 [117–212]					
Geological (onshore)	38 [13–53]					
Wild animals	2 [1–3]					
Termites	9 [3–15]					
Wildfires	g					
Permafrost soils (direct)	1 [0–1]					
Vegetation	f					
Oceanic sources	13 [9–22]					
Geological (offshore)	7 [5–12]					
Biogenic open and coastal ^b	6 [4–10]					
Total natural sources	369 [245–485]	215 [176–243]	371 [245–488]	218 [183–248]	367 [243–489]	232 [194–267]
Anthropogenic sources						
Agriculture and waste	192 [178–206]	202 [198–219]	206 [191–223]	217 [207–240]	213 [198–232]	227 [205–246]
Enteric ferm. & manure	104 [93–109]		111 [106–116]		115 [110–121]	
Landfills & waste	60 [55–63]		65 [60–69]		68 [64–71]	
Rice cultivation	28 [23–34]		30 [25–38]		30 [24–40]	
Fossil fuels	110 [94–129]	101 [71–151]	128 [113–154]	111 [81–131]	135 [121–164]	108 [91–121]
Coal mining	32 [24–42]		42 [29–61]		44 [31–63]	
Oil & gas	73 [60–85]		80 [68–92]		84 [72–97]	
Industry	2 [0–6]		3 [0–7]		3 [0–8]	
Transport	4 [1–11]		4 [1–12]		4 [1–13]	
Biomass & biof. burn.	31 [26–46]	29 [23–35]	30 [26–40]	30 [22–36]	29 [24–38]	28 [25–32]
Biomass burning	19 [15–32]		17 [14–26]		16 [11–24]	
Biofuel burning	12 [9–14]		12 [10–14]		13 [10–14]	
Total anthropogenic sources^c	334 [321–358]	332 [312–347]	366 [349–393]	359 [336–376]	380 [359–407]	364 [340–381]
Sinks						
Total chemical loss	595 [489–749]	505 ^d [459–516]	595 [489–749]	518 ^d [474–532]	595 [489–749]	531 ^d [502–540]
Tropospheric OH	553 [476–677]					
Stratospheric loss	31 [12–37]					
Tropospheric Cl	11 [1–35]					
Soil uptake	30 [11–49]	34 [27–41]	30 [11–49]	38 [27–45]	30 [11–49]	40 [37–47]
Total sinks	625 [500–798]	540 [486–556]	625 [500–798]	556 [501–574]	625 [500–798]	571 [540–585]
Sources – sink imbalance						
Total sources	703 [566–842]	547 [524–560]	737 [594–881]	576 [550–594]	747 [602–896]	596 [572–614]
Total sinks	625 [500–798]	540 [486–556]	625 [500–798]	556 [501–574]	625 [500–798]	571 [540–585]
Imbalance	78	3 [–10–38] ^d	112	13 [0–49] ^d	120	12 [0–41] ^d
Atmospheric growth		5.8 [4.9–6.6]		18.2 [17.3–19.0]		16.8 [14.0–19.5]

(a) Freshwater includes lakes, ponds, reservoirs, streams, and rivers. (b) Includes flux from hydrates considered to be 0, includes estuaries. (c) Total anthropogenic emissions are based on estimates of a full anthropogenic inventory and not on the sum of the “agriculture and waste”, “fossil fuels”, and “biofuel and biomass burning” categories. (d) Some inversions did not provide the chemical sink. These values are derived from a subset of the inversion ensemble. (e) Atmospheric growth is given in the same unit (Tg CH₄ yr⁻¹), based on the conversion factor of 2.75 Tg CH₄ ppb⁻¹ given by Prather et al. (2012) and the atmospheric growth rates provided in the text in parts per billion per year. (f) Uncertain but likely small for upland forest and aerobic emissions, potentially large for forested wetland, but likely included elsewhere. (g) We stop reporting this value to avoid potential double-counting with satellite-based products of biomass burning.

The total CH₄ source reported via bottom-up approaches is notably larger than the top-down total source estimate, with the 2008-2017 mean bottom-up estimate of 737 Tg CH₄ year⁻¹ being approximately 30% larger than the mean bottom-up value of 576 Tg CH₄ year⁻¹. The main source of this discrepancy is the significant difference between top-down and bottom-up estimate of “other natural sources” where the 2008-2017 top-down estimate of 37 [21-50] Tg CH₄ year⁻¹ is around six times lower than the bottom-up estimate of 222 [143-306] Tg CH₄ year⁻¹. Top-down and bottom-up natural sources typically have much larger uncertainties associated with them than with anthropogenic sources; the 2008-2017 bottom-up total natural sources have around a 65% uncertainty associated with them (371 [245-488] Tg CH₄ year⁻¹) whereas top-down estimates have a smaller but still notable uncertainty of ~30% (218 [183-248] Tg CH₄ year⁻¹). Large uncertainties in natural sources are likely the result of their high sensitivity to meteorological conditions (temperature, precipitation) as well as the difficulty in estimating the physical size and distribution of some natural sources (particularly wetlands and rivers/lakes) (Melton et al., 2013; Poulter et al., 2017). It is also important to note that there are very limited numbers of studies on many of the smaller natural CH₄ sources, with accurate process models not existing for many of these sources. Further research on all CH₄ source processes is required in order to help constrain them further and reduce uncertainty in the global budget (Saunio et al., 2020).

Wetlands represent the largest single source of CH₄, accounting for approximately a third of the total CH₄ source to the atmosphere (according to top-down estimates). CH₄ is produced by methanogenic archaea under anaerobic conditions, which are often found in anoxic soil microsites or in waterlogged soil where oxygen availability is lower. CH₄ produced in soils is emitted to the atmosphere via diffusion out of the soil along the concentration gradient, release in gas bubbles (ebullition), or release facilitated through plant vascular transport systems (Serrano-Silva et al., 2014). Despite being classified as a purely natural source, CH₄ production by methanogens in wetland ecosystems is highly sensitive to temperature, therefore a positive feedback system exists in which temperature increase driven by anthropogenic GHG emission could result in higher CH₄ emission from wetlands, which in turn could contribute to further warming. There is evidence that this positive wetland feedback has already resulted in increased CH₄ emissions (Gedney et al., 2004; McGuire et al., 2009). The climate-wetland coupled positive feedback system is especially prevalent in high northern latitudes due to the Arctic amplification

phenomenon. Arctic amplification is the advanced warming of high latitude polar regions relative to mid latitudes, and is believed to primarily occur due to melting of arctic sea ice which reduces albedo and hence allows enhanced absorption of solar radiation, resulting in amplified warming (Serreze and Barry, 2011; Dai et al., 2019). Arctic amplification has already resulted in Arctic regions warming at approximately twice the rate of the rest of the Earth over the past 30 years (Pithan and Mauritsen, 2014). Large stocks of organic carbon exist within permafrosts in Arctic regions (1100 - 1500 Pg C, Hugelius et al., 2014). As more permafrost thaws with increasing arctic temperature, more of this organic carbon stock is therefore susceptible to reduction by methanogenic microbes, resulting in large arctic wetland CH₄ emissions predicted with future warming. It is therefore of specific importance to monitor CH₄ emissions from wetlands in arctic regions, as these may be susceptible to significant emission increases with future warming.

In addition to permafrosts and wetlands, methane hydrates, which are solid deposits of CH₄ locked within the crystal structure of ice, are an important emission source that could result in large CH₄ emissions with Arctic warming. The amount of CH₄ stored in methane hydrates is poorly understood, Kvenvolden (1988) first estimated a methane hydrate store of 10,000 Pg C, but this has since been revised to ~1800 Pg C (Ruppel and Kessler, 2017). These deposits exist in many locations across the globe, including within sediments in the Arctic Ocean, it has therefore been theorised that Arctic amplified temperature increase could result in the destabilisation of hydrate deposits and subsequent release of CH₄ from the Arctic Ocean. As of the present day, it is believed that no significant release of CH₄ from methane hydrates has occurred thus far, and current ocean-atmosphere emissions are negligible (Archer, 2007; Saunio et al., 2020).

The dominant sink of atmospheric CH₄ is chemical reaction with OH radicals in the troposphere which eventually forms water and CO₂ as end products (Ehhalt, 1974). Figure 1.9 shows the oxidation cycle of CH₄ within the troposphere, where after proton abstraction from CH₄ to form water and a methyl radical, a methoxy-radical (CH₃O₂) is eventually formed. Methoxy and other peroxy-radicals play an important role in the NO_x-O₃ cycle by converting nitric oxide (NO) to nitrogen dioxide (NO₂). The net removal of NO by peroxy-radicals results in toxic O₃ production in the troposphere. Compared to more complex Non-Methane Volatile Organic Compounds (NMVOCs), CH₄ reacts relatively slowly with OH, thus CH₄ in the presence of NO_x contributes little to

tropospheric O_3 in polluted air, with other NMVOCs reacting far more rapidly with OH and hence producing ozone rapidly in the presence of NO_x . CH_4 does however contribute to background O_3 levels, and a ~10% reduction in CH_4 emissions would result in a predicted 0.4 – 0.7 ppb (1 – 2%) decrease in background tropospheric O_3 . CH_4 emissions therefore have a small but quantifiable impact on background air quality.

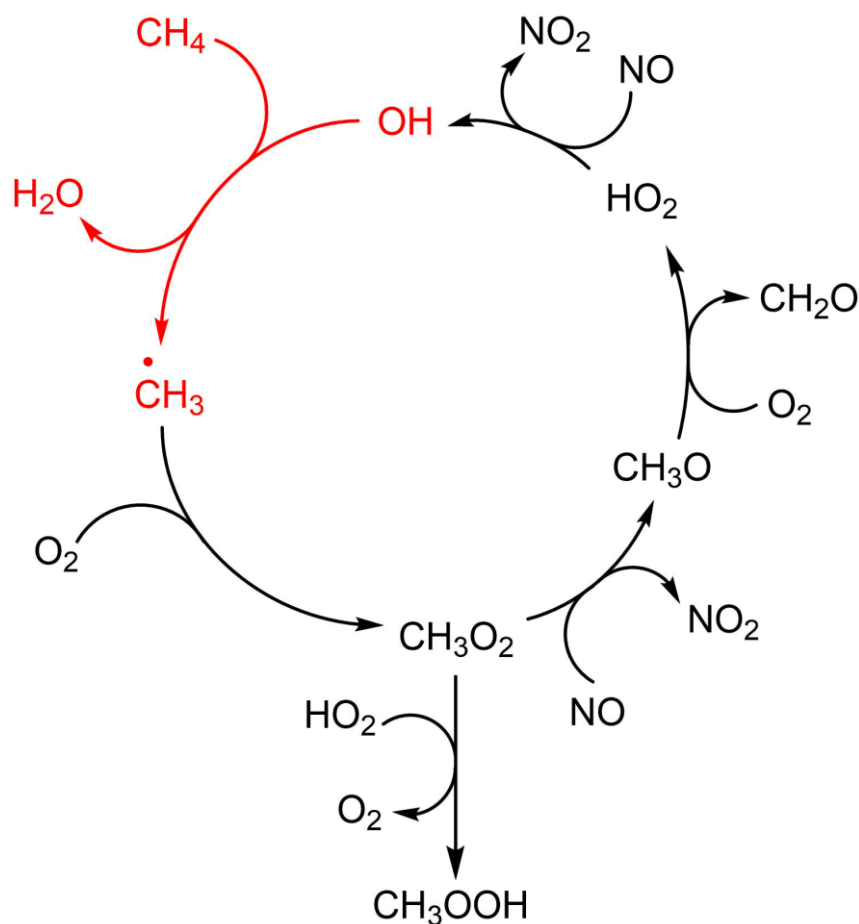


Figure 1.9: The oxidation cycle of methane in the troposphere, the reaction of methane with OH is highlighted in red, while the formation and reaction of the peroxy-radical CH_3O_2 to reform OH is shown in black. Formaldehyde (CH_2O) is eventually fully oxidised to CO_2 in the troposphere (not shown). The initial formation of OH via UV photolysis of O_3 is shown in equations 1.1 and 1.2.

The reaction of OH with tropospheric CH₄ accounts for the removal of ~90% of all surface emissions (IPCC, 2021b), with CH₄ removal by OH being relatively rapid in comparison to removal processes of more stable GHGs such as N₂O. The fast removal of CH₄ by OH results in a short lifetime of 9.1 ± 0.9 years for CH₄ in the troposphere. Furthermore, the short lifetime of CH₄ could potentially allow its overall warming potential to be mediated quickly via mitigation of emissions, providing a “quick win” for climate change mitigation. OH abundances are spatially and temporally variable due to its reactivity with a range of other atmospheric trace gases, and its sensitivity to UV radiation and hence stratospheric H₂O photolysis rates (Nicely et al., 2018). The lifetime of CH₄ is therefore highly sensitive to OH abundance, and can vary significantly with latitude, cloud cover, abundance of other pollutants, and climatological phenomena (e.g. El Niño) (Anderson et al., 2021). Understanding trends and variability in OH is therefore essential for assessing the past and current global CH₄ sink. Recent global modelling studies (Stevenson et al., 2020; Zhao et al., 2020) have attempted to quantify spatial and temporal OH variability, yet there are significant uncertainties associated with these model estimates, and further work in quantifying OH variability is required in order to close the global CH₄ budget from a sink perspective.

OH represents approximately 80 – 90% of the total CH₄ sink (IPCC, 2021b; Saunio et al., 2020), however smaller atmospheric chemical sinks of CH₄ do exist. CH₄ can react with free chlorine radicals in the troposphere in an analogous way to OH, where a methyl radical is formed along with hydrochloric acid (HCl). The removal of CH₄ by chlorine is minimal relative to OH, with Cl account for just ~2.6% of all tropospheric chemical CH₄ loss (Hossaini et al., 2016). However, there is evidence that this CH₄ removal pathway may be more prominent within the marine boundary layer (Allen et al., 2007). A small proportion of tropospheric CH₄ is transported up to the stratosphere, where it is chemically removed by OH, free halogen radicals, and O(¹D). This sink accounted for the removal of 31 [12-37] Tg CH₄ year⁻¹ between 2000 - 2009, or around 5% of the total sink. The only significant CH₄ sink that does not occur via atmospheric chemistry is the uptake of CH₄ via methanotrophic bacteria in soils. Unlike methanogens which prefer anoxic conditions, methanotrophs require oxygen as an electron acceptor and hence only exist in well-oxygenated soils, the methanotrophs use CH₄ as an energy source by oxidising it through various intermediates to CO₂ (Topp and Pattey, 1997). Methanotroph

activity is far less widespread than methanogenesis in wetlands, as the soil sink only accounts for the removal of 30 Tg CH₄ year⁻¹ on average (Saunois et al., 2020).

1.3. Nitrous oxide

Nitrous oxide (N₂O) is a linear nitrogenous molecule that is the third most impactful GHG behind CH₄ and CO₂ in its contribution to the total greenhouse effect. The growth in N₂O abundance has been small relative to CO₂ and CH₄ and the N₂O atmospheric mole fraction is notably lower than both of these gases. However, the per-molecule potency of N₂O is significantly higher than both CO₂ and CH₄, being 264 times more effective at trapping infrared radiation than CO₂ over a 20-year period, and around three times as potent as CH₄ per-molecule over 20 years. Unlike CH₄, where its potency decreases over longer timeframes due to its relatively short atmospheric lifetime (see section 1.2), the potency of N₂O remains 265 times more potent than CO₂ over a 100-year timeframe due to its much higher stability and longer atmospheric lifetime. There is therefore increased risk of increasing anthropogenic emissions of N₂O persisting for longer in the atmosphere. This section will discuss recent growth trends in N₂O abundance, and will describe the key sources, sinks and atmospheric budget of N₂O (IPCC, 2021a).

1.3.1. Atmospheric abundance and temporal variability

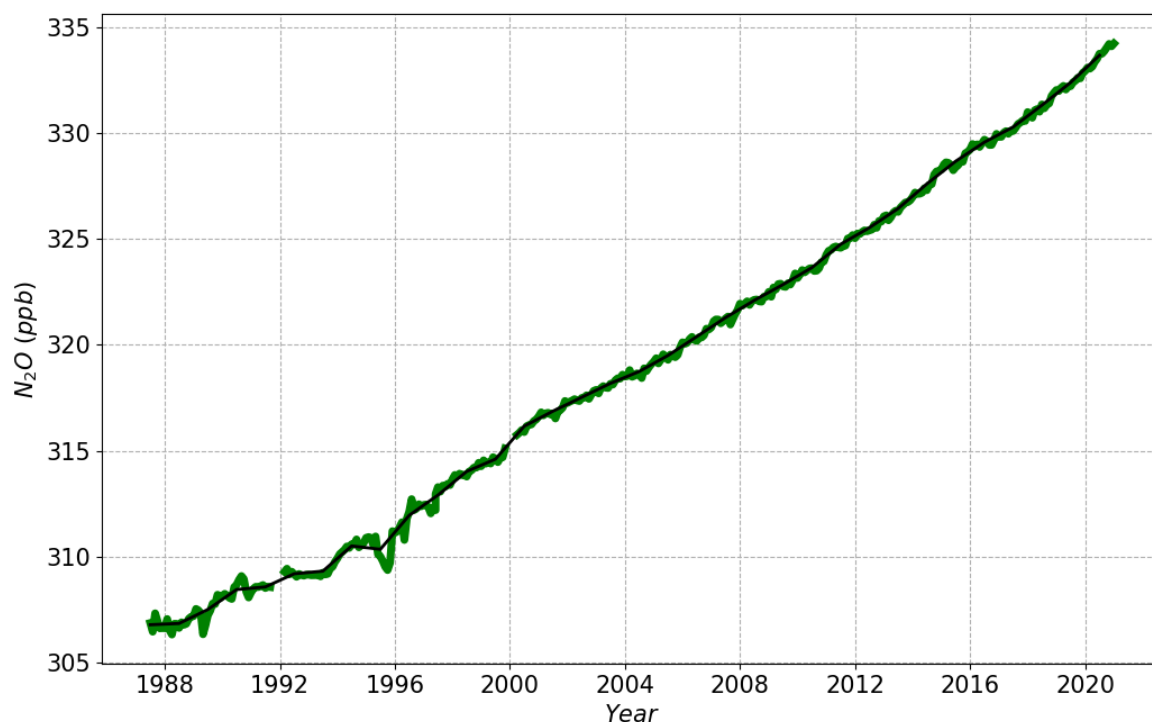


Figure 1.10: N_2O mole fraction from June 1987 to December 2020 measured from in situ spectroscopic measurements (1987-1997) and flask samples (1997-present) taken from the Mauna Loa Atmospheric Observatory, Hawaii. The green plot shows weekly N_2O mole fraction data, while the black line shows the yearly rolling average N_2O mole fraction (NOAA, 2021b).

N_2O has risen from a pre-industrial mean mole fraction of 270 ppb to a current concentration of 334.1 ppb as of May 2021 (IPCC, 2021b; NOAA, 2021b). The growth rate of N_2O abundance has remained relatively constant over the past 33 years as seen in figure 1.10, ranging between a 0.1 – 0.7% increase per year (Saikawa et al., 2014). In contrast to the variation in CH_4 abundance over recent years, N_2O shows much lower seasonal variability than CH_4 , with almost no intra-year patterns discernible from figure 1.10. In fact, a very weak seasonal cycle in N_2O abundance does exist, with stronger variability (up to ~1 ppb) in high latitudes in the northern hemisphere (Jiang et al., 2007). The N_2O seasonal cycle typically experiences northern-hemispheric winter maxima (December-February) and summer minima (April-September) for both the northern and southern hemispheres. Despite this pattern, modelled N_2O variability by Nevison et al. (2004) predicted peak seasonal N_2O in summer months concurrent with increased N_2O emission from soils. The discrepancy can be explained by the influence of stratosphere-troposphere vertical transport on N_2O seasonality, N_2O is almost exclusively removed

via stratospheric photochemistry, which results in large N₂O concentration gradients between the upper troposphere and lower stratosphere (Liao et al., 2004). Seasonal intrusions of low-N₂O stratospheric air occurring in springtime are now believed to be the dominant driver of the seasonal N₂O cycle, however the specific mechanisms for seasonal stratosphere-troposphere transport variability are currently poorly understood (Nevison et al., 2004; Ishijima et al., 2010). Some research suggests that the Arctic polar vortex can facilitate troposphere-stratospheric mixing on a seasonal cycle, accounting for the more pronounced seasonal N₂O cycle in the northern hemisphere (Nevison et al., 2011). There is also evidence for N₂O emission via oceanic ventilation playing a dominant role in the southern-hemispheric N₂O seasonal cycle, which may explain the lower seasonal amplitude observed there (Jiang et al., 2008; Yang et al., 2020).

1.3.2. Isotopic signature

In an analogous way to CH₄, ratios of N₂O isotopomers can be used to infer information about the source of N₂O emissions, however the use of N₂O isotopic ratios is much less well developed than the use of $\delta^{13}\text{C}$ -CH₄ for CH₄. For N₂O, the isotopic ratio of both nitrogen ($^{15}\text{N}/^{14}\text{N}$) and oxygen ($^{18}\text{O}/^{16}\text{O}$) can be considered, allowing $\delta^{15}\text{N}$ -N₂O and $\delta^{18}\text{O}$ -N₂O to be determined. As N₂O has two nitrogen atoms, two isotopomers with one ^{15}N atom exist and can be differentiated between, this allows calculation of two separate $\delta^{15}\text{N}$ ratios; $\delta^{15}\text{N}_\alpha$ for the “alpha” nitrogen (central) and $\delta^{15}\text{N}_\beta$ for the “beta” nitrogen (terminal). An average of these two ratios is often reported and is denoted $\delta^{15}\text{N}^{\text{bulk}}$. N₂O emitted from bacterial processes in soils tends to be more depleted in ^{15}N and ^{18}O relative to atmospheric background (Perez et al., 2001; Röckmann et al., 2003). Oceanic N₂O is produced via microbial processes that can result in either $^{15}\text{N}/^{18}\text{O}$ depletion or enrichment, so their effect on total isotopic ratio can vary (Prokopiou et al., 2018). In addition to the isotopic ratios themselves, the difference between the $\delta^{15}\text{N}_\alpha$ and $\delta^{15}\text{N}_\beta$ isotopomer ratios (known as “site preference” or $\delta^{15}\text{N}_{\text{SP}}$) can be used to differentiate between different enzymatic processes used by bacteria in N₂O production, providing further in-depth source information (Sutka et al., 2006). Conversely, photochemical destruction of N₂O in the stratosphere leads to enrichment of heavier ^{15}N and ^{18}O isotopes in the remaining stratospheric N₂O, so vertical transport of heavier N₂O from the stratosphere can result in an increase in tropospheric $\delta^{15}\text{N}^{\text{bulk}}$ -N₂O and $\delta^{18}\text{O}$ -N₂O ratios (Kaiser et al., 2002). Additionally, there is evidence that N₂O emissions from fossil fuel burning are more enriched in ^{15}N and ^{18}O (Toyoda et al., 2008). N₂O isotope records from

ice core samples have shown that $\delta^{15}\text{N}\text{-N}_2\text{O}$ and $\delta^{18}\text{O}\text{-N}_2\text{O}$ ratios remained relatively stable during the pre-industrial era, but both began to decrease from the onset of the industrial revolution in line with increased soil N_2O emissions from anthropogenically fertilised agricultural land (Röckmann et al., 2003; Ishijima et al., 2007). Despite this observation, there is also evidence that $\delta^{15}\text{N}^{\text{bulk}}\text{-N}_2\text{O}$ and $\delta^{18}\text{O}\text{-N}_2\text{O}$ ratios have varied at differing rates during the post-industrial period, suggesting that N_2O has originated from a wider range of source components rather than from a single dominant anthropogenic source (Sowers et al., 2000). Due to the multitude of soil and oceanic microbial pathways that can lead to N_2O production and the variables that may impact which pathway is favoured, it is probable that the isotopic signature of emitted N_2O varies significantly in space and time resulting in large uncertainties in global isotopic ratio estimates (Perez et al., 2001; Prokopiou et al., 2018). Therefore, more accurate estimates of global N_2O isotopic ratios are required before they can be used effectively for purposes such as source apportionment.

1.3.3. Sources, sinks, and budget

The majority of N_2O emitted to the atmosphere occurs through the activity of microorganisms in soils, oceans, and freshwater systems. The two principal pathways in which N_2O can be produced by microbes are nitrification and denitrification. Nitrification is the oxidation of ammonium (NH_4^+) to nitrite (NO_2^-) and then subsequently to nitrate (NO_3^-) by bacteria. N_2O is produced as a minor side-product when NO_2^- is used as an electron acceptor instead of oxygen in O_2 -limited conditions. The rate of N_2O emission has also been found to be influenced by soil moisture content, with drier soils facilitating free diffusion of gases to the atmosphere (Firestone and Davidson, 1989; Parton et al., 1996; Bremner et al., 1997). Denitrification is in essence the reverse of the nitrification process, where NO_3^- is first reduced to NO_2^- and then to gaseous NO , N_2 , and N_2O . As is the case with nitrification, N_2O production via denitrification occurs optimally in anaerobic environments, where NO_3^- is used as an electron acceptor in place of O_2 (Wrage et al., 2001). In soils, the variables that affect N_2O production by nitrification and denitrification are relatively well understood. However, in oceans the understanding of microbial processes is far less well understood. Research has suggested that in contrast to soils, nitrification is the primary pathway for N_2O production in oceans, and denitrification only accounts for around 7% of produced N_2O (Freing et al., 2012). However, other studies have also suggested that N_2O produced by denitrification may be

vastly underestimated in suboxic regions of the ocean (low dissolved O₂, but not as low as anoxic regions) (Babbin et al., 2015). Despite this, there is still very limited understanding on how oceanic N₂O production by both nitrification and denitrification varies spatially and temporally, and if anthropogenic climate change may result in positive feedback of ocean N₂O emissions (Battaglia et al., 2018; Babbin et al., 2020).

Table 1.2: The estimated global N₂O budget between 2000-2010 and 2007-2016. N₂O sources and sinks are reported in units of Tg N year⁻¹, and atmospheric burdens are reported in units of Tg N. Literature minima and maxima for each source are reported as well as the mean values for each time period. Data are obtained from Tian et al., (2020).

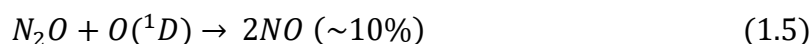
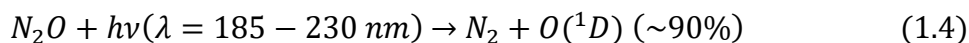
		Tian et al., (2020)					
		2000s			2007-2016		
		Mean	Min.	Max.	Mean	Min.	Max.
Anthropogenic sources							
Direct emissions from nitrogen additions in the agricultural sector (Agriculture)	Direct soil emissions	2	1.3	3.4	2.3	1.4	3.8
	Manure left on pasture	1.1	0.8	1.2	1.2	0.9	1.3
	Manure management	0.3	0.2	0.5	0.3	0.2	0.5
	Aquaculture	0.1	0.02	0.2	0.1	0.02	0.2
	Subtotal	3.4	2.3	5.2	3.8	2.5	5.8
Other direct anthropogenic sources	Fossil fuels and industry	0.9	0.8	1	1	0.8	1.1
	Waste and wastewater	0.3	0.2	0.4	0.3	0.2	0.5
	Biomass burning	0.6	0.6	0.6	0.6	0.5	0.8
	Subtotal	1.8	1.6	2.1	1.9	1.6	2.3
Indirect emissions from anthropogenic nitrogen additions	Inland waters, estuaries, coastal zones	0.4	0.2	0.6	0.5	0.2	0.7
	Atmospheric nitrogen deposition on land	0.7	0.4	1.3	0.8	0.4	1.4
	Atmospheric nitrogen deposition on ocean	0.1	0.1	0.2	0.1	0.1	0.2
	Subtotal	1.2	0.6	2.1	1.3	0.7	2.2
Perturbed fluxes from climate/CO ₂ /land cover change	CO ₂ effect	-0.3	-0.5	0.1	-0.3	-0.6	0.1
	Climate effect	0.7	0.3	1.2	0.8	0.3	1.3
	Post-deforestation pulse effect	0.7	0.7	0.8	0.8	0.7	0.8
	Long-term effect of reduced mature forest area	-1.0	-0.9	-1.1	-1.1	-1.0	-1.1
	Subtotal	0.2	-0.4	0.9	0.2	-0.6	1.1
Anthropogenic total		6.7	4.1	10.3	7.3	4.2	11.4
Natural sources							
Natural soils baseline		5.6	5	6.5	5.6	4.9	6.5
Ocean baseline		3.5	2.7	4.3	3.4	2.5	4.3
Natural (inland waters, estuaries, coastal zones)		0.3	0.3	0.4	0.3	0.3	0.4
Lightning and atmospheric production		0.4	0.2	1.2	0.4	0.2	1.2
Surface sink		-0.01	0	-0.3	-0.01	0	-0.3
Natural total		9.8	8.2	12	9.7	8	12
Bottom-up total source		16.4	12.3	22.4	17	12.2	23.5
Top-down ocean		5.1	3.1	7.2	5.1	3.4	7.1
Top-down land		10.8	9.3	12.5	11.8	10.6	13.8
Top-down total source		15.9	15.1	16.9	16.9	15.9	17.7
Top-down stratospheric sink		12.1	11.4	13.1	12.4	11.7	13.3
Observed atmospheric chemical sink^a		13.3	12.2	14.4	13.5	12.4	14.6
Change in atmospheric abundance^b		3.7	3.2	4.2	4.3	3.8	4.8
Atmospheric burden		1,531	1,510	1,552	1,555	1,533	1,577

(a) Calculated from satellite observations with a photolysis model (about 1% of this sink occurs in the troposphere). (b) Calculated from the combined NOAA and AGAGE record of surface N₂O, and adopting the uncertainty of the IPCC Assessment Report 5 (Chapter 6).

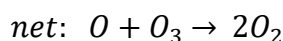
Table 1.2 shows the estimated atmospheric N₂O budget between 2000 and 2016 as reported by Tian et al. (2020). It can be seen that soils and oceans are included in both natural and anthropogenic source estimates. Nitrification and denitrification in natural soils leads to a mean baseline emission of 5.6 Tg N year⁻¹, but input of nitrogen from fertilisers used on agricultural land results in enhanced microbial production of N₂O within these soils, accounting for an extra 2.5 Tg N year⁻¹ on average (Bouwman, 1996). Additionally, fertiliser runoff and leaching into areas of inland water, estuaries, and coastal zones result in the ocean and freshwater N₂O emission estimate being

anthropogenically enhanced by $0.5 \text{ Tg N year}^{-1}$ on average (Reay et al., 2005). Deposition of anthropogenic atmospheric nitrogen compounds can also add nitrogen to soils and oceans, resulting in the emission of an extra $0.9 \text{ Tg N year}^{-1}$ (Suntharalingam et al., 2012; Yang et al., 2021). N_2O emissions from biomass burning and industrial activity such as fossil fuel burning and synthesis of certain chemical precursors (nitric acid and adipic acid) make up the only non-microbial sources of N_2O included in the Tian et al. (2020) budget. Biomass burning and industrial activity account for the emission of $0.6 \text{ Tg N year}^{-1}$ and 1 Tg N year^{-1} respectively. Table 1.2 also includes small N_2O sources resulting from positive climate feedbacks and land use change. The increase of N_2O emission as a result of climate change and increased surface temperatures is estimated to be $0.8 \text{ Tg N year}^{-1}$ on average. Additionally, deforestation is known to cause a temporary ‘pulse’ in N_2O emissions due to the remaining high content of nitrogen of soils after forested land has been cleared, this effect results in the mean emission of $0.8 \text{ Tg N year}^{-1}$ (Verchot et al., 1999).

The single largest sink of N_2O is removal via atmospheric chemistry. Unlike CH_4 which is removed by tropospheric chemical processes, N_2O is removed almost exclusively within the stratosphere where the majority is photolyzed to N_2 gas and $\text{O}(^1\text{D})$ (see equation 1.4) (Blake et al., 2002):



Approximately 90% of N_2O transported up to the stratosphere is destroyed by this pathway, the remaining 10% reacts with $\text{O}(^1\text{D})$ to form NO (see equation 1.5). The presence of NO in the stratosphere catalytically destroys O_3 (equations 1.6 and 1.7), resulting in N_2O contributing significantly to ozone layer depletion.



N₂O is now understood to be the dominant ozone-depleting substance emitted today, and will continue being the largest contributor to ozone depletion well into the 21st century due to N₂O being unregulated by the Montreal Protocol (Ravishankara et al., 2009).

The stratospheric chemical N₂O sink accounts for the mean removal of 12.4 Tg N year⁻¹, which is almost 80% of the total yearly source of N₂O to the atmosphere. As N₂O must first be transported from the troposphere to the stratosphere to be removed, N₂O in the troposphere has a long lifetime of 114 ± 9 years (Prather et al., 2015). In contrast to CH₄ with its short tropospheric lifetime, N₂O emission mitigation strategies may take decades before a reduction in N₂O abundance is observed, whereas CH₄ emission mitigation may result in rapid reduction in abundance. Due to the nature of the stratospheric N₂O sink, a feedback system exists in which increasing abundance of N₂O leads to a reduction in its lifetime. As more N₂O is removed in the stratosphere and hence more O₃ is destroyed, less UV radiation is filtered out by stratospheric O₃ and therefore more N₂O can be photolyzed (Prather, 1998). It is estimated that the lifetime of N₂O decreases by 0.5% for every 10% increase in N₂O abundance due to this effect, and the mean N₂O lifetime has been revised from 120 years to 114 years due to identification of this phenomenon (Ehhalt and Prather, 2001).

Aside from the stratospheric N₂O sink, there are very few other N₂O sinks present in the Earth system, and these account for <10% of the total N₂O sink. To a small extent, soils can act as sinks of N₂O where denitrifying bacteria reduce N₂O to N₂. This process is difficult to accurately quantify as disaggregation of N₂O uptake and N₂O production in soils is often not possible. Soils are estimated to remove 0.01 Tg N year⁻¹ from the atmosphere on average (Chapuis-Lardy et al., 2007). Atmospheric CO₂ and land use change can also result in indirect N₂O removal. Higher CO₂ atmospheric abundance enhances the growth of plant life, which in turn reduces nitrogen content in surrounding soils and reduces N₂O emission. The indirect effect of CO₂ leads to the mean N₂O removal of 0.3 Tg N year⁻¹ (Zaehle et al., 2011). Finally, the conversion of forested land where soils are large N₂O emitters to non-fertilised pasture or agricultural land where N₂O emissions are lower accounts for the indirect N₂O removal of 1.1 Tg N year⁻¹ (Davidson et al., 2007).

To a greater extent than with CH₄, the current source and sink estimates of N₂O have large uncertainties associated with them primarily due to large spatiotemporal variability

in the strength of microbial emissions controlled by a wide number of physical and chemical variables that are poorly understood (Butterbach-Bahl et al., 2013). As N₂O emissions are usually smaller in magnitude than CH₄ emissions, there is an added challenge of physically measuring emissions, as current experimental techniques struggle to resolve small magnitude fluxes seen from some N₂O emission sources. More in situ and modelling studies investigating source emissions of N₂O are needed in order to better understand the controls on emission variability, and to help reduce uncertainty in the global N₂O budget.

Chapter 2

Introduction Part 2: Emission Quantification and Instrumentation

2.1. Current measurement networks and infrastructure

Globally distributed networks of GHG measurements are required to understand the spatial variability of GHG abundance across the globe and to quantify changes in global burdens over time. Global GHG measurement networks are currently well-established, utilising different measurement platforms such as tall towers, ships, aircraft, and satellites.

The most significant network of atmospheric baseline GHG measurement platforms is currently coordinated by the World Meteorological Organisation Global Atmosphere Watch (WMO-GAW, WMO, 2022a). These consist of a core network of 30 global measurement sites, and 400 regional sites making continuous GHG measurements alongside other trace gas species, aerosols, and meteorological parameters. Many other independent observation sites also contribute towards the WMO-GAW measurement network, including the Total Carbon Column Observation Network (TCCON, Wunch et al., 2011) where carbon column average measurements are made via ground-based Fourier transform infrared instruments, and the European Integrated Carbon Observation System (ICOS) (Heiskanen et al., 2022). The ground-based measurement sites aim to measure reliable background GHG mole fractions that are influenced minimally by local pollution sources, and hence allow for a comprehensive understanding of how GHG abundance growth and seasonality varies over space and time. In addition to measurement platforms, the WMO-GAW infrastructure also involves a globally adopted quality assurance system for instrument calibration traceability. The WMO publishes trace gas calibration scales based on gas chromatographic (GC) mole fraction analysis of primary standards, the current scales are the X2004A scale for CH₄ and the NOAA-2006A scale for N₂O (WMO, 2022b; Hall et al., 2007). Instrument calibration gas standards can be

certified against WMO standards, making them traceable to a common established calibration scale.

The WMO-GAW network is not limited to ground-based measurements, the In-service Aircraft for a Global Observing System (IAGOS, Nédélec et al., 2015) infrastructure involves using commercial aircraft as platforms for trace gas, aerosol, and meteorological observations. Ten international airlines participate in the IAGOS project, with 20 total aircraft equipped with in situ instrumentation suites. In addition to networks of commercial aircraft, specialised airborne atmospheric measurement platforms exist, such as those operated by the UK Facility for Airborne Atmospheric Measurement (FAAM, McBeath et al., 2014) and the Institute of Atmospheric Physics at the German Aerospace Center (DLR, Krautstrunk and Giez, 2012). These aircraft are heavily modified for atmospheric observation, and can be equipped with a larger range of instrumentation than the commercial IAGOS aircraft. Furthermore, these aircraft can specifically target and fully characterise emission sources of interest, whereas commercial IAGOS aircraft measure only along their set flight path.

Airborne observation networks and specialist platforms can provide measurements with higher spatial resolution than ground-based measurement networks or platforms, for example a commercial IAGOS aircraft could fully characterise latitudinal variations in CH₄ during a single flight, whereas ground-based networks rely on single location measurements with poor spatial resolution as a whole. The spatial coverage of IAGOS flights since the projects' inception is shown in figure 2.1. Aircraft are also able to vertically profile the atmosphere, observing variability in trace gases throughout the boundary layer and free troposphere. Ground-based measurements are limited in this respect, as they only sample at one height, and ground-based column measurements cannot resolve variability within the column. A notable limitation with airborne measurements is the lack of temporal sampling intensity, aircraft can only provide a 'snapshot' sample of a point in space and time, whereas permanent ground-based sites can continuously measure one location with high temporal resolution. Chapters 3 and 4 involve measurements of CH₄, N₂O, and other trace gas and meteorological parameters taken aboard the specialist FAAM BAe-146 atmospheric research aircraft.

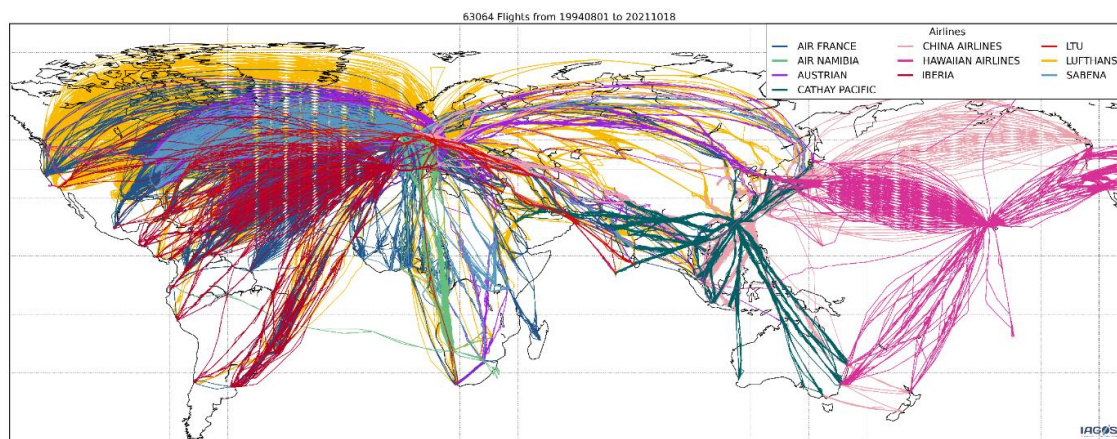


Figure 2.1: Flight tracks of all IAGOS network sampling flights from 01/08/1994 to 18/10/2021. Flight tracks are coloured by operating airline (IAGOS, 2022).

In contrast to the in situ measurements taken by ground-based and aircraft networks, satellite-based measurement platforms use remote sensing techniques to determine global GHG abundances at high spatial and temporal resolution. One such satellite-mounted remote sensing instrument is the TROPospheric Monitoring Instrument (TROPOMI, Lorente et al., 2021) mounted on the Copernicus Sentinel 5-P polar-orbiting satellite. TROPOMI is a passive multispectral imaging instrument that can measure in the visible, UV, and infrared spectral regions, it can perform total column measurements of CH₄ and various other trace gases, aerosol, cloud, and UV index. TROPOMI currently provides the highest resolution measurements of CH₄ currently available from a satellite platform, with a maximum resolution of 50 km² (Tollefson, 2018). In order to improve the standard of future satellite CH₄ measurements, current research by the Environmental Defense Fund (EDF, New York, NY, USA) is focused on a dedicated CH₄ remote sensing satellite named MethaneSAT (EDF, 2022). This satellite is planned to launch in 2023, and will provide global total column CH₄ at up to 1 km² resolution, with a specific focus on oil and gas CH₄ emissions.

A major advantage of GHG measurement by satellite remote sensing is that all regions of the Earth can be sampled non-invasively in a relatively quick time frame, with full global coverage possible within a single day for the Sentinel 5-P satellite (Borsdorff et al., 2018). There are often significant geographical and/or political constraints on aircraft and ground-based sampling which limit the locations in which this sampling can take place, whereas an orbiting satellite platform does not require any ground or air presence to take measurements. However, satellite instruments cannot be calibrated against

certification scales (such as the WMO scale) as is done with in situ techniques. Satellite retrievals must therefore be validated against ground-based networks such as TCCON sites, which has the potential to introduce significant biases into mole fraction data (Lorente et al., 2021; Palmer et al., 2021).

2.2. Emission quantification techniques

The measurement networks described in the previous section ultimately exist to reduce the uncertainty on global GHG budgets, the individual observations within these networks rely on an array of techniques for quantifying emissions. These techniques range from highly precise emission estimates (known as fluxes) over limited spatial and or temporal scales, to regional or global scale fluxes spanning multiple years at low spatial resolution or with higher uncertainty. This section will describe the range of in situ and modelling techniques used to quantify GHG sources and sinks, and the relative strengths and weaknesses of each technique. A summary of the techniques discussed in Section 2.2 is shown in Table 2.1.

2.2.1. Flux chambers

Flux chambers are often used for quantifying surface exchange of trace gas species from a range of target areas such as wetlands (Morin et al., 2014; O'Shea et al., 2014a), agricultural soils (Ambus et al., 1993; Rochette et al., 2008) and landfill sites (Reinhart et al., 1992; Di Trapianni et al., 2013). Flux chambers often take the form of “static” chambers, where a closed container with a known volume is placed over the area of interest for a period of time. The change in trace gas concentration within the container over time is measured via external analysis of samples, and is used to derive a flux. The major limitation of this approach is that the closed container can alter the microclimate of the sample location and result in under- or over-estimations of the flux (Collier et al., 2014). In order to reduce the effect of the chamber on microclimate, “Dynamic” flux chamber techniques using open chambers are often used. These chamber systems involve circulation of known-concentration air through the flux chamber apparatus, air is passed continuously to a trace gas analyser and flux is derived from these continuous measurements. Dynamic flux chambers avoid changing the conditions of the study area as is often the case with static chambers, however the apparatus is often more complex

and the use of many flux chambers over a wide area is more difficult with dynamic chambers (Moore and Roulet, 1991; Pavelka et al., 2018).

Table 2.1: Summary of the emission quantification techniques presented in Section 2.2. The spatial and temporal scales that the techniques are effective over is shown, as well as common examples of their use.

Flux Technique	Spatial scale	Temporal scale	Example of Use
Flux Chambers	Small	Large (if continuously monitoring)	Soil fluxes
Eddy Covariance	Medium	Large (if continuously monitoring)	Forest/urban area fluxes
Mass Balance	Variable	Small (snapshot)	Wetland fluxes/oil and gas plumes
Emission Ratios/Factors	Variable	Variable (small for individual emission factor, emission inventory depends on activity data)	Biomass burning/vehicular emissions
Process Modelling	Large	Depends on <i>a priori</i> inputs	Large-scale wetland emissions
Inversion Modelling	Large	Depends on <i>a priori</i> inputs	Emissions for entire countries/regions

Flux chambers are relatively cheap to implement and can be installed for long periods of time in order to investigate temporal variability of emissions. Due to sampling at ground level very close to an emission source, flux chambers also have high sensitivity to small changes in trace gas concentration and hence can resolve small fluxes that may fall below the limit of detection of other techniques. As previously mentioned, a major limitation is that flux chambers are a more invasive technique than other methods, and their presence may directly affect fluxes obtained by changes in microclimate or ecosystem dynamics. An additional drawback is that flux chambers can only sample surface-level sources, and only a very limited source area can be investigated by a single chamber at a time, so information on the spatial variability in a surface source cannot be

obtained and upscaling chamber fluxes to a wider area would have to assume homogeneity in the source.

2.2.2. Eddy covariance

The eddy covariance technique is a commonly used micrometeorological flux quantification approach. This method obtains a flux by correlating trace gas concentration measurements with turbulent vertical wind velocity measurements from within the surface boundary layer. In principle, source or sink behaviour of a surface will result in either enhancement or reduction of local trace gas mole fraction over the background, which is measured via turbulent vertical transport of air parcels at the surface upwards towards a measurement sensor (Baldocchi, 2003). Calculation of flux via eddy covariance is expressed by equation 2.1:

$$F = \bar{\rho}_a \cdot \overline{w'c'} \quad (2.1)$$

Where $\bar{\rho}_a$ is the air density averaged over a set time interval, $\overline{w'}$ is the average fluctuation of vertical wind velocity from the mean over the set time interval, and $\overline{c'}$ is the average fluctuation of trace gas mole fraction from the mean over the set time interval. The parameters of eddy covariance flux calculation are averaged over a set time period to account for the constantly varying magnitude and sign of vertical wind velocity. As the average turbulent fluctuation of vertical wind and mole fraction is required for flux calculation, any longer-term trends in these parameters must first be removed (Aubinet et al., 2012).

Traditional eddy covariance techniques require high frequency (>10 Hz) measurements of mole fraction and 3D wind speed and direction. The relaxed eddy accumulation method was first developed to allow the technique to be applied with instruments with slower response times and thus allow the technique to be applied to a wider array of trace gases. Relaxed eddy accumulation relies on collecting air into updraft and downdraft “reservoirs” over a given sampling period, of which the flow rate into each reservoir is constant, and purely dependent on the sign of the vertical wind velocity. This achieves the same result as eddy covariance while sacrificing some of the fine information on wind velocity and concentration (Bowling et al., 1998). The need to obtain statistically significant air transport reservoirs results in averaging time typically being longer for relaxed eddy accumulation (McInnes and Heilman, 2015)

A key assumption in the eddy covariance technique is that the emission rate of the target area is homogenous over the span of the averaging time period, eddy covariance is therefore less appropriate for areas with complex mixtures of different sources with rapidly changing magnitudes, as eddy covariance will not be able to resolve changes in source strength over timescales shorter than the averaging period. Nevertheless, eddy covariance has been used to derive trace gas fluxes from a range of different environments, such as CH₄ emission from wetlands (Hargreaves et al., 2001; Desai et al., 2015), CO₂ uptake from forests (Goulden et al., 1996; Van Dijk and Dolman, 2004), and even N₂O emissions from urban environments (Famulari et al., 2010; Järvi et al., 2014). The fluxes obtained via eddy covariance take the form of a flux “footprint”, which is the area-normalised flux for an area of between 100 m² and 2000 m² surrounding the measurement location (Schmid, 1994; Liang and Wang, 2019), therefore eddy covariance fluxes have a higher spatial coverage than single chamber fluxes, but may not be able to resolve spatial and temporal flux variations within the footprint. Measurements for eddy covariance are most commonly made at height from stationary flux towers, or less commonly from aircraft. Global measurement networks of eddy covariance flux towers now exist such as the international FLUXNET network and the European ICOS eddy covariance network that provide constant eddy covariance CO₂, CH₄, N₂O, CO, and H₂O flux measurements from a number of globally distributed towers situated at key source/sink locations (Baldocchi et al., 2001; Alam et al., 2019). The major limitation of the eddy covariance technique is with the cost and complexity of the infrastructure. High frequency (>10 Hz) measurements of trace gas mole fraction and 3D wind speed and direction are required from a tall measurement platform or aircraft in order to calculate an eddy covariance flux, which is considerably more complex and expensive than simple flux chambers where samples can be taken and analysed off-site.

2.2.3. Mass balance

The mass balance method technique is commonly used to calculate regional trace gas fluxes from airborne measurements, where the mass of a species advecting through a vertical plane downwind of an emission source is quantified. Mass balance models an area within the convective boundary layer (CBL) around an emission source as a 3D box, where flux calculation is expressed by equation 2.2:

$$F = \int_0^z \int_{x_0}^{x_i} (C_{Enh} - C_0) \cdot U_{\perp} dx dz \quad (2.2)$$

Where z is the height of the CBL, which is the vertical constraint of the mass balance box model where entrainment between the CBL and the free troposphere is assumed to be negligible. x_i and x_0 are the horizontal bounds of the box measured perpendicular to the wind direction. C_{Enh} is the enhanced mole fraction and C_0 is the background mole fraction of the species under investigation, C_{Enh} is measured directly downwind of the emission source, whereas C_0 can be measured upwind of the source or to the side of the downwind emission plume. U_{\perp} is the wind speed perpendicular to the plane of the downwind measurement (Mays et al., 2009; Cambaliza et al., 2014). An illustration of mass balance experimental setup, along with upwind and downwind locations of C_0 is shown in figure 2.1. As the flux is integrated over the vertical and horizontal dimensions of the box, measurements of the emission plume must firstly ensure that the emission plume is fully characterised horizontally (i.e. a clear background can be seen either side of the plume) or that the enhanced concentration is homogenous on the downwind measurement leg. Secondly, it must be ensured that the plume is well mixed up to the top of the boundary layer.

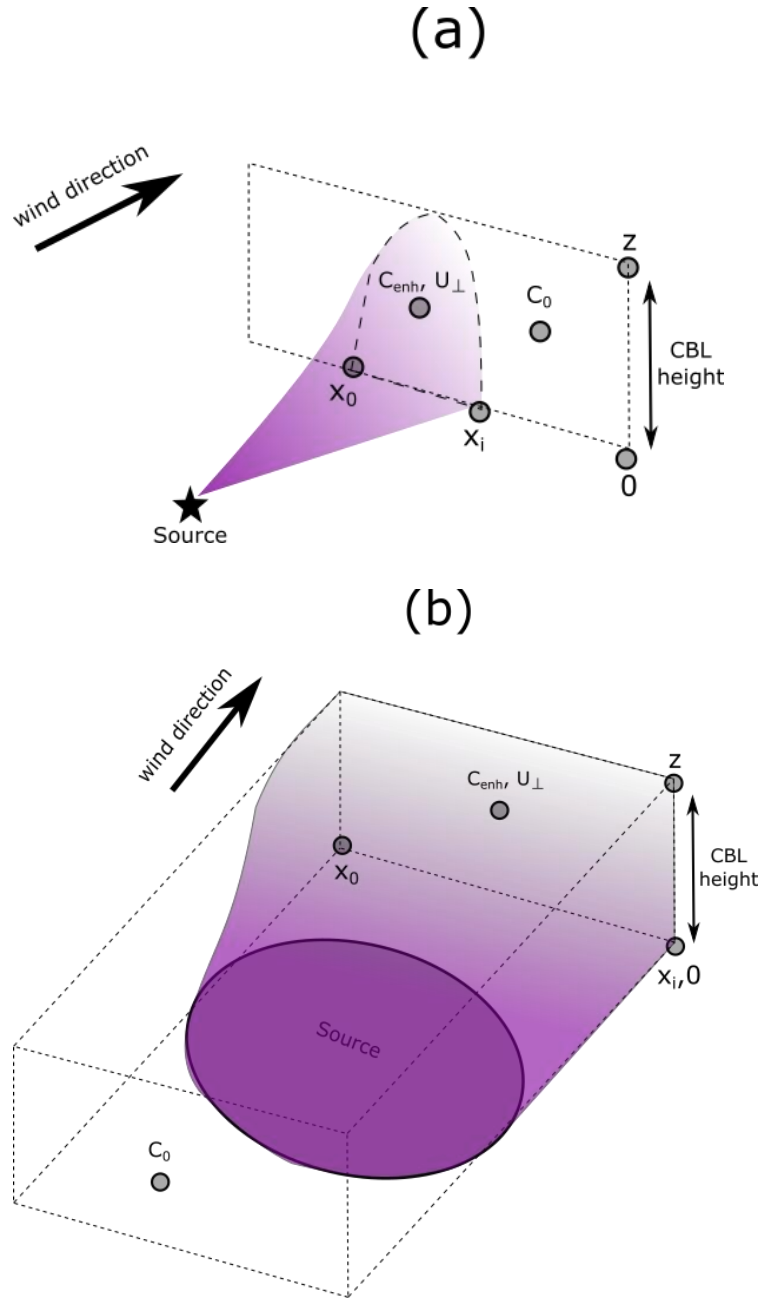


Figure 2.1: Experimental set up for the practical use of the mass balance technique. (a) shows a point source example where the background mole fraction, C_0 , is taken downwind, and (b) shows an area source case where C_0 is measured upwind.

Mass balance is a versatile technique for quantifying emissions from a range of natural and anthropogenic sources, including fossil fuel extraction (Karion et al., 2015; Fiehn et al., 2020), metropolitan areas (Heimbürger et al., 2017; Pitt et al., 2019), wetlands (O'Shea et al., 2014a), and agriculture (Gvakharia et al., 2020). The mass balance technique can derive fluxes from much larger source areas (such as entire cities) than is possible using chamber or eddy covariance methods. Furthermore, the common use of an

airborne measurement platform allows specific point sources to be targeted with high specificity, which is considerably more difficult for other techniques. The main limitations of mass balance are the considerable cost of mobile airborne measurements, as well as the intense sampling of the plume required throughout the entirety of the CBL. Additionally, mass balance only provides a single temporal “snapshot” flux that is only truly representative of the time of measurement, it therefore cannot resolve temporal variability in source/sink behaviour as is possible with chambers and eddy covariance unless multiple measurements are made over time. Chapter 4 will describe the use of aircraft mass balance to derive CH₄ and CO₂ fluxes from European arctic wetlands, and how these results compare with other techniques.

2.2.4. Emission ratios and emission factors

Emission ratios (ER) and emission factors (EF) are important metrics often used for quantifying emissions from biomass burning. ER are calculated for an emission plume using equation 2.3:

$$ER_{x/y} = \frac{\Delta X}{\Delta Y} = \frac{X_{plume} - X_{background}}{Y_{plume} - Y_{background}} \quad (2.3)$$

Where ΔX is the excess mixing ratio of the species in question, X, within the plume, and ΔY is the excess plume mixing ratio of a tracer species, Y, which X is normalised against. In the case of biomass burning, the tracer species Y is commonly CO, with CO₂ and CH₄ occasionally used (Andreae, 2019). Measurement of ER is most accurate when fresh plumes are sampled close to source, in plumes transported over longer distances chemical aging and mixing with background air from different airmasses can change the plume composition and hence the relative excess mixing ratios of X and Y. In more aged plumes (>1 day) the solution to equation 2.3 is referred to as normalised excess mixing ratio (NEMR), and “true” ER are calculated using equation 2.3 only in fresh plumes (Yokelson et al., 2013)

ER can be used to subsequently calculate EF for biomass burning plumes. In a comparable way to traditional fluxes, EF quantify the mass of a species emitted to the atmosphere. In contrast to fluxes in which emission is normalised to area and time, EF are normalised to the mass of fuel burnt, and are usually expressed in units of grams of species emitted per kilogram of fuel burnt. EF are calculated using equation 2.4:

$$EF_x = F_C \cdot \frac{M_x}{M_C} \frac{C_x}{C_{total}} \cdot 1000(g\ kg^{-1}) \quad (2.4)$$

Where F_C is the estimated fraction of carbon in the fuel, which is typically in the range of 45-55% (Susott et al., 1996; Yokelson et al., 2009). M_x and M_C are the molar masses of species x and carbon respectively. C_x/C_{total} is the molar ratio of species x to the total carbon in the plume, which is given by equation 2.5:

$$\frac{C_x}{C_{total}} = \frac{ER_{x/CO}}{1 + ER_{CO_2/CO} + ER_{CH_4/CO}} \quad (2.5)$$

As per equation 2.5, total carbon in the plume is assumed to be the sum of CO, CO₂, and CH₄, however small amounts of other carbonaceous species are emitted by fires that are often not all accounted for, therefore estimation of total carbon in the plume by equation 2.5 is typically underestimated by 1 – 2% (Yokelson et al., 1999).

EFs have been compiled for a wide range of chemical species and biomass burning fuels (Andreae, 2019). EF provide a convenient method for estimating global emissions of many chemical species (including GHGs) from a range of biomass burning fuel types simply by multiplying EFs with estimates of fuel mass burned over space and/or time. Biomass burning emission models, such as the current iteration of the Global Fire Emission Database (GFED4) often estimate fuel mass burnt by using remote sensing inputs of burnt land area combined with vegetation models (van der Werf et al., 2017). Estimates of total carbon emissions from models such as GFED4 are highly variable, recent research has found that modelled organic carbon and black carbon fire emissions can differ by factors of 3.8 and 3.4 respectively between individual models. This highlights the high sensitivity of fire emission models to estimates of burnt area, vegetation models, and emission factors used (Pan et al., 2020). Chapter 3 of this thesis is focused on measurements of sub-Saharan African biomass burning, and reports GHG EFs for wildfires in different locations and with different probable fuel types.

The use of EF for estimates of wider regional or global emissions is not limited to biomass burning. In general, emission inventories for various sectors of GHG emissions are compiled as shown in equation 2.6:

$$Emission = Activity \times Emission\ Factor \quad (2.6)$$

As is the case with biomass burning, EFs are the mass of species emitted normalised to the activity of the source. For fires, the activity of the source is the mass of biomass burned, but for different sources the activities vary (e.g. energy produced for fossil fuels, or distance travelled for vehicular emissions). Large regional emission inventories such as the UK National Emissions Inventory (NAEI, Tsagatakis et al., 2022) compile emission factors and activity data from a full range of sectors to provide full bottom-up emission estimates for an entire region. As with biomass burning emission modelling from EF data, estimation of activity data and EFs for specific sectors or technologies can prove to be very difficult, and often have large uncertainties associated with them that propagate to large errors in regional emission estimates.

2.2.5. Process modelling

Process-based modelling is often used to estimate emission and uptake of GHGs over large biogeochemical source areas. Process modelling requires an understanding of various chemical and physical inputs and conditions present in biogeochemical ecosystems that result in GHG emission or uptake. Process models estimate the flux by parameterising meteorological and biogeochemical data and using these as inputs.

The Joint UK Land Environment Simulator (JULES) model is an example of a land surface biogeochemical process model that can estimate CH₄ flux from wetland environments and CO₂ uptake via photosynthesis (Clark et al., 2011). CH₄ flux from wetlands is estimated by JULES using equation 2.7 (Gedney et al., 2004):

$$F_{CH_4} = k_{CH_4} \cdot f_w \cdot C_s \cdot Q_{10}(T_{soil})^{\frac{T_{soil}-T_0}{10}} \quad (2.7)$$

Where k_{CH_4} is a constant which is tuned to give global CH₄ flux, f_w is the wetland fraction inferred from water table height data, C_s is the soil carbon content, Q_{10} is a measure of the sensitivity of soil respiration to temperature change which is calculated for the temperature of the top 10 cm of soil (T_{soil}), and T_0 is standard atmospheric temperature (273.15 K). The CH₄ emission model is coupled to large-scale land surface schemes that provide inputs of soil moisture, water table height, and soil carbon content.

As is clear from process models such as JULES, global estimates of GHG emissions from biogenic sources can easily be estimated over large temporal scales as long as input

data exists. However, estimates of individual model parameters are often highly uncertain, and multiple approaches for obtaining model inputs exist, which can introduce significant variability between process models. Furthermore, biogenic GHG emission and uptake processes are extremely complex, and the JULES CH₄ flux example in equation 2.7 shows a simple flux quantification model where the input data is relatively easy to obtain. A balance exists between the need to fully characterise soil microbial processes to provide more accurate fluxes where the data inputs for said processes may be less readily available, and using simplified model parameters that may not fully capture the complexity of soil processes, but will allow fluxes to be obtained far more readily. Chapter 4 in this thesis involves intercomparison of mass balance CH₄ fluxes from European Arctic peatlands with those reported by several process models, including JULES.

2.2.6. Inversion modelling

Inverse modelling is a top-down technique used for regional or global emission estimates by combining mole fraction measurements with some form of atmospheric chemical transport model, and are commonly used for large-scale emission estimation from ground-based measurement network data and satellite observations. Inverse models initially require an *a priori* estimate of emissions for the source location, usually obtained from existing emission inventories. Chemical transport models are used to determine an emission footprint from the in situ measurements locations by investigating the air mass movement from source to receptor. An *a posteriori* flux is obtained by optimising the existing *a priori* flux with current trace gas measurements and source locations, and finding the best fit between prior emission distribution and measured data by the minimisation of a cost function, this is the basic approach taken by Bayesian inversion emission models, yet individual methods can differ significantly between studies (Chen and Prinn, 2006; Rigby et al., 2011; Maione et al., 2014).

Atmospheric inversions have been used to quantify both CH₄ and N₂O emissions globally (Monteil et al., 2013; Thompson et al., 2019) and regionally (Zhao et al., 2009; Manning et al., 2011), and are useful for top-down emission estimation from much larger spatial and temporal scales than are possible from techniques such as mass balance. Inverse techniques also benefit from the ability to ingest observational data from a variety of platforms, including fixed ground-based measurement networks, aircraft

measurements, and satellites (Ganesan et al., 2015; Yu et al., 2021; Wecht et al., 2014). A major limitation of atmospheric inversion is that a prior estimate of emissions is first required in order to derive a posterior flux, so novel sources with little prior characterisation in emission inventories cannot be quantified by atmospheric inversion.

Eulerian atmospheric transport models, which are commonly used for inversions and calculate transport on a known coordinate grid, commonly face issues with aggregating emissions from smaller-scale sources into larger bulk regions, and hence incorrectly estimating spatial emission distribution within bulk regions. This aggregation issue is lessened with the use of a Lagrangian transport model, where trajectory “particles” representing individual air parcels are modelled backwards in time to simulate movement of airmasses from sources to receptors. The major issues with Lagrangian transport models is that there is significant difficulty and uncertainty with resolving airmass boundaries, and airmasses are only modelled backwards for a limited time span, so boundary conditions must be determined for emissions outside the time span of the airmass transport (Rigby et al., 2011).

2.3. GHG measurement techniques

Many of the emission quantification strategies described in section 2.2 rely on in situ observations of GHGs from airborne or ground-based instrumentation, which usually involves a form of infrared absorption spectroscopy. This section will describe the basic principles behind absorption spectroscopy, and how infrared absorption spectroscopy is used to measure mole fractions of GHG species.

2.3.1. The Beer-Lambert law and infrared spectroscopy

Absorption spectroscopy is reliant on the attenuation of a light source by an absorbing species which can be used to derive the concentration of the absorber by means of the Beer-Lambert law (Swinehart, 1962):

$$I_0/I = e^{-\epsilon l c} \quad (2.8)$$

Where I_0 is the intensity of the incident light, I is the intensity after travelling through the absorbing medium, ϵ is the molar attenuation coefficient which is a property of the specific chemical species under study, ϵ is also dependent on electromagnetic frequency of the light source, temperature, and pressure. C is the concentration of the absorbing

species, and l is the path length of the light beam through the absorbing medium. absorption spectrometers measure incident (I_0) and attenuated (I) light intensity in order to derive concentration (C) of the absorber species using equation 2.8.

For GHGs, their intrinsic ability to absorb infrared radiation results in their greenhouse effect on the atmosphere. Using the Beer-Lambert law, the infrared-absorbing property of GHGs can be exploited in order to determine their atmospheric concentration. In the gas-phase, absorption of infrared radiation by a molecule results in a transition to higher vibrational and rotational excited states. Vibrational and rotational energy levels are quantised, and hence transitions occur between discrete energy levels with certain amounts of infrared energy, this results in distinct absorption lines in gaseous infrared absorption spectra, with the wavelength of each line corresponding to the energy of that specific ro-vibrational transition.

Spectral lines in real absorption spectra take the form of peaks due to the existence of several spectral line broadening processes. The random motion within a sample of gas results in some absorber molecules moving towards the incident infrared source, and some moving away. This introduces a degree of temperature-dependent Doppler shift in the infrared transition frequency, resulting in small energy variability within a spectral line in the form of a Gaussian distribution, this is known as Doppler broadening. Collisions between molecules within a gas sample also introduces a pressure-dependent form of spectral broadening known as collisional broadening, which follows a Lorentzian distribution. Finally, there is inherent uncertainty in the energy of transitions due to the Heisenberg uncertainty principle, also resulting in Lorentzian line broadening known as natural broadening. The combination of all three forms of spectral broadening in gaseous infrared spectra results in spectral lines with a combination of Gaussian and Lorentzian shapes, known as a Voigt distribution.

The type of laser used in infrared spectrometers is important when considering the species that is being measured, tunable continuous-wave diode lasers are ideal for probing the near-infrared region (800 – 2500 nm), and are therefore ideal for CH_4 and CO_2 infrared spectroscopy as these species have strong overtone and combination absorption features in the near-infrared. Diode lasers are cheap, robust and widely commercially available, making them ideal for use in commercial infrared spectrometers. As opposed to CH_4 and CO_2 , N_2O is problematic in that it does not absorb strongly in the near-

infrared, it only has strong fundamental bands in the mid-infrared, therefore diode lasers are typically unsuitable for measurements of N₂O. Quantum Cascade Lasers (QCL) are more commonly used instead of diode lasers for N₂O measurements. QCLs are typically more stable and higher resolution than diode lasers, but they are far more expensive as they are a relatively new technology, and they require cooling in order to function. Both QCLs and diode lasers are currently used in a range of commercially available infrared spectrometers, which are highly optimised for measurements of GHG abundances in the atmosphere.

2.3.2. Cavity enhanced absorption spectroscopy

A major challenge with using infrared spectroscopy to measure GHGs is the low atmospheric abundance of these gases. As per equation 2.8, absorbance (I_0/I) decreases exponentially with decreasing concentration, so infrared spectra of GHGs with ppm to ppb scale abundances result in absorbances with low signal to noise ratios that are below the limit of detection of short path length spectrometers. Increasing the path length of the infrared beam through a sample increases the signal to noise ratio of GHG absorption features by increasing the absorption of the infrared source, allowing accurate quantification of GHG mole fraction.

In practice, infrared GHG spectrometers increase path length by including multi-pass sample cells with high-reflectivity mirrors (>99.99%) at each end. An infrared laser beam is reflected thousands of times through the sample cell before entering the detector, giving an effective path length of several kilometers in a comparatively small sample cavity and hence increasing the spectroscopic sensitivity to low-abundance atmospheric trace gases.

Cavity enhanced spectrometers measure the output infrared transmission through the cell to the detector after multiple passes of the cell, and assumes a steady state between the incident light entering the cavity and the light absorbed by the sample or transmitted through the cell. Changes in intensity from this steady state are assumed to be entirely due to changes in absorber concentration in the cell (Paul et al., 2001) The change in infrared intensity as a result of a molecular absorber (ΔI) is related to incident infrared intensity (I_0) by the equation 2.9 (Gupta et al., 2002):

$$\Delta I/I_0 = \frac{GA}{1 + GA} \quad (2.9)$$

Where A is the absorption, which is related to the molar attenuation coefficient (ϵ), distance between mirrors (L), and concentration (C) by the equation 2.10:

$$A = 1 - e^{-\epsilon L C} \quad (2.10)$$

G is related to the reflectivity of the cavity mirrors (R) by equation 2.11:

$$G = \frac{R}{1 - R} \quad (2.11)$$

Mirror reflectivity is determined by abruptly switching the laser off, and measuring the time taken for the laser intensity to decay to $1/e$ of its original value, known as ring-down time (Baer et al., 2002).

In order to obtain an absorption spectrum, the laser current is ramped in order to sweep the laser frequency across a spectral region of interest. The acquired spectrum is then fitted against a known absorption spectra from a database such as the HIGH-resolution TRANsmission absorption database (HITRAN, Rothman, 2021) and corrected for temperature and pressure broadening effects. Despite absorption (A) being an absolute measurement, the molar absorption coefficient (ϵ) is highly dependent on temperature and pressure which adds significant uncertainty into absorption determination. It is for this reason that frequent calibration is required to account for the uncertainty introduced by varying temperature and pressure.

Cavity enhanced absorption spectroscopy has undergone improvement since its first iteration. Off-Axis Integrated Cavity Output Spectrometers (OA-ICOS) manufactured by Los Gatos Research (LGR, San Jose, CA, USA) orient the laser at a slight angle to the axis of the cavity, this maximises cell passes by the laser and reduces the sensitivity of the optical alignment to temperature and pressure, the off-axis alignment of the laser also minimises optical fringe effects caused by constructive/destructive interference of the laser beam with itself (Paul et al., 2001). LGR continuous-wave diode laser OA-ICOS spectrometers are used to measure CH_4 and CO_2 mole fractions in Chapters 3, 4 and 5, whereas an Aerodyne Research Inc. (ARI, Billerica, MA, USA) QCL cavity enhanced spectrometer is used for N_2O mole fraction measurements in Chapters 3, 4, and 5.

2.3.3. Cavity ring-down spectroscopy

Cavity ring-down spectroscopy (CRDS) is an alternate cavity enhanced spectroscopy technique that does not rely on direct absorption to derive the mole fraction of an absorbing gas. As previously stated, cavity enhanced absorption spectrometers determine mirror reflectivity by measuring the exponential decay of laser intensity after turning the laser off at the end of each frequency sweep, this e-folding ring-down time (τ) is related to trace gas concentration (C) using the following expression:

$$\tau = \frac{L}{c(1 - R + \epsilon L C)} \quad (2.12)$$

Where c is the speed of light, equation 2.12 relates the ring-down time to reflectivity (R) where some laser intensity is lost through the mirrors on each pass, and absorption by a trace gas in the cavity, which is related to concentration via the Beer-Lambert law (Keefe and Deacon, 1988).

A major advantage of CRDS instruments is that they are not sensitive to fluctuations in incident laser intensity which can lower the signal to noise ratio in absorption spectra, this effect can be present in cavity enhanced absorption techniques. However, CRDS can only typically operate over a smaller wavelength spectral range than with direct absorption techniques. Additionally, a much more precise optical alignment is required in cavity ring-down systems, making them more sensitive to changes in atmospheric pressure and motion than OA-ICOS systems (Maithani and Prathan, 2020).

2.3.4. Other techniques

The previous sections have focused on purely spectroscopic techniques for GHG measurement, yet alternative methods for GHG mole fraction measurement exist that rely upon non-spectroscopic analytical measurement techniques.

Gas Chromatography with Flame Ionisation Detection (GC-FID) has been historically used for high precision GHG measurements within ground-based networks, such as the WMO-GAW stations (Rasmussen and Khalil, 1981). GC is primarily used to separate an air sample into the individual constituent gases (i.e. CO_2 , CH_4 , and N_2O elute separately from each other). The FID module then ionises the individual gas analytes via combustion, where the concentration of ions produced is proportional to the

concentration of gas in the sample. The ions are then passed across an electrode, across which they induce a current which can be used to directly derive ion concentration and hence GHG concentration (Harley et al., 1958). GC-FID was among the dominant GHG measurement techniques used first in situ measurement stations as it was able to achieve higher measurement precisions than alternative techniques. In recent years, the advent of OA-ICOS and CRDS technologies have facilitated cheaper and more portable GHG measurements without sacrificing measurement precision. Currently operating WMO-GAW GHG measurement stations have adopted CRDS or OA-ICOS systems, replacing GC-FID (Zellweger et al., 2016).

Despite their reduced prevalence in GHG mole fraction measurements, GC-based techniques are important for measurements of $\delta^{13}\text{C}$ isotope ratios as spectroscopic methods often cannot effectively resolve individual spectral features from different isotopes with very low abundances (Eyer et al., 2016). Gas Chromatography-Isotope Ratio Mass Spectrometry (GC-IRMS) is commonly used for high-precision determination of $\delta^{13}\text{C}$ CO_2 and CH_4 measurements. The constituent gas separation by GC does not separate out the individual gas isotopologues, but the following mass spectrometry separates ionised gas molecules by their molecular weight, allowing determination of an isotope ratio (Muccio and Jackson, 2009; Fisher et al., 2005)

2.4. Thesis outline

The underlying aim of the work outlined in this thesis is to better understand GHG emissions from sources that have previously seen little in situ study (such as African biomass burning or recreational N_2O use), or from sources that are particularly sensitive to climate feedbacks (such as Arctic wetland emissions). In situ observations of GHGs from these sources detailed in this thesis are imperative for constraining global emission budgets for these gases, and reconciling the discrepancies between top-down and bottom-up emission estimates. This thesis is comprised of three main chapters, each of which describes the quantification or characterisation CH_4 and N_2O emissions using in situ airborne and ground-based measurements. The remainder of this thesis also demonstrates the utility of these measurements for investigating GHG emissions over a wide range of spatial scales, from regional-scale biomass burning and peatland emissions over

thousands of km², to urban recreational N₂O emissions from local sources on the order of <1 km².

For the measurements undertaken in this thesis, an Aerodyne QCL cavity-enhanced absorption spectrometer instrument modified for airborne use is used for N₂O mole fraction measurements. An LGR OA-ICOS system, also modified for airborne operation, is used for measurements of CH₄ mole fraction. Chapters 3 and 4 both involve airborne measurements of GHGs conducted from the FAAM research aircraft, allowing spatial flexibility in emission sampling methodology.

Chapter 3 describes in situ airborne sampling of biomass burning emission plumes in Senegal in 2017 and Uganda in 2019. Multiple fire plumes were sampled both close to source (near-field) and further from source where emission outflow was more well mixed (far-field). Fire plumes were sampled using the FAAM research aircraft, which allowed multiple passes through fire plumes very close to source fires. Plume mole fraction measurements were used to derive emission ratios and emission factors (Section 2.2.4) for CH₄, N₂O, CO₂ and CO using an individual plume integration method introduced in this paper. The linear response of CH₄ emission factors to the combustion efficiencies of individual fires was also investigated for the two sampling locations.

Chapter 4 also presents a FAAM aircraft in situ sampling case study, in this case CH₄ emissions are quantified from a large (~78,000 km²) area of European arctic peatland in northern Sweden, Finland, and Norway. CH₄ fluxes are calculated using the aircraft mass balance technique (Section 2.2.3) for three distinct areas within a box-shaped flight track, and CO₂ biospheric uptake is also quantified using mass balance. The CH₄ fluxes from each area are compared to Global Carbon Project (GCP) process model ensembles (Section 2.2.5) and chamber flux estimates (Section 2.2.1) for the same target region, and differences between top-down and bottom-up methods are discussed.

In contrast to Chapters 3 and 4, Chapter 5 focuses on ground-based measurements of N₂O mole fraction over the course of a year taken from an area of student accommodation in a busy urban environment in Fallowfield, Manchester. This paper discusses the potential presence of a recreational source of N₂O originating from surrounding accommodation, and describes the difference in the temporal and spatial distribution of N₂O emissions compared to traffic-dominated NO_x, CO, and CH₄ emissions. Calculation

of an N₂O flux is also attempted using a short-range atmospheric dispersion model, which is detailed in the Appendix section A.3.

Finally, Chapter 6 will summarise the main conclusions from each of the chapters, as well as placing the findings in context of constraining the global CH₄ and N₂O budgets on a wider scale. Chapter 6 will also discuss future work that could be undertaken in order to answer the outstanding questions posed by this thesis.

Chapter 3

Manuscript 1: Airborne measurements of fire emission factors for African biomass burning sampled during the MOYA campaign

Barker, P. A., Allen, G., Gallagher, M., Pitt, J. R., Fisher, R. E., Bannan, T., Nisbet, E. G., Bauguutte, S. J. B., Pasternak, D., Cliff, S., Schimpf, M. B., Mehra, A., Bower, K. N., Lee, J. D., Coe, H. and Percival, C. J.: Airborne measurements of fire emission factors for African biomass burning sampled during the MOYA campaign, *Atmos. Chem. Phys.*, 20(23), 15443–15459, doi:10.5194/acp-20-15443-2020, 2020.

The following chapter has been published in the journal *Atmospheric Chemistry and Physics*. P. A. Barker operated the N₂O instrumentation during MOYA II and processed the N₂O data for the MOYA II campaign. They also analysed the calibrated concentration data, including calculation of all emission ratios, emission factors, and combustion efficiencies. P. A. Barker also designed the manuscript concept with assistance from G. Allen and J. R. Pitt, and wrote the majority of the manuscript from initial draft stages throughout. Any other specific writing contributions not made by P. A. Barker will be detailed here. G. Allen contributed to the planning of individual MOYA I and II flights, obtained funding for the MOYA project as a whole, and provided writing contributions and corrections throughout drafting stages of the manuscript. G. Allen also provided general supervision to P. A. Barker. M. Gallagher provided feedback on draft iterations of the manuscript. J. R. Pitt operated the N₂O instrumentation during MOYA I and some of MOYA II, and processed the N₂O data for the MOYA I flights. They also provided assistance with emission ratio calculation, as well as providing feedback on manuscript drafts. R. E. Fisher wrote Subsection 2.5, detailing the isotopic analysis of whole air samples, R. E. Fisher also carried out the isotopic analysis and provided the $\delta^{13}\text{C}$ -CH₄ data. T. Bannan and A. Mehra collected, processed, and provided HCN and HNCO data

from the chemical ionisation mass spectrometer. T. Bannan also wrote Subsection 2.4, where the HCN and HNCO measurements are detailed. S. J. B. Bauguitte wrote Subsection 2.8 describing measurement uncertainties and systematic CO biases, and also collected, processed, and provided calibrated CH₄, CO₂, and CO data for MOYA I and II. D. Pasternak operated the CH₄, CO₂ and CO instrumentation during some of the MOYA II flights. D. Pasternak and S. Cliff processed raw CH₄, CO₂ and CO data and provided this to P. A. Barker. M. Schimpf operated the CH₄, CO₂, and CO instrumentation during the MOYA I flights. E. G. Nisbet obtained funding for the MOYA project, contributed to the flight methodology for MOYA I and II, and provided feedback on draft manuscript iterations. K. N. Bower contributed to the planning and design of MOYA II flights, and provided feedback on manuscript drafts. J. D. Lee contributed to planning and design of MOYA I and II flights, obtained funding for the MOYA project, and gave feedback on draft manuscript iterations. H. Coe and C. J. Percival provided assistance with HCN and HNCO data analysis and interpretation. All co-authors provided commentary on draft versions of the manuscript.



Airborne measurements of fire emission factors for African biomass burning sampled during the MOYA campaign

Patrick A. Barker¹, Grant Allen¹, Martin Gallagher¹, Joseph R. Pitt², Rebecca E. Fisher³, Thomas Bannan¹, Euan G. Nisbet³, Stéphane J.-B. Bauguitte⁴, Dominika Pasternak⁵, Samuel Cliff⁵, Marina B. Schimpf⁶, Archit Mehra¹, Keith N. Bower¹, James D. Lee⁵, Hugh Coe¹, and Carl J. Percival⁷

¹School of Earth and Environmental Sciences, University of Manchester, Manchester, M13 9PL, UK

²School of Marine and Atmospheric Sciences, 145 Endeavour Hall, Stony Brook University, Stony Brook, NY 11794-5000, USA

³Department of Earth Sciences, Royal Holloway, University of London, Egham, Surrey, TW20 0EX, UK

⁴FAAM Airborne Laboratory, National Centre for Atmospheric Sciences, Building 146, College Road, Cranfield, MK43 0AL, UK

⁵Wolfson Atmospheric Chemistry Laboratories, Department of Chemistry, University of York, Heslington, York YO10 5DD, UK

⁶German Aerospace Center (DLR), Flight Experiments, Instrumentation and Data Science, Muenchener Strasse 20, 82234 Weßling, Germany

⁷Jet Propulsion Laboratory, California Institute of Technology, 4800 Oak Grove Drive, M/S 183-901, Pasadena, California 91109, USA

Correspondence: Patrick A. Barker (patrick.barker@manchester.ac.uk)

Received: 8 June 2020 – Discussion started: 10 July 2020

Revised: 9 October 2020 – Accepted: 2 November 2020 – Published: 11 December 2020

Abstract. Airborne sampling of methane (CH₄), carbon dioxide (CO₂), carbon monoxide (CO), and nitrous oxide (N₂O) mole fractions was conducted during field campaigns targeting fires over Senegal in February and March 2017 and Uganda in January 2019. The majority of fire plumes sampled were close to or directly over burning vegetation, with the exception of two longer-range flights over the West African Atlantic seaboard (100–300 km from source), where the continental outflow of biomass burning emissions from a wider area of West Africa was sampled. Fire emission factors (EFs) and modified combustion efficiencies (MCEs) were estimated from the enhancements in measured mole fractions. For the Senegalese fires, mean EFs and corresponding uncertainties in units of gram per kilogram of dry fuel were 1.8 ± 0.19 for CH₄, 1633 ± 171.4 for CO₂, and 67 ± 7.4 for CO, with a mean MCE of 0.94 ± 0.005 . For the Ugandan fires, mean EFs were 3.1 ± 0.35 for CH₄, 1610 ± 169.7 for CO₂, and 78 ± 8.9 for CO, with a mean modified combustion efficiency of 0.93 ± 0.004 . A mean N₂O EF of 0.08 ± 0.002 g kg⁻¹ is also reported for one flight over Uganda; issues with temper-

ature control of the instrument optical bench prevented N₂O EFs from being obtained for other flights over Uganda. This study has provided new datasets of African biomass burning EFs and MCEs for two distinct study regions, in which both have been studied little by aircraft measurement previously. These results highlight the important intracontinental variability of biomass burning trace gas emissions and can be used to better constrain future biomass burning emission budgets. More generally, these results highlight the importance of regional and fuel-type variability when attempting to spatially scale biomass burning emissions. Further work to constrain EFs at more local scales and for more specific (and quantifiable) fuel types will serve to improve global estimates of biomass burning emissions of climate-relevant gases.

1 Introduction

The atmospheric burdens of the greenhouse gases (GHGs) CO₂, CH₄, and N₂O have been increasing since the onset of the Industrial Revolution. It is widely accepted that this increase is driven by anthropogenic emissions arising from rapid industrialization and socio-economic development (Montzka et al., 2011; Ciais et al., 2013). However, there is significant uncertainty about the budgets of these greenhouse gases, as their sources and sinks, both natural and anthropogenic, remain poorly constrained. In particular, the continued growth in atmospheric methane since a period of stagnation from 1999–2006, alongside the concurrent shift in ¹³CH₄/¹²CH₄ isotopic ratio, has yet to be accounted for (Nisbet et al., 2016, 2019; Turner et al., 2019; Schaefer, 2019). In order to accurately attribute the causes of the growth in greenhouse gas burdens, whether from increased sources or reduced sinks, all emission sources need to be quantified with accuracy and precision, and with fine detail in temporal and spatial variability.

Biomass burning is a major source, known to contribute significantly to the global budgets of many atmospheric trace gases and aerosols. In addition to CO₂, incomplete combustion of biomass fuel produces both methane and CO, as well as N₂O. It has been estimated that 1.6–4.1 Pg of CO₂, 11–53 Tg CH₄, and 0.1–0.3 Tg of N₂O are emitted to the atmosphere annually as a result of biomass burning on a global scale (Crutzen and Andreae, 2016). The contribution of biomass burning to global GHG budgets will likely increase over time due to climate warming and more widespread drought-stress conditions which increase the likelihood and spread of wildfire events (Liu et al., 2014).

It is estimated that Africa accounts for approximately 52 % of all biomass burning carbon emissions, with the northern sub-Saharan African region alone accounting for 20 %–25 % of global biomass burning carbon emissions (van der Werf et al., 2010; Ichoku et al., 2016). Many or most of these fires are anthropogenic in origin and are started deliberately for reasons such as clearing land for agricultural use, crop waste burning, management of natural savannah vegetation, or pest control (Andreae, 1991). Other fires may simply be accidental (e.g. cigarette disposal). Anthropogenic fires are typically lit in the winter dry season. Natural fires, lit by lightning, can occur in the first early summer wet season thunderstorms over dry growth from the previous year. Despite the importance of the African contribution to global biomass burning emissions, there are limited in situ studies of African wildfire emissions.

The UK Natural Environment Research Council (NERC) Methane Observations and Yearly Assessments (MOYA) project is focused primarily on closing the global methane budget through new in situ observations and analysis of existing datasets. This is being achieved (in part) through targeted field campaigns to constrain poorly quantified methane sources on local and regional scales, as well as the use

of atmospheric chemical transport models, such as GEOS-CHEM, to provide global estimates of methane emission trends (Bey et al., 2001; Holmes et al., 2013; Saunio et al., 2016).

This paper presents the results of airborne surveys conducted over regions of Senegal and Uganda with high prevalence of biomass burning events. Two aircraft-based field campaigns, using the UK Facility for Airborne Atmospheric Measurements Atmospheric Research Aircraft (FAAM ARA), were conducted in widely separated parts of northern sub-Saharan Africa as part of the MOYA project. The first was based in Senegal between 27 February 2017 and 3 March 2017, and the second was based in Uganda between 16 and 30 January 2019 (henceforth referred to as MOYA-I and MOYA-II for the 2017 and 2019 campaigns respectively).

The primary focus of the Senegal campaign was to study fires in the winter dry season. The focus in the Ugandan campaign, which was carried out in the brief January dry season, was on equatorial wetlands, with the aim of quantifying methane emissions from these sources using regional-scale flux techniques (O'Shea et al., 2014; Heimbürger et al., 2017), but the study of fires of opportunity in the savannah of northern Uganda was also a major target. The aircraft campaigns also aimed to provide emission estimates for methane and other trace gas and aerosol species from other sources, including anthropogenic emissions from Kampala.

In particular, emission factors (EFs) for CH₄, CO₂, N₂O, and CO can be determined from the enhancement in trace gas mixing ratio observed when a biomass burning plume was intercepted. These EFs were calculated for multiple fires observed in Senegal and Uganda. A comparison is made between these Senegalese and Ugandan EFs, to assess and interpret intracontinental variability. Comparisons are also made between EFs determined in this study and EFs from Andreae (2019), who includes up to 50 studies reporting fire EFs and modified combustion efficiencies from multiple biomass burning types, such as tropical forest burning, savannah and grassland burning, and agricultural residue burning.

2 Description of flights and experimental methods

2.1 MOYA-I: Senegal 2017

During the first MOYA flying campaign (MOYA-I), four research flights (flight numbers C004, C005, C006, and C007) were conducted using the UK Facility for Airborne Atmospheric Measurement (FAAM) BAe 146-301 Atmospheric Research Aircraft (ARA) to specifically sample fire plumes from biomass burning. The ARA was based in Dakar for the duration of this flying campaign. Near-field biomass burning plumes were sampled in C004 and C005 above the Casamance region of wooded savannah in the south-west of Senegal, and longer-range biomass burning outflow for a

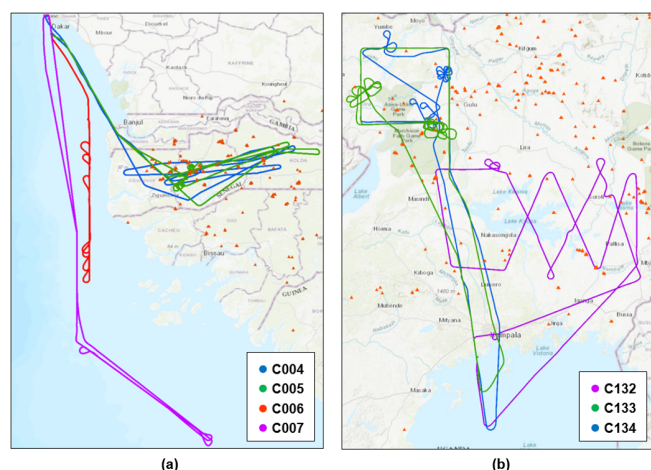


Figure 1. FAAM ARA flight tracks of (a) MOYA-I biomass burning sampling flights C004 (blue), C005 (green), C006 (red), and C007 (purple) over the south-western region of Senegal and the Atlantic seaboard and (b) MOYA-II biomass burning sampling flights C132 (purple), C133 (green), and C134 (blue) over northern Uganda. MODIS infrared satellite retrievals of fires present between (a) 28 February and 2 March 2017 and (b) 28 and 29 January 2019 are also shown (orange triangles). © OpenStreetMap contributors and the GIS user community 2020. Distributed under a Creative Commons BY-SA License.

wider West African region was sampled in C006 and C007 over the Atlantic seaboard.

Figure 1 shows the NASA MODerate Resolution Imaging Spectrometer (MODIS) satellite retrievals of locations that were actively burning during the MOYA-I fire sampling flights, which both took place between 28 February 2017 and 2 March 2017. Several straight and level (constant altitude and heading) runs were made in the central Casamance region of south-west Senegal, to sample near-field biomass burning emissions from directly above the source fires. Straight and level runs were also carried out during flights C006 and C007 but aimed to sample longer-range regional outflow of biomass burning emissions from the wider inland area of interest.

Visual observation during low passes (< 200 m) in the flight showed that the fires were in wooded savannah terrain, in dry winter and brown winter forest tracts. The forests have been described by de Wolf (1998) and by Fredericksen and Lawesson (1992).

The likely fuels were C₃ forest leaf litter and dropped branches as well as savannah grass. The Casamance forests in the overflow area were typically low trees with a generally open canopy. A photograph of one of the near-field fires sampled during flight C005 is shown in Fig. 2

2.2 MOYA-II: Uganda 2019

The flying campaign in Uganda (MOYA-II) took place in late January 2019, a relatively dry month, when northern Uganda



Figure 2. Photograph of Senegalese wildfire taken from aboard the FAAM ARA during flight C005 of the MOYA-I campaign.

experiences its winter dry season, and equatorial southern Uganda is in a short January dry period. The aircraft was based at Entebbe, located on the Equator. Two dedicated biomass burning sampling research flights were conducted (flight numbers C133 conducted on 28 January 2019 and C134 conducted on 29 January 2019), which targeted burning occurring in the north-west of Uganda. Figure 1 shows the flight tracks and MODIS-retrieved fire locations for the MOYA-II flights. The fires were concentrated towards the north of Uganda in this period.

Figure 1 shows both dedicated biomass burning sampling flights (C133 and C134), which focussed on the north-western corner of Uganda. This region is far enough north (around 3° N) to experience dry season Northern Hemisphere winter. A box pattern was flown around the region, including several passes downwind of fires in the area seen with the clover-like flight patterns.

In addition to these dedicated fire flights, flight C132 (conducted on 28 January 2019) is also included in emission analyses. This flight was over Lake Kyoga, closer to the Equator at about 1.5° N. The primary purpose of flight C132 was to survey biogenic methane emissions from Lake Kyoga and the surrounding wetlands. Flight C132 involved straight and level runs across Lake Kyoga. No fires were specifically targeted during this flight but plumes were intercepted from fires over the northern area of Lake Kyoga, as seen by the deviations in the C132 flight path shown in Fig. 1. EFs from these fires are included in this study.

From visual observation, flights C133 and C134 likely included fires mainly burning C₄ tropical grasses, and on flight C132 the fuel was likely agricultural crop waste, which presumably included C₄ maize waste, a major local crop.

2.3 CH₄, CO₂, CO, and N₂O instrumentation

During the MOYA-I and MOYA-II campaigns, the FAAM ARA was equipped with a suite of instrumentation for high-

accuracy and high-precision trace gas measurement. All airborne trace gas measurements are time synchronized to an on-board time server. For CH_4 and CO_2 mole fractions, a Los Gatos Research fast greenhouse gas analyser (FGGA) was used. This instrument uses a cavity-enhanced absorption spectroscopy technique and two continuous-wave near-IR diode lasers. A more detailed description of this instrument, along with its modification for airborne measurements, is provided by O'Shea et al. (2013b). The FGGA was calibrated using three calibration gas standards, all of which were traceable to the NOAA/ESRL WMO-X2007 scale for CO_2 and the WMO-X2004A scale for CH_4 . Two of these gas standards provide high- and low-concentration span calibrations that are linearly interpolated over an entire flight in order to account for instrument drift. The remaining gas standard was used as a target to define instrumental measurement uncertainty across multiple flights. During MOYA-I the FGGA had a data acquisition rate of 1 Hz, whereas in MOYA-II we used an upgraded system with a 10 Hz acquisition rate. Accounting for all sources of uncertainty associated with these instruments, the mean biases and associated 1σ overall uncertainties are estimated to be 0.004 ± 0.431 ppm and 0.04 ± 2.27 ppb for 1 Hz CO_2 and CH_4 measurements respectively during MOYA-I and -0.048 ± 0.626 ppm and -1.22 ± 2.93 ppb respectively for 10 Hz CO_2 and CH_4 measurements during MOYA-II, which have been averaged to 1 Hz prior to analysis.

N_2O dry-air mole fractions were measured using an Aerodyne quantum cascade laser absorption spectrum (QCLAS) as described by Pitt et al. (2016). This instrument uses a single thermoelectrically cooled quantum cascade laser tuned to a wavelength of ~ 4.5 μm . The QCLAS is calibrated using three calibration gas standards, all of which are traceable to the World Meteorological Organization (WMO) X2006 calibration scale for N_2O . A 1σ uncertainty of 0.58 ppb was estimated for 1 Hz N_2O mole fraction measurements during the MOYA-II flights. We only report data for the MOYA-II (Uganda) campaign in this study as this instrument was not fitted to the aircraft during the MOYA-I (Senegal) campaign.

The Aerodyne QCLAS N_2O measurements can be impacted by changes in both cabin pressure and aircraft motion. Changes in altitude and hence cabin pressure change the refractive index in the open path section of the laser beam. This leads to normally static optical fringes moving across the spectral baseline of the instrument, introducing both long-term drift and short-term artefacts into the N_2O mole fraction data. Sharp changes in aircraft roll angle in tight turns also introduce short-term artefacts as forces acting on optical components cause slight changes in alignment. These issues are described in further detail in Pitt et al. (2016). A further issue encountered solely during the MOYA-II campaign was occasional loss of optical bench temperature control due to the high temperatures experienced within the aircraft during some flights.

Despite these issues, the N_2O plumes from which EF could be calculated were sampled at constant altitude with wings level and at constant optical bench temperature. So the instrument issues detailed likely have a minimal influence on data quality during these periods.

Measurements of CO dry-air mole fractions were sampled using an Aero-Laser AL5002 vacuum-UV fast fluorescence instrument. Specifics about the principles of operation for this instrument are provided by Gerbig et al. (1999). The instrument was calibrated in-flight using a gas standard traceable to the NOAA/ESRL WMO-X2014A scale for CO. We have demonstrated that the linear interpolation of in-flight calibrations yields a mean bias < 1 ppb with a 2σ precision of 1.8 ppb at 150 ppb for 1 Hz CO measurements, when the instrument is operated optimally. However we recently discovered that a faulty inlet drier may have impacted the accuracy of our CO measurements in 2017–2019 and yielded a $+9 \pm 9$ ppb bias in our data. The potential impact of this positive bias is further discussed.

Both the Aero-Laser CO instrument and the FGGA were mounted within the pressurized cabin of the aircraft within a single 48.26 cm rack. Air was sampled by means of a window-mounted rearward facing inlet comprised of 3/8 in. PFA tubing housed within 1/2 in. stainless-steel tubing for the CO inlet and 3/8 in. stainless steel tubing for the FGGA inlet (O'Shea et al., 2013b; Gerbig et al., 1999).

2.4 HCN and HNCO instrumentation (chemical ionization mass spectrometer)

The University of Manchester time-of-flight chemical ionization mass spectrometer (ToF-CIMS) that has been described in detail by Priestley et al. (2018a, b) for ground-based deployment has recently been modified and certified for use on the FAAM ARA and was used for real-time detection of hydrogen cyanide (HCN) and isocyanic acid (HNCO) in this study. The instrument and its subsequent modification are described in detail here, as this study presents the first measurements from the modified ToF-CIMS aboard the FAAM ARA. The original instrument was manufactured by Aerodyne Research Inc. and employs the ARI/Tofwerk high-resolution time-of-flight mass spectrometer. Briefly, iodide ions cluster with sample gases, creating a stable adduct that is analysed using time-of-flight mass spectrometry, with an average mass resolution of 4000 ($m \Delta m^{-1}$).

The inlet design was based on the configuration characterized by Le Breton et al. (2014), an atmospheric pressure, rearward-facing, short-residence-time inlet, consisting of a 3/8 in. diameter polytetrafluoroethylene (PTFE) tubing with a total length to the instrument of 48 cm and based on the design shown in Lee et al. (2018). A constant flow of 12 SLM (standard litres per minute) is mass flow controlled to the ion–molecule reaction region (IMR) using a rotary vane pump (Picolino VTE-3). A total of 1 SLM is then subsampled into the IMR for measurement. An Iris system as de-

scribed by Lee et al. (2018) was then employed to pressure- and mass-flow-control the sample flow into the instrument, avoiding sensitivity changes that would be associated with large variations in pressures in flight that are not controlled sufficiently by the constant flow inlet. This works upon the principle of the manipulation of the size of the critical orifice in response to changes in the IMR pressure. As with the Lee et al. (2018) design, this works by having a stainless-steel plate with a critical orifice and a movable PTFE plate on top of this, also with a critical orifice. These orifices either align fully and allow maximum flow into the instrument or misalign to reduce flow. This movement is controlled by the 24VDC output of the IMR Pirani pressure gauge in relation to the set point, and the control unit was designed collaboratively with Aerodyne Research Inc. The IMR set point was 80 mbar for the MOYA campaign, which is set through a combination of pumping capacity on the region (Agilent IDP3), mass-flow-controlled reagent ion flow, and sample flow. The reagent ion flow is 1 SLM of ultra-high-purity (UHP) nitrogen mixed with 2 SCCM (standard cubic centimetres per minute) of a pressured known concentration gas mix of CH_3I in nitrogen, passed through the radioactive source, ^{210}Po . The total flow through the IMR is measured (MKS MFM) at the exhaust of the Agilent IDP3 pump so that not only the IMR pressure is monitored but the sample flow also. All mass flow controllers and mass flow meters are measured and controlled using EyeOn. The 1σ variability in the IMR pressure during MOYA is 4 % and 6 % in the sample flow.

A standard Aerodyne pressure controller is also employed on the short segmented quadrupole (SSQ) region, with two purposes, easily setting the required pressure during start-up but also making subtle adjustments in this region should the IMR pressure change significantly. This works upon the principle controlling an electrically actuated solenoid valve in a feedback loop with the SSQ pressure gauge to actively control a leak of air into the SSQ pumping line. The SSQ is pumped using an Ebara PDV 250 pump and held at 1.8 mbar. The 1σ variability in the SSQ pressure during MOYA is < 1 %.

Instrument backgrounds are programmatically run for 6 s every minute for the entire flight, by overflowing the inlet at the point of entry into the IMR with UHP nitrogen. Here a 1/16 in. PTFE line enters through the movable PTFE top plate, ensuring that the flow exceeds that of the sample flow. Inlet backgrounds are often run multiple times during flights manually by overflowing as close to the end of the inlet as possible with 20 SLM. Data are taken at 4 Hz during a flight, which is routinely averaged to 1 Hz for analysis. Of the six points in each background, the first two and last point are unused and the mean of the background is calculated using custom Python scripting. Using linear interpolation, a time series of the instrument background is determined and humidity is corrected if required and then subtracted to give the final time series of each measured mass. Instrument sensitiv-

ity to increased humidity changes influences the sensitivity of the instrument to HCN, and corrections are applied here to correct both the instrumental backgrounds and final time series of HCN reported here. Only qualitative HCN and HNCO data are reported here as quantitative data are not required for the approach of plume identification used in this study.

The CIMS instrument analysis software (ARI Tofware version 3.1.0) was utilized to attain high-resolution 1 Hz time series of the compounds presented here. For the University of Manchester CIMS, mass-to-charge calibration was performed for five known masses, I^- , $\text{I}^-\cdot\text{H}_2\text{O}$, $\text{I}^-\cdot\text{HCOOH}$, I_2^- , and I_3^- , covering a mass range of 127 to 381 m/z . The mass-to-charge calibration was fitted to a third-order polynomial and was accurate to within 2 ppm. HCN and HNCO in this case were identified with a 1 ppm error.

2.5 Whole-air sampling and methane isotopic analysis

Whole-air samples (WASs) were collected on board the aircraft in 3L silica passivated stainless-steel canisters (Thames Restek, UK). Sample collection was triggered manually to sample within and outside of fire plumes, guided by the real-time methane measurements from the FGGA on board and visual identification of when the plumes were being crossed. Fill times when sampling the fire plumes ranged between 10 and 40 s depending on sampling altitude, representative of an integrated air sample over a 1–4 km track. WAS start and end times are recorded using the time on the FAAM ARA on-board time server. Methane mole fraction in the WAS flasks was measured in the Royal Holloway greenhouse gas laboratory using a Picarro 1301 cavity ring-down spectroscopy analyser, and methane isotopic analysis ($\delta^{13}\text{C}$) was carried out by gas chromatography – isotope ratio mass spectrometry using a trace gas preconcentrator and isoprime mass spectrometer (see Fisher et al., 2006, for details of the technique).

2.6 Calculation of emission ratios and emission factors

In order to select when sampled air was influenced by biomass burning emissions, HCN and CO were used as biomass burning tracers. HCN was chosen as it is almost exclusively emitted from biomass burning, representing 70 %–85 % of the total global HCN source (Li et al., 2003), and it has a sufficiently long atmospheric lifetime (relative to advection timescales prior to sampling) of 2–4 months, making HCN a suitable inert tracer for characterizing biomass burning plumes (Li et al., 2000).

Like HCN, significant amounts of CO, which has an atmospheric lifetime of 1–3 months (Ehhalt and Prather, 2001), are emitted from biomass burning. CO is also emitted by vehicles, primarily petrol-fuelled and less so by diesel. However, it is likely that biomass burning is the dominant source of carbonaceous emissions in rural areas of Africa as studied here, whereas vehicular carbon emissions are likely concentrated towards urban centres (Gatari and Boman, 2003).

HCN was used as a biomass burning tracer for the MOYA-II (Uganda) analysis. However, as the ToF-CIMS was not fitted to the aircraft during the MOYA-I campaign, no HCN measurement is available for this dataset, and hence CO is used as the biomass burning tracer for MOYA-I analysis.

In order to quantify biomass burning emissions from the enhancements in trace gas mole fraction seen in fire plumes, emission ratios (ERs) and EFs were calculated for each species in each fire plume. In this case, an ER is defined as the ratio of a species X relative to a reference species Y . The reference species chosen for this work was CO, as it is relatively inert in the timescale of these measurements, had a relatively stable regional background concentration during these campaigns, and in these rural field areas is almost exclusively emitted during combustion processes and not by other sources such as vehicles (Andreae and Merlet, 2001). The expression for ER calculation is shown in Eq. (1).

$$\text{ER}_{\frac{X}{\text{CO}}} = \frac{\Delta X}{\Delta \text{CO}} = \frac{X_{\text{plume}} - X_{\text{background}}}{\text{CO}_{\text{plume}} - \text{CO}_{\text{background}}} \quad (1)$$

ERs calculated using this approach are also referred to as normalized excess mixing ratios (NEMRs). When fresh plumes are sampled close to source as they are in the near-field sampling flights, NEMRs can be treated as ERs, calculated using Eq. (1). However in aged plumes, this approach cannot be used to calculate ER, and NEMR is no longer equal to ER. This is due both to chemical processes within the plume that can change composition and to mixing of background air into plume air (Andreae and Merlet, 2001; O'Shea et al., 2013a; Yokelson et al., 2013). HYSPLIT back-trajectory analysis of the MOYA-I far-field flights show that the plume age is < 12 h for flight C006; hence chemical ageing of biomass burning emissions is unlikely to significantly impact the ER calculation for this flight. Plume ages during flight C007 are more variable and can exceed 2 d in some cases, so significant ageing may have occurred. This is discussed in further detail in Sect. 3.2. All near-field flights sample biomass burning emissions at the source, so no significant plume ageing is assumed. Equation (1) can therefore be used to calculate ERs confidently for most flights.

In order to calculate ERs for near-field biomass burning plumes, a baseline mixing ratio ($X_{\text{background}}$) was calculated as the average mixing ratio over 10 s of sampled data to either side of each detected plume. The same baseline data periods chosen for each plume were used for all gas species, to ensure that ERs were comparable and not influenced by inconsistent baseline criteria. Plumes were selected using a statistical method, but the start and the end of each plume as well as the background regions were chosen manually. The area under the plume was then determined by integrating the peak in the concentration vs. time data series, giving a total plume concentration (X_{plume}). These values were then used in Eq. (1), along with the corresponding values for CO, to determine an ER. Due to the absence of individual sharp enhancements resolved for specific fire plumes in the far-field

flights, a least-squares linear regression of all in-plume points of X vs. in-plume points of CO is used to determine ERs for the far-field flights. The ER is equal to the slope of this linear regression.

Using the calculated ER for each species, EFs were calculated using the carbon mass balance technique (Ward and Hardy, 1984; Radke et al., 1991). An EF is defined as the mass of species emitted (in grams) per kilogram of dry matter burnt. The expression for calculating emission factor is given in Eq. (2).

$$\text{EF}_X = F_C \cdot 1000 \left(\text{g kg}^{-1} \right) \cdot \frac{M_X}{M_C} \frac{C_X}{C_{\text{total}}}, \quad (2)$$

where F_C is the mass fraction of carbon in the dry fuel. A value of 0.475 was assumed in this work to best represent African biomass carbon content, and a $\pm 10\%$ uncertainty in this value is assumed (Cofer et al., 1996; Ward et al., 1996; Yokelson et al., 2009). M_X is the molecular weight of species X and M_C is the atomic mass of carbon-12. The term $\frac{C_X}{C_{\text{total}}}$ is the molar ratio of species X to total carbon in the plume, which is calculated using Eq. (3).

$$\frac{C_X}{C_{\text{total}}} = \frac{\text{ER}_{\frac{X}{\text{CO}}}}{1 + \frac{\Delta \text{CO}_2}{\Delta \text{CO}} + \frac{\Delta \text{CH}_4}{\Delta \text{CO}}} \quad (3)$$

In Eq. (3), total carbon in the fire plume was assumed to be the sum of CO, CO₂, and CH₄ emitted. However, as all carbon-containing species could not be measured in this study, the total carbon present in the plume may be underestimated by 1 %–2 % (as reported by Yokelson et al., 1999).

A statistical threshold approach was used to determine when a biomass burning plume was sampled during flights. For flights where HCN measurements are available, HCN enhancements exceeding 7 standard deviations above the local background were used to select data for ER and EF calculation. Where HCN was not available during MOYA-I, a CO threshold of 7 standard deviations over the local background concentration was used. For the far-field flights during MOYA-I (C006 and C007) CO mixing ratios exceeding 15 standard deviations above the local background were chosen for analysis.

2.7 Modified combustion efficiency

In addition to EF, the modified combustion efficiency (MCE) is another useful parameter that can be calculated for each biomass burning plume. MCE is here defined by Eq. (4).

$$\text{MCE} = \frac{\Delta \text{CO}_2}{\Delta \text{CO}_2 + \Delta \text{CO}} \quad (4)$$

MCE can be used to determine the degree to which a fire is smouldering or flaming (Ward and Radke, 1993). Higher MCE values (towards 0.99) indicate that burning is purely flaming, whereas lower MCE values in the range 0.65–0.85

indicate that smouldering conditions dominate. The proportion of trace gases (such as CO and CH₄) emitted typically depends on the completeness of combustion, which is to say that more oxidized products are expected from fires with a high degree of flaming. It is therefore useful to investigate the trend between EF and MCE for different fire plumes (Urbanski, 2013). In the following section, we calculate EFs and MCEs for sampled fire plumes in the MOYA-I and MOYA-II campaigns.

2.8 Uncertainties

The standard error of the mean (SE) and the mean measurement uncertainty (MU) are reported for each mean EF and MCE displayed in Table 1. The SE here is determined from all EFs and MCEs calculated for a single flight and represents the variability of EF and MCE within a flight. The MU is propagated from the instrument uncertainties; therefore each EF and MCE from each fire plume sampled has a measurement uncertainty associated with it. The MUs reported in Table 1 are the average of all individual MUs for all fire plumes sampled during a given flight.

ER_x is calculated using Eq. (1) by subtracting CO_{background} from CO_{plume}; any CO measurement systematic positive offset would therefore cancel out and not affect the uncertainty of ER_x. The detection of CO_{plume} during MOYA-I is based on the exceedance of either 7 or 15 standard deviations above background. A CO measurement offset on the background may therefore affect this data filtering step; however due to the wide dynamic range of CO measurements encountered during the plume sampling, we believe a bias will have a very minimal effect on the filtered plume dataset used in our analysis. Similarly, the calculations of EF_x using Eqs. (2) and (3), and MCE using Eq. (4), rely on ΔCO, which is unaffected by CO measurement bias as previously stated.

3 Results and discussion

In this section, mean EFs and MCEs are reported on a per-flight basis, and the differences in relative EFs and MCE between individual flights and between Senegal and Uganda are discussed.

3.1 Near-field sampling

3.1.1 MOYA-I

Flights C004 and C005. The near-field Senegalese fire sampling flights (flight C004 and C005) were carried out on 28 February and 1 March 2017 respectively. The operating area was over the south-western Casamance region of Senegal. A time series of trace gas mixing ratios (CO, CH₄, and CO₂) during flight C004 is shown in Fig. 3. An equivalent time series for flight C005 is displayed in the Supplement in Fig. S1.

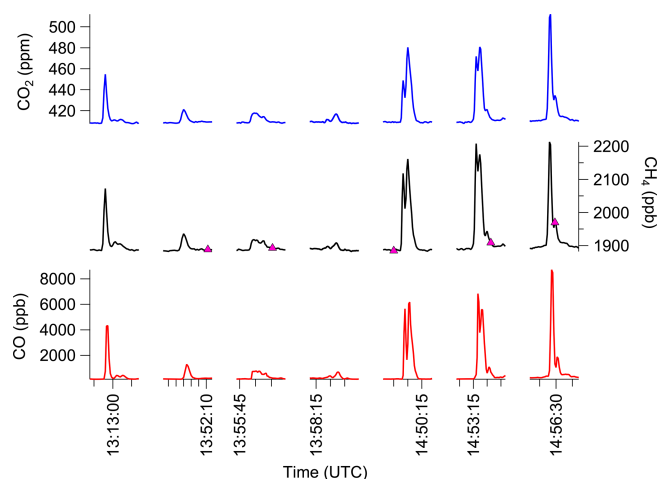


Figure 3. Time series of CO (red), CH₄ (black), CO₂ (blue), and concentrations in the plumes analysed for flight C005. Median WAS canister fill times are marked on the CH₄ time series as pink triangles. Note that some WASs taken in background regions are not shown here.

The $\delta^{13}\text{C}$ -CH₄ isotopic ratio of biomass burning emissions can provide information on the content of the biomass fuel that is burned. In C₄ vegetation (e.g. tropical grassland), ¹³CO₂ is concentrated during the photosynthetic pathway; hence C₄ plants tend to be enriched in ¹³C and emissions show a higher $\delta^{13}\text{C}$ -CH₄ isotopic ratio. C₃ vegetation (woody forest) does not involve the same ¹³C fractionation as C₄; therefore emissions show a lower $\delta^{13}\text{C}$ -CH₄ ratio relative to C₃ plants (Brownlow et al., 2017). Chanton et al. (2000) analysed biomass burning emissions via Keeling plot analysis ($\delta^{13}\text{C}$ -CH₄ vs. inverse CH₄ mole fraction) from a range of fuel sources. They found that African grass burning emitted methane with $\delta^{13}\text{C}$ -CH₄ ranging between −17‰ and −26‰, whereas African woodland burning produced methane with a $\delta^{13}\text{C}$ -CH₄ ratio of approximately −30‰. For both near-field and far-field MOYA-I flights, whole-air samples were taken of the biomass burning plumes sampled, as well as of the local background. $\delta^{13}\text{C}$ -CH₄ isotopic ratios and mean CH₄ mole fractions are determined from these whole-air samples. Further details of this analysis are provided in Sect. 2.5. Keeling plots for all MOYA-I flights analysed in this work are shown in Fig. 4. Flight C005 shows a linear relationship between inverse CH₄ mole fraction (enhanced CH₄) and $\delta^{13}\text{C}$ -CH₄ signature. This suggests that biomass burning emissions were captured by whole-air sampling during flight C005. One sample taken during flight C004 appears to have an enriched $\delta^{13}\text{C}$ -CH₄ signal; however this is not included in the linear fit as the single point does not conclusively mean a linear relationship is present. The *Y* intercept of -33.7 ± 1.1 ‰ agrees well with the Chanton et al. (2000) estimate for African forest burning, and suggests that C₃ vegetation (forest) is included in the fuel burned during flight C005 (Dlugokencky et al., 2011, Chan-

Table 1. Mean CH₄, CO₂, N₂O, and CO EFs and MCE for all MOYA-I (Senegal) and MOYA-II (Uganda) fire sampling flights. Both the standard error on the mean and the mean measurement uncertainty (MU) for EFs and MCEs during each flight for each species are also given. EFs and MCEs compiled from studies of tropical forest and savannah biomass burning by Andreae (2019) are also shown. All EFs are reported in units of grams per kilogram.

	Flight no.	N	CH ₄			CO ₂			CO			N ₂ O			MCE		
			Mean	SE	MU	Mean	SE	MU	Mean	SE	MU	mean	SE	MU	Mean	SE	MU
MOYA-I	C004	7	2.3	0.13	0.24	1612	3.4	170	84	2.3	8.7	–	–	–	0.93	0.0047	0.0031
	C005	12	1.4	0.11	0.15	1647	4.3	174	61	2.9	6.2	–	–	–	0.95	0.0024	0.0030
	C006		1.6	–	0.18	1625	–	170	–	–	–	–	–	–	0.94	–	0.0041
	C007		2.4	–	0.25	1663	–	173	–	–	–	–	–	–	0.96	–	0.0037
MOYA-II	C132	2	5.2	0.15	0.55	1554	4.0	164	109	2.3	11.3	–	–	–	0.90	0.0021	0.0042
	C133	11	2.8	0.21	0.30	1620	7.0	171	72	2.6	7.4	–	–	–	0.94	0.0038	0.0041
	C134	9	3.1	0.70	0.22	1609	23.9	174	79	14.0	8.1	0.08^a	0.01	0.01	0.93	0.0128	0.0042
Andreae (2019)	Tropical forest		6.5	–	1.6	1620	–	70	104	–	39	–	–	–	0.91	–	0.03
	Savannah and grassland		2.7	–	2.2	1660	–	90	69	–	20	0.17	–	0.09	0.94	–	0.02

^a Note that N₂O EFs could only be calculated for six of the nine fire plumes sampled during flight C134.

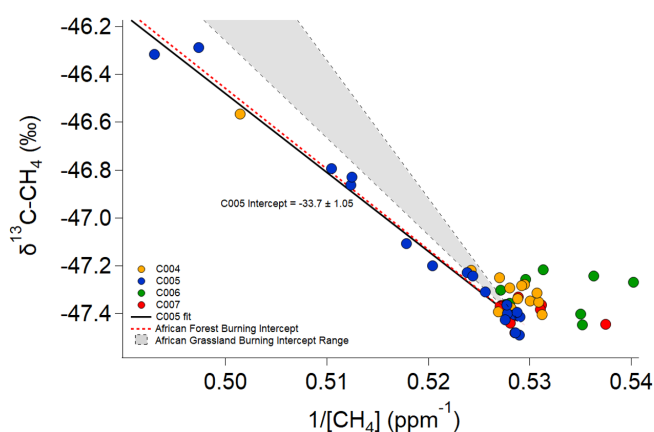


Figure 4. Keeling plot ($\delta^{13}\text{C}-\text{CH}_4$ vs. inverse CH₄ mixing ratio) for all flights in the MOYA-I (Senegal) analyses. A linear fit of points from flight C005 (blue) is also displayed. Simulated fits of African forest (red dashed line) and grassland (grey shaded area) burning using the intercepts and intercept ranges reported by Chanton et al. (2000) are also shown.

ton et al., 2000). Unfortunately, flights over mixed sources in Uganda meant that Keeling plot analysis could not be used to determine the isotopic composition of fire emissions in the same way as carried out for Senegal. The Keeling plot for the MOYA-II isotope samples is shown in the Supplement (Fig. S2)

Table 1 shows the EFs calculated for all species during flights C004 and C005, as well as savannah and grassland and tropical forest fire EFs reported by Andreae (2019). The methane EFs for C004 and C005 (2.3 ± 0.24 and $1.4 \pm 0.15 \text{ g kg}^{-1}$ respectively) in this region, at the northern fringe of the African moist tropics, are more comparable to the savannah and grassland methane EFs ($2.7 \pm 2.2 \text{ g kg}^{-1}$) averaged from multiple previous studies by Andreae (2019). Additionally, mean CO EFs ($84 \pm 8.7 \text{ g kg}^{-1}$ for C004 and

$61 \pm 6.2 \text{ g kg}^{-1}$ for C005) are also more comparable to the savannah and grassland CO EF of $69 \pm 20 \text{ g kg}^{-1}$ than the tropical forest CO EF of $104 \pm 39 \text{ g kg}^{-1}$ reported by Andreae (2019).

The magnitude of methane EFs can be affected by multiple factors, such as fuel moisture (affecting combustion efficiency) as well as fuel type (Brownlow et al., 2017). It is worth noting that the majority of studies included in the Andreae (2019) tropical forest analysis focus on burning associated with Amazonian deforestation, which consists mostly of broad-leaved evergreen forest. In contrast, the Casamance region consists of facultatively deciduous broad-leaved forested savannah, which was observed from the aircraft and is shown by the land cover map in Fig. 5a. It is thus possible that any forest matter burned during the MOYA-I flights consists of dry leaf-litter fuel, whereas the Andreae (2019) study comprising mostly Amazonian land clearing may have included burning of whole evergreen tree structures. In addition to this, the modified combustion efficiencies of the C004 and C005 fires (0.93 ± 0.0031 and 0.95 ± 0.0030 respectively) are both higher than that reported in Andreae (2019) for tropical forest (0.91 ± 0.03) and are more comparable with the Andreae (2019) MCE for savannah and grassland burning (0.94 ± 0.02). This is likely due to the lower fuel moisture content of dry leaf-litter and savannah grasses as opposed to Amazonian evergreen; hence the methane EFs are likely driven by combustion efficiency.

From the EF and $\delta^{13}\text{C}-\text{CH}_4$ results from flights C004 and C005, it is likely that the biomass fuel is a mixture of both deciduous forest matter and savannah grasses as inferred from the isotope and EF results, as well as visual observations of forested savannah and the presence of shrubland and open forest in the land cover classification (Fig. 5a).

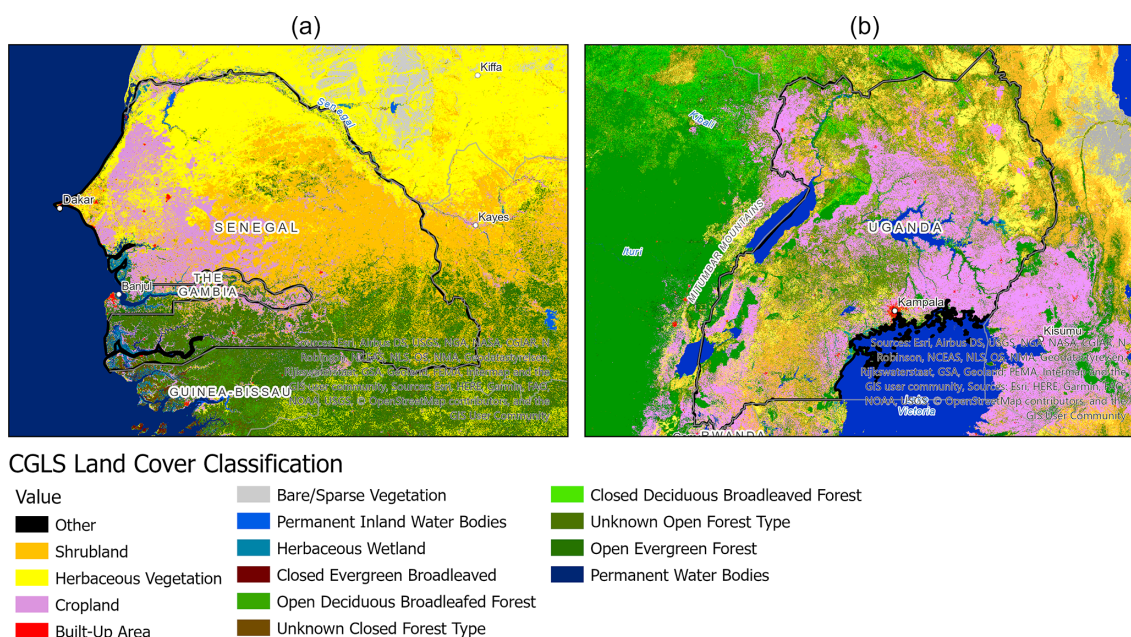


Figure 5. (a) Land cover classification map of Uganda from 2019. (b) Land cover classification map of Senegal from 2017. Data are obtained from the Copernicus Global Land Service Africa Land Cover Maps, which are derived from PROBA-V satellite observations (Buchhorn et al., 2019). © OpenStreetMap contributors and the GIS user community 2020. Distributed under a Creative Commons BY-SA License.

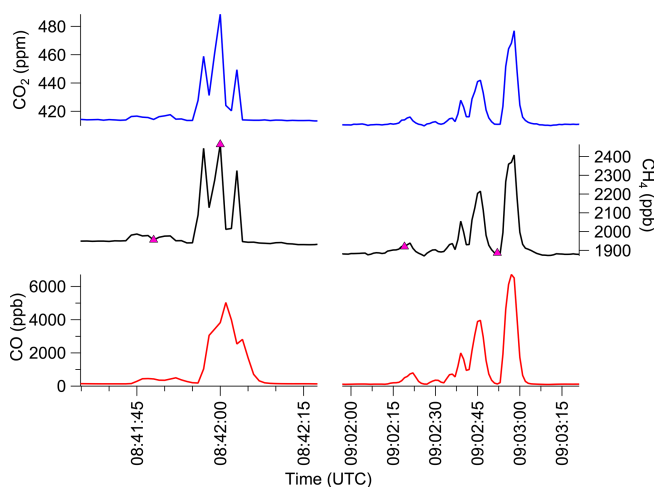


Figure 6. Time series of CO (red), CH₄ (black), CO₂ (blue), and concentrations in the plumes analysed for flight C005. Median WAS canister fill times are marked on the CH₄ time series as pink triangles. Note that some WASs taken in background regions are not shown here.

3.1.2 MOYA-II

Flight C132. Flight C132 was undertaken on 28 January 2019, as a survey of the Lake Kyoga wetland area. Two crop waste biomass burning plumes were sampled from two distinct fires in the area (see Fig. 1). A time series of various trace gas mixing ratios during this flight is shown in Fig. 6.

As seen in Fig. 6, enhancements (relative to background) in all trace gases were observed in the two biomass burning plumes. However, N₂O mixing ratio data during the two enhancements were discarded due to aircraft turbulence, which may have corrupted data quality. As a result of the discarded data, as well as instrument drift owing to malfunction of the laser coolant system, N₂O EFs are not reported for flight C132.

Figure 5b shows the land cover of Uganda where the fire sampling flights were carried out. In agreement with on-board observations from the aircraft, much of the land surrounding Lake Kyoga is classified as cropland, and the fuel for the fires appeared to be primarily crop waste. This is a major farming region, with the main crops including maize (a C₄ plant) and cassava (C₃) south of Lake Kyoga and sorghum (C₄) north of the lake. (FEWS NET, 2020). The mean EFs calculated for C132 ($5.2 \pm 0.55 \text{ g kg}^{-1}$ for CH₄, $1554 \pm 164.2 \text{ g kg}^{-1}$ for CO₂, and $109 \pm 11.3 \text{ g kg}^{-1}$ for CO) agree within overlapping uncertainty with mean agricultural burning EFs of $5.7 \pm 6.0 \text{ g kg}^{-1}$ for CH₄, $1430 \pm 240 \text{ g kg}^{-1}$ for CO₂, and $76 \pm 55 \text{ g kg}^{-1}$ for CO reported by Andreae (2019). The mean MCE obtained for the C132 fires (0.90 ± 0.0042) is also in agreement with the Andreae (2019) MCE for agricultural residue burning (0.92 ± 0.06). Furthermore, compared to northern Uganda, the Lake Kyoga region has a shorter dry season and higher rainfall. In addition, the fires were bordering a wetland area. Thus the moister conditions of the Lake Kyoga fires could have resulted in lower tem-

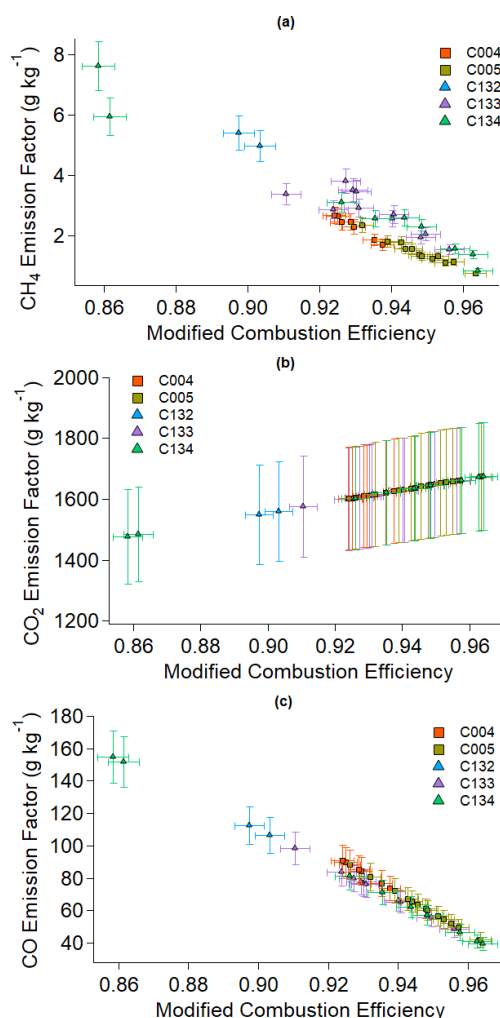


Figure 7. (a) Methane, (b) CO₂, and (c) CO EF vs. modified combustion efficiency for all biomass burning plumes sampled over all flights (squares are MOYA-I and triangles are MOYA-II). Points are coloured by flight number.

perature, moister combustion, and therefore more incomplete burning.

Flights C133 and C134. Flights C133 and C134 were dedicated fire sampling flights surveying the winter savannah of north-west Uganda. Both flights involved box patterns flown over this region, with deviations taken in order to sample biomass burning plumes visibly identified over the course of the flights. C133 and C134 were undertaken on 28 and 29 January 2019 respectively. The trace gas time series for these flights are shown in the Supplement in Figs. S3 and S4.

The EFs determined for the fire plumes encountered during flight C133 (2.8 ± 0.30 for CH₄, 1620 ± 171.2 for CO₂ and 72 ± 7.4 g kg⁻¹ for CO) agreed well with Andrae (2019) savannah burning EFs (2.7 ± 2.2 g kg⁻¹ for CH₄, 1660 ± 90 g kg⁻¹ for CO₂, and 69 ± 20 g kg⁻¹ for CO). The mean CH₄ and CO₂ EFs for C134 (3.1 ± 0.22 and 1609 ± 173.8 g kg⁻¹ respectively) are broadly comparable

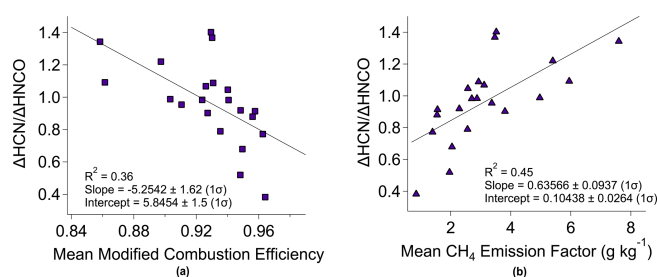


Figure 8. Plot of HCN enhancement over HNCO enhancement in biomass burning plumes vs. (a) mean modified combustion efficiency and (b) mean methane EF in grams per kilogram for all MOYA-II data.

with the CH₄ and CO₂ EFs calculated for C133. Additionally, the mean MCE for C134 (0.93 ± 0.0042) is comparable to that of C133 (0.94 ± 0.0041). The mean MCEs for C133 and C134 demonstrate that the burning observed in these flights was characterized by more complete flaming combustion than that observed in flight C132 (0.90 ± 0.0042), resulting in the comparatively higher CO₂ EFs and lower CH₄ EFs determined for C133 and C134 relative to C132. The trends in mean MCE and EFs observed during C132, C133, and C134 suggest that EFs are mostly determined by the completeness of combustion over other factors, which is illustrated by the linear relationships between CH₄, CO₂, and CO EFs vs. MCE shown in Fig. 7. In particular, fires sampled during C134 may have had a larger smouldering component, and they appeared to have involved less complete combustion on average than in C133, which would explain the lower emissions of more highly oxidized CO₂ and higher emissions of more reduced CH₄ than were observed in C134.

The ratio of HCN enhancement to HNCO enhancement within the plumes is informative to quantify combustion completeness and in order to provide redundancy in estimating fire combustion efficiency. Molar ratios of HCN to HNCO in fire emissions have been shown to decrease linearly with increasing combustion temperature (Hansson et al., 2004). Hence lower $\Delta\text{HCN}/\Delta\text{HNCO}$ ratios should be expected from fires with more complete combustion. Figure 8a shows $\Delta\text{HCN}/\Delta\text{HNCO}$ decreasing linearly ($R^2 = 0.36$) with increasing modified combustion efficiency for the MOYA-II fires. Consequently, Fig. 8b shows the methane emission factor decreasing with a lower $\Delta\text{HCN}/\Delta\text{HNCO}$ ratio. This further affirms that difference in combustion completeness is the primary driver of methane EF variability observed during MOYA-II. Unfortunately, a similar analysis could not be carried out for MOYA-I as the ToF-CIMS was not fitted to the aircraft during the MOYA-I flights.

As in flight C132, N₂O measurements for flight C133 were unreliable, and data were discarded due to the effects of aircraft motion on the instrument optical bench during turbulence. Furthermore, issues with the temperature control of the QCLAS optical bench meant that the baseline noise and drift

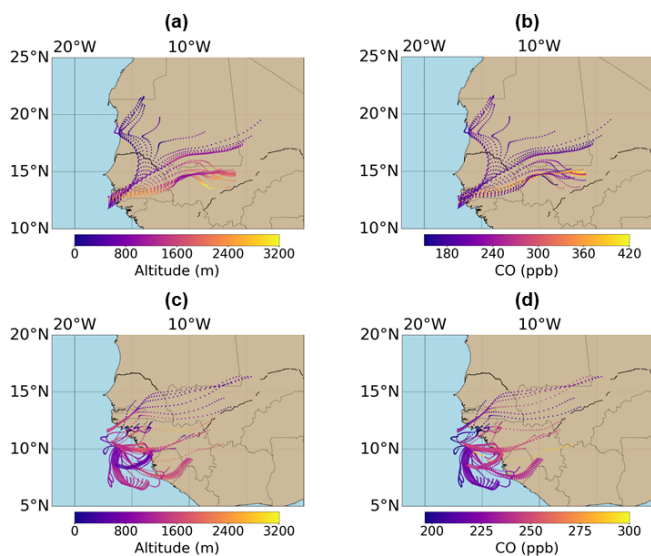


Figure 9. The 2 d HYSPLIT back trajectories from sections of the flight tracks of flights C006 and C007 during which biomass burning emissions were sampled (the in-fire-plume data from Fig. 10). The back trajectories are coloured by (a) trajectory altitude and (b) CO mixing ratio at the trajectory end point on the flight C006 flight track. Panels (c) and (d) show the back trajectories for flight C007, coloured by trajectory altitude and CO mixing ratio respectively. Trajectories are run at 60 s intervals of in-plume flight data. The base maps are obtained from Global Self-consistent, Hierarchical, High-resolution Geography Database (GSHHG) data (Wessel and Smith, 1996).

of the N_2O signal increased during this flight. This resulted in a reduced signal-to-noise ratio of N_2O in the plume. For these reasons, an N_2O EF is not reported for flight C133. However, optical bench temperature control was adequate during flight C134, and aircraft turbulence did not impact N_2O data quality significantly during sampling of some fire plumes. Hence calculation of N_2O EFs was possible for six of the nine fire plumes sampled during flight C134.

In general, the N_2O mixing ratio enhancements in the fire plumes are small (< 10 ppb) relative to the background variability (and instrumental noise) of the N_2O dataset (up to 2 ppb). Hence the signal-to-noise ratios of the in-plume N_2O enhancements are poorer than the in-plume enhancements of other species. As a result of this, the uncertainty relative to the mean N_2O EF for C134 is larger than those seen in the other species measured. Despite the combination of instrument issues and poor signal-to-noise ratio, the N_2O EF for flight C134 ($0.08 \pm 0.01 \text{ g kg}^{-1}$) agrees within overlapping uncertainty with the savannah fire N_2O EF reported by Andreae (2019) ($0.17 \pm 0.09 \text{ g kg}^{-1}$).

Figure 7 shows strong linear relationships between MCE and CH_4 , CO_2 , and CO EFs for both MOYA-I and MOYA-II. There is no discernible linear relationship between the N_2O EFs from C134 and MCE, which is shown in the Supplement in Fig. S5. It is worth noting that CH_4 EFs and correspond-

ing MCEs for the far-field flights C006 and C007 are not included in Fig. 7, as the EFs from these flights are representative of multiple fires with a mixture of phases, whereas the near-field EFs are representative of single fires with a single combustion efficiency associated with them. This trend is expected as higher MCEs, and hence more complete flaming combustion, would lead to increased emission of more oxidized combustion products (CO_2) and less emission of more reduced compounds such as CH_4 . Despite this, CH_4 EFs measured in Uganda appear to be significantly higher than those measured in Senegal at the same MCE; hence methane emissions from the Ugandan wildfires sampled appear to be higher, and this difference is independent of combustion efficiency. The difference in the linear regressions could possibly be accounted for by differences in the Senegalese and Ugandan fuel mixtures. However, due to detailed analysis of the fuel burned in this study being impossible, and with the likelihood of the fuel source being mixed, the effect of differing fuel content is difficult to quantify. An additional hypothesis is that higher average soil moisture in northern Uganda compared to south-west Senegal could result in soil parching and consequent release of methane-rich air from the soil surrounding wildfires; however more work is required to investigate whether soil moisture could affect wildfire methane EFs in this way.

3.2 Far-field sampling

Flights C006 and C007 were designed to characterize the regional continental outflow of air masses influenced by biomass burning from Senegal and wider West Africa. C006 and C007 involved sampling at various altitudes from 16 to 6500 m a.s.l. over the West African Atlantic coastline. C006 involved straight and level runs directly west of the Casamance region of Senegal targeted during the near-field flights C004 and C005. A strong measured easterly wind indicated continental outflow from the south-west Casamance region of Senegal during flight C006. Sampling during flight C007 was conducted further south, running parallel to the coastline of Guinea-Bissau due to the more complex meteorology encountered during the flight.

In order to identify the approximate origin and age of the biomass burning emissions sampled during the far-field flights, the National Oceanic and Atmospheric Administration (NOAA) Hybrid Single-Particle Lagrangian Integrated Trajectory (HYSPLIT) model was used to calculate three-dimensional single-particle back trajectories of air masses sampled during C006 and C007 (Stein et al., 2015). HYSPLIT back trajectories were run at 60 s intervals during times where biomass burning emissions were sampled (Figs. S6 and S7 in the Supplement). The back trajectories for C006 shown in Fig. 9a and b indicate that the age of the biomass burning plumes sampled was approximately 8 h. Furthermore, the sampled air mass appeared to have advected over the south-western Casamance region, with the highest CO

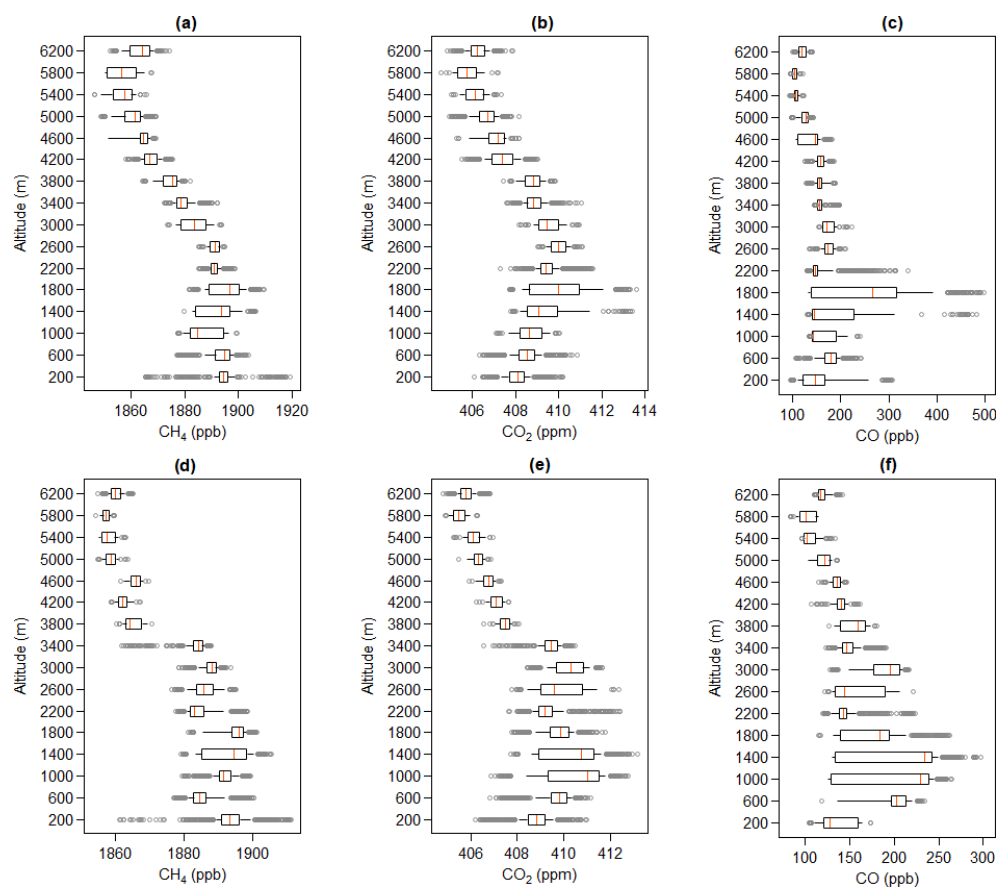


Figure 10. Box-whisker plots of (a) CH₄, (b) CO₂, and (c) CO altitude profiles for flight C006 and (d) CH₄, (e) CO₂, and (f) CO altitude profiles for flight C007. Altitude is divided into 400 m vertical bins for all box-whisker plots. The boxes represent the 25th and 75th percentiles, whiskers represent 10th and 90th percentiles, and the grey circular points are outliers.

concentrations observed in air masses that passed directly over this region. Thus, the sampled outflow represents a well-mixed air mass influenced by the fire regions targeted in the near field. The HYSPLIT back trajectories for C007 shown in Fig. 9c and d highlight the much more complex atmospheric dynamics influencing the sampled air masses during flight C007 as opposed to C006. The biomass burning emissions sampled during C007 originated from Guinea-Bissau, Guinea, Sierra Leone, and south-western Senegal, all of which were undergoing active burning during this time as shown in Fig. 1a. With these complex air masses, the approximate age of the biomass burning emissions observed in C007 was estimated to be older than that in C006, with an approximate age of 1–2 d. Consequently, the emissions sampled in C007 were representative of a wider area of West African biomass burning than C006, spanning from south-west Senegal down to Sierra Leone. Due to the significantly older plume age of the C007 biomass burning emissions, it is possible that significant chemical ageing and/or mixing of background air with plume air has occurred, and hence the ERs or EFs derived from this flight may not be representative of single source regions (see Sect. 2.6).

Box-whisker altitude profiles for flights C006 and C007 are shown in Fig. 10. Figure 10c shows peak CO concentrations in air masses at approximately 1600 m a.s.l. during flight C006. This is also consistent with fire plume injection heights observed during near-field sampling. Both CH₄ and CO₂ altitude profiles in Fig. 10a and b also show enhanced concentrations up to approximately 1600 m a.s.l., with a rapid decrease in mean CO concentration from 2000 m a.s.l., indicating free-tropospheric air above this. This was confirmed by analysis of measured thermodynamic profiles (not shown in this work). The altitude profiles in Fig. 10d–f show that during flight C007, peak CO concentration as well as the highest mean CO concentration was measured at approximately 1400 m a.s.l. Concurrently, CH₄ and CO₂ mixing ratios were enhanced up to approximately 3400 m a.s.l. Above this, CO, CH₄ and CO₂ mixing ratios decreased to background free-tropospheric concentrations with comparatively small ranges. In comparison to flight C006, in C007 the biomass burning emissions appeared to be more mixed throughout the polluted boundary layer.

A linear weighted regression was fitted to data points for CH₄ and CO₂ vs. tracer CO (Fig. 11) for samples within

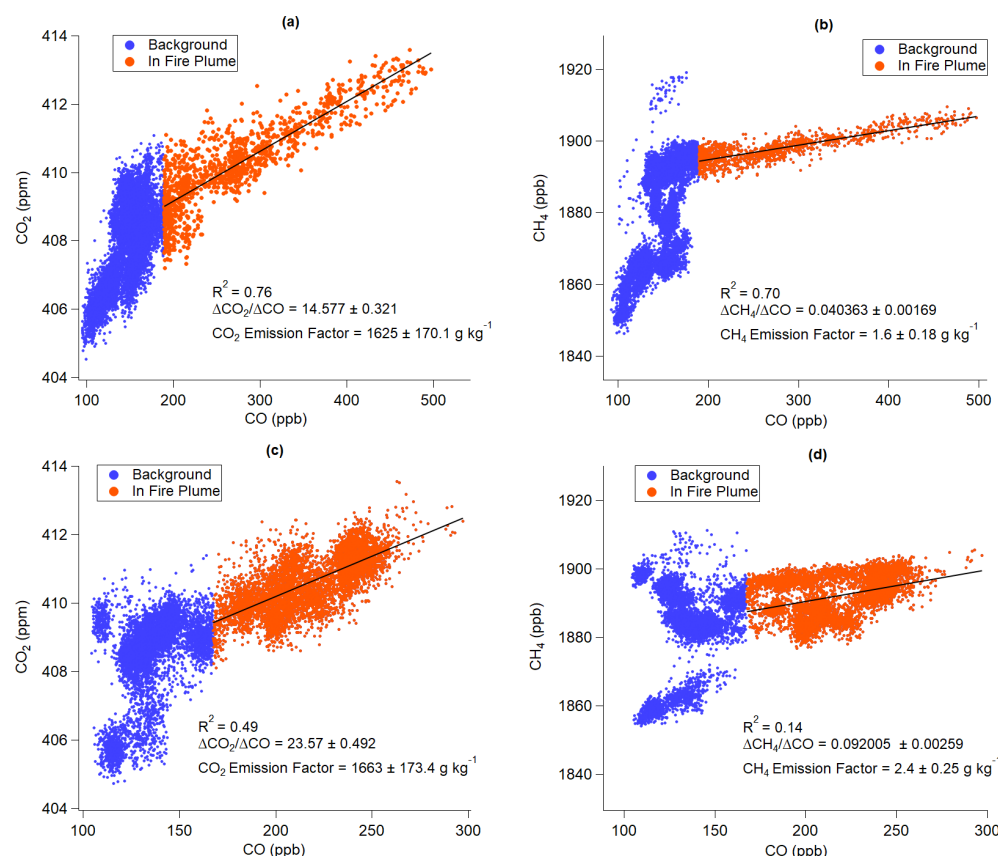


Figure 11. Linear regressions of in-plume (a) CH_4 and (b) CO_2 mixing ratio vs. in-plume CO mixing ratio for flight C006 and (c) CH_4 and (d) CO_2 mixing ratio vs. in-plume CO for flight C007. The linear regressions are calculated using the York regression method and are weighted towards CO and CH_4/CO_2 measurement uncertainty (York et al., 2004). ERs obtained from the slope are also shown, as well as the calculated EFs.

the biomass burning plume, using a statistical CO threshold to identify the smoke plumes from fires (as described in Sect. 2.6). The gradient of this fit was equivalent to the ERs with respect to CO and included in Table 1. Figure 11a and b show strong linear trends between in-plume CH_4 and CO_2 vs. CO for flight C006, with R^2 values of 0.70 and 0.76 respectively.

Although some degree of linearity is identifiable, the observed trends shown in Fig. 11c and d are significantly weaker than those seen for flight C006, with R^2 values of 0.14 for CH_4 vs. CO and 0.49 for CO_2 vs. CO . The higher variance in the C007 linear regressions, when compared with C006, could be attributed to mixed phases of burning and/or mixed degrees of chemical ageing present within the same biomass-burning-influenced air mass. Therefore homogenization of species from individual fire areas within the whole enhanced plume in C007 may be incomplete, and multiple fire phases with distinct combustion efficiencies or plume ageing may explain the poorer fits seen in C007.

As observed in Sect. 3.1 in the near-field sampling flights C004 and C005, the methane EF calculated for C006 ($1.6 \pm 0.18 \text{ g kg}^{-1}$) and C007 ($2.4 \pm 0.25 \text{ g kg}^{-1}$) is more compa-

table to savannah and grassland burning methane EF ($2.7 \pm 2.2 \text{ g kg}^{-1}$) reported by Andreae (2019). This is attributed to the mixed nature of the fuel source, likely comprised of facultatively deciduous forest litter and savannah grasses

MCE values of 0.94 ± 0.0041 for C006 and 0.96 ± 0.0037 for C007 are also shown in Table 1. It is likely that biomass burning signatures with a higher smouldering component were sampled in C006, which is further evidenced by the lower CO_2 EFs determined for C006. In contrast, the CH_4 EF is higher for C007, in which more complete combustion is inferred from the MCE. It is expected that this is due to the ageing of species sampled offshore in a recirculated air mass in C007 (as shown Fig. 12) and hence an indication that ERs and EFs may not be representative of the source fires. Despite ERs and EFs being shown for C007 in Fig. 11c and d, the EFs for C007 are not included in the mean calculation for Senegalese biomass burning EFs.

4 Conclusions

Airborne observations of CH₄, CO₂, and CO emissions from biomass burning were carried out in southern Senegal in February–March 2017 and northern Uganda in January 2019. Mean EFs of $1.8 \pm 0.19 \text{ g kg}^{-1}$ for CH₄, $1633 \pm 171.4 \text{ g kg}^{-1}$ for CO₂, and $67 \pm 7.4 \text{ g kg}^{-1}$ for CO were obtained from the Senegalese fires, with a mean modified combustion efficiency of 0.94 ± 0.005 . Mean EFs of $3.1 \pm 0.35 \text{ g kg}^{-1}$ for CH₄, $1610 \pm 169.7 \text{ g kg}^{-1}$ for CO₂, and $78 \pm 8.9 \text{ g kg}^{-1}$ for CO were obtained for the Ugandan fires, with a mean modified combustion efficiency of 0.93 ± 0.004 . A mean N₂O EF of $0.08 \pm 0.01 \text{ g kg}^{-1}$ is also reported for six fire plumes sampled over Uganda. CH₄ EFs showed strong linear relationships with modified combustion efficiency for both Senegal and Uganda. The variability in EFs within each study area was attributed to the mixed-phase nature of the fires, with a range of combustion efficiencies observed. These results also suggest that Ugandan fires have a higher methane emission factor for the equivalent combustion efficiency observed for Senegal. This may be a consequence of the difference in fuel between the Ugandan savannah grass and cropland waste fuels and the Senegalese forest litter and grassland fuel. This highlights the importance of considering both regional and local variability when attempting to spatially scale biomass burning emissions and suggests that singular regional EF values may lead to inaccurate estimates. Further work to constrain EFs at more local scales and for more specific (and quantifiable) fuel types will serve to improve global estimates of biomass burning emissions of climate-relevant gases.

This work demonstrates the value of airborne measurements for characterizing biomass burning emissions from multiple fires over wide areas. This study has provided unique in situ datasets in two geographical regions where there has hitherto been little study by aircraft measurement. The results will improve understanding of the role of African biomass burning in the global carbon budget, and the work demonstrates the importance of good knowledge of fuel mixture for the accurate reporting of EFs. This study demonstrates the utility of airborne measurements for characterizing biomass burning emissions from multiple fires over wide areas. Further work is required to investigate the link that fire fuel content may have on the emission of methane from biomass burning.

Data availability. FAAM ARA data from the MOYA project can be found on the CEDA archive at <https://catalogue.ceda.ac.uk/uuid/d309a5ab60b04b6c82eca6d006350ae6> (FAAM, NERC, Met Office, 2017).

Supplement. The supplement related to this article is available online at: <https://doi.org/10.5194/acp-20-15443-2020-supplement>.

Author contributions. PAB was the lead author, with writing contributions from GA, SJ-BB, REF, and TB. The flight methodology was devised by GA, EGN, JDL, and KNB. The paper methodology was designed by PAB, GA, JRP, and HC. Measurements aboard the aircraft were taken by PAB, JRP, REF, TB, SJ-BB, DP, SC, MBS, and AM. Data curation and validation were undertaken by PAB, JRP, REF, TB, SJ-BB, DP, and SC with input from CJP and HC. Review of the draft manuscript was undertaken by all co-authors. Funding was acquired by EGN, GA, and JDL.

Competing interests. The authors declare no conflict of interest.

Acknowledgements. The data used in this publication have been collected as part of the Methane Observations and Yearly Assessments (MOYA) project funded by the Natural Environment Research Council (NERC) (The Global Methane Budget, University of Manchester reference: NE/N015835/1 Royal Holloway, University of London reference: NE/N016211/1). Airborne data were obtained using the BAe-146-301 Atmospheric Research Aircraft (ARA) flown by Airtask Ltd and managed by FAAM Airborne Laboratory, jointly operated by UK Research and Innovation (UKRI) and the University of Leeds. We would like to give special thanks to the Airtask pilots and engineers and all staff at FAAM Airborne Laboratory for their hard work in helping plan and execute successful MOYA project flights. We acknowledge the use of MODIS data and imagery from LANCE FIRMS operated by NASA's Earth Science Data and Information System (ESDIS) with funding provided by NASA Headquarters (<https://doi.org/10.5067/FIRMS/MODIS/MCD14DL.NRT.006>). The maps used in Figs. 1 and 5 are obtained from ArcGIS software (sources: Esri, HERE, Garmin, Intermap, Increment P Corp., GEBCO, USGS, FAO, NPS, NRCAN, GeoBase, IGN, Kadaster NL, Ordnance Survey, Esri Japan, METI, Esri China (Hong Kong), © OpenStreetMap contributors and the GIS user community). The maps used in Fig. 9 are produced using the Python Matplotlib Basemap package, using Global Self-consistent, Hierarchical, High-resolution Geography Database (GSHHG) coastline and border data (Wessel and Smith, 1996). P. A. Barker is in receipt of a PhD studentship as part of the NERC Earth, Atmosphere and Ocean Doctoral Training Partnership (EAO DTP) (NERC grant reference: NE/L002469/1).

Financial support. This research has been supported by the Natural Environment Research Council (grant no. NE/L002469/1, NEN015835/1 and NE/N016211/1).

Review statement. This paper was edited by Drew Gentner and reviewed by two anonymous referees.

References

Andreae, M. O.: Biomass burning: Its history, use and distribution and its impact on environmental quality and global climate, in:

- Global Biomass Burning: Atmospheric, Climate and Biospheric Implications, edited by: Levine, J. S., MIT Press, Cambridge, MA, USA, 3–21, 1991.
- Andreae, M. O.: Emission of trace gases and aerosols from biomass burning – an updated assessment, *Atmos. Chem. Phys.*, 19, 8523–8546, <https://doi.org/10.5194/acp-19-8523-2019>, 2019.
- Andreae, M. O. and Merlet, P.: Emission of trace gases and aerosols from biomass burning, *Global Biogeochem. Cy.*, 15, 955–966, <https://doi.org/10.1029/2000GB001382>, 2001.
- Bey, I., Jacob, D. J., Yantosca, R. M., Logan, J. A., Field, B. D., Fiore, A. M., Li, Q., Liu, H. Y., Mickley, L. J., and Schultz, M. G.: Global modeling of tropospheric chemistry with assimilated meteorology: Model description and evaluation, *J. Geophys. Res.-Atmos.*, 106, 23073–23095, <https://doi.org/10.1029/2001JD000807>, 2001.
- Brownlow, R., Lowry, D., Fisher, R. E., France, J. L., Lanoisellé, M., White, B., Wooster, M. J., Zhang, T., and Nisbet, E. G.: Isotopic Ratios of Tropical Methane Emissions by Atmospheric Measurement, *Global Biogeochem. Cy.*, 31, 1408–1419, <https://doi.org/10.1002/2017GB005689>, 2017.
- Buchhorn, M., Smets, B., Bertels, L., Lesiv, M., Tsendbazar, N.-E., and Li, L.: Copernicus Global Land Service: Land Cover 100m, epoch 2018, Africa Demo (Version V2.1.1), <https://doi.org/10.5281/zenodo.3518087>, 2019.
- Chanton, J. P., Rutkowski, C. M., Schwartz, C. C., Ward, D. E., and Boring, L.: Factors influencing the stable carbon isotopic signature of methane from combustion and biomass burning, *J. Geophys. Res.-Atmos.*, 105, 1867–1877, <https://doi.org/10.1029/1999JD900909>, 2000.
- Ciais, P., Sabine, C., Bala, G., Bopp, L., Brovkin, V., Canadell, J., Chhabra, A., DeFries, R., Galloway, J., Heimann, M., Jones, C., Quéré, C. Le, Myneni, R. B., Piao, S., and Thornton, P.: The physical science basis. Contribution of working group I to the fifth assessment report of the intergovernmental panel on climate change, *Chang. IPCC Clim.*, Cambridge University Press, Cambridge, United Kingdom and New York, NY, USA, 465–570, <https://doi.org/10.1017/CBO9781107415324.015>, 2013.
- Cofer, W., Levine, J., Winstead, E., Cahoon, D., Sebach, D., Pinto, J., and Stocks, B.: Source compositions of trace gases released during African savanna fires, *J. Geophys. Res.-Atmos.*, 101, 23597–23602, 1996.
- Crutzen, P. J. and Andreae, M. O.: Biomass Burning in the Tropics: Impact on Atmospheric Chemistry and Biogeochemical Cycles, in: Paul J. Crutzen: A Pioneer on Atmospheric Chemistry and Climate Change in the Anthropocene, edited by: Crutzen, P. J. and Brauch, H. G., Springer International Publishing, Cham., 165–188, 2016.
- De Wolf, J.: Species composition and structure of the woody vegetation of the Middle Casamance region (Senegal), *Forest Ecol. Manag.*, 111, 249–264, 1998.
- Dlugokencky, E. J., Nisbet, E. G., Fisher, R., and Lowry, D.: Global atmospheric methane: Budget, changes and dangers, *Philos. T. R. Soc. A*, 369, 2058–2072, <https://doi.org/10.1098/rsta.2010.0341>, 2011.
- Ehhalt, D. and Prather, M.: Atmospheric Chemistry and Greenhouse Gases, *Clim. Chang. 2001 Sci. Basis*, Pacific Northwest National Lab. (PNNL), Richland, WA, USA, 239–287, <https://doi.org/10.2753/JES1097-203X330403>, 2001.
- Facility for Airborne Atmospheric Measurements: Natural Environment Research Council; Met Office: MOYA: ground station and in-situ airborne observations by the FAAM BAE-146 aircraft. Centre for Environmental Data Analysis, available at: <http://catalogue.ceda.ac.uk/uuid/d309a5ab60b04b6c82eca6d006350ae6> (last access: March 2019), 2017.
- FEWS NET: Uganda, available at: <https://fews.net/east-africa/uganda>, last access: 25 March 2020.
- Fisher, R., Lowry, D., Wilkin, O., Sriskantharajah, S., and Nisbet, E. G.: High-precision, automated stable isotope analysis of atmospheric methane and carbon dioxide using continuous-flow isotope-ratio mass spectrometry, *Rapid Commun. Mass Sp.*, 20, 200–208, <https://doi.org/10.1002/rcm.2300>, 2006.
- Frederiksen, P. and Lawesson, J. E.: Vegetation types and patterns in Senegal based on multivariate analysis of field and NOAA-AVHRR satellite data, *J. Veg. Sci.*, 3, 535–544, 1992.
- Gatari, M. J. and Boman, J.: Black carbon and total carbon measurements at urban and rural sites in Kenya, East Africa, *Atmos. Environ.*, 37, 1149–1154, [https://doi.org/10.1016/S1352-2310\(02\)01001-4](https://doi.org/10.1016/S1352-2310(02)01001-4), 2003.
- Gerbig, C., Schmitgen, S., Kley, D., Volz-Thomas, A., Dewey, K., and Haaks, D.: An improved fast-response vacuum-UV resonance fluorescence CO instrument, *J. Geophys. Res.-Atmos.*, 104, 1699–1704, [doi:10.1029/1998JD100031](https://doi.org/10.1029/1998JD100031), 1999.
- Hansson, K. M., Samuelsson, J., Tullin, C. and Åmand, L. E.: Formation of HNC, HCN, and NH₃ from the pyrolysis of bark and nitrogen-containing model compounds, *Combust. Flame*, 137, 265–277, <https://doi.org/10.1016/j.combustflame.2004.01.005>, 2004.
- Heimbürger, A. M. F., Harvey, R. M., Shepson, P. B., Stirr, B. H., Gore, C., Turnbull, J., Cambaliza, M. O. L., Salmon, O. E., Kerlo, A. E. M., Lavoie, T. N., Davis, K. J., Lauvaux, T., Karion, A., Sweeney, C., Brewer, W. A., Hardesty, R. M., and Gurney, K. R.: Assessing the optimized precision of the aircraft mass balance method for measurement of urban greenhouse gas emission rates through averaging, *Elementa*, 5, 26, <https://doi.org/10.1525/elementa.134>, 2017.
- Holmes, C. D., Prather, M. J., Søvde, O. A., and Myhre, G.: Future methane, hydroxyl, and their uncertainties: key climate and emission parameters for future predictions, *Atmos. Chem. Phys.*, 13, 285–302, <https://doi.org/10.5194/acp-13-285-2013>, 2013.
- Ichoku, C., Ellison, L. T., Willmot, K. E., Matsui, T., Dezfui, A. K., Gatebe, C. K., Wang, J., Wilcox, E. M., Lee, J., Adegoke, J., and Okonkwo, C.: Biomass burning, land-cover change, and the hydrological cycle in Northern sub-Saharan Africa, *Environ. Res. Lett.*, 11, 95005, <https://doi.org/10.1088/1748-9326/11/9/095005>, 2016.
- Le Breton, M., Bacak, A., Muller, J. B. A., Bannan, T. J., Kennedy, O., Ouyang, B., Xiao, P., Bauguitte, S. J. B., Shallcross, D. E., Jones, R. L., Daniels, M. J. S., Ball, S. M., and Percival, C. J.: The first airborne comparison of N₂O₅ measurements over the UK using a CIMS and BBCEAS during the RONOCO campaign, *Anal. Methods*, 6, 9731–9743, <https://doi.org/10.1039/c4ay02273d>, 2014.
- Lee, B. H., Lopez-Hilfiker, F. D., Veres, P. R., McDuffie, E. E., Fibiger, D. L., Sparks, T. L., and Iyer, S.: Flight deployment of a high-resolution time-of-flight chemical ionization mass spec-

- trometer: Observations of reactive halogen and nitrogen oxide species. *J. Geophys. Res.-Atmos.*, 123, 7670–7686, 2018.
- Li, Q., Jacob, D. J., Bey, I., Yantosca, R. M., Zhao, Y., Kondo, Y., and Notholt, J.: Atmospheric hydrogen cyanide (HCN): Biomass burning source, ocean sink?, *Geophys. Res. Lett.*, 27, 357–360, 2000.
- Li, Q., Jacob, D. J., Yantosca, R. M., Heald, C. L., Singh, H. B., Koike, M., Zhao, Y., Sachse, G. W., and Streets, D. G.: A global three-dimensional model analysis of the atmospheric budgets of HCN and CH₃CN: Constraints from aircraft and ground measurements, *J. Geophys. Res.-Atmos.*, 108, 8827, <https://doi.org/10.1029/2002jd003075>, 2003.
- Liu, Y., Goodrick, S., and Heilman, W.: Wildland fire emissions, carbon, and climate: Wildfire-climate interactions, *Forest Ecol. Manag.*, 317, 80–96, <https://doi.org/10.1016/j.foreco.2013.02.020>, 2014.
- Montzka, S. A., Dlugokencky, E. J., and Butler, J. H.: Non-CO₂ greenhouse gases and climate change, *Nature*, 476, 43–50, <https://doi.org/10.1038/nature10322>, 2011.
- Nisbet, E., Dlugokencky, E., Manning, M., Lowry, D., Fisher, R., France, J., Michel, S., Miller, J., White, J., Vaughn, B. and Bousquet, P.: Rising atmospheric methane: 2007–2014 growth and isotopic shift, *Global Biogeochem. Cy.*, 30, 1356–1370, 2016.
- Nisbet, E. G., Manning, M., Dlugokencky, E., Fisher, R., Lowry, D., Michel, S., and Brownlow, R.: Very strong atmospheric methane growth in the 4 years 2014–2017: Implications for the Paris Agreement, *Global Biogeochem. Cy.*, 33, 318–342, 2019.
- O'Shea, S. J., Allen, G., Gallagher, M. W., Bauguutte, S. J.-B., Illingworth, S. M., Le Breton, M., Muller, J. B. A., Percival, C. J., Archibald, A. T., Oram, D. E., Parrington, M., Palmer, P. I., and Lewis, A. C.: Airborne observations of trace gases over boreal Canada during BORTAS: campaign climatology, air mass analysis and enhancement ratios, *Atmos. Chem. Phys.*, 13, 12451–12467, <https://doi.org/10.5194/acp-13-12451-2013>, 2013a.
- O'Shea, S. J., Bauguutte, S. J.-B., Gallagher, M. W., Lowry, D., and Percival, C. J.: Development of a cavity-enhanced absorption spectrometer for airborne measurements of CH₄ and CO₂, *Atmos. Meas. Tech.*, 6, 1095–1109, <https://doi.org/10.5194/amt-6-1095-2013>, 2013b.
- O'Shea, S. J., Allen, G., Fleming, Z. L., Bauguutte, S. J.-B., Percival, C. J., Gallagher, M. W., Lee, J., Helfter, C., and Nemitz, E.: Area fluxes of carbon dioxide, methane, and carbon monoxide derived from airborne measurements around Greater London: A case study during summer 2012, *J. Geophys. Res.-Atmos.*, 119, 4940–4952, <https://doi.org/10.1002/2013JD021269>, 2014.
- Pitt, J. R., Le Breton, M., Allen, G., Percival, C. J., Gallagher, M. W., J.-B. Bauguutte, S., O'Shea, S. J., Muller, J. B. A., Zahniser, M. S., Pyle, J., and Palmer, P. I.: The development and evaluation of airborne in situ N₂O and CH₄ sampling using a quantum cascade laser absorption spectrometer (QCLAS), *Atmos. Meas. Tech.*, 9, 63–77, <https://doi.org/10.5194/amt-9-63-2016>, 2016.
- Priestley, M., le Breton, M., Bannan, T. J., Worrall, S. D., Bacak, A., Smedley, A. R. D., Reyes-Villegas, E., Mehra, A., Allan, J., Webb, A. R., Shallcross, D. E., Coe, H., and Percival, C. J.: Observations of organic and inorganic chlorinated compounds and their contribution to chlorine radical concentrations in an urban environment in northern Europe during the wintertime, *Atmos. Chem. Phys.*, 18, 13481–13493, <https://doi.org/10.5194/acp-18-13481-2018>, 2018a.
- Priestley, M., Le Breton, M., Bannan, T. J., Leather, K. E., Bacak, A., Reyes-Villegas, E., De Vocht, F., Shallcross, B. M. A., Brazier, T., Anwar Khan, M., Allan, J., Shallcross, D. E., Coe, H., and Percival, C. J.: Observations of Isocyanate, Amide, Nitrate, and Nitro Compounds From an Anthropogenic Biomass Burning Event Using a ToF-CIMS, *J. Geophys. Res.-Atmos.*, 123, 7687–7704, <https://doi.org/10.1002/2017JD027316>, 2018b.
- Radke, L. F., Hegg, D. a, Hobbs, P. V., Nance, J. D., Lyons, J. H., Laursen, K. K., Weiss, R. E., Riggan, P. J., and Ward, D. E.: Particulate and Trace Gas Emissions from Large Biomass Fires in North America, in: *Global Biomass Burning: Atmospheric, Climatic, and Biospheric Implications*, edited by: Levine, J. S., MIT Press, Cambridge, MA, USA, 1991.
- Saunois, M., Bousquet, P., Poulter, B., Pregon, A., Ciais, P., Canadell, J. G., Dlugokencky, E. J., Etiope, G., Bastviken, D., Houweling, S., Janssens-Maenhout, G., Tubiello, F. N., Castaldi, S., Jackson, R. B., Alexe, M., Arora, V. K., Beerling, D. J., Bergamaschi, P., Blake, D. R., Brailsford, G., Brovkin, V., Bruhwiler, L., Crevoisier, C., Crill, P., Covey, K., Curry, C., Frankenberg, C., Gedney, N., Höglund-Isaksson, L., Ishizawa, M., Ito, A., Joos, F., Kim, H.-S., Kleinen, T., Krummel, P., Lamarque, J.-F., Langenfelds, R., Locatelli, R., Machida, T., Maksyutov, S., McDonald, K. C., Marshall, J., Melton, J. R., Morino, I., Naik, V., O'Doherty, S., Parmentier, F.-J. W., Patra, P. K., Peng, C., Peng, S., Peters, G. P., Pison, I., Prigent, C., Prinn, R., Ramonet, M., Riley, W. J., Saito, M., Santini, M., Schroeder, R., Simpson, I. J., Spahni, R., Steele, P., Takizawa, A., Thornton, B. F., Tian, H., Tohjima, Y., Viovy, N., Voulgarakis, A., van Weele, M., van der Werf, G. R., Weiss, R., Wiedinmyer, C., Wilton, D. J., Wiltshire, A., Worthy, D., Wunch, D., Xu, X., Yoshida, Y., Zhang, B., Zhang, Z., and Zhu, Q.: The global methane budget 2000–2012, *Earth Syst. Sci. Data*, 8, 697–751, <https://doi.org/10.5194/essd-8-697-2016>, 2016.
- Schaefer, H.: On the Causes and Consequences of Recent Trends in Atmospheric Methane, *Curr. Clim. Change Rep.*, 5, 259–274, <https://doi.org/10.1007/s40641-019-00140-z>, 2019.
- Stein, A. F., Draxler, R. R., Rolph, G. D., Stunder, B. J. B., Cohen, M. D., and Ngan, F.: NOAA's hysplit atmospheric transport and dispersion modeling system, *B. Am. Meteorol. Soc.*, 96, 2059–2077, <https://doi.org/10.1175/BAMS-D-14-00110.1>, 2015.
- Turner, A. J., Frankenberg, C., and Kort, E. A.: Interpreting contemporary trends in atmospheric methane, *P. Natl. Acad. Sci. USA*, 116, 2805–2813, <https://doi.org/10.1073/pnas.1814297116>, 2019.
- Urbanski, S.: Combustion efficiency and emission factors for wildfire-season fires in mixed conifer forests of the northern Rocky Mountains, US, *Atmos. Chem. Phys.*, 13, 7241–7262, <https://doi.org/10.1016/j.foreco.2013.05.045>, 2013.
- van der Werf, G. R., Randerson, J. T., Giglio, L., Collatz, G. J., Mu, M., Kasibhatla, P. S., Morton, D. C., DeFries, R. S., Jin, Y., and van Leeuwen, T. T.: Global fire emissions and the contribution of deforestation, savanna, forest, agricultural, and peat fires (1997–2009), *Atmos. Chem. Phys.*, 10, 11707–11735, <https://doi.org/10.5194/acp-10-11707-2010>, 2010.
- Ward, D. E. and Hardy, C. C.: Advances in the characterization and control of emissions from prescribed fires, in: *Proceedings, Annual Meeting – Air Pollution Control Association*, San Francisco, CA, USA, 24–29 June, 1984.

- Ward, D. E. and Radke, L. F.: Emissions Measurements from Vegetation Fires?: A Comparative Evaluation of Methods and Results, in: *Fire Environ. Ecol. Atmos. Clim. Importance Veg. Fires*, John Wiley & Sons, Chichester, England, 53–76, 1993.
- Ward, D. E., Hao, W. M., Susott, R. A., Babbitt, R. E., Shea, R. W., Kauffman, J. B., and Justice, C. O.: Effect of fuel composition on combustion efficiency and emission factors for African savanna ecosystems, *J. Geophys. Res.-Atmos.*, 101, 23569–23576, <https://doi.org/10.1029/95jd02595>, 1996.
- Wessel, P. and Smith, W. H. F.: A global, self-consistent, hierarchical, high-resolution shoreline database, *J. Geophys. Res.-Sol. Ea.*, 101, 8741–8743, <https://doi.org/10.1029/96jb00104>, 1996.
- Yokelson, R., Goode, J., Ward, D., Susott, R., Babbitt, R., Wade, D., Bertschi, I., Griffith, D., and Hao, W.: Emissions of formaldehyde, acetic acid, methanol, and other trace gases from biomass fires in North Carolina measured by airborne Fourier transform infrared spectroscopy, *J. Geophys. Res.-Atmos.*, 104, 30109–30125, 1999.
- Yokelson, R. J., Crounse, J. D., DeCarlo, P. F., Karl, T., Urbanski, S., Atlas, E., Campos, T., Shinozuka, Y., Kapustin, V., Clarke, A. D., Weinheimer, A., Knapp, D. J., Montzka, D. D., Holloway, J., Weibring, P., Flocke, F., Zheng, W., Toohey, D., Wennberg, P. O., Wiedinmyer, C., Mauldin, L., Fried, A., Richter, D., Walega, J., Jimenez, J. L., Adachi, K., Buseck, P. R., Hall, S. R., and Shetter, R.: Emissions from biomass burning in the Yucatan, *Atmos. Chem. Phys.*, 9, 5785–5812, <https://doi.org/10.5194/acp-9-5785-2009>, 2009.
- Yokelson, R. J., Andreae, M. O., and Akagi, S. K.: Pitfalls with the use of enhancement ratios or normalized excess mixing ratios measured in plumes to characterize pollution sources and aging, *Atmos. Meas. Tech.*, 6, 2155–2158, <https://doi.org/10.5194/amt-6-2155-2013>, 2013.
- York, D., Evensen, N. M., Martinez, M. L., and De Basabe Delgado, J.: Unified equations for the slope, intercept, and standard errors of the best straight line, *Am. J. Phys.*, 72, 367–375, <https://doi.org/10.1119/1.1632486>, 2004.

Chapter 4

Manuscript 2: Airborne quantification of net methane and carbon dioxide fluxes from European Arctic wetlands in Summer 2019

Barker, P. A., Allen, G., Pitt, J. R., Bauguitte, S. J.-B., Pasternak, D., Cliff, S., France, J. L., Fisher, R. E., Lee, J. D., Bower, K. N. and Nisbet, E. G.: Airborne quantification of net methane and carbon dioxide fluxes from European Arctic wetlands in Summer 2019, *Philos. Trans. R. Soc. A Math. Phys. Eng. Sci.*, 380(2215), doi:10.1098/rsta.2021.0192, 2021.

The following chapter has been published in the journal Philosophical Transactions of the Royal Society A. P. A. Barker operated the N₂O instrumentation during all flights of the MOYA-Arctic campaign, and processed the raw N₂O data. P. A. Barker also contributed towards the flight planning during MOYA-Arctic. They designed the manuscript structure and concept, and carried out formal data analysis including calculation of mass balance fluxes. P. A. Barker also wrote the majority of the manuscript from first draft stages to final submitted draft, any other specific writing contributions not made by P. A. Barker will be detailed here. G. Allen obtained funding for the MOYA project as a whole, contributed to MOYA-Arctic flight planning, and provided writing contributions to all draft iterations of the manuscript. G. Allen also provided general supervision to P. A. Barker. J. R. Pitt provided assistance with the N₂O instrumentation, and gave feedback on draft manuscript iterations. S. J. B. Bauguitte operated CH₄ and CO₂ instrumentation aboard MOYA-Arctic flights. They also, processed and calibrated raw CH₄ and CO₂ data, and provided this data to P. A. Barker. D. Pasternak and S. Cliff operated the CH₄ and CO₂ instrumentation during some of the MOYA-Arctic flights, and also processed raw CH₄ and CO₂ data. J. L. France and R. E. Fisher collected whole air samples and Tedlar

bag samples during MOYA-Arctic flights, and both contributed to isotopic analysis of air samples. J. L. France carried out the land cover fraction analysis for the flight area, providing land class percentage cover data to P. A. Barker. J. D. Lee and K. N. Bower contributed to MOYA-Arctic flight planning, and provided feedback on draft iterations of the manuscript. E. G. Nisbet contributed to the general planning of MOYA-Arctic flights and logistics, contributed to funding acquisition for the wider MOYA project, and provided feedback on draft manuscript iterations. All co-authors provided commentary on draft versions of the manuscript.

Research



Cite this article: Barker PA *et al.* 2021

Airborne quantification of net methane and carbon dioxide fluxes from European Arctic wetlands in Summer 2019. *Phil. Trans. R. Soc. A* **380**: 20210192.

<https://doi.org/10.1098/rsta.2021.0192>

Received: 27 May 2021

Accepted: 3 August 2021

One contribution of 10 to a discussion meeting issue 'Rising methane: is warming feeding warming? (part 2)'.

Subject Areas:

atmospheric chemistry, atmospheric science, biogeochemistry, climatology

Keywords:

methane, carbon dioxide, wetland, Arctic, aircraft, flux

Author for correspondence:

Patrick A. Barker

email: patrick.barker@manchester.ac.uk

[†]Present address: School of Earth and Environmental Sciences, University of Manchester, Manchester, M13 9PL, UK.

Electronic supplementary material is available online at <https://doi.org/10.6084/m9.figshare.c.5680525>.

Airborne quantification of net methane and carbon dioxide fluxes from European Arctic wetlands in Summer 2019

Patrick A. Barker^{1,†}, Grant Allen¹, Joseph R. Pitt², Stéphane J.-B. Bauguitte³, Dominika Pasternak⁴, Samuel Cliff⁴, James L. France^{5,6}, Rebecca E. Fisher⁵, James D. Lee⁴, Keith N. Bower¹ and Euan G. Nisbet⁵

¹School of Earth and Environmental Sciences, University of Manchester, Manchester M13 9PL, UK

²School of Marine and Atmospheric Sciences, Stony Brook University, 145 Endeavour Hall, Stony Brook, NY 11794-5000, USA

³FAAM Airborne Laboratory, National Centre for Atmospheric Sciences, Building 146, College Road, Cranfield MK43 0AL, UK

⁴Wolfson Atmospheric Chemistry Laboratories, Department of Chemistry, University of York, Heslington, York YO10 5DD, UK

⁵Department of Earth Sciences, Royal Holloway, University of London, Egham, Surrey TW20 0EX, UK

⁶British Antarctic Survey, Natural Environment Research Council, Cambridge CB3 0ET, UK

PAB, 0000-0001-8754-4278; GA, 0000-0002-7070-3620; JRP, 0000-0002-8660-5136; JLF, 0000-0002-8785-1240; EGN, 0000-0001-8379-857X

Arctic wetlands and surrounding ecosystems are both a significant source of methane (CH₄) and a sink of carbon dioxide (CO₂) during summer months. However, precise quantification of this regional CH₄ source and CO₂ sink remains poorly characterized. A research flight using the UK Facility for Airborne Atmospheric Measurement was conducted in July 2019 over an area (approx. 78 000 km²) of mixed

© 2021 The Authors. Published by the Royal Society under the terms of the Creative Commons Attribution License <http://creativecommons.org/licenses/by/4.0/>, which permits unrestricted use, provided the original author and source are credited.

peatland and forest in northern Sweden and Finland. Area-averaged fluxes of CH₄ and carbon dioxide were calculated using an aircraft mass balance approach. Net CH₄ fluxes normalized to wetland area ranged between $5.93 \pm 1.87 \text{ mg m}^{-2} \text{ h}^{-1}$ and $4.44 \pm 0.64 \text{ mg m}^{-2} \text{ h}^{-1}$ (largest to smallest) over the region with a meridional gradient across three discrete areas enclosed by the flight survey. From largest to smallest, net CO₂ sinks ranged between $-513 \pm 74 \text{ mg m}^{-2} \text{ h}^{-1}$ and $-284 \pm 89 \text{ mg m}^{-2} \text{ h}^{-1}$ and result from net uptake of CO₂ by vegetation and soils in the biosphere. A clear gradient of decreasing bulk and area-averaged CH₄ flux was identified from north to south across the study region, correlated with decreasing peat bog land area from north to south identified from CORINE land cover classifications. While N₂O mole fraction was measured, no discernible gradient was measured over the flight track, but a minimum flux threshold using this mass balance method was calculated. Bulk (total area) CH₄ fluxes determined via mass balance were compared with area-weighted upscaled chamber fluxes from the same study area and were found to agree well within measurement uncertainty. The mass balance CH₄ fluxes were found to be significantly higher than the CH₄ fluxes reported by many land-surface process models compiled as part of the Global Carbon Project. There was high variability in both flux distribution and magnitude between the individual models. This further supports previous studies that suggest that land-surface models are currently ill-equipped to accurately capture carbon fluxes in the region.

This article is part of a discussion meeting issue 'Rising methane: is warming feeding warming? (part 2)'.

1. Introduction

As of 2020, atmospheric abundances of the greenhouse gases methane (CH₄) and carbon dioxide (CO₂) have increased by approximately 1155 ppb and 132 ppm, respectively, since 1850 AD, and continue to rise at an estimated rate of 9 ppb per year for CH₄ and 2 ppm per year for CO₂ [1]. The global atmospheric emission budgets of both CH₄ and CO₂ still remain uncertain, with the balance between total anthropogenic and biospheric sources and sinks yet to be fully understood and accounted for. A temporary stagnation in CH₄ growth between 1998 and 2007 [2], and renewed growth with a concurrent shift in carbon-13 isotopic ratio to lighter bulk abundance since 2007, further compound the current uncertainties associated with CH₄ source and sink apportionment [3–5].

Wetlands are understood to be a key ecosystem in terms of the surface exchange of climate-relevant trace gases. CH₄ is produced by methanogenic archaea under anoxic conditions with high soil organic carbon (SOC) in wetland soils. The magnitude of CH₄ production within wetland soils is highly sensitive to temperature, SOC availability, presence of vegetation, and water table height and hence oxygen content of the soil [6–9]. Consequently, the number of variables affecting CH₄ production, as well as their spatial and temporal variability, cause significant difficulty in parametrizing and predicting current and future CH₄ emissions from wetlands accurately [10]. Global wetlands are thought to represent the largest single natural source of atmospheric CH₄, contributing approximately 101–179 Tg CH₄ yr⁻¹ to the global CH₄ budget which represents 20% of the global yearly CH₄ source to the atmosphere [9,11,12]. In addition to producing CH₄, well-drained mineral soils under aerobic conditions can facilitate oxidation of CH₄ to CO₂ by methanotrophic microorganisms [13], while the surface exchange of CO₂ is controlled by the balance between respiratory CO₂ production from soil carbon stocks and photosynthetic CO₂ uptake by vegetation [14]. The Arctic is currently a net CO₂ sink, with an average of $-0.13 \text{ Pg CO}_2 \text{ year}^{-1}$ taken up by the terrestrial arctic; this CO₂ sink is highest in the summer months, when gross primary productivity is at a maximum [15]. Recent research has identified that longer Arctic growing seasons, increased precipitation and evapotranspiration rates may be driving increases in the Arctic CO₂ sink magnitude. Conversely,

higher ecosystem respiration rates and hence CO₂ emission have been linked to higher air temperatures in the Arctic. It is therefore evident that the rapidly changing climate in the Arctic has the potential to significantly impact the source–sink dynamics of CO₂ exchange in this area, and continuous *in situ* monitoring is crucial to assess the impact of climate change on Arctic CO₂ fluxes [16–18]

Approximately 53% of global wetland area is situated in northern latitudes above 50°N [19]. Therefore, Arctic and Boreal wetlands contribute significantly to the global CH₄ budget [20]. In addition to the current high CH₄ emission from high-latitude wetlands, these areas are sensitive to increasing CH₄ emission from positive climate feedbacks and Arctic climate amplification. Arctic mean air temperatures have increased at more than twice the rate of the global average, with current arctic temperature growth over 1.5°C higher than the 1971–2000 global average temperature growth with further warming predicted for the future [21,22]. Higher temperature may result in increased microbial activity in wetland ecosystems, leading to enhanced methanogenesis [23]. Furthermore, thawing of permafrost as a result of increasing temperature may result in an increase in arctic wetland extent as well as enabling the release of organic carbon from the estimated approximately 1700 Pg of stored SOC in arctic permafrost [24–27]. It is therefore clear that the CH₄ emissions from high-latitude wetlands may become increasingly important over time due to their high sensitivity to climate change.

Wetland trace gas emissions are commonly determined via top-down inversion modelling, bottom-up process-based modelling [7], or upscaling of eddy covariance or chamber fluxes to a wider wetland area. [28,29]. Process modelling of CH₄ fluxes from the wider Arctic often feature large uncertainty ranges due to the highly complex set of variables that influence microbial CH₄ production and emission processes to atmosphere. Additionally, the spatial and temporal heterogeneity of wetland environments, as well as the poorly defined boundaries of wetlands that often change seasonally, add significant uncertainty to annualized emission estimates as process models often account poorly for fine spatial and temporal variability in emissions [7,9]. *In situ* measurements of wetland emissions can be used to evaluate and improve process model estimates. However, the majority of *in situ* flux measurements are on a much smaller spatial scale than typical model outputs (typically on a 0.5° grid), and there are currently few *in situ* measurements on an appropriate scale for more direct model comparison [29,30]. Aircraft measurement platforms allow *in situ* measurements of trace gas emissions to be carried out on a similar spatial scale to process models, albeit as discrete snapshots of flux, and may allow the uncertainties on emission estimates from such models to be better constrained [31–33].

The Methane Observations and Yearly Assessments (MOYA) project aimed to use *in situ* measurements, targeted field campaigns and modelling to constrain global CH₄ sources and sinks from a variety of key CH₄ emission hotspots, such as African biomass burning [34] and Tropical wetlands (Shaw *et al.* in review). *In situ* measurements of CH₄ fluxes in these key areas will aid in reducing the uncertainty in their contribution to the global CH₄ budget and may provide a clearer explanation for currently rising atmospheric CH₄ mole fractions (MFs). As part of the MOYA project, the MOYA-Arctic field campaign was conducted from 29 July 2019 to 2 August 2019 based in Kiruna, Sweden. This field campaign used *in situ* aircraft measurements to quantify emissions of CH₄ and other trace gases from northern Swedish and Finnish (Fennoscandian) wetlands (66–69°N, 22–28°E) during the summer period. This work presents *in situ* aircraft measurements of CH₄, CO₂ and N₂O MF during one of the survey flights carried out during the MOYA-Arctic campaign. From these measurements, mass balance flux estimates for CH₄ and CO₂ were calculated and compared with previous similar aircraft studies in the region by O’Shea *et al.* [33]. Despite no direct flux being attainable from the N₂O data, a minimum flux threshold using this mass balance method was calculated for N₂O. Additionally, this study compares the fluxes obtained via aircraft mass balance with fluxes from Global Carbon Project (GCP) wetland process models, where both the magnitude and spatial distribution of CH₄ fluxes are compared with the aircraft results.

2. Methods

(a) Airborne instrumentation

The FAAM BAe 146-301 Atmospheric Research Aircraft (FAAM ARA) was operated for *in situ* sampling during the MOYA-Arctic campaign. Thermodynamic and meteorological parameters such as temperature, pressure and three-dimensional wind vector were measured by the FAAM ARA core instrument suite [35]. Temperature was measured by a Rosemount 102 sensor, with an estimated uncertainty of 0.1 K. Static pressure was measured by a series of pitot tubes distributed across the aircraft surface, with an uncertainty of 0.3 hPa. The three-dimensional wind vector is measured by a nose-mounted five port turbulence probe, with an uncertainty of 0.2 m s^{-1} .

A Los Gatos Research Fast Greenhouse Gas Analyser (FGGA) was used for 10 Hz measurements of CO_2 and CH_4 MF. The FGGA instrument uses a Cavity-Enhanced Absorption Spectroscopy technique and two continuous-wave near-IR diode lasers. The FGGA is mounted within a 19-inch rack in the cabin of the aircraft with ambient air pumped via a rearward-facing 3/8" stainless steel inlet mounted to a window blank. The FGGA was calibrated using three calibration gas standards: high- and low-concentration calibrations to account for instrument drift over the course of a flight, and a target calibration to assess long-term instrument precision and bias over multiple flights. All three calibration standards were traceable to the National Oceanic and Atmospheric Administration/Earth System Research Laboratory (NOAA/ESRL) World Meteorological Organisation (WMO) X2004A scale for CH_4 and X2007 scale for CO_2 [34,36]. Accounting for all sources of uncertainty, the mean (calibrated) biases and associated 1σ overall uncertainties are estimated to be $-0.048 \pm 0.626 \text{ ppm}$ and $-1.22 \pm 2.93 \text{ ppb}$, respectively for 10 Hz CO_2 and CH_4 sampling during MOYA-Arctic. One hertz measurements of N_2O MF were sampled by an Aerodyne Quantum Cascade Laser Absorption Spectrometer (QCLAS). The QCLAS was calibrated by means of three calibration gas standards, which were traceable to the WMO X2006 calibration scale [34,37]. An overall 1σ uncertainty of 0.58 ppb was estimated for 1 Hz N_2O MF measurements during the MOYA-Arctic flights.

(b) Aircraft mass balance flux technique

Aircraft mass balance flux techniques are well established in their ability to quantify trace gases fluxes from various sources, including regional-scale city emissions [38–40], point-source oil and gas emissions [41–43] and regional-scale biospheric trace gas emission/uptake [33,44]. For reliable flux quantification using aircraft mass balance, several criteria must be satisfied. First, MF measurements must be made downwind of a targeted emission source. Second, background measurements should be made, either within the centre of the well-mixed boundary layer upwind of the targeted emission source, or from downwind measurements either side of the emissions plume from the targeted emission source. These background measurements represent an estimate of the MF that would have been measured downwind of the targeted source in the absence of any emissions from that source. Additionally, wind direction should ideally be perpendicular to upwind and downwind sampling to ensure the measured airmass advects over the emission source, and wind speed should be constant for mass balance calculations. The meteorological conditions at the time of the survey flight reported here were highly favourable for this approach and the survey design was optimized to sample accordingly (described in §3). Flux determination by aircraft mass balance is expressed by equation (2.1).

$$\text{Flux} = \int_0^z \int_{x_0}^{x_i} (C_{\text{Enh}} - C_0) U_{\perp} dx dz \quad (2.1)$$

and

$$C_{(\text{gm}^{-3})} = \frac{\text{MF}_{(\text{ppb})}}{10^9} \times \rho_{\text{air}} \times \frac{M_x}{M_{\text{air}}} \quad x = \text{CH}_4 \text{ or } \text{CO}_2 \quad (2.2)$$

The flux of a trace gas species in g s^{-1} is defined as the enhancement in trace gas concentration (C_{Enh} is the enhanced concentration downwind in this case, C_0 is the background concentration). MFs are first converted to concentrations in units of g m^{-3} using equation (2.2), where ρ_{air} is the molar density of air, M_x is the molar mass of CH_4 or CO_2 and M_{air} is the molar mass of air. $(C_{\text{Enh}} - C_0)$ is then multiplied by the windspeed perpendicular to the flight track in m s^{-1} , U_{\perp} , integrated over the length of the downwind flight transect, x , and the height of the convective boundary layer, z . Measured statistical variability in the background concentration and wind vector, as well as measurement uncertainty and quantified systematic uncertainty in the height of boundary layer mixing (diagnosed from thermodynamic profiles), are propagated through equation (2.1) to determine flux uncertainty [33]. In addition to mass balance flux techniques, the FAAM ARA is capable of quantifying trace gas fluxes using the eddy covariance technique [45,46]; however, the magnitude of vertical windspeed during flight C195 was not sufficient for reliable calculation of CH_4 or CO_2 fluxes using eddy covariance in this study.

(c) Chamber fluxes

The mass balance fluxes derived from airborne measurements have also been compared to area-weighted chamber flux measurements, which were carried out in the same study area investigated here as part of the CH_4 and other greenhouse gases in the Arctic—Measurements, process studies and Modelling (MAMM) project. These chamber experiments were carried out daily between 12 July 2012 and 2 August 2012 and yielded area fluxes by specific land type for wetland ($4.5 \pm 3.7 \text{ mg m}^{-2} \text{ h}^{-1}$) and forest ($0.05 \pm 0.07 \text{ mg m}^{-2} \text{ h}^{-1}$) for summer. These area fluxes were scaled using the total wetland and forested area fraction with each of the three flux areas surveyed here according to the CORINE land cover map. The total wetland area was calculated as the sum of the peat bog and inland marsh grid cells within each area, and the total forested area was determined as the sum of all forest subclasses (broadleaved, coniferous and mixed forest) cells for each area. The chamber area fluxes were then multiplied by the total wetland or forest areas to give a bulk flux value for each of the three distinct flux areas.

(d) Flight description and strategy

The target area of FAAM ARA Flight C195 (figure 1) is mostly Northern Finnish Lapland, but also encompasses parts of Northeast Sweden (Norrbotten County) and North Norway (Finnmark County). The area surveyed was comprised boreal (Taiga) forest interspersed with peat bogs and lakes. Seasonal thaw of accumulated winter snow and ice typically results in the high prevalence of semi-permanent water bodies and peatland mires in the summer months. Flight C195 was carried out on 31 July 2019 between 10:00 and 14:30 CEST and involved four straight aircraft transects of approximately 200 km length across the wetland area, each at constant latitude. The first of these transects was the northernmost upwind leg at 69°N latitude, and the legs step down southwards in increments of 1°N with the final southernmost downwind leg at 66°N (as shown in figure 1). These constant latitude transects at 69°N , 68°N , 67°N and 66°N are referred to as transects 1, 2, 3 and 4 throughout. All transects across the wetland were conducted at altitudes between 300 m and 600 m above ground level (agl). Six deeper profiles (three ascents, three descents) from approximately 300 m agl to approximately 2500 m agl were carried out at the start, middle and end of the flight in order to assess planetary boundary layer (PBL) height and development used to derive mixing height for equation (2.1) over the course of the sampling period. A single biomass burning plume was intercepted at approximately 12:22 CEST, but this was removed from the CO_2 and CH_4 data prior to flux calculations. Measurements of carbon monoxide (CO) remained constant during the flight (with the exception of the single fire plume), strongly suggesting that this biomass burning event as well as any other anthropogenic sources did not have any impact on CH_4 MFs further downwind.

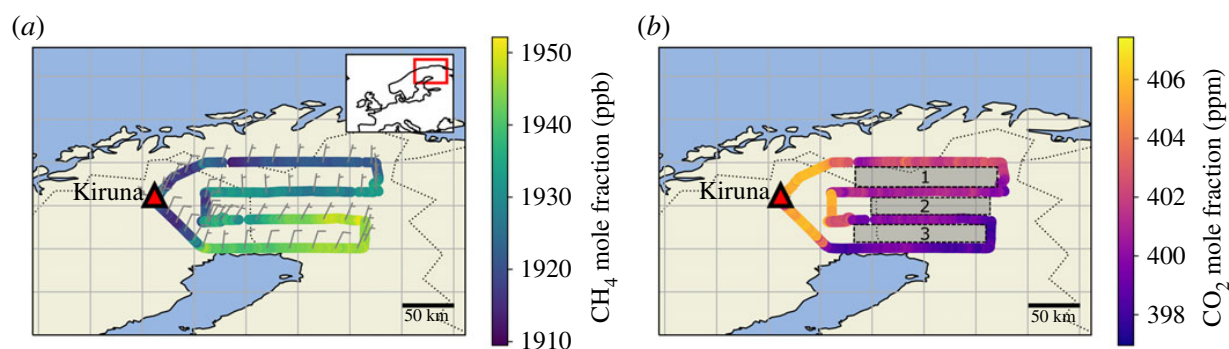


Figure 1. Flight track of FAAM flight C195 over northern Fennoscandian wetland areas; the flight tracks are coloured by (a) CH₄ MF and (b) CO₂ MF. Wind barbs are shown at 5 min intervals on (a) and Areas 1, 2 and 3 are shown on (b). (Online version in colour.)

3. Results and discussion

(a) Methane and carbon dioxide fluxes

Figure 1 shows the CH₄ and CO₂ MF variability over the course of flight C195. It can be seen that CH₄ MF increases towards the southernmost extent of the flight track, with an approximate 40 ppb increase in CH₄ between transect 1 and transect 3, with smaller MF increases between the southernmost transect 3 and transect 4. The isotopic signature of the CH₄ emissions during this flight strongly suggests that the CH₄ originates from a wetland source (see electronic supplementary material). The CO₂ MF decreases by approximately 5 ppm between transect 1 and transect 4, consistent with net biospheric CO₂ uptake over the survey area. There was no significant gradient in N₂O MF observed over the course of flight C195 so N₂O mass balance fluxes could not be calculated (see electronic supplementary material, figure S2). However, a theoretical ‘limit of detection’ for N₂O mass balance fluxes using the aircraft instrumentation was derived using the standard deviation of the N₂O MF over transect 1, and this is detailed in the electronic supplementary material.

Figure 2 shows the potential temperature (θ), CH₄ and CO₂ MFs during the six altitude profiles carried out in flight C195. All profiles were conducted within the near vicinity of the study area at the start, middle and end of the flight, and the profiles bracket the four longitudinal transects across the study area (see electronic supplementary material, figure S3). There was very little change in PBL height between the first and second set of vertical profiles as diagnosed from the characteristic sharp change in potential temperature gradient seen at PBL top (dashed blue lines in figure 2). However, there is a significant difference between the final profile ascent (figure 2e) and the final profile descent (figure 2f), as the PBL height is observed to be approximately 1000 m agl, whereas the descent shows a PBL height approximately 450 m higher at approximately 1450 m AGL, this final descent profile is therefore not used in PBL determination for mass balance calculations. To account for this change in mixing height used in the mass balance approach, the nearest available thermodynamic profile to each transect was used to determine PBL height in the flux calculations (i.e. only the ascending profile in figure 2e is used). The relatively small increase in PBL height over the course of flight C195 suggests that any entrainment of free tropospheric air into the PBL can be considered to be negligible and therefore will not significantly affect the uncertainty of flux estimates calculated here. Furthermore, MFs of CH₄ and CO₂ within the PBL were observed to be constant within each of the deep profiles, suggesting that the PBL was well mixed throughout the study region.

Wind direction over the course of flight C195 was predominantly northerly during transect 1 and transect 2 as shown in table 1 and by the wind barbs in figure 1a. As the flight progressed, the average wind direction changed from northerly to more north-easterly winds towards the southern end of the flight track was also confirmed by HYSPLIT back-trajectories with trajectory

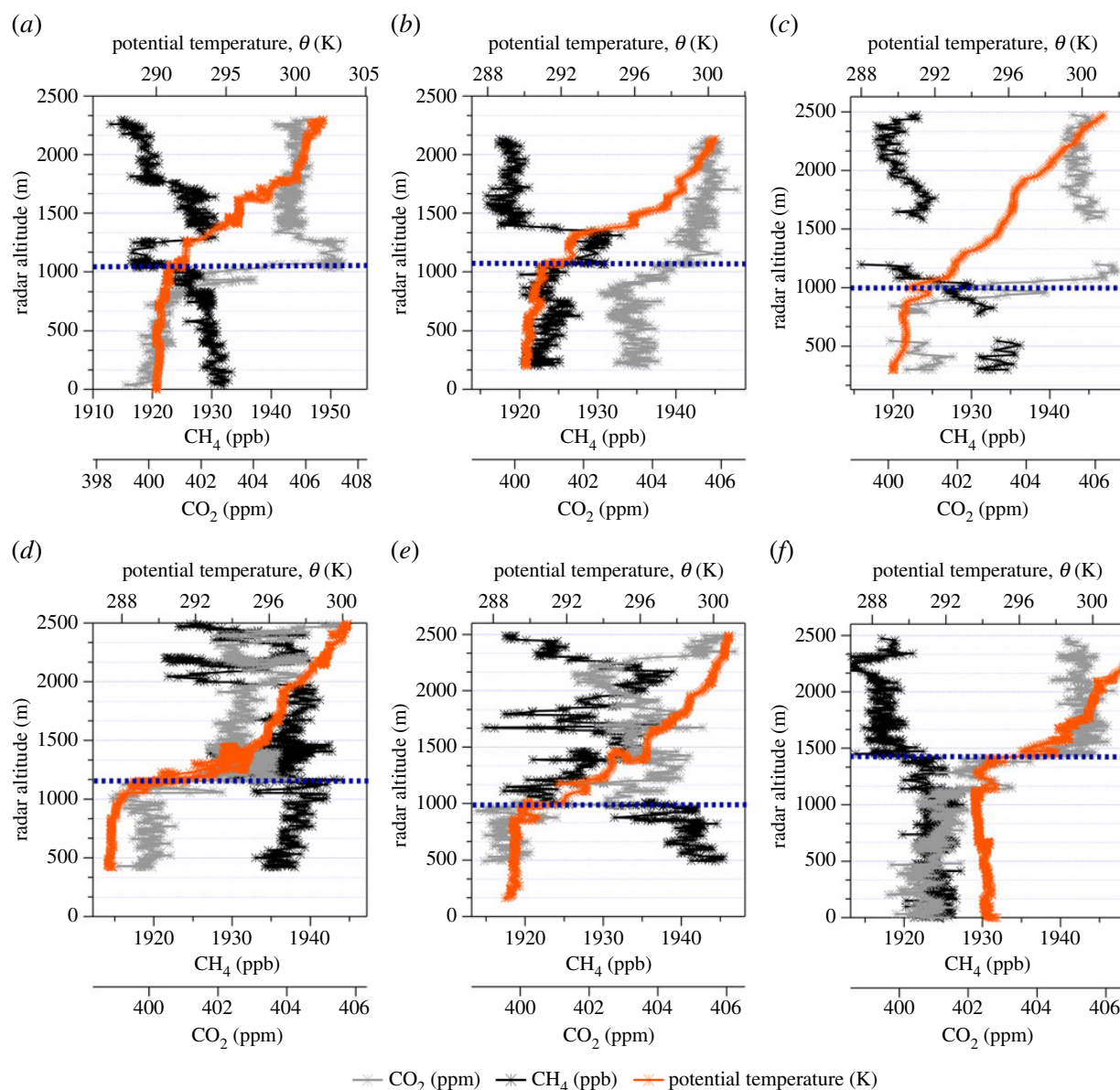


Figure 2. Vertical profiles of potential temperature, CH₄ mixing ratio and CO₂ mixing ratio during the six profiles (labelled chronologically (a–f)) carried out by the FAAM ARA during flight C195. Approximate convective mixing heights, determined by a change in vertical gradient in potential temperature, for each profile are also displayed as blue dashed lines. (Online version in colour.)

endpoints calculated for each transect shown in figure 3. Owing to this gradual change in wind direction over the course of the flight, a mass balance flux calculation across the entire flight area (i.e. using transect 1 as the background and transect 4 as the enhanced run) would be inappropriate, as transect 1 does not sample the same airmass as transect 4. Therefore individual fluxes were calculated between parallel meridional transect pairs, with the northern transect of each pair used to determine the upwind background, and the southern transect to determine the CH₄ gradient over the distance between each pair. The three areas between the meridional transect pairs are referred to as Area 1, Area 2 and Area 3 throughout. Area 1 is between transect 1 (69°N) and transect 2 (68°N), Area 2 is between transect 2 (68°N) and transect 3 (67°N), and Area 3 is between transect 3 (67°N) and transect 4 (66°N).

Table 1 shows the total CH₄ and CO₂ fluxes calculated for flight C195. Area-normalized fluxes are presented in units of mg m² h^{−1} for comparison with fluxes reported by process models (see §3.3). The CH₄ area fluxes calculated in this work agree well with previous analogous studies in the region in Arctic summer. For example, O’Shea *et al.* calculated CH₄ and CO₂ fluxes using

Table 1. Aircraft mass balance CH₄ and CO₂ flux parameters for flight C195. Total fluxes and hourly area fluxes within three distinct flux areas enveloped by a southern background transect and northern enhanced transect are also included for CH₄ and CO₂. CH₄ area fluxes are reported normalized to the total land area within each of the three study areas, and also normalized to the total wetland area within each study area.

parameter	Area 1 (transect 1 - transect 2)	Area 2 (transect 2 - transect 3)	Area 3 (transect 3 - transect 4)
CH ₄ enhancement over background (ppb)	9.98	11.12	1.65
CO ₂ enhancement over background (ppm)	−1.19	−1.08	−0.96
(C _{Enh} − C ₀) (CH ₄)	$6.37 \times 10^{-6} \pm 2.98 \times 10^{-10} \text{ g m}^{-3}$	$7.32 \times 10^{-6} \pm 3.88 \times 10^{-10} \text{ g m}^{-3}$	$1.08 \times 10^{-6} \pm 3.87 \times 10^{-10} \text{ g m}^{-3}$
(C _{Enh} − C ₀) (CO ₂)	$-2.11 \times 10^{-3} \pm 1.87 \times 10^{-7} \text{ g m}^{-3}$	$-1.94 \times 10^{-3} \pm 1.66 \times 10^{-7} \text{ g m}^{-3}$	$-1.72 \times 10^{-3} \pm 1.78 \times 10^{-7} \text{ g m}^{-3}$
perpendicular windspeed, U _⊥	$5.61 \pm 1.32 \text{ m s}^{-1}$	$4.19 \pm 1.32 \text{ m s}^{-1}$	$7.63 \pm 1.09 \text{ m s}^{-1}$
mean wind direction	183°	207°	196°
transect Length, x	$2.28 \times 10^5 \text{ m}$	$1.93 \times 10^5 \text{ m}$	$2.17 \times 10^5 \text{ m}$
boundary layer height, z	962 m	1073 m	1202 m
CH ₄ scaled chamber flux (O'Shea <i>et al.</i>)	$6.86 \pm 5.75 \text{ kg s}^{-1}$	$5.04 \pm 4.26 \text{ kg s}^{-1}$	$2.48 \pm 2.20 \text{ kg s}^{-1}$
CH ₄ flux (emission rate)	$7.85 \pm 1.06 \text{ kg s}^{-1}$	$6.37 \pm 2.01 \text{ kg s}^{-1}$	$2.15 \pm 0.31 \text{ kg s}^{-1}$
CH ₄ hourly area flux (total land area)	$1.11 \pm 0.26 \text{ mg m}^{-2} \text{ h}^{-1}$	$1.07 \pm 0.34 \text{ mg m}^{-2} \text{ h}^{-1}$	$0.32 \pm 0.046 \text{ mg m}^{-2} \text{ h}^{-1}$
CH ₄ hourly area flux (wetland area)	$5.31 \pm 0.72 \text{ mg m}^{-2} \text{ h}^{-1}$	$5.93 \pm 1.87 \text{ mg m}^{-2} \text{ h}^{-1}$	$4.44 \pm 0.64 \text{ mg m}^{-2} \text{ h}^{-1}$
CO ₂ flux (emission rate)	$-2601 \pm 615 \text{ kg s}^{-1}$	$-1692 \pm 533 \text{ kg s}^{-1}$	$-3431 \pm 493 \text{ kg s}^{-1}$
CO ₂ hourly area flux (total land area)	$-369 \pm 87 \text{ mg m}^{-2} \text{ h}^{-1}$	$-284 \pm 89 \text{ mg m}^{-2} \text{ h}^{-1}$	$-513 \pm 74 \text{ mg m}^{-2} \text{ h}^{-1}$

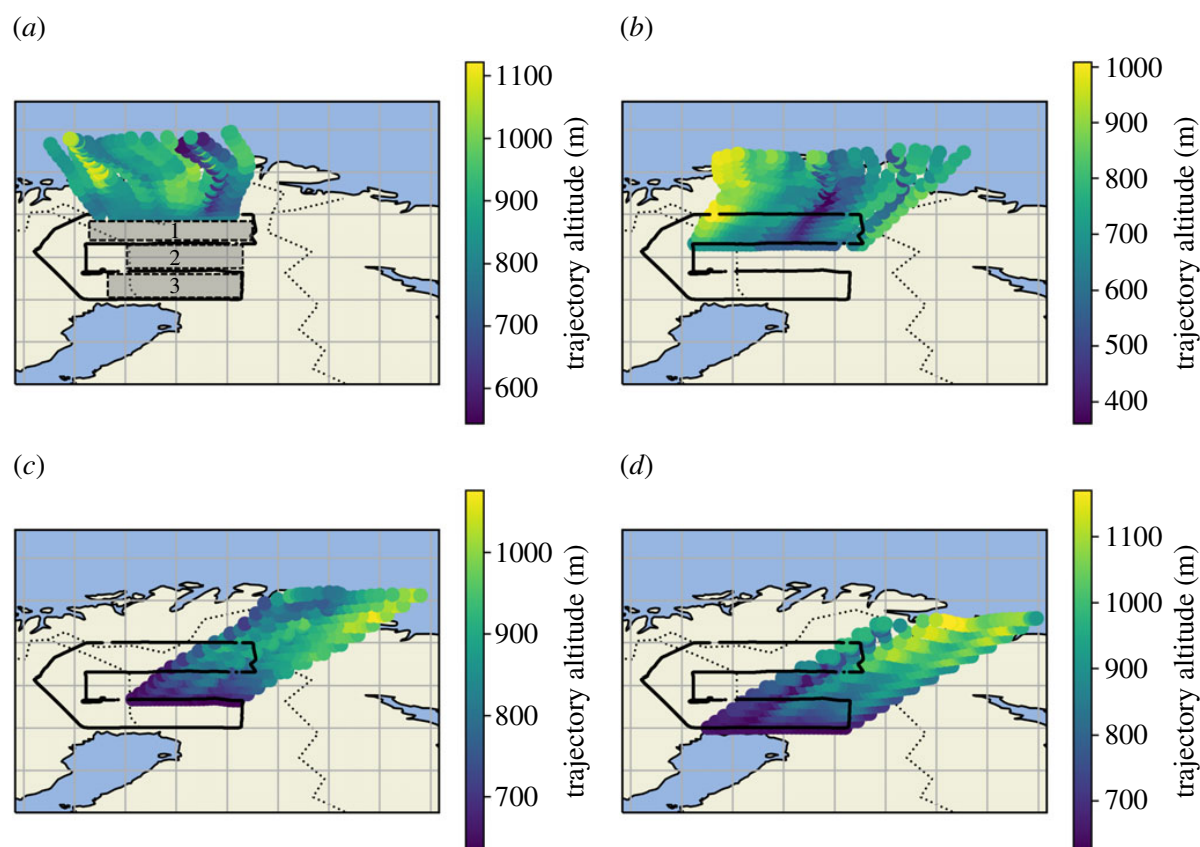


Figure 3. HYSPLIT 12 h back-trajectories coloured by trajectory altitude run every 60 s from each constant latitude leg. Areas 1, 2 and 3 are shown on (a). (Online version in colour.)

aircraft mass balance in a similar study area of northern Sweden and Finland [33]. The CH_4 flux of $1.2 \pm 0.5 \text{ mg m}^{-2} \text{ h}^{-1}$ reported by O'Shea *et al.* agrees within overlapping 1σ uncertainty for the Area 1 and Area 2 fluxes derived during this work ($1.11 \pm 0.26 \text{ mg m}^{-2} \text{ h}^{-1}$ for Area 1 and $1.07 \pm 0.34 \text{ mg m}^{-2} \text{ h}^{-1}$ for Area 2) but agrees poorly with the CH_4 flux of $0.32 \pm 0.26 \text{ mg m}^{-2} \text{ h}^{-1}$ for Area 3. The O'Shea *et al.* study involved a July 2012 aircraft survey in the same region as Areas 1 and 2, which explains why fluxes from these areas agree best with the O'Shea *et al.* results. From the fluxes presented in this work and previous fluxes reported for the same area, it appears that CH_4 emission in this area of the Arctic has not increased significantly from the period 2012–2019. However, climatological data from within the study area in Sodankylä shows that both 2012 and 2019 had similar July average temperatures (13.6°C for 2012 and 13.3°C for 2019), which may account for some of the similarity between the CH_4 fluxes. In addition, both July average temperature and precipitation for 2012 and 2019 are below the average for the period 1981–2010 (14.3°C , 73 mm), which suggests that CH_4 fluxes could be higher in years where temperature and precipitation anomalies are higher [47].

The net CO_2 uptake observed during this study is higher than that reported in previous work. The CO_2 sink reported from Arctic wetlands by O'Shea *et al.* is $-350 \pm 143 \text{ mg m}^{-2} \text{ h}^{-1}$, which agrees within overlapping 1σ uncertainty for CO_2 area fluxes reported here for each area (table 1), despite the maximum average CO_2 flux value calculated in this study being 24% higher than that determined in O'Shea *et al.* However, the Christensen *et al.* chamber CO_2 flux of $-96 \pm 33 \text{ mg m}^{-2} \text{ h}^{-1}$ is significantly lower than the CO_2 area fluxes for Area 1 and Area 2 [24]. Biospheric CO_2 fluxes are known to exhibit strong spatio-temporal variability that is highly sensitive to temperature, precipitation, insolation and leaf area index of the vegetation types studied, and therefore a close agreement between studies conducted on different days and years is not expected.

Table 1 shows that the mean CH_4 emission rate and area flux decreases with decreasing latitude from Area 1 to Area 3. Figure 4 shows the 2018 Copernicus Land Monitoring Service

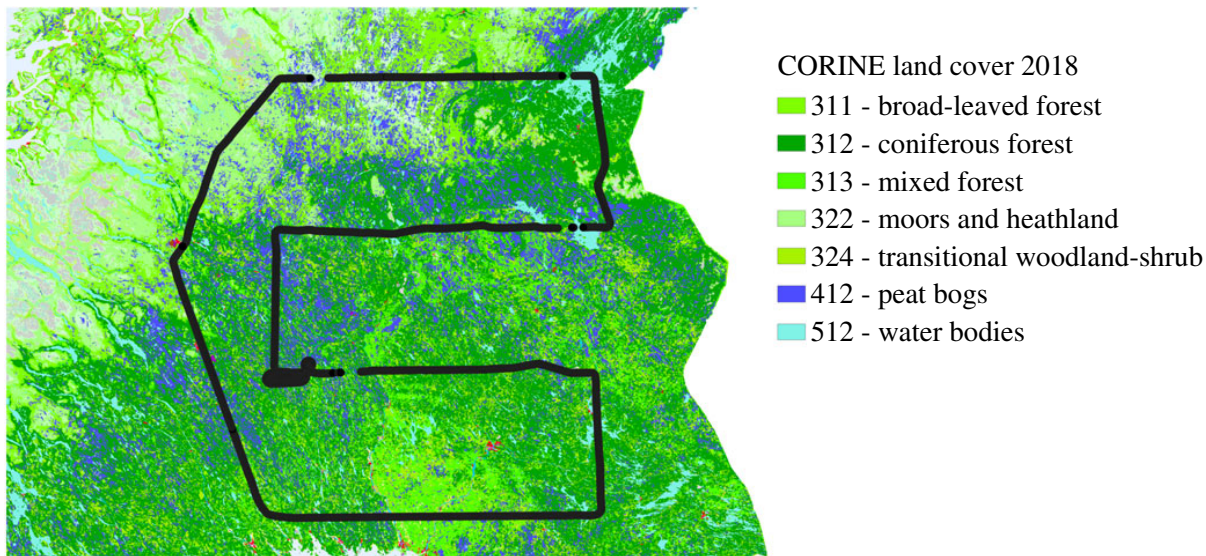


Figure 4. CORINE 2018 land cover map of the northern European wetland area surveyed during flight C195. The flight track is also displayed. (Online version in colour.)

Table 2. Top 5 CORINE land cover classes by percentage for each mass balance flux box.

Area 1		Area 2		Area 3	
land class	percentage cover	land class	percentage cover	land class	percentage cover
coniferous forest	41.2	coniferous forest	42.8	coniferous forest	49.8
peat bogs	22.9	mixed forest	21.5	mixed forest	18.6
broad leaf forest	13.2	peat bogs	20.0	woodland shrub	16.4
heathland and moors	5.51	woodland shrub	11.2	peat bogs	7.28
mixed forest	4.93	water bodies	2.80	water bodies	5.06

CORINE land cover classification of the study area (<https://land.copernicus.eu/pan-european/corine-land-cover/clc2018>), and table 2 shows the most abundant land classes within each flux area by percentage. It can be seen from both table 2 and visually from figure 4 that the abundance of peat bogs decreases towards the south of the survey area. Peat bogs comprise 22.9% of the land cover within the northernmost Area 1 between transect 1 and transect 2, this decreases slightly to 20.0% within Area 2 and decreases further to 7.28% within the southernmost Area 3. The decreasing peat bog abundance towards the southern end of the survey area provides a likely explanation for the gradually decreasing CH_4 flux seen from north to south in table 2. Additionally, there is a positive correlation between CO_2 sink magnitude and CORINE vegetation cover within the three areas of the flight (electronic supplementary material, figure S5). However, the correlation between CO_2 sink and vegetation cover is weaker than the CH_4 flux-peatland area correlation. This is likely due to the differing CO_2 uptake capacities of specific vegetated land types (e.g. dense forest will sequester more CO_2 than an equivalent area of cropland).

The mass balance fluxes of CH_4 derived in this study are compared to upscaled chamber CH_4 flux measurements that were previously taken in the same study area. A description of the chamber measurements as well as the method of upscaling these fluxes can be found in §2.3. The chamber flux results are shown in table 1 and figure 5. It can be seen that the scaled chamber fluxes have a larger relative error of between 84% and 88% of the flux value when compared to the mass balance fluxes (between 14% and 31%); however, the mean mass balance and chamber bulk fluxes agree very well within overlapping 1σ uncertainty for all three flux areas. The mean bulk fluxes

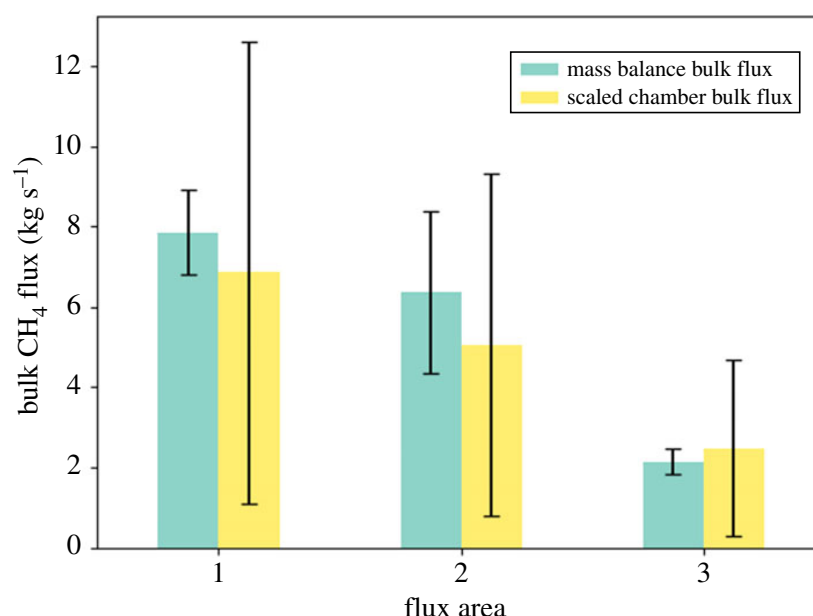


Figure 5. Bar plot comparison of bulk CH₄ flux from the three flux areas for the mass balance method and the upscaled chamber fluxes from the MAMM project. Error bars indicate the 1- σ standard deviation flux uncertainty in each case. (Online version in colour.)

from mass balance for Areas 1 and 2 ($7.85 \pm 1.06 \text{ kg s}^{-1}$ and $6.37 \pm 2.01 \text{ kg s}^{-1}$, respectively) are approximately 15–25% higher than the scaled chamber fluxes of $6.86 \pm 5.75 \text{ kg s}^{-1}$ for Area 1 and $5.04 \pm 4.26 \text{ kg s}^{-1}$ for Area 2. The slightly higher fluxes from mass balance could be associated with the presence of plant-mediated wetland CH₄ emission via the transport of CH₄ through specialized plant tissues. Emission from this pathway would be detectable using mass balance techniques but may be missed when using flux chamber apparatus mounted at ground level. However, the agreement between the two techniques provides support for the efficacy of the mass balance technique compared to ground-based flux quantification techniques and demonstrates the potential for spatial scalability and interpretation of point measurements such as chamber fluxes.

(b) Comparison with land-surface model methane fluxes

Top-down *in situ* flux estimates such as those derived in this work can provide an important comparison to emission estimates from bottom-up biogeochemical process models and anthropogenic emission inventories and can provide crucial validation of such models. Wetland CH₄ fluxes are typically derived by land-surface models by parametrizing key biogeochemical characteristics, such as CH₄ production, transport and oxidation within wetland soils, as well as the amount and type of vegetation present. These initial parameters are then forced by environmental variables such as precipitation, temperature, respiration and atmospheric CO₂ concentration in order to account for seasonal and interannual differences in CH₄ emission [48,49]. The CH₄ flux density output from biogeochemical parametrization is then combined with a wetland distribution map for a given area to spatially distribute the CH₄ flux and produce a flux map [7]. Recent research by Saunio *et al.* has compiled monthly CH₄ flux data from 13 different land-surface wetland models over the period 2000–2017 as part of the GCP. These model outputs, along with top-down atmospheric inversions, have provided an updated estimate for the global CH₄ budget for the 2000–2017 period. Mean modelled CH₄ flux for every July month was taken from the years 2000–2017 to best represent the northern hemisphere summertime period corresponding to the flight C195 survey data. There was found to be no significant trend of increasing or decreasing CH₄ flux reported by the models over the 2000–2017 period as shown in electronic supplementary material, figure S6. All land-surface models shown

here use a diagnostic means of prescribing wetland cover, namely the Wetland Area Dynamics for Methane Modelling (WAD2 M) which uses satellite microwave remote-sensing inputs [50]. Seven of the 13 process models also include prognostic with internal wetland prescription in each model.

Figure 6a,b show modelled CH₄ flux distribution maps for the diagnostic and prognostic models, respectively. The majority of diagnostic models share a common spatial distribution of CH₄ flux due to the WAD2M product that these models use to prescribe wetland cover. This common flux pattern shows flux hotspots in the northern two-thirds of the study area, particularly to the northeast. The prognostic model outputs do not show a common pattern of CH₄ flux distribution as with the diagnostic models, and flux distributions are much more variable in these model variants. The majority of diagnostic GCP models and a select few of the prognostic models (namely LPX-Bern and ORCHIDEE) show peak fluxes in the northern two-thirds of the study area, which broadly agrees with the mass balance flux observations where the highest fluxes were also measured in the northern two-thirds. Additionally, the aforementioned models also appear to show flux hotspots towards the eastern end of the study area. The mass balance technique could not explicitly resolve west to east flux gradient in this case; however, figure 1 appears to show higher CH₄ MFs towards the eastern end of the flight track suggesting that CH₄ fluxes may be higher towards this eastern end. Despite the differences and similarities in flux distribution between models and mass balance, it should be noted that the model outputs presented here are July averages over period of 17 years. It is therefore highly probable that wetland distribution in this area has changed over this time period, and good agreement between model flux distribution and mass balance flux distribution is not necessarily expected due to this.

Figure 7 shows bar plots of the CH₄ flux from the diagnostic and prognostic process models along with the mean mass balance fluxes from the three distinct flux areas identified in table 1. Most of the diagnostic and prognostic models report significantly lower CH₄ fluxes for all three study areas compared to the mass balance results. In general, the prognostic models report higher CH₄ fluxes for all three areas than the diagnostic models, most notably with the ORCHIDEE diagnostic model where fluxes for Areas 1 and 2 ($1.32 \pm 0.47 \text{ mg m}^{-2} \text{ h}^{-1}$ and $1.29 \pm 0.54 \text{ mg m}^{-2} \text{ h}^{-1}$, respectively) agree well within overlapping uncertainty with the mass balance fluxes for Areas 1 and 2. Despite the general disagreement between modelled and mass balance CH₄ fluxes in this case, it is worth noting that the mass balance results represent a single temporal snapshot from a single daytime flux from July 2019, whereas the model outputs are July monthly averages from 2000 to 2017. A likely source of disagreement between mass balance and process modelling in this case is that the mass balance may not be truly representative of the monthly average model output over multiple years. Having said this, an average air temperature of 12.2°C was measured on 31 July 2019 from the Sodankylä Lokka weather station during the time of the flight, which was slightly lower than the July mean temperature between 2000 and 2017 for the same weather station ($14.5 \pm 1.6^\circ\text{C}$). In addition, the average precipitation for July 2019 (33.4 mm) was also significantly lower than the July average precipitation between 2000 and 2017 ($77.4 \pm 28.2 \text{ mm}$) [51]. Lower temperature and precipitation for July 2019 suggest that the mass balance CH₄ fluxes reported in this work may actually be lower than previous years, yet many of the GCP process models report significantly lower fluxes for the years previous to this study.

In summary, the land-surface models assessed here generally provide a lower estimate of wetland CH₄ flux than top-down aircraft mass balance techniques for the study area of northern Sweden and Finland. However, the mass balance flux was measured during the daytime whereas the July average model outputs are comprised 24 h flux outputs. Wetland fluxes in the Arctic are known to exhibit a diurnal cycle with daytime flux maxima and night-time minima [52]; the inclusion of nocturnal low flux periods within the model outputs may partially account for the lower estimates of CH₄ flux compared to mass balance. In addition to this, the GCP models only account for CH₄ emission from areas classified as wetlands and do not account for lake, riverine or other biogenic CH₄ sources. Mass balance will capture the flux footprint from all sources in the study area, not solely wetland. Therefore this could also account for the higher mass balance

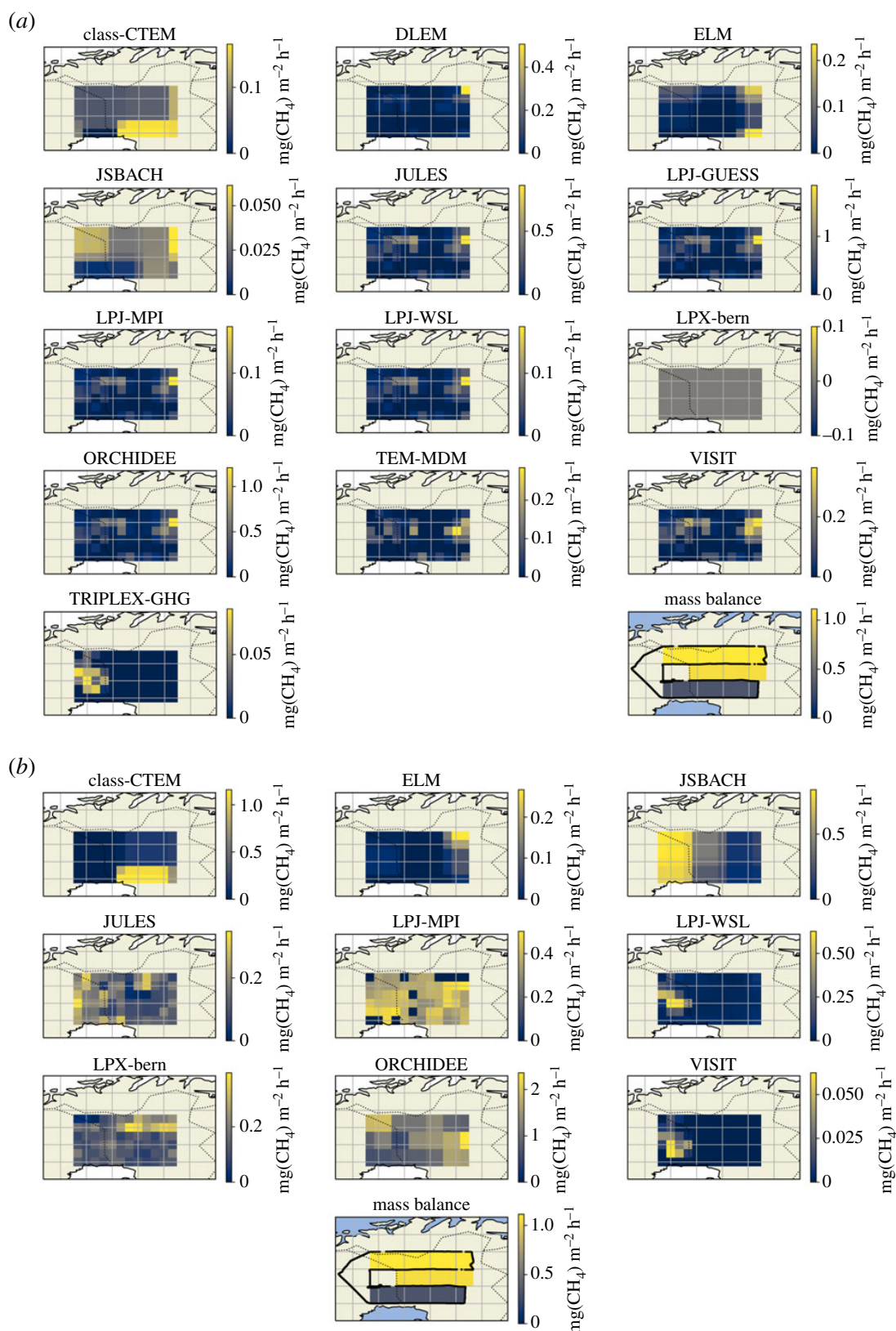


Figure 6. Maps of modelled CH_4 flux in $\text{mg m}^{-2} \text{h}^{-1}$ for the study area of flight C195 from various land-surface process models; (a) shows model outputs that have used the diagnostic WAD2M remote-sensing product to prescribe wetland cover and dynamics, (b) shows models that have used prognostic wetland cover information determined by the models themselves. The model data are obtained from the supplementary data of Saunois *et al.* [9]. Maps of the aircraft mass balance flux results are also shown in figure 6a,b. (Online version in colour.)

flux estimate relative to the model outputs, although isotopic analysis (electronic supplementary material, figure S4) suggests arctic peatlands are the primary CH_4 source. Despite the previous points, there is still significant disagreement between individual model estimates of CH_4 flux

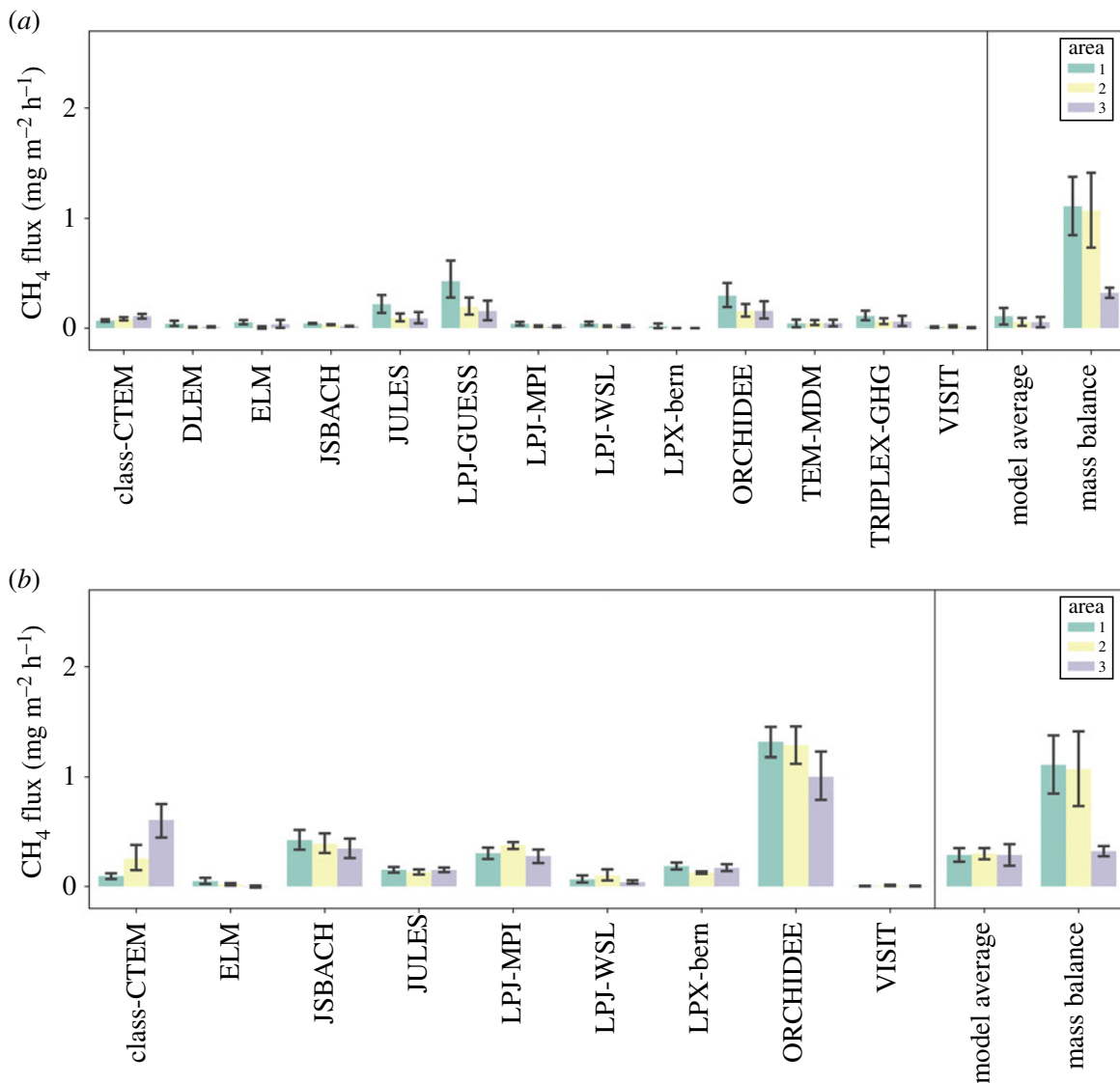


Figure 7. Bar plots of CH₄ flux (in units of mg m⁻² h⁻¹) coloured by the three distinct flux areas of flight C195 from various land-surface process models and the aircraft mass balance results. Error bars indicate 1-σ standard deviations for the fluxes; (a) shows models with the diagnostic WAD2M wetland prescription and (b) shows models with the prognostic wetland cover information determined within the models. The model data are obtained from the supplementary data of Saunois *et al.* [9]. (Online version in colour.)

magnitude and distribution, and the models likely estimate lower CH₄ flux even when taking the previous points into account. In order to provide model fluxes that are both more precise and more accurate, improvements in model inputs that more successfully estimate CH₄ flux in comparison to *in situ* measurements, as well as standardized, accurate estimates of wetland cover and dynamics, are clearly both required. More frequent observational flux measurements are also ideally needed to provide important intercomparison and evaluation for model techniques. Put simply, the GCP models disagree markedly with one another, and with the measurements reported here for the region studied. It is imperative that this is addressed as a priority in order to more meaningfully use GCP models for Arctic carbon emissions, especially given the Arctic's rapidly changing climate.

4. Summary and Conclusion

A single research flight was carried out by the UK FAAM ARA across a wide area of northern European mixed peatland and forest. A peak wetland area-normalized flux of

$5.93 \pm 0.72 \text{ mg m}^{-2} \text{ h}^{-1}$ was obtained for CH_4 , and a peak total land area-normalized flux of $-513 \pm 74 \text{ mg m}^{-2} \text{ h}^{-1}$ was obtained for CO_2 using the aircraft mass balance flux method for this area of northern Sweden and Finland (approximately $78\,000 \text{ km}^2$). The bulk CH_4 fluxes determined via mass balance were found to agree well with upscaled chamber fluxes for the same study area. These results indicate that the wetlands in this area are a significant net source of CH_4 , and the area also represents a notable biospheric CO_2 sink. A clear gradient of decreasing CH_4 flux was identified between the northern and southern end of the flight track, which appears to correlate with decreasing peat bog land cover percentage from north to south. The mass balance fluxes were also compared with a variety of GCP land-surface process model fluxes, the majority of which were found to significantly underestimate CH_4 emission in this area when compared to the mass balance. The results from this study provide an important wetland trace gas emission dataset that will aid validation of global land-surface models and will help further constrain the contribution of Arctic wetland and vegetation to global CH_4 and CO_2 budgets. Furthermore, the results highlight the sensitivity of bottom-up process models to accurate wetland cover and dynamics estimations and other input parameters when quantifying flux using these methods. This study also highlights an urgent need to improve land-surface models by using high-accuracy observational wetland cover datasets as model inputs, and by continuing *in situ* measurements as a means to evaluate the performance of these models. Continued improvements to land-surface models will allow them to more accurately predict summer CH_4 emissions in the Arctic.

Data accessibility. **Aircraft data:** FAAM ARA data from the MOYA project can be found on the CEDA archive (<http://archive.ceda.ac.uk/>) at <https://catalogue.ceda.ac.uk/uuid/d309a5ab60b04b6c82eca6d006350ae6> (FAAM, NERC, Met Office. 2017).

Basemap data: The basemap used in figure 4 is obtained from ArcGIS software (Sources: Esri, HERE, Garmin, Intermap, Increment P Corp., GEBCO, USGS, FAO, NPS, NRCAN, GeoBase, IGN, Kadaster NL, Ordnance Survey, Esri Japan, METI, Esri China (Hong Kong). © OpenStreetMap contributors and the GIS User Community). The maps used in figures 1, 3, 6 and electronic supplementary material, figure S1 are produced using the Python Cartopy package, where maps are obtained from Natural Earth. Free vector and raster map data @ naturalearthdata.com.

Land cover data: The land cover maps used are obtained from the Copernicus Land Monitoring Service 2018 CORINE land cover dataset © European Union, Copernicus Land Monitoring Service 2021, European Environment Agency (EEA), f.ex. in 2018: © European Union, Copernicus Land Monitoring Service 2018, European Environment Agency (EEA).

Model data: The GCP model data used in this work and first reported by Saunio *et al.* [9] are obtained from the Integrated Carbon Observation System (ICOS) website (<https://www.icos-cp.eu/GCP-CH4/2019>, doi:10.18160/gcp-ch4-2019).

Meteorological data: Met data from the Sodankylä Lokka weather station were obtained from the Finnish Meteorological Institute (FMI) website (<https://en.ilmatieteenlaitos.fi/download-observations>)

The data are provided in the electronic supplementary material [53].

Authors' contributions. P.A.B. was the lead author, with writing contributions from G.A., R.F. and J.R.P. The flight methodology was devised by G.A., E.G.N., J.D.L. and K.N.B. The paper methodology was designed by P.A.B. and G.A. Measurements aboard the aircraft were taken by P.A.B., J.R.P., R.E.F., J.F., S.J.B.B., D.P. and S.C. Data curation and validation was undertaken by P.A.B., J.R.P., R.E.F., S.J.B.B., D.P. and S.C. Formal data analysis was carried out by P.A.B., with contributions from J.F. and R.E.F. Review of the draft manuscript was undertaken by all co-authors. Funding was acquired by E.G.N., G.A. and J.D.L.

Competing interests. We declare we have no competing interests.

Funding. The data used in this publication have been collected as part of the MOYA project funded by the Natural Environment Research Council (NERC) (The Global Methane Budget, University of Manchester reference no. NE/N015835/1 Royal Holloway, University of London reference no. NE/N016211/1). P.A.B. is in receipt of a PhD studentship as part of the NERC Earth, Atmosphere and Ocean Doctoral Training Partnership (EAO DTP) (NERC grant reference no. NE/L002469/1)

Acknowledgements. Airborne data was obtained using the BAe-146-301 Atmospheric Research Aircraft (ARA) flown by Airtask Ltd and managed by FAAM Airborne Laboratory, jointly operated by UK Research and Innovation (UKRI) and the University of Leeds. We would like to give special thanks to the Airtask pilots and engineers and all staff at FAAM Airborne Laboratory for their hard work in helping plan and execute successful MOYA-Arctic project flights. We acknowledge the use of various land-surface models compiled as

References

1. NOAA/GML. See www.esrl.noaa.gov/gmd/ccgg/trends/ (accessed 5 May 2021).
2. Dlugokencky EJ, Houweling S, Bruhwiler L, Masarie KA, Lang PM, Miller JB, Tans PP. 2003 Atmospheric methane levels off: temporary pause or a new steady-state? *Geophys. Res. Lett.* **30**. (doi:10.1029/2003GL018126)
3. Nisbet EG *et al.* 2016 Rising atmospheric methane: 2007–2014 growth and isotopic shift. *Glob. Biogeochem. Cycles* **30**, 1356–1370. (doi:10.1002/2016GB005406)
4. Nisbet EG *et al.* 2019 Very strong atmospheric methane growth in the 4 years 2014–2017: implications for the Paris agreement. *Glob. Biogeochem. Cycles* **33**, 318–342. (doi:10.1029/2018GB006009)
5. Schwietzke S *et al.* 2016 Upward revision of global fossil fuel methane emissions based on isotope database. *Nature* **538**, 88–91. (doi:10.1038/nature19797)
6. Cao M, Gregson K, Marshall S. 1998 Global methane emission from wetlands and its sensitivity to climate change. *Atmos. Environ.* **32**, 3293–3299. (doi:10.1016/S1352-2310(98)00105-8)
7. Melton JR *et al.* 2013 Present state of global wetland extent and wetland methane modelling: conclusions from a model inter-comparison project (WETCHIMP). *Biogeosciences* **10**, 753–788. (doi:10.5194/bg-10-753-2013)
8. Olefeldt D, Turetsky MR, Crill PM, McGuire AD. 2013 Environmental and physical controls on northern terrestrial methane emissions across permafrost zones. *Glob. Chang. Biol.* **19**, 589–603. (doi:10.1111/gcb.12071)
9. Saunois M *et al.* 2020 The global methane budget 2000–2017. *Earth Syst. Sci. Data* **12**, 1561–1623. (doi:10.5194/essd-12-1561-2020)
10. Bridgman SD, Cadillo-Quiroz H, Keller JK, Zhuang Q. 2013 Methane emissions from wetlands: biogeochemical, microbial, and modeling perspectives from local to global scales. *Glob. Chang. Biol.* **19**, 1325–1346. (doi:10.1111/gcb.12131)
11. Kirschke S *et al.* 2013 Three decades of global methane sources and sinks. *Nat. Geosci.* **6**, 813–823. (doi:10.1038/ngeo1955)
12. Tian H *et al.* 2016 The terrestrial biosphere as a net source of greenhouse gases to the atmosphere. *Nature* **531**, 225–228. (doi:10.1038/nature16946)
13. Topp E, Pattey E. 1997 Soils as sources and sinks for atmospheric methane. *Can. J. Soil Sci.* **77**, 167–177. (doi:10.4141/s96-107)
14. Raich JW, Potter CS. 1995 Global patterns of carbon dioxide emissions from soils. *Glob. Biogeochem. Cycles* **9**, 23–36. (doi:10.1029/94GB02723)
15. Bruhwiler L, Parmentier FJW, Crill P, Leonard M, Palmer PI. 2021 The Arctic carbon cycle and its response to changing climate. *Curr. Clim. Chang. Rep.* **7**, 14–34. (doi:10.1007/s40641-020-00169-5)
16. Le Quéré C *et al.* 2018 Global carbon budget 2018. *Earth Syst. Sci. Data* **10**, 2141–2194. (doi:10.5194/essd-10-2141-2018)
17. Coffey MM, Hestir EL. 2019 Variability in trends and indicators of CO₂ exchange across Arctic wetlands. *J. Geophys. Res. Biogeosci.* **124**, 1248–1264. (doi:10.1029/2018JG004775)
18. McFadden JP, Eugster W, Chapin FS. 2003 A regional study of the controls on water vapor and CO₂ exchange in arctic tundra. *Ecology* **84**, 2762–2776. (doi:10.1890/01-0444)
19. Petrescu AMR, Van Beek LPH, Van Huissteden J, Prigent C, Sachs T, Corradi CAR, Parmentier FJW, Dolman AJ. 2010 Modeling regional to global CH₄ emissions of boreal and arctic wetlands. *Glob. Biogeochem. Cycles* **24**. (doi:10.1029/2009GB003610)
20. Ito A. 2019 Methane emission from pan-Arctic natural wetlands estimated using a process-based model, 1901–2016. *Polar Sci.* **21**, 26–36. (doi:10.1016/j.polar.2018.12.001)
21. Cohen J *et al.* 2014 Recent Arctic amplification and extreme mid-latitude weather. *Nat. Geosci.* **7**, 627–637. (doi:10.1038/ngeo2234)
22. Overland JE, Wang M, Walsh JE, Stroeve JC. 2014 Future Arctic climate changes: adaptation and mitigation time scales. *Earth's Futur.* **2**, 68–74. (doi:10.1002/2013ef000162)

23. Yvon-Durocher G, Allen AP, Bastviken D, Conrad R, Gudas C, St-Pierre A, Thanh-Duc N, Del Giorgio PA. 2014 Methane fluxes show consistent temperature dependence across microbial to ecosystem scales. *Nature* **507**, 488–491. (doi:10.1038/nature13164)
24. Christensen TR, Friborg T, Sommerkorn M, Kaplan J, Illeris L, Soegaard H, Nordstroem C, Jonasson S. 2000 Trace gas exchange in a high-arctic valley 1. Variations in CO₂ and CH₄ flux between tundra vegetation types. *Glob. Biogeochem. Cycles* **14**, 701–713. (doi:10.1029/1999GB001134)
25. Tarnocai C, Canadell JG, Schuur EAG, Kuhry P, Mazhitova G, Zimov S. 2009 Soil organic carbon pools in the northern circumpolar permafrost region. *Glob. Biogeochem. Cycles* **23**. (doi:10.1029/2008GB003327)
26. Hugelius G *et al.* 2014 Estimated stocks of circumpolar permafrost carbon with quantified uncertainty ranges and identified data gaps. *Biogeosciences* **11**, 6573–6593. (doi:10.5194/bg-11-6573-2014)
27. Zhang Z, Zimmermann NE, Stenke A, Li X, Hodson EL, Zhu G, Huang C, Poulter B. 2017 Emerging role of wetland methane emissions in driving 21st century climate change. *Proc. Natl Acad. Sci. USA* **114**, 9647–9652. (doi:10.1073/pnas.1618765114)
28. Zhang Y, Sachs T, Li C, Boike J. 2012 Upscaling methane fluxes from closed chambers to eddy covariance based on a permafrost biogeochemistry integrated model. *Glob. Chang. Biol.* **18**, 1428–1440. (doi:10.1111/j.1365-2486.2011.02587.x)
29. Peltola O *et al.* 2019 Monthly gridded data product of northern wetland methane emissions based on upscaling eddy covariance observations. *Earth Syst. Sci. Data* **11**, 1263–1289. (doi:10.5194/essd-2019-28)
30. Peischl J *et al.* 2012 Airborne observations of methane emissions from rice cultivation in the Sacramento Valley of California. *J. Geophys. Res. Atmos.* **117**. (doi:10.1029/2012JD017994)
31. Miller JB, Gatti LV, d'Amelio MTS, Crotwell AM, Dlugokencky EJ, Bakwin P, Artaxo P, Tans PP. 2007 Airborne measurements indicate large methane emissions from the eastern Amazon basin. *Geophys. Res. Lett.* **34**. (doi:10.1029/2006GL029213)
32. Beck V *et al.* 2012 Methane airborne measurements and comparison to global models during BARCA. *J. Geophys. Res. Atmos.* **115**. (doi:10.1029/2011JD017345)
33. O'Shea SJ *et al.* 2014 Methane and carbon dioxide fluxes and their regional scalability for the European Arctic wetlands during the MAMM project in summer 2012. *Atmos. Chem. Phys.* **14**, 13 159–13 174. (doi:10.5194/acp-14-13159-2014)
34. Barker PA *et al.* 2020 Airborne measurements of fire emission factors for African biomass burning sampled during the MOYA campaign. *Atmos. Chem. Phys.* **20**, 15 443–15 459. (doi:10.5194/acp-20-15443-2020)
35. Petersen GN, Renfrew IA. 2009 Aircraft-based observations of air-sea fluxes over Denmark Strait and the Irminger sea during high wind speed conditions. *Q. J. R. Meteorol. Soc.* **135**, 2030–2045. (doi:10.1002/qj.355)
36. O'Shea S, Bauguitte S, Gallagher M, Lowry D, Percival C. 2013 Development of a cavity-enhanced absorption spectrometer for airborne measurements of CH₄ and CO₂. *Atmos. Meas. Tech.* **6**, 1095–1109. (doi:10.5194/amt-6-1095-2013)
37. Pitt JR *et al.* 2016 The development and evaluation of airborne in situ N₂O and CH₄ sampling using a quantum cascade laser absorption spectrometer (QCLAS). *Atmos. Meas. Tech.* **9**, 63–77. (doi:10.5194/amt-9-63-2016)
38. Cambaliza MOL *et al.* 2015 Quantification and source apportionment of the methane emission flux from the city of Indianapolis. *Elementa* **3**. (doi:10.12952/journal.elementa.000037)
39. Heimbürger AMF *et al.* 2017 Assessing the optimized precision of the aircraft mass balance method for measurement of urban greenhouse gas emission rates through averaging. *Elementa* **5**. (doi:10.1525/elementa.134)
40. Pitt JR, Allen G, Bauguitte SJB, Gallagher MW, Lee JD, Drysdale W, Nelson B, Manning AJ, Palmer PI. 2019 Assessing London CO₂, CH₄ and CO emissions using aircraft measurements and dispersion modelling. *Atmos. Chem. Phys.* **19**, 8931–8945. (doi:10.5194/acp-19-8931-2019)
41. Lavoie TN *et al.* 2015 Aircraft-based measurements of point source methane emissions in the Barnett Shale Basin. *Environ. Sci. Technol.* **49**, 7904–7913. (doi:10.1021/acs.est.5b00410)
42. Hajny KD *et al.* 2019 Observations of methane emissions from natural gas-fired power plants. *Environ. Sci. Technol.* **53**, 8976–8984. (doi:10.1021/acs.est.9b01875)

43. France JL *et al.* 2021 Facility level measurement of offshore oil and gas installations from a medium-sized airborne platform: method development for quantification and source identification of methane emissions. *Atmos. Meas. Tech.* **14**, 71–88. (doi:10.5194/amt-14-71-2021)
44. Chou WW, Wofsy SC, Harriss RC, Lin JC, Gerbig C, Sachse GW. 2002 Net fluxes of CO₂ in Amazonia derived from aircraft observations. *J. Geophys. Res. Atmos.* **107**. (doi:10.1029/2001JD001295)
45. Vaughan AR *et al.* 2016 Spatially resolved flux measurements of NO_x from London suggest significantly higher emissions than predicted by inventories. *Faraday Discuss.* **189**, 455–472. (doi:10.1039/c5fd00170f)
46. Baldocchi D, Valentini R, Running S, Oechel W, Dahlman R. 1996 Strategies for measuring and modelling carbon dioxide and water vapour fluxes over terrestrial ecosystems. *Glob. Chang. Biol.* **2**, 159–168. (doi:10.1111/j.1365-2486.1996.tb00069.x)
47. Finnish Meteorological Institute 2021 Climate Statistics. See <https://en.ilmatieteenlaitos.fi/statistics-from-1961-onwards> (accessed 20 July 2021).
48. Paudel R, Mahowald NM, Hess PGM, Meng L, Riley WJ. 2016 Attribution of changes in global wetland methane emissions from pre-industrial to present using CLM4.5-BGC. *Environ. Res. Lett.* **11**, 034020. (doi:10.1088/1748-9326/11/3/034020)
49. Bonan GB, Doney SC. 2018 Climate, ecosystems, and planetary futures: the challenge to predict life in Earth system models. *Science* **259**. (doi:10.1126/science.aam8328)
50. Schroeder R, McDonald KC, Chapman BD, Jensen K, Podest E, Tessler ZD, Bohn TJ, Zimmermann R. 2015 Development and evaluation of a multi-year fractional surface water data set derived from active/passive microwave remote sensing data. *Remote Sens.* **7**, 16 688–16 732. (doi:10.3390/rs71215843)
51. Finnish Meteorological Institute 2021 Data Download. See <https://en.ilmatieteenlaitos.fi/download-observations> (accessed 22 July 2021).
52. Sriskantharajah S *et al.* 2012 Stable carbon isotope signatures of methane from a Finnish subarctic wetland. *Tellus Ser. B Chem. Phys. Meteorol.* **64**, 18818. (doi:10.3402/tellusb.v64i0.18818)
53. Barker PA *et al.* 2021 Data from: airborne quantification of net methane and carbon dioxide fluxes from European Arctic wetlands in Summer 2019. Figshare.

Chapter 5

Manuscript 3: Measurement of recreational N₂O emissions from an urban environment in Manchester, UK

Barker, P. A., Allen, G., Flynn, M., Riddick, S. & Pitt, J. R.: Measurement of recreational N₂O emissions from an urban environment in Manchester, UK. *Urban Clim.* 46, 101282, doi:10.1016/j.uclim.2022.101282, 2022.

The following chapter has been published in the journal *Urban Climate*. P. A. Barker designed the study, operated and calibrated the N₂O instrumentation, and also collated the N₂O data with other measurements taken at the Manchester air quality supersite. P. A. Barker carried out all data analysis, including spatial and temporal mole fraction analysis, and wrote the manuscript from first draft to final submitted draft. G. Allen provided supervision to P. A. Barker, and assisted in the manuscript design. S. Riddick contributed towards writing of parts of the introduction section. M. Flynn calibrated and maintained all instrumentation at the Manchester air quality supersite with the exception of the N₂O instrument. All co-authors provided commentary on draft versions of the manuscript.

N₂O flux calculations were attempted using dispersion modelling software, however these are not included in the final accepted manuscript, or in supplementary materials published alongside the manuscript. Details of these flux calculations are provided in Appendix A.3.



Measurement of recreational N₂O emissions from an urban environment in Manchester, UK

Patrick A. Barker^{a,*}, Grant Allen^a, Michael Flynn^a, Stuart Riddick^b, Joseph R. Pitt^c

^a School of Earth and Environmental Sciences, University of Manchester, Manchester M13 9PL, UK

^b The Energy Institute, Colorado State University, 430 N. College Avenue, Fort Collins, CO 80523, USA

^c School of Chemistry, University of Bristol, Cantock's Close, Bristol BS8 1TS, UK

ARTICLE INFO

Keywords:

Nitrous oxide
Greenhouse gas
Recreational N₂O
UK

ABSTRACT

Nitrous oxide (N₂O) is a potent greenhouse gas that is currently the third largest contributor to anthropogenic radiative forcing. It is also a strong ozone depleting substance. Given this importance, mitigation of N₂O emissions remains important and sources must be understood in greater detail. In this study, in situ measurements of N₂O alongside a variety of other trace gases and aerosols were made from a ground-based air quality observation site in an urban environment of Fallowfield, Manchester, United Kingdom over a period of 12 months between October 2020 and October 2021. N₂O mole fraction was observed to be poorly correlated with other atmospheric pollutant tracers during the measurement period, with little evidence of co-enhancement (and therefore common source relationships) between N₂O and other local pollutant trace gases and aerosol. Large N₂O enhancements (> 400 ppb above background) over short time scales (< 2 min) were seen with no co-enhancement of other trace gases and aerosol concentrations, suggesting discrete N₂O sources in the near vicinity of the measurement site. Measured N₂O concentrations showed a consistent temporal pattern over day, week, and year timescales with consistently large weekend enhancements observed between the hours of 18:00 and 02:00 local time, suggesting the source of N₂O may be associated with night-time recreational use by nearby residents. These weekend-night-time temporal patterns were not correlated with other trace gases measured at the same location. Analysis of the air transport history of N₂O measurements showed high mean nocturnal mole fractions originating from the west and south-west of the observation site, suggesting that emissions may have originated from nearby areas of student accommodation and dense areas of private housing to the west. This study finds evidence for a detectable recreational N₂O source that appears to be dominant over other potential N₂O sources for the area studied. Further study is needed to quantify the local and national emission rates of this potentially increasing atmospheric pollution source, and to compare the magnitude of this source to other locations within the UK. The study demonstrates an important need to assess and validate National Atmospheric Emission Inventory (NAEI) estimates for recreational N₂O emissions.

1. Introduction

Nitrous oxide (N₂O) is a potent greenhouse gas with a global warming potential 298 times that of carbon dioxide, and the third most

* Corresponding author at: National Physical Laboratory, Hampton Road, Teddington, Middlesex TW11 0LW, UK.

E-mail address: pat.barker@npl.co.uk (P.A. Barker).

important greenhouse gas in terms of contribution to anthropogenic climate change (IPCC, 2013). In addition, N₂O is the dominant stratospheric ozone depleting substance emitted in the 21st Century (Ravishankara et al., 2009). N₂O persists in the atmosphere for 114 ± 9 years (Prather et al., 2015), meaning that the impact of current emissions on climate and ozone will persist for many years to come. Mitigation of N₂O emissions can therefore benefit both climate impact and stratospheric ozone depletion. The global average mole fraction of N₂O in the troposphere has increased from a pre-industrial level of ~ 270 ppb to a current abundance of 334 ppb as of July 2021 (NOAA, 2021). Atmospheric growth of N₂O mole fraction persists at an estimated rate of 2% per decade, with post-industrial growth understood to be driven by anthropogenic activity, most significantly from the widespread use of fertilisers in agriculture (Tian et al., 2020).

Gaseous N₂O is frequently used as an anaesthetic during childbirth and in dentistry. However, it has also been used as a recreational substance throughout history due to its euphoria-inducing side effects (Zuck et al., 2012), with dangerous (and sometimes deadly) health implications (Randhawa and Bodenham, 2016). N₂O gas is typically inhaled when used recreationally from balloons filled from pressurised stainless-steel canisters designed for use in the food industry (shown in Fig. 1). Recreational use of N₂O in the UK is widespread (Ehirim et al., 2018; UK Home Office, 2018) and increasing (Randhawa and Bodenham, 2016). An estimated 7.6% of 16 to 24-year-olds in the UK reported recreational N₂O use in 2014 (Randhawa and Bodenham, 2016), which increased to 8.8% in 2018 (UK Home Office, 2018). Even though the physical risks, including dizziness, asphyxiation, and vitamin B12 deficiency, and environmental concerns regarding the casual disposal (littering) of the stainless-steel canisters have been reported, there is little public awareness of the additional environmental threat of N₂O emissions as a greenhouse gas or ozone-depleting substance. As there is no metabolism of N₂O in the body (Banks and Hardman, 2005), N₂O breathed in is exhaled to the atmosphere. The UK National Atmospheric Emission Inventory (NAEI) estimates an emission of 13 t of N₂O via recreational use in 2019, representing $\sim 0.02\%$ of the total UK N₂O budget for 2019 (75 Kt) (NAEI/BEIS, 2022). Despite the relatively small estimated contribution of recreational N₂O to the total source, there has been no measurement work to validate the NAEI estimate for recreational N₂O. In situ measurement studies of this source are therefore crucial for assessing the accuracy of inventory-reported recreational N₂O emissions.

There has hitherto been little research on N₂O emission sources from urban areas, and no known measurement-led study of detectable emissions from recreational use. Many studies have focused on soil N₂O emission from fertilised urban lawns and turf grasses (Townsend-Small and Czimczik, 2010; Van Delden et al., 2016), or riverine N₂O emissions from sewage input into urban river systems or from sewage treatment plants (Tallec et al., 2008; De Mello et al., 2013; Yu et al., 2013). Eddy covariance flux measurements of N₂O were reported for an urban environment in Edinburgh, UK by Famulari et al. (2010), in which a mean net flux of $91 \text{ ng m}^{-2} \text{ s}^{-1}$ was measured, and a diurnal pattern indicated traffic N₂O emissions were a major source. A similar eddy covariance study was carried out in an urban area of Helsinki, Finland by Järvi et al. (2014), where a median N₂O flux of $21 \text{ ng m}^{-2} \text{ s}^{-1}$ was measured. Significant fluxes were measured from traffic and from urban green areas, but the urban soils appeared to be the largest N₂O emission sources in the Järvi et al. (2014) study. In summary, there are limited examples of urban N₂O emission studies where direct fluxes have been derived, and there has yet to be any in situ measurement studies investigating the presence and extent of N₂O emission from recreational sources.

This paper presents results from continuous in situ N₂O mole fraction measurements from a ground-based observation site in an urban environment. Measurements were made over a period of 12 months between October 2020 and October 2021 from an air quality measurement site in Fallowfield, Manchester operated by the University of Manchester. In the following sections, a statistical climatology of the measurements over the year-long period is described in conjunction with spatial and temporal trends, where N₂O mole fractions demonstrate weak correlations with other atmospheric pollutant tracers that would otherwise suggest co-emission from sources other than recreational use. Finally, the presence of a potential recreational source in the vicinity of the site based on diurnal mole fraction variability and weekend overnight maxima are discussed.



Fig. 1. Photograph of discarded nitrous oxide whipped cream charger canisters in Manchester, UK. Nitrous oxide from these canisters is used to fill balloons, from which the gas is then inhaled for short-term euphoric effect.

2. Materials and methods

2.1. Site description

Measurements of typical urban pollutant trace gases, aerosols, and meteorological parameters (see Table 1) were made at the Manchester Air Quality Supersite (MAQS) (53° 26′ 39.20″N, 2° 12′ 52.20″W) situated in the University of Manchester Fallowfield campus, approximately four kilometres south of Manchester city centre. Fig. 2 shows the location of the MAQS and the surrounding Fallowfield area. Two single-carriage British A-class roads pass along the south and west of the measurement site, with a high density of shops, bars and restaurants situated to the southwest. Student accommodation buildings surround the site from the south to north-east in a clockwise direction. Three car parks are also situated to the north, east, and south-east of the measurement site.

2.2. Instrumentation

The MAQS is comprised of a stack of four shipping containers housing an array of in situ trace gas and aerosol instrumentation, a picture of the MAQS site is shown in Fig. 3. All enclosures are mains-powered and air-conditioned. Inlets for all instruments and meteorological instrumentation are situated on the top of the shipping container stack at a height of 7 m above ground level. Continuous measurement of N₂O mole fraction started at 13:30 UTC on 28 October 2020 and remains ongoing at the time of writing (reported up to 19 October 2021 in this study). Concurrent measurements of CH₄, CO₂, CO, O₃, NO, NO₂, PM_{2.5}, PM₁₀, and meteorological parameters were recorded throughout the same period. All data were averaged to a 1-minute sampling frequency for analysis in this work. The parameters used in this work, along with their instruments, operational ranges and precisions, and sampling frequencies are displayed in Table 1.

N₂O dry-air mole fractions were measured using an Aerodyne Quantum Cascade Laser Absorption Spectrum (QCLAS), described by Pitt et al. (2016). The QCLAS instrument uses a single thermoelectrically cooled quantum cascade laser tuned to a wavelength of ~4.5 μm and calibrated using three calibration gas standards, all of which are traceable to the World Meteorological Organisation (WMO) X2006A calibration scale for N₂O. A 1σ precision of 0.3 ppb was calculated for 1 Hz N₂O mole fraction measurements during the measurement period. Mole fractions of CH₄ and CO₂ were measured using a Los Gatos Research (LGR) Multi-gas Carbon Emissions Analyser, which utilises the off-axis Integrated Cavity Output Spectroscopy (OA-ICOS) technique. The LGR instrument had a precision of 0.3 ppm for CO₂ and 2 ppb for 1 Hz CH₄ measurements. Mole fractions of CO were measured with a Thermo Scientific Model 48i Infrared CO Analyser, with an uncertainty of 0.1 ppb at 20 s sampling frequency. Mole fractions of NO were measured using a Thermo Scientific Model 42i-y Chemiluminescence NO_y Analyser, which has an uncertainty of 0.4 ppb at 20 s sampling rate. NO₂ was measured using a Teledyne API T500U Cavity Attenuated Phase Shift (CAPS) Analyser, with an uncertainty of 10% at 10 s measurement frequency. Particulate matter (PM_{2.5} and PM₁₀) concentrations in μg m⁻³ were measured at 1 min sampling frequency using a Palas Fidas 200 S Aerosol Spectrometer, with a < 10% uncertainty on these measurements. Measurements of wind speed and direction were acquired using a Gill Windmaster Sonic Anemometer, with a precision of 0.01 m s⁻¹ for wind speed and 0.1° for wind direction.

3. Results and discussion

This section will discuss the spatial and temporal trends in N₂O and other trace-gas concentrations over the 12-month measurement period to assess source behaviour and location. Section 3 will first discuss the correlation of N₂O mole fraction with other atmospheric tracers to understand potential sources of co-emission. Following this, the temporal variability of N₂O and other trace gases over an average day, week, and over the course of the year will be discussed to determine likely source behaviour based on temporal enhancement patterns. In addition to temporal analysis, qualitative spatial analysis of trace gas variability with wind speed and direction will also be described, including a brief overview of the climatology during the measurement period followed by an analysis of trace gas enhancement as with wind direction.

Table 1
Trace gases, aerosols, and meteorological parameters measured at the MAQS that feature in this work, the instruments models, instrumental ranges and precisions, and measurement frequencies are also shown.

Species/Parameter	Instrument	Range and Precision	Sampling Frequency
Ozone (O ₃)	Thermo 49i	0.5 ppb – 200 ppm, 1 ppb	20 s
Nitric Oxide (NO)	Thermo 42i-y	50 ppt – 1000 ppb, 0.4 ppb	20 s
Nitrogen Dioxide (NO ₂)	Teledyne API T500U (CAPS)	40 ppt – 1000 ppb, 0.5%	10 s
Carbon Monoxide (CO)	Thermo 48i	0.04–10,000 ppm, 0.1 ppm	20 s
Carbon Dioxide (CO ₂)	LGR Multi-gas Carbon Emissions Analyser	0.1–3000 ppm, 0.3 ppm	1 s
Methane (CH ₄)	LGR Multi-gas Carbon Emissions Analyser	0.3 ppb – 100 ppm, 2 ppb	1 s
Nitrous Oxide (N ₂ O)	Aerodyne QCLAS	Precision: 0.58 ppb	1 s
Particulate Matter (PM _{2.5} , PM ₁₀)	Palas FIDAS200	0–10,000 μg m ⁻³ , < 10%	1 min
Wind Speed and Direction	Gill Windmaster Sonic Anemometer	0–50 m s ⁻¹ , 0.01 m s ⁻¹ 0–359°, 0.1°	20 Hz
Temperature and Pressure		T: –40 - +60 °C P: 500–1100 hPa	1 min

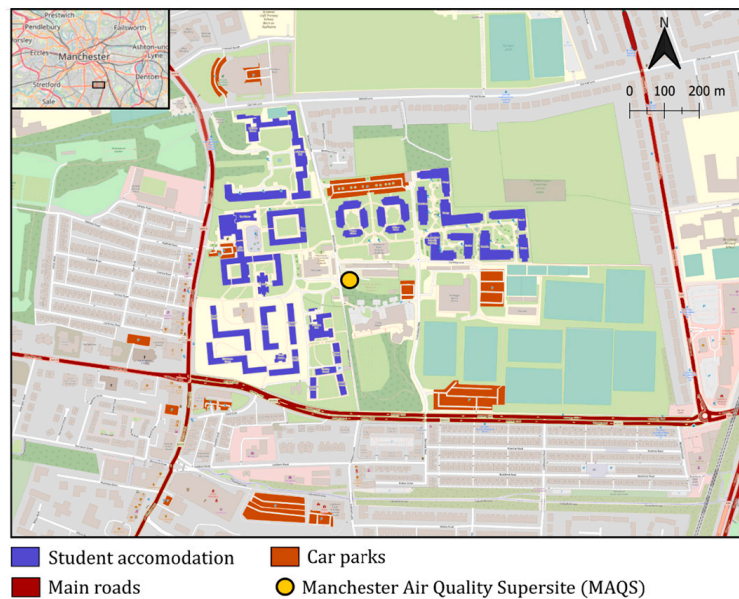


Fig. 2. Map of the area surrounding the MAQS (shown as a yellow circle). Student accommodation buildings are highlighted in blue, main roads are shown in red, and car parking areas are shown in orange. (For interpretation of the references to colour in this figure legend, the reader is referred to the web version of this article.)



Fig. 3. Photograph of the MAQS. Trace gas and aerosol instruments are enclosed within the shipping containers. Instrument inlets, pressure and temperature sensors, and the sonic anemometer are situated on top of the container stack.

3.1. N_2O -tracer relationships

Fig. 4 shows a time series of measured pollutant trace gas and aerosol concentrations across the measurement period. Small gaps in the N_2O dataset (e.g. early Jan 2021) were due to unscheduled power losses and technical issues. Fig. 4 shows evidence of co-emission between some of the trace gases measured at the site, most notably CH_4 , CO_2 , CO , NO_x and, to some extent, particulate matter. Emission of these species and the correlation between them is expected to be associated with vehicles from nearby roads (Ketzel et al., 2003), whereas the large enhancements in particulate matter accompanied by more modest enhancements in NO_x , CO , and greenhouse gases are likely the result of biomass burning (Andreae, 2019). Of particular note is the potential relationship with the use of fireworks

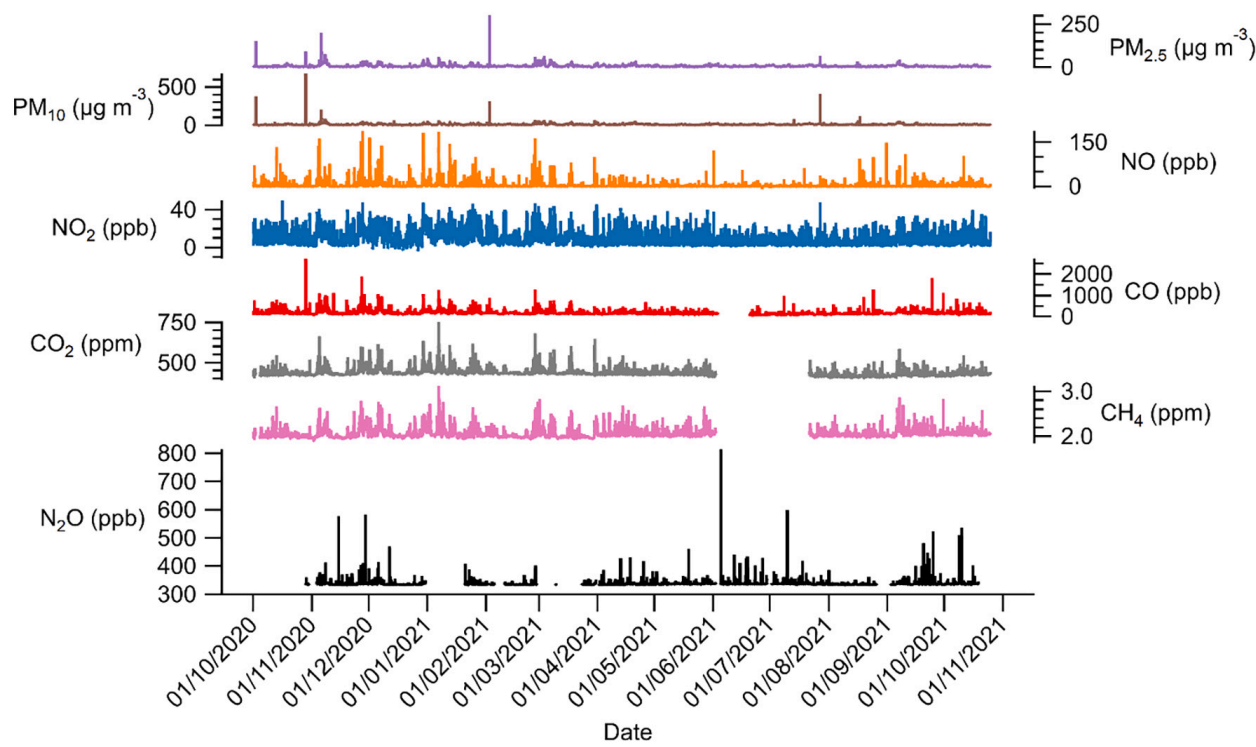


Fig. 4. One-minute-average time series of concentrations of PM_{2.5}, PM₁₀, NO, NO₂, CO, CO₂, CH₄, and N₂O from the MAQS from October 2020 to October 2021.

as a number of the large particulate matter enhancements occur close to Guy Fawkes Night (05 November 2021), when fireworks and urban outdoor fires are common in the UK (Vecchi et al., 2008). Contrary to typical urban source relationships between air quality tracers (such as those indicative of traffic emissions), N₂O does not display the same common pattern of enhancement with other trace gas and aerosol species.

The common emission patterns observed between tracers are also illustrated by the correlation matrix in Fig. 5. Relatively high correlation coefficients (> 0.5) were observed between CH₄, CO₂, CO, and NO_x, which all showed common patterns of enhancement seen in the time series in Fig. 4. High correlation between relatively well-mixed and unreactive trace gases such as CO₂ and CH₄ is likely influenced by diurnal mole fraction variation with boundary layer dynamics over the day/night. Vertical turbulent motion during the daytime mixes pollution into background air more effectively, resulting in lower mean mole fractions during daylight hours.

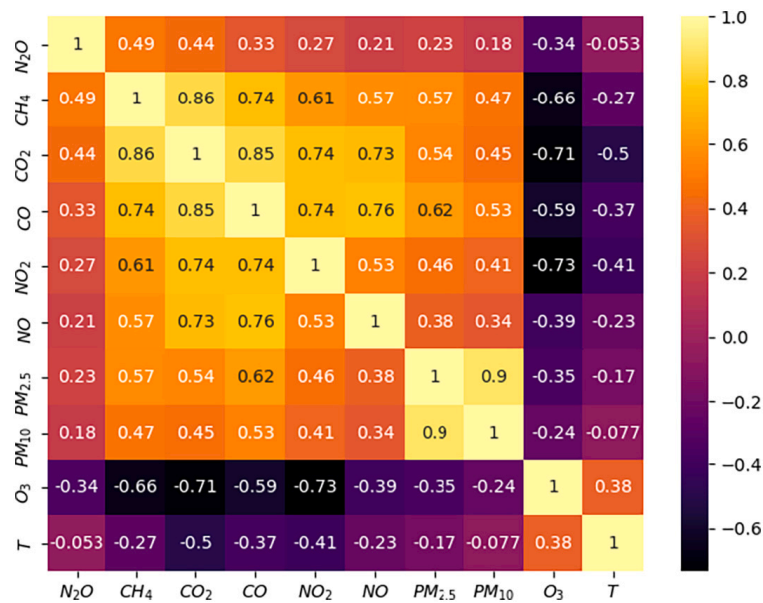


Fig. 5. Correlation matrix for various trace gases, aerosols and temperature measured at the MAQS between October 2020 and October 2021. Pearson correlation coefficients of the various species/parameters are shown in the boxes, and boxes are coloured by correlation coefficient.

In contrast, the nocturnal boundary layer is typically more stable, trapping urban surface emissions and resulting in higher average nocturnal mole fractions. N_2O is notably less well correlated with all other trace gases, with correlation coefficients consistently lower than 0.5. Of all species, N_2O mole fraction has the highest positive correlation with CH_4 and CO_2 mole fractions, with coefficients of 0.49 and 0.44 respectively.

Fig. 6 shows scatter plots of selected species and temperature versus N_2O mole fraction. It can be seen that there were modest enhancements of N_2O (approximate 10–20 ppb above background) that coincided with high enhancements of NO_x , CO, CO_2 and CH_4 . However, very high N_2O enhancements (up to 400 ppb above background) do not appear to be correlated with enhancements of any other species measured at the MAQS site, as shown by the horizontal linear enhancements shown in Fig. 6. Rather, all of the aforementioned large N_2O enhancements appear to be relatively sudden increases in mole fraction that were only observed on timescales of a few minutes. The sudden onset and transient nature of N_2O enhancement (relative to other gases) suggests that the source of these N_2O emissions was in relatively close proximity to the measurement site rather than originating from longer range transport of a more well-mixed airmass.

In summary, there appears to be weak correlation between N_2O and other trace gas and aerosol species, especially at lower N_2O concentrations (< 50 ppb over background), which we expect to be a result of co-emission from traffic, biomass burning, and other typical urban emission sources. Much larger enhancements in N_2O (50–400 ppb over background) were observed with no correlation to any other measured tracers, suggesting the presence of a significant nearby source of solely N_2O that does not appear to originate from other urban emission sources such as traffic or combustion.

3.2. Temporal variability

The temporal trends in trace gas observations are used here to understand emission source behaviour and to identify the dominant emission sources in the area.

3.2.1. Time of day

Fig. 7 shows the statistical variability of N_2O , CH_4 , CO and NO over daily, weekly, and yearly timescales, with variability over the span of a day shown on the left panels. Solid lines show the median concentrations, darker shaded regions show the 25th to 75th percentile range, and the lighter shaded areas show the 5th to 95th percentile range. N_2O exhibits a diurnal pattern of enhanced nocturnal mole fraction relative to daytime concentrations, with mole fractions increasing from ~18:00 onwards, peaking at approximately 02:00 before declining rapidly thereafter. The most prevalent use of recreational N_2O is known to occur at house parties (van Amsterdam et al., 2015). Such events most often occur from evening to early morning, which coincides with the nocturnal period of enhanced N_2O shown in Fig. 7. It is therefore a strong possibility that the evening to early morning N_2O enhancements observed here

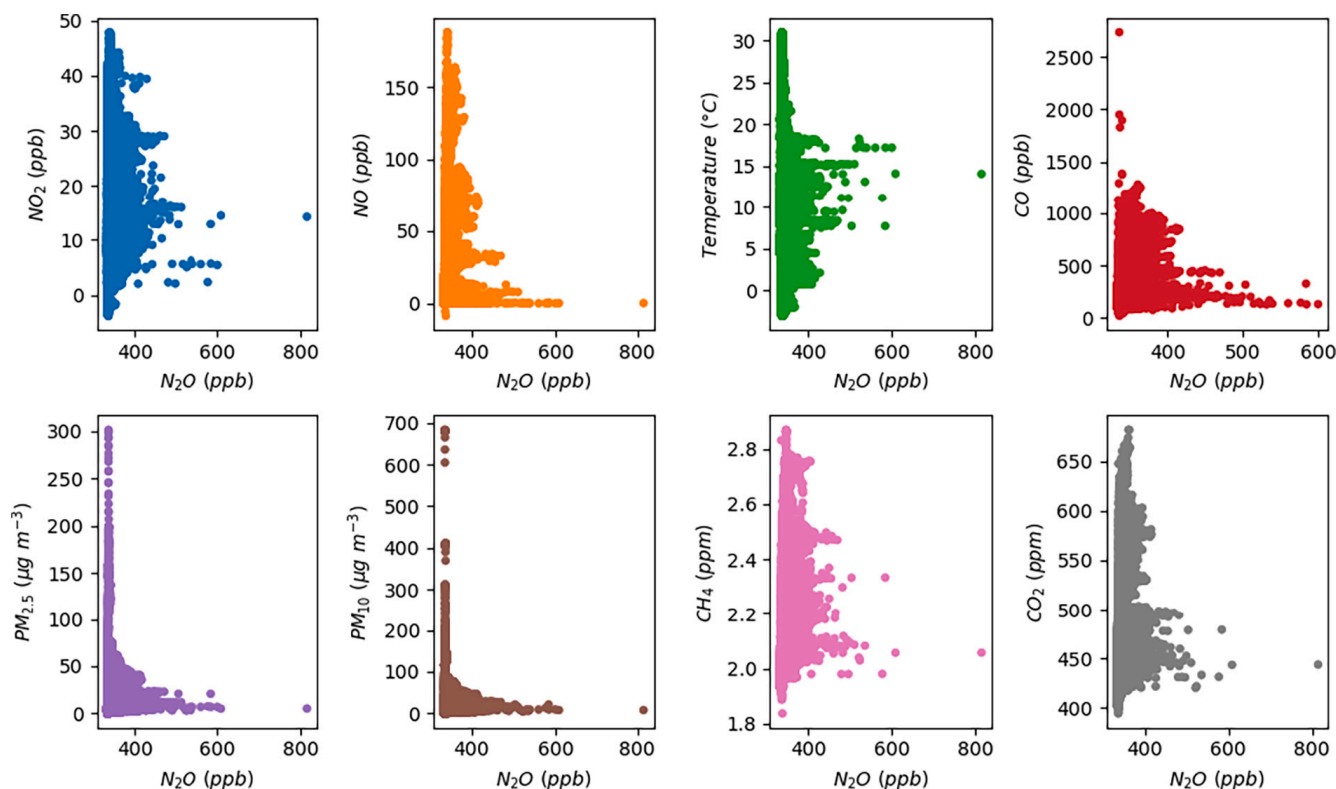


Fig. 6. Scatter plots of NO_2 , NO, CO, CH_4 , CO_2 , $PM_{2.5}$, PM_{10} , and temperature versus N_2O for October 2020 – October 2021 measurements at the MAQS.

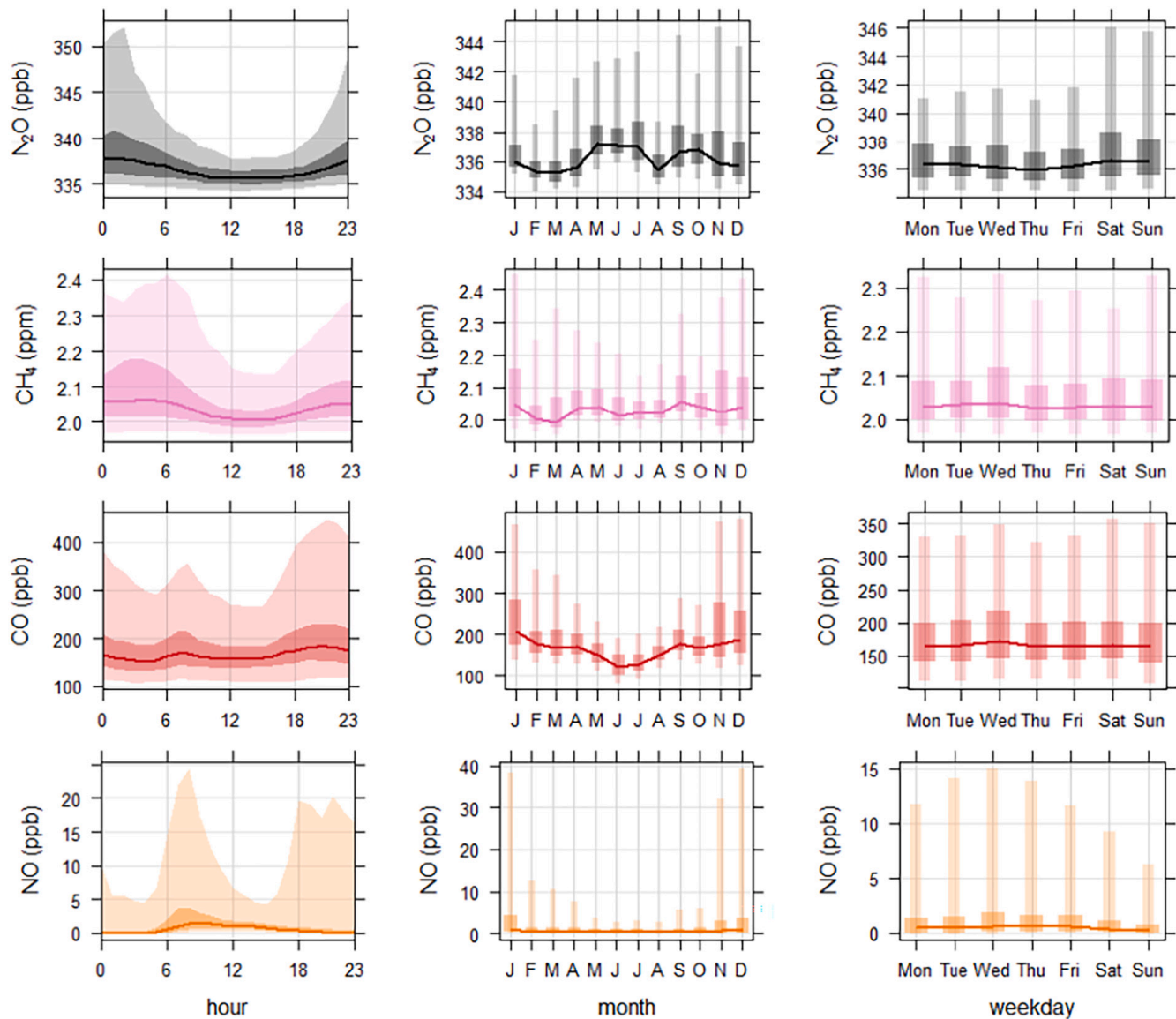


Fig. 7. N_2O , CH_4 , CO , and NO mole fraction variability with hour of the day (left), month of the year (middle), and day of the week (right). Solid lines represent median values, darker shaded areas represent the 25th to 75th percentile range, and lighter shaded areas represent the range between the 5th and 95th percentiles.

primarily result from recreational N_2O use.

As with N_2O , CH_4 displays a diurnal enhancement pattern, with a 95th percentile maximum between approximately 21:00 and 06:00, before declining thereafter to a minimum between 12:00 and 17:00. There are a lack of significant CH_4 point sources within close proximity of the site that follow a nocturnal pattern of emission seen in Fig. 7; traffic CH_4 emissions would be minimal, and would show likely exhibit morning-afternoon commuter traffic spikes (Squires et al., 2020), large-scale gas leaks may represent a significant source, but are likely transient in nature, and would not persist throughout the measurement period. It is therefore likely that CH_4 mole fraction is well mixed at the MAQS. As a result of the well-mixed nature of CH_4 here, the nocturnal enhancements are consistent with ventilation and dilution as a result of boundary layer dynamics (Davies et al., 2007). Pooling of local emissions (i.e. from small leaks in domestic gas infrastructure or from wastewater treatment) at night and subsequent reduction in mole fraction with boundary layer development (mixing and ventilation) in daylight hours (Helfter et al., 2016; Daelman et al., 2012). Despite the presence of diurnal patterns in both N_2O and CH_4 , there appear to be notable differences between the time profiles of both gases. Firstly, N_2O enhancement peaks earlier in the morning than CH_4 ; N_2O decreases sharply after 02:00 whereas CH_4 remains enhanced until 06:00 before the mole fraction begins to decrease. Furthermore, the nocturnal N_2O enhancement is sustained for a far shorter time than with CH_4 , with a rapid increase to peak enhanced N_2O at 02:00 followed by a sharp decline as opposed to relatively constant enhanced CH_4 between 23:00 and 16:00. The difference between the diurnal profiles of N_2O and CH_4 suggests that while daily CH_4 mole fraction variability is governed largely by boundary layer dynamics, N_2O variability is additionally influenced by a combination of boundary layer dynamics and a strong nearby recreational N_2O source as evidenced by the difference in temporal profile with CH_4 .

As opposed to the diurnal profiles of N_2O and CH_4 , NO and CO both exhibit a similar daily trend of morning enhancement peaking

at approximately 07:00, followed by an afternoon enhancement from approximately 17:00 onwards. This morning-afternoon trend is consistent with emissions from commuter traffic. There is some evidence of the same boundary layer driven diurnal profile seen in CH_4 present in CO, but not in NO. NO does not exhibit the same diurnal pattern associated with boundary layer dynamics as seen in longer-lived species such as CH_4 and CO, due to its short lifetime (on the order of hours depending on solar radiation, temperature, and O_3 abundance (Larin and Kuskov, 2014; Kenagy et al., 2018)). The absence of a commuter traffic source pattern in the temporal profile of N_2O suggests that traffic is not a dominant N_2O source in this region, hence nocturnal recreational N_2O emissions may be significantly higher than N_2O from a vehicular source in this area.

3.2.2. Day of week

The right-hand panels of Fig. 7 shows the variability in trace gas mole fraction over a weekly timescale. It can be seen that N_2O mole fraction is relatively constant during weekdays, but significantly enhanced on Saturdays and Sundays. The 95th percentile N_2O mole fraction is in the range of 341–342 ppb from Monday to Friday but increases by ~ 4 ppb to 345–346 ppb during the weekend. Fig. 8 shows the variability in mean N_2O mole fraction over the course of a day, but is coloured by day of the week in order to further illustrate changes observed at the weekend. It can be seen that there are two clear modes of N_2O mole fraction variability for weekends and weekdays which appear to only deviate from each other between 20:00 and 06:00. Interestingly, Friday evenings are similar to weekend mode of N_2O enhancement, whereas Sunday evenings do not follow this weekend pattern, instead more closely resembling the typical weekday mode. The specific times during the weekend (approximately 20:00 to 06:00 from Fig. 8) that N_2O is enhanced relative to weekdays suggest that the source of the nocturnal N_2O enhancements could be from the use of N_2O as a recreational substance. In contrast to N_2O , NO mole fraction is lower on weekend days with a minimum on Sundays due to commuter traffic being the dominant NO_x source in the area. Additionally, there appears to be little sensitivity of CH_4 or CO mole fraction to the day of week, with median values and interquartile ranges remaining relatively consistent between days of the week. The lack of weekend sensitivity in CH_4 and CO is consistent with the boundary layer influence on their mole fractions identified in Section 3.2.1, as this behaviour would be constant throughout the week. None of the other species share the pattern of weekend enhancement seen in N_2O mole fraction, suggesting that the source of N_2O responsible for these enhancements is discrete, with no co-emission of other tracers.

3.2.3. Time of year

The variability of trace gas mole fraction over the course of the year-long measurement period is shown in the central column of Fig. 7. There appears to be little seasonal sensitivity in N_2O mole fraction in contrast to other trace gases, with minima in median, 75th, and 95th percentile N_2O mole fraction in February, March, and August. The lower February and March mole fractions are potentially a result of the significant gaps in N_2O data acquisition during these months due to unplanned instrument shutdowns. N_2O mole fraction appears to rapidly decrease from July to August, but recovers to a similar magnitude in September. This sharp August drop could be the result of the summer university break from 11 June 2021 to 20 September 2021. There is likely a lower number of students occupying nearby accommodation buildings in August, resulting in a reduced recreational N_2O source from these buildings during this time.

As opposed to N_2O , CO and NO mole fractions display a more predictable seasonal variability that can be explained by changing meteorological conditions. Both CO and NO show lower mole fraction enhancement over summer months than winter, with NO and CO minima occurring in July and maxima in December. This is to be expected from the vertical convection of surface emissions in warmer summer months, resulting in better air quality. There is evidence of the same yearly pattern in CH_4 mole fraction shown by the generally higher 95th percentile mole fractions during winter months, however this pattern is not as clear as it is with NO and CO. The presence of near-field urban sources likely mask the natural seasonal variability in CH_4 mole fraction.

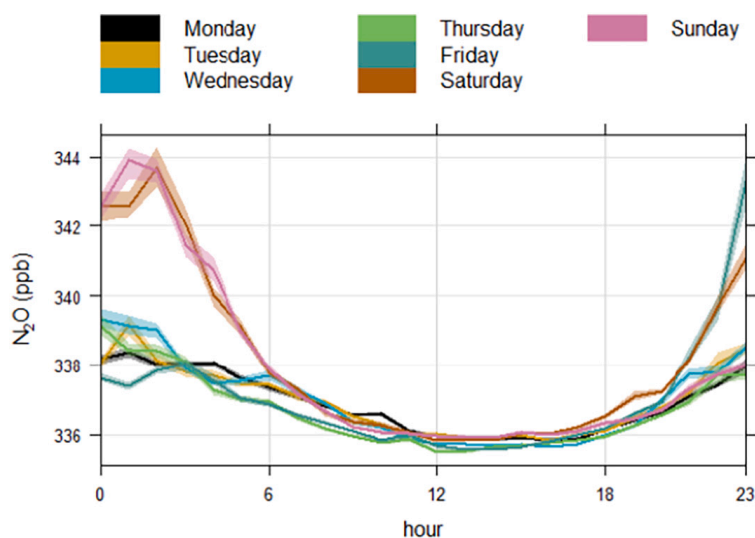


Fig. 8. Mean N_2O mole fraction variability with hour of the day. Solid lines represent mean values and shaded areas represent 95% confidence intervals.

3.3. Airmass and wind climatology

As shown in Fig. 9, the dominant wind directions over the course of the year-long measurement period are south westerly and east-south easterly. The strong and dominant southwesterly wind component is typical of prevailing westerly winds from the Atlantic in the north west of England. A marked east-southeasterly wind component is expected to be partially a result of the less obtrusive topography in the vicinity of the site. Buildings and trees in the area to the southeast of the site are relatively sparse compared with other radial directions. The presence of such obstacles may affect our ability to accurately and quantitatively capture the mean near-surface flow representative of the wider area around the measurement site. However, in this study, we only interpret measured wind direction in a broad and qualitative sense to infer the likely upwind origins of sources of pollution observed at the MAQS site.

3.4. Spatial variability

Using measurements of wind direction and wind speed from the MAQS coincident with pollutant measurements, the spatial variability of enhancements and hence potential emission sources can be investigated. Fig. 10 shows polar annulus plots of selected trace gases from MAQS measurements, these plots show the variability of mean mole fraction with wind vector as well as showing temporal variability of mean mole fraction throughout the outer radius of the annulus (with the radial dimension representing hour-of-day). Fig. 10 therefore allows for spatial analysis of emission sources with temporal sensitivity (i.e. emissions from commuter traffic).

All species show moderately enhanced mole fractions from all wind directions, highlighting the dense urban location of the measurement site with emission sources distributed in all directions. However, there is a clear trend of high mean mole fractions hotspots to the northeast and southeast seen with all species in Fig. 10. The mean mole fraction hotspot to the northeast seen in all species could result from pollution from Manchester City Centre advected southwards towards the MAQS. The southeast mole fraction hotspot is likely a result of the complex urban topography within the study area as seen in Fig. 1, there are relatively few buildings situated to the southeast of the MAQS, therefore it is likely that airflow and hence pollution, is funnelled from the southeast due to the lack of building obstruction, this is also illustrated by the higher proportion of southeasterly wind directions shown in Fig. 9.

N₂O mole fraction does appear to show the same northeast and southeast hotspot activity as the other species, yet the largest mean N₂O mole fraction hotspot in excess of 342 ppb originates from a southwest wind direction. No emission hotspots from any of the other species in Fig. 10 are present from this wind vector, therefore suggesting that the majority of emissions from the previously identified recreational N₂O source may originate from the region west of the measurement site. It is worth noting that CH₄ mole fraction also exhibits a small mole fraction hotspot from the southwest wind direction, albeit not as prominent as with N₂O. This could potentially be a result of CH₄ emission from domestic gas heating systems (Lebel et al., 2020) and from natural gas distribution infrastructure supplying residential areas (McKain et al., 2015). Recreational N₂O use likely occurs from within residential buildings, so recreational N₂O emissions from the southwest could be coincident with CH₄ emissions from gas-powered heating systems in homes as well as gas leaks from pipelines supplying areas of housing.

The previous trend of nocturnal N₂O enhancements with a particular sensitivity for weekend nights is illustrated again in Fig. 11,

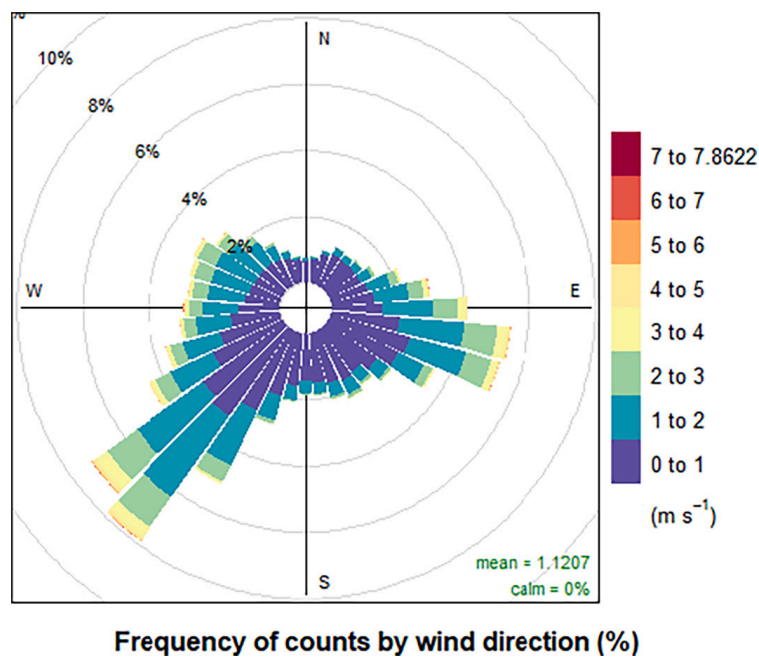


Fig. 9. Wind rose for measurements at the MAQS between October 2020 and October 2021, showing the percentage contribution of specific wind directions to all wind direction measurements. Wind rose segments are coloured by wind speed in m s⁻¹. (For interpretation of the references to colour in this figure legend, the reader is referred to the web version of this article.)

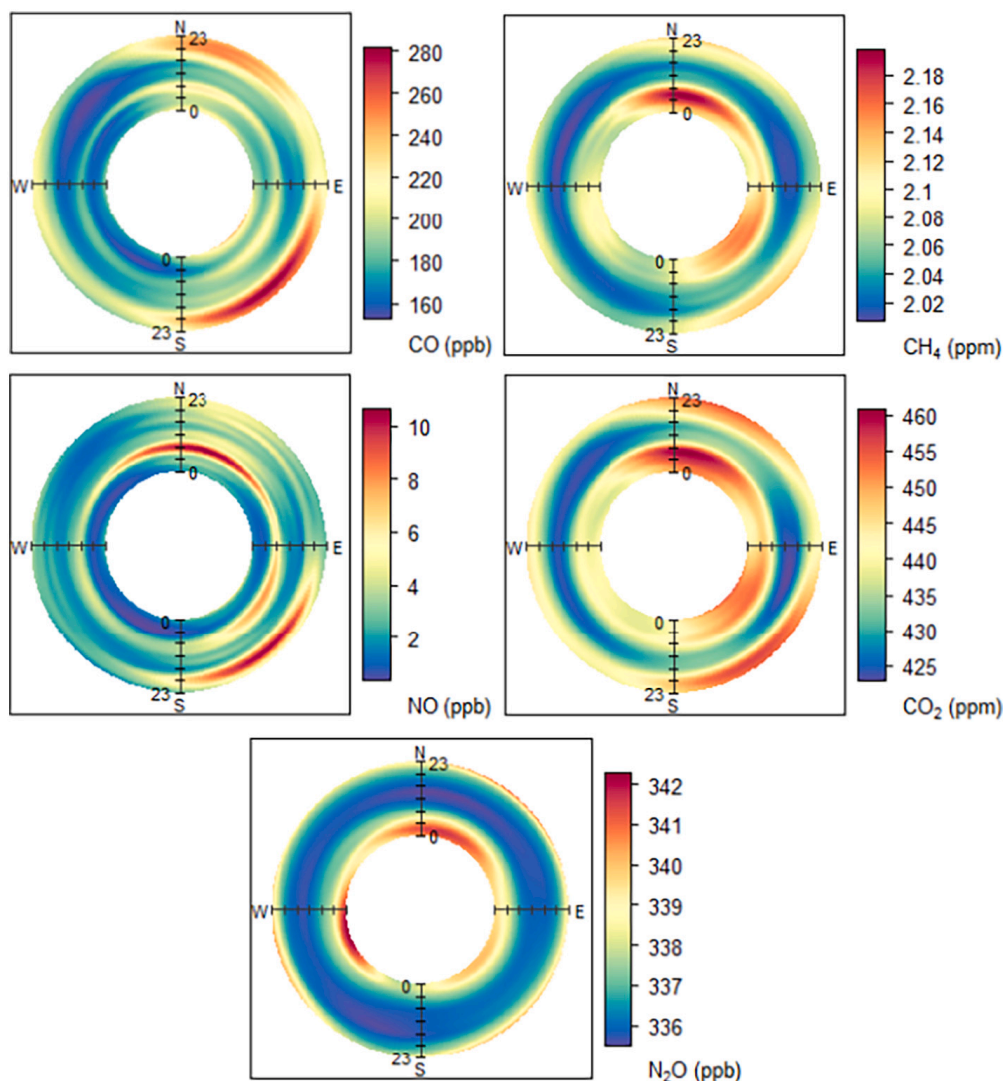


Fig. 10. Polar annulus plots of mean CH_4 , CO_2 , N_2O , NO , CO , and $\text{PM}_{2.5}$ concentration for October 2020 – October 2021 measurements at the MAQS.

with significantly higher mean N_2O mole fractions during the night as opposed to the day, and peak mean mole fractions in excess of 410 ppb occurring during Saturday night time. The nocturnal N_2O hotspots appear to originate from a southwesterly direction in Fig. 11, reiterating the hotspot shown in the polar annulus plots of Fig. 8. Peak mean enhancements also appear to occur at relatively low wind speeds ($< 2 \text{ m s}^{-1}$), which is consistent with a source relatively close to the site. As seen in Fig. 2, a number of student accommodation buildings are located to the immediate west of the measurement site which may contribute to this N_2O hotspot. Use of N_2O canisters at house parties both inside and outside university accommodation buildings may represent a nearby source location. As the measurement period coincided with COVID-19 lockdown restrictions, the frequency of the aforementioned house party events may have been higher relative to times without restricted social mobility, hence there is a reasonable likelihood that these areas of university accommodation may contribute to the nearby recreational N_2O source. However, other areas of student accommodation exist to the northeast of the site, which are not seen on the nocturnal polar plots in Fig. 11. In addition to student accommodation, a high-density area of terraced housing exists to the west of the measurement site past the student accommodation buildings it is possible that recreational use of N_2O from these residences could also contribute to the strong southwesterly nocturnal N_2O hotspot.

4. Conclusions and future work

In situ ground-based measurements of N_2O , alongside CH_4 , CO_2 , CO , NO_x , $\text{PM}_{2.5}$, and PM_{10} were made at the Manchester Air Quality Supersite situated in Fallowfield, Manchester between October 2020 and October 2021. Emissions of N_2O were detected that appeared to be independent of any other measured tracers. These N_2O emissions peaked at 02:00, and are independent from commuter traffic emissions seen in NO and CO . The diurnal pattern of N_2O enhancement was more prominent between the period of Friday night to Saturday morning than during weekday periods. The spatial origin of these emissions appears to be different to that of all other species measured at the supersite, with a peak mean N_2O mole fraction hotspot southwest of the measurement site, downwind of areas

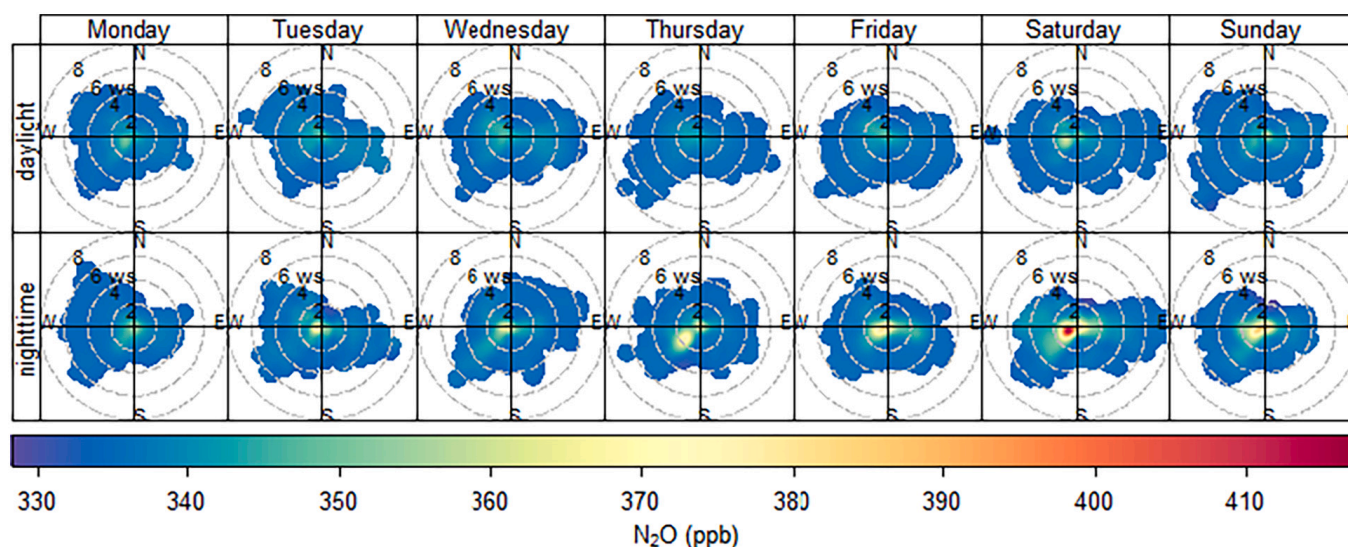


Fig. 11. Bivariate polar plots of mean N_2O mole fraction from the year-long measurement period. These plots show mole fraction variability with both wind direction and wind speed. The plots are divided into day of the week, and are also show measurements during daylight and night-time hours.

of student accommodation and dense terraced housing. Both the temporal and spatial distribution of N_2O enhancement strongly suggest a significant nearby recreational source of N_2O from the use of N_2O whipped-cream chargers as a party drug. There has been very little previous study of N_2O emissions from its use as a recreational substance, and while the work here is purely qualitative, there is potential for this source to be significant due to the dominant temporal pattern in N_2O over more expected source patterns such as from commuter traffic. Future study should focus on quantification of this source, and comparison to NAEI for recreational N_2O .

Author contributions

P. A. Barker was the lead author, with writing contributions from G. Allen and S. Riddick. Data curation and validation was undertaken by P. A. Barker and M. Flynn. Formal data analysis was carried out by P. A. Barker. All co-authors provided commentary on draft versions of the manuscript.

Declaration of Competing Interest

The authors declare no conflict of interest.

Acknowledgements

The photograph used in Fig. 1 is licensed under CC BY 2.0. The basemap used in Fig. 2 is obtained from ArcGIS software (Sources: Esri, HERE, Garmin, Intermap, Increment P Corp., GEBCO, USGS, FAO, NPS, NRCAN, GeoBase, IGN, Kadaster NL, Ordnance Survey, Esri Japan, METI, Esri China (Hong Kong). © OpenStreetMap contributors and the GIS User Community). Figs. 6–10 were created using the Openair package in R (Carslaw and Ropkins, 2012). P. A. Barker is in receipt of a PhD studentship as part of the NERC Earth, Atmosphere and Ocean Doctoral Training Partnership (EAO DTP) (NERC grant reference no. NE/L002469/1).

References

- Andreae, M., 2019. Emission of trace gases and aerosols from biomass burning—An updated assessment. *Atmos. Chem. Phys.* 1–27, 2019. <https://doi.org/10.5194/acp-2019-303>.
- Banks, A., Hardman, J.G., 2005. Nitrous oxide. *Contin. Educ. Anaesth. Crit. Care Pain* 5 (5), 145–148. <https://doi.org/10.1093/bjaceaccp/mki039>.
- Carslaw, D.C., Ropkins, K., 2012. *openair* - An r package for air quality data analysis. *Environ. Model. Softw.* 27–28, 52–61. <https://doi.org/10.1016/j.envsoft.2011.09.008>.
- Daelman, M.R.J., van Voorthuizen, E.M., van Dongen, U.G.J.M., Volcke, E.I.P., van Loosdrecht, M.C.M., 2012. Methane emission during municipal wastewater treatment. *Water Res.* 46 (11), 3657–3670. <https://doi.org/10.1016/j.watres.2012.04.024>.
- Davies, F., Middleton, D.R., Bozier, K.E., 2007. Urban air pollution modelling and measurements of boundary layer height. *Atmos. Environ.* 41 (19), 4040–4049. <https://doi.org/10.1016/j.atmosenv.2007.01.015>.
- De Mello, W.Z., Ribeiro, R.P., Brotto, A.C., Kligerman, D.C., Piccoli, De S., Oliveira, J.L.M., 2013. Nitrous oxide emissions from an intermittent aeration activated sludge system of an urban wastewater treatment plant. *Quim Nova* 36 (1), 16–20. <https://doi.org/10.1590/S0100-40422013000100004>.
- Ehirim, E.M., Naughton, D.P., Petróczy, A., 2018. No laughing matter: presence, consumption trends, drug awareness, and perceptions of “hippy crack” (nitrous oxide) among young adults in England. *Front. Psychiatry* 8 (JAN), 1–10. <https://doi.org/10.3389/fpsy.2017.00312>.
- Famulari, D., Nemitz, E., Di Marco, C., Phillips, G.J., Thomas, R., House, E., Fowler, D., 2010. Eddy-covariance measurements of nitrous oxide fluxes above a city. *Agric. For. Meteorol.* 150 (6), 786–793. <https://doi.org/10.1016/j.agrformet.2009.08.003>.

- Helfter, C., Tremper, A.H., Halios, C.H., Kotthaus, S., Björkegren, A., Grimmond, C.S.B., Barlow, J.F., Nemitz, E., 2016. Spatial and temporal variability of urban fluxes of methane, carbon monoxide and carbon dioxide above London, UK. *Atmos. Chem. Phys.* 16, 10543–10557. <https://doi.org/10.5194/acp-16-10543-2016>.
- IPCC, 2013. In: Stocker, T., Qin, D., Plattner, G.-K., Tignor, M., Allen, S., Boschung, J., Nauels, A., Xia, Y., Bex, V., Midgley, P. (Eds.), *Anthropogenic and Natural Radiative Forcing*, in: *Climate Change 2013: The Physical Science Basis. Contribution of Working Group I to the Fifth Assessment Report of the Intergovernmental Panel on Climate Change*. Cambridge University Press, Cambridge, United Kingdom and New York, NY, USA.
- Järvi, L., Nordbo, A., Rannik, Ü., Haapanala, S., Mammarella, I., Pihlatie, M., Vesala, T., Riikonen, A., 2014. Urban nitrous-oxide fluxes measured using the eddy-covariance technique in Helsinki, Finland. *Boreal Environ. Res.* 19 (September), 108–121.
- Kenagy, H.S., Sparks, T.L., Ebben, C.J., Wooldrige, P.J., Lopez-Hilfiker, F.D., Lee, B.H., Thornton, J.A., McDuffie, E.E., Fibiger, D.L., Brown, S.S., et al., 2018. NOx lifetime and NOy partitioning during WINTER. *J. Geophys. Res. Atmos.* 123 (17), 9813–9827. <https://doi.org/10.1029/2018JD028736>.
- Ketzel, M., Wählin, P., Berkowicz, R., Palmgren, F., 2003. Particle and trace gas emission factors under urban driving conditions in Copenhagen based on street and roof-level observations. *Atmos. Environ.* 37 (20), 2735–2749. [https://doi.org/10.1016/S1352-2310\(03\)00245-0](https://doi.org/10.1016/S1352-2310(03)00245-0).
- Larin, I.K., Kuskov, M.L., 2014. Daytime and nighttime lifetimes of minor atmospheric components in the troposphere. *Russ. J. Phys. Chem. B* 8 (2), 254–260. <https://doi.org/10.1134/S199079311402016X>.
- Lebel, E.D., Lu, H.S., Speizer, S.A., Finnegan, C.J., Jackson, R.B., 2020. Quantifying methane emissions from natural gas water heaters. *Environ. Sci. Technol.* 54 (9), 5737–5745. <https://doi.org/10.1021/acs.est.9b07189>.
- McKain, K., Down, A., Raciti, S.M., Budney, J., Hutyra, L.R., Floerchinger, C., Herndon, S.C., Nehrkorn, T., Zahniser, M.S., Jackson, R.B., Phillips, N., Wofsy, S.C., 2015. Methane emissions from natural gas infrastructure and use in the urban region of Boston, Massachusetts. *Proc. Natl. Acad. Sci. U. S. A.* 112 (7), 1941–1946. <https://doi.org/10.1073/pnas.1416261112>.
- NAEI/BEIS, 2022. National Atmospheric Emissions Inventory UK Emissions Data Selector [online] Available from: <https://naei.beis.gov.uk/data/data-selector>. Accessed 05 January 2022.
- NOAA/GML, 2021. http://gml.noaa.gov/ccgg/trends_n2o (Accessed 12 November 2021).
- Pitt, J.R., Le Breton, M., Allen, G., Percival, C.J., Gallagher, M.W., Bauguette, J.-B., O'Shea, S.J., Muller, J.B.A., Zahniser, M.S., Pyle, J., Palmer, P.I., 2016. The development and evaluation of airborne in situ N₂O and CH₄ sampling using a quantum cascade laser absorption spectrometer (QCLAS). *Atmos. Meas. Tech.* 9 (1), 63–77. <https://doi.org/10.5194/amt-9-63-2016>.
- Prather, M.J., Hsu, J., Deluca, N.M., Jackman, C.H., Oman, L.D., Douglass, A.R., Fleming, E.L., Strahan, S.E., Steenrod, S.D., Søvde, O.A., Isaksen, I.S.A., Froidevaux, L., Funke, B., 2015. Measuring and modeling the lifetime of nitrous oxide including its variability. *J. Geophys. Res. Atmos.* 120, 5693–5705. <https://doi.org/10.1002/2015JD023267>.
- Randhawa, G., Bodenham, A., 2016. The increasing recreational use of nitrous oxide: history revisited. *Br. J. Anaesth.* 116 (3), 321–324. <https://doi.org/10.1093/bja/aev297>.
- Ravishankara, A.R., Daniel, J.S., Portmann, R.W., 2009. Nitrous oxide (N₂O): The dominant ozone-depleting substance emitted in the 21st century. *Science* (80-) 326 (5949), 123–125. <https://doi.org/10.1126/science.1176985>.
- Squires, F.A., Nemitz, E., Langford, B., Wild, O., Drysdale, W.S., Joe, W., Fu, P., Sue, C., Hamilton, J.F., Nicholas Hewitt, C., Hollaway, M., Kotthaus, S., Lee, J., Metzger, S., Pingthia-Durden, N., Shaw, M., Vaughan, A.R., Wang, X., Wu, R., Zhang, Q., Zhang, Y., 2020. Measurements of traffic-dominated pollutant emissions in a Chinese megacity. *Atmos. Chem. Phys.* 20 (14), 8737–8761. <https://doi.org/10.5194/acp-20-8737-2020>.
- Talleg, G., Garnier, J., Billen, G., Gossailles, M., 2008. Nitrous oxide emissions from denitrifying activated sludge of urban wastewater treatment plants, under anoxia and low oxygenation. *Bioresour. Technol.* 99 (7), 2200–2209. <https://doi.org/10.1016/j.biortech.2007.05.025>.
- Tian, H., Xu, R., Canadell, J.G., Thompson, R.L., Winiwarter, W., Suntharalingam, P., Davidson, E.A., Ciais, P., Jackson, R.B., Janssens-Maenhout, G., Prather, M.J., et al., 2020. A comprehensive quantification of global nitrous oxide sources and sinks. *Nature* 586 (7828), 248–256. <https://doi.org/10.1038/s41586-020-2780-0>.
- Townsend-Small, A., Czimczik, C.I., 2010. Carbon sequestration and greenhouse gas emissions in urban turf. *Geophys. Res. Lett.* 37, 1–5. <https://doi.org/10.1029/2009GL041675>.
- UK Home Office, 2018. Drug Misuse: Findings from the 2017/18 Crime Survey for England and Wales [online] Available from: https://assets.publishing.service.gov.uk/government/uploads/system/uploads/attachment_data/file/729249/drug-misuse-2018-hosb1418.pdf. Accessed 22 June 2020.
- van Amsterdam, J., Nabben, T., van den Brink, W., 2015. Recreational nitrous oxide use: prevalence and risks. *Regul. Toxicol. Pharmacol.* 73 (3), 790–796. <https://doi.org/10.1016/j.yrtph.2015.10.017>.
- Van Delden, L., Rowlings, D.W., Scheer, C., Grace, P.R., 2016. Urbanisation-related land use change from forest and pasture into turf grass modifies soil nitrogen cycling and increases N₂O emissions. *Biogeosciences* (II), 6095–6106. <https://doi.org/10.5194/bg-13-6095-2016>.
- Vecchi, R., Bernardoni, V., Cricchio, D., D'Alessandro, A., Fermo, P., Lucarelli, F., Nava, S., Piazzalunga, A., Valli, G., 2008. The impact of fireworks on airborne particles. *Atmos. Environ.* 42 (6), 1121–1132. <https://doi.org/10.1016/j.atmosenv.2007.10.047>.
- Yu, Z., Deng, H., Wang, D., Ye, M., Tan, Y., Li, Y., Chen, Z., Xu, S., 2013. Nitrous oxide emissions in the Shanghai river network: implications for the effects of urban sewage and IPCC methodology. *Glob. Chang. Biol.* 19 (10), 2999–3010. <https://doi.org/10.1111/gcb.12290>.
- Zuck, D., Ellis, P., Dronsfield, A., 2012. Nitrous Oxide: Are You Having a Laugh? [online] Available from: <http://www.rsc.org/eic>. Accessed 11 June 2021.

Chapter 6

Conclusions and future work

As previously stated in Section 2.4, the overarching aim of this thesis is to better understand the extent of GHG emissions from sources that have previously seen little to no dedicated in situ study. Additionally, the thesis aims to better characterise GHG emissions from source types that exhibit a particular sensitivity to anthropogenic climate change (i.e. biomass burning and wetlands, which are both perturbed by climate feedback cycles). Understanding sources that exist within climate feedback cycles is important for future assessment of GHG emission behaviour in a changing climate.

Global GHG emission budgets are often constructed from large-scale emission inventories where emission factors are upscaled to wider areas via activity data, or biogeochemical process models which involve parameterisation of GHG production processes in soils, wetlands etc. and upscaling to produce a wider emission estimate. The issue with this large-scale bottom-up emission estimation is that fine variability in emissions may not be fully captured by emission process parameterisation or emission factors. Hence uncertainties in these aspects of bottom-up emission models will propagate to large uncertainties in global emission estimates. In situ emission measurements are vital for capturing fine scale temporal and/or spatial variability in emissions that may not be captured by bottom-up techniques. In situ measurements can be used as a crucial validation tool for bottom-up emission estimation, but further than this, in situ emission observations from areas with little previous study (e.g. novel wildfire emission factor datasets) can be incorporated into new bottom-up emission inventories, resulting in a global emission dataset with reduced overall uncertainties that better encompasses the fine-scale variability in emission behaviour.

This thesis has presented three distinct case studies that quantify or otherwise characterise emissions of CH₄ and N₂O from poorly-studied or climate sensitive sources using aircraft and ground-based in situ measurements. Chapter 3 (Paper 1) was focused on airborne measurement of African biomass burning emissions, and calculation emission factors for two distinct burning locations. Chapter 4 (Paper 2) quantified fluxes of CH₄ from arctic peatland in Northern Fennoscandia, and compared these fluxes with process modelled

methane emission. Chapter 5 (Paper 3) described ground-based observation of N₂O in an urban environment in the UK, where evidence for the presence of a recreational N₂O source is presented. This chapter will summarise the main conclusions of these studies, as well as discussing future directions for these areas of research.

6.1. Conclusions

6.1.1. Biomass burning

As a result of the work outlined in Chapter 3, two sets of emission factors were calculated for CH₄, CO₂, and CO for wildfires in two distinct areas of Northern sub-Saharan Africa, one set for Senegalese fires in February/March 2017, and a second set for Ugandan fires in January 2019. CH₄ emission factors ranged between 2.8 and 5.2 g kg⁻¹ for the fires in Uganda, whereas a range of 1.4 – 2.4 g kg⁻¹ was observed in Senegalese fires. Additionally, it was also possible to derive a mean N₂O emission factor (0.08 ± 0.002 g kg⁻¹) for a single flight over Ugandan wildfires.

The range of emission factors observed provide some degree of information on the fuel mix present in each location; the Senegalese fires were likely comprised of savannah grass and forest litter, whereas the Ugandan fires likely included crop waste as well as grass matter. Strong linear relationships were observed between CH₄ emission factor and combustion efficiency for both study areas. Additionally, a significant difference in these linear responses was observed between Senegal and Uganda; plumes of Senegalese fires featured lower enhancements of CH₄ than Ugandan fires for an equivalent fire combustion efficiency, which is likely an additional result of the different fuel types between the two regions. The variability of emission factors and hence biomass burning fuel within regions as well as between them highlights the fine spatial variability of biomass burning emissions locally and regionally, which must be accounted for by emission databases in order to accurately report emissions.

The emission factors calculated in Chapter 3 will likely be included in future biomass burning emission factor compilation publications such as Andreae et al. (2019) and Akagi et al. (2011). Emission factors compiled by these publications are incorporated into databases such as GFED4 to estimate wider regional and global biomass burning emissions for use in atmospheric models and global emission budgets. Prior to the MOYA aircraft wildfire surveys, there had been no in situ measurement-based study of

fires in the targeted areas of Senegal and Uganda, previous emission estimates from these regions likely used existing emission factors for fuel types inferred from existing land cover maps, yet with little in situ study, there is an inevitable lack of representation of African biomass burning in fuel-specific emission factor estimates that are usually averaged from globally-distributed studies. Therefore the emission factors published as a part of this thesis will in some small part to help improve the accuracy of regional and global scale biomass burning emission estimation, and to help better represent Africa in globally-averaged emission factors from savannah, forest, and cropland burning.

Prior to the aircraft surveys outlined in Chapter 3, there had been no in situ measurement-based study of fires in the targeted areas of Senegal and Uganda, hence this work contributes a novel emission factor dataset that furthers understanding into variability of greenhouse gas emissions from biomass burning.

6.1.2. Arctic wetlands

As with Chapter 3, Chapter 4 uses in situ aircraft observations to quantify greenhouse gas emissions, yet this work focuses on biogenic CH₄ emissions from arctic peatlands and the calculation of fluxes using the aircraft mass balance method. This study involved a single survey flight across a wide area (~ 78,000 km²) of northern Sweden and Finland. From this flight, CH₄ fluxes in the range 0.32 - 1.11 mg m⁻² hr⁻¹ and CO₂ sinks ranging between -284 and -513 mg m⁻² hr⁻¹ were calculated for three discrete areas within the bounds of the flight track. The bulk and area normalised CH₄ fluxes were lowest in the southernmost area of the flight track, and CH₄ fluxes were positively correlated with the fraction of peatland within each discrete area as determined using a land surface classification map.

Relative to the mass balance CH₄ fluxes, CH₄ flux was generally underestimated by an ensemble of bottom-up biogeochemical process models within the same study area, highlighting the need for an improvement in the parameterisation of bottom-up models for CH₄ emission estimation. However, some of the discrepancy between process model outputs and mass balance results may be accounted for by the limited temporal coverage of the aircraft mass balance experiment, and the possible presence of riverine or lake CH₄ emission that is not accounted for by process models.

This study in Chapter 4 has shown that this region of the European arctic is a significant biogenic source of CH₄ over the summer thaw period, and vegetation in the

area represents a notable CO₂ sink. Due to the presence of arctic climate change amplification, careful monitoring of CH₄ emissions from arctic regions is especially important, as rapid mobilisation of permafrost carbon stores and subsequent emission of this carbon as CH₄ is possible with rapidly changing arctic climate. The top-down quantification of fluxes from this region will serve as an important dataset for intercomparison and validation of future bottom-up process models. In comparison to a previous aircraft survey of the same area of Fennoscandian wetland undertaken in the summer of 2012 (O'Shea et al., 2014), fluxes are not significantly higher in this study undertaken seven years later, perhaps suggesting that arctic amplification has not yet had an impact on wetland methane emissions in this region. However, it is difficult to draw conclusions on the variability of climate-sensitive GHG emission sources from two isolated aircraft-based case studies. Therefore more frequent in situ studies investigating arctic wetland GHG exchange are required to better characterise the temporal variability in emissions from arctic regions, and to help improve global budgeting of wetland methane emissions in future years.

6.1.3. Urban emissions

As a departure from the aircraft-based studies of Chapters 3 and 4, Chapter 5 involves ground-based measurements of N₂O from a fixed-base measurement site in the urban environment in Manchester, UK. Continuous measurements of N₂O along with other trace gases, aerosols, and meteorological parameters were measured for a period of 12 months between October 2020 and 2021. Large enhancements in N₂O (up to 450 ppb above background) were observed with no co-emission in any other trace gas or aerosol species, suggesting the presence of a discrete near-field source of N₂O that was detached from emissions of other pollutants.

Over the measurement period, a consistent temporal pattern of enhanced N₂O between the hours of 18:00 and 02:00 was observed. These nocturnal peaks in N₂O mole fraction were particularly prominent during Friday night to Saturday morning periods, and Saturday night to Sunday morning period. The presence of peak enhancements at late night/early morning, in conjunction with higher weekend enhancement, suggest that the discrete source of N₂O originated from its use as a recreational substance, where it is inhaled from whipped cream charger canisters.

Concurrent measurements of wind speed and 2D wind direction were used to assess the air transport history and determine pollutant source locations. A unique hotspot of high mean N₂O mole fraction not seen in the spatial profiles of other pollutants was observed to the southwest of the measurement site. This spatial feature likely corresponds to a dense area of terraced housing and a busy central street with a high abundance of bars and restaurants, as well as areas of student accommodation. It is therefore possible that recreational use of N₂O from these locations could have resulted in this southwest enhancement hotspot.

The research outlined in Chapter 5 is the first in situ measurement-led study of N₂O emissions from its use as a recreational substance. While previous studies have investigated urban N₂O emission sources, emissions from recreational N₂O use were not identified, thus a robust top-down assessment of N₂O emissions from a recreational source has not been possible previously. The NAEI provides an annual UK emission estimate for N₂O from recreational use (0.014 kt in 2020, (NAEI/BEIS, 2022)), yet there is no publicly-available description as to how the final emission estimate is derived in the budget. Recreational N₂O emission factors are likely relatively accurate, as whipped cream canister design is relatively standardised, with each containing a known quantity of N₂O. The most significant source of uncertainty in the recreational N₂O emission inventory is the activity data, as it is difficult to accurately estimate how many canisters are used for recreational purposes. In situ studies can provide top-down validation of emission inventory estimates, yet many more targeted in situ studies covering different potential source locations are required before a UK-wide top-down recreational N₂O emission estimate can be attempted. Additionally, in situ studies must acknowledge the presence of other N₂O sources that may be present in complex urban environments, which may complicate emission accounting.

6.2. Future directions

6.2.1. Biomass burning

A significant strength of the work presented in Chapter 3 is that emission plumes from multiple fires occurring in relatively remote locations could be characterised. However, the issue with an airborne measurement platform in this case is that detailed information on fuel composition could not be obtained, the fuels burned in the sampled fires could

only be inferred from land cover maps or from visual observation of the fires from the aircraft. Future studies that expand on the work carried out in Chapter 3 could involve a ground-based element in order to accurately quantify fuel mixtures. This would likely take the form of physical identification of the mix of plant types, laboratory analysis of biomass in the sample area to determine carbon fraction, and trace gas observation of prescribed fires in the study area.

Despite the improved information on fuel type, there is the added difficulty of accessing more remote locations for ground-based sampling, which is a lesser problem for aircraft sampling. Despite the difficulties in accessibility, recent studies by Vernooij et al. (2021) and Laris et al. (2021) involved ground-based measurement studies of African biomass burning GHG emissions, both of which are situated in remote locations in sub-Saharan Africa and involve detailed analysis of fuel composition. In addition, the study by Vernooij et al. involves Unpiloted Aerial Vehicle (UAV) surveys to sample the fire plumes, surveys by UAVs allow for some degree of spatial flexibility in sampling, allowing plumes to be fully characterised horizontally and vertically as they can be with fixed-wing aircraft surveys. This study includes the benefits of in-depth ground-based fuel analysis with the spatial robustness of airborne sampling.

In situ measurements of biomass burning emissions are required in order to obtain well-characterised fire emission factors that are representative of the emissions when a certain biomass fuel type is burned. Without continued in situ emission surveys in areas with little previously study, emission factors for specific fuels will remain poorly characterised resulting in significant uncertainties in global fire emission budgets. While the aircraft surveys presented in Chapter 3 are a necessary step forward for better characterised emission factors, many more similar studies are needed. In order to achieve this, expanding the methods in Chapter 3, along with the approaches mentioned in this section, to the rest of the African continent, would allow for full characterisation of African GHG emission factors for a range of fuel types. Furthermore, applying this rigorous in situ methodology to other regions with a high prevalence of biomass burning (e.g. Australia, North America) would allow for a detailed regional comparison of emission factors for the same fuel types. If significant regional variability was found between emission factors on a global scale, an updated set of emission factors with continent/region-specific values for given fuel types may help capture the nuances in

emission variability for like fuel types, and hence result in higher accuracy biomass burning emission budgeting.

6.2.2. Arctic wetlands

The work presented in Chapter 4 provides single daytime summer CO₂ and CH₄ fluxes over a large area of Fennoscandian wetland to a high level of precision and accuracy, yet this by itself does not allow for extrapolation over time to assess temporal variability in emissions. As mentioned previously, there is difficulty in comparing temporal snapshot fluxes with long-term process model ensembles. Moreover, the variability of fluxes over the annual freeze-thaw cycle cannot be determined from a single daytime flux. Additionally, the change in climate-cryosphere feedbacks over multiple years and their impact on GHG emissions in the arctic cannot be assessed from fluxes from a single case study, therefore the next stage of this research should involve more temporally intensive monitoring of GHG emissions from the European arctic.

Aircraft studies excel at providing highly precise and accurate snapshot emission estimates, yet budget and logistical constraints make aircraft surveys unsuitable for high frequency temporal surveillance of emission sources. As an alternative, a number of semi-permanent eddy covariance flux towers could be distributed across the Fennoscandian wetland extent, these would be placed in order to ensure total coverage of the wetland area from the flux footprints. Such a network would allow a long term CH₄ wetland emission dataset to be established; short-term diurnal emission cycles, intermediate-term trends such as spring-time thaw emission pulses (Christensen et al., 2004; Tokida et al., 2007), and long-term emission trends due to amplified arctic warming could all be characterised in high detail, and at higher spatial resolution than aircraft mass balance techniques could achieve. The flux tower network could be supplemented with concurrent aircraft flux surveys and local flux chamber measurements, both to provide redundancy in flux measurement and to allow for validation and intercomparison of each method.

In addition to ground-based flux measurements, the use of remote sensing techniques would also allow for temporally intensive study of wetland CH₄ emissions, with the added benefit of total column CH₄ measurements being possible in regions that are difficult to access by ground or aircraft. Flux inversions from satellite overpasses could be combined with flux estimates from the previously mentioned techniques to produce a

robust arctic wetland flux ensemble dataset. Previous studies have characterised CH₄ enhancements as a result of wetland methanogenesis using TROPOMI satellite instrument data (Hu et al., 2018), and have even quantified fluxes by combining TROPOMI data with atmospheric chemical transport models (Liu et al., 2021; Lunt et al., 2021). This temporally-intensive measurement strategy could be applied to other areas of Arctic wetland responsible for significant CH₄ emissions, such as Canadian Boreal wetlands

In addition to top-down observations, a major finding of Chapter 4 was the relatively poor agreement of the aircraft-observed fluxes with bottom-up process modelled CH₄ fluxes. In order to put top-down flux observations in better context when compared to bottom-up models, quantitative measurements of soil chemical and ecological parameters such as soil organic carbon, pH, water table height, and the extent of oxidation within soils could be made at ground-based sites. A greater understanding of soil processes from in situ observations would help to parameterise CH₄ fluxes derived from tower, chamber, or aircraft measurements, and could aid in the development of new process models as well as improvement of existing models for estimating arctic wetland CH₄ emissions, helping to reconcile the differences between top-down and bottom-up emission estimates and hence reduce the uncertainty in wetland contribution to the global methane budget.

6.2.3. Urban emissions

Chapter 5 currently presents strong evidence for a significant recreational source of N₂O in a single urban area in Manchester, UK by qualitative analysis of temporal and spatial mole fraction trends. However, due to the complex micrometeorology and ambiguous nature of the source locations, quantification of an N₂O flux from this source was not possible in this study. Future related studies could involve targeted measurement campaigns at locations where recreational N₂O use would be expected, such as music festivals or nightclubs. N₂O emissions could be sampled downwind of such sources using a UAV platform with a tethered inlet from the drone to a ground-based spectrometer, such as the one used in Chapter 5 (Shaw et al., 2021). The UAV measurement would allow for complete horizontal and vertical characterisation of an N₂O emission plume, and fluxes could be determined using the mass balance technique (as in Chapter 4), or via Gaussian plume modelling (Shah et al., 2019).

The source location attribution presented in Chapter 5 currently relies on simple 2D wind speed and direction analysis with N₂O concentration enhancement. This aspect of the study could be further improved upon with the use of a short-range atmospheric dispersion model. The Atmospheric Dispersion Modelling System – Urban (ADMS-Urban) is a short-range modelling system that can model atmospheric pollution dispersion at very high resolution, and can account for urban building topography in the dispersion scheme (Stocker et al., 2012). Using ADMS-Urban, likely source locations for recreational N₂O could be set, along with the location of the Fallowfield measurement site. The dispersion model would then simulate N₂O mole fraction variability over time, which could be compared with the observed mole fractions (Hoare et al., 2020). The simulated atmospheric dispersion from ADMS-Urban could be used for a local scale N₂O emission inversion from the local area. This would allow of the magnitude of the recreational N₂O source relative to other urban N₂O emission sources to be understood.

A major limitation with ADMS-Urban emission inversion in this case is the lack of available *a priori* emission data, which are required for inversion set up. The NAEI includes recreational N₂O emission estimates as an annual UK emission, but not as a spatially gridded inventory which would be required for an accurate inversion. A rough estimate of *a priori* spatial emission distribution could be used, but an inaccurate prior input will likely result in non-convergence of the inversion and inability to minimise the cost function. Alternatively, installation of eddy covariance flux apparatus at the MAQS would allow for N₂O flux quantification from the near vicinity, along with information on the spatial distribution of emission sources.

In order to meaningfully compare the NAEI estimate for UK recreational N₂O emissions with top-down methods, emission quantification studies must be extended to wider areas of the UK. Such studies should follow a similar structure to the that shown in Chapter 5, yet with inclusion of eddy covariance flux apparatus. UK-wide recreational N₂O studies should target likely hotspots of recreational N₂O use, such as festivals, bars, nightclubs and inner-city urban areas

6.3. Closing remarks and outstanding research questions

The core work presented in this thesis demonstrates how in situ GHG measurements are an invaluable tool for investigating poorly understood emission sources, and for assessing

how GHG sources may vary over time with the onset of climate change. Chapters 3 and 4 have shown how in situ aircraft observations can yield accurate estimates of source emissions with well constrained uncertainties, which can be used to yield new updated emission factors for use in global emission inventories or used in direct comparisons with bottom-up biogeochemical process models. Chapter 5 has displayed how simple temporal and climatological analysis can provide clear qualitative characterisation of previously unstudied GHG sources, providing a measurement framework for future targeted emission quantification studies.

While the GHG emission case studies in Chapters 3 – 5 are important in terms of their contribution to reducing global GHG emission budget uncertainties, more in situ emission measurement studies examining sources with little or no previous investigation are needed. As global GHG emission budgets are often underpinned by in situ observations, a more comprehensive global in situ emission dataset will allow global GHG emission budgets better reflect fine scale temporal and spatial variability in emissions, and hence provide more accurate estimates of natural and anthropogenic GHG emissions in the future.

Specific understanding of the drivers of current methane abundance growth remains a point of contention within the scientific community, it is therefore critical that more efforts focused on methane source apportionment are needed in order to accurately assess the relative contributions of sources and/or sinks to methane growth. This cannot be solely achieved by increased in situ observation of emission fluxes; other information is required to shed light on the balance between source types. As discussed in Section 1.2., studies investigating changing methane isotope ratios are crucial for understanding the balance between biogenic, thermogenic and pyrogenic methane sources on a global scale, and continued study on isotopes is crucial for refining global methane budget source contributions. Furthermore, the use of ethane as a marker for fossil-fuel methane is a key tool for assessing the relative contribution of direct anthropogenic methane emissions to global budgets, more global studies investigating ethane will improve the community understanding of fossil fuel methane emissions in context of emission budgets.

The work in this thesis focuses primarily on aircraft and ground based in situ GHG surveys. However, further efforts to reduce uncertainty in GHG emission budgets should utilise and develop all emission estimation strategies, both top-down and bottom-up. For

example, satellite-borne instruments such as TROPOMI can retrieve moderate resolution (5.5 x 7 km) total column CH₄ data for the entire globe within a period of a single day, combining the spatial coverage possible from aircraft studies with the temporal coverage of ground-based methods (Lorente et al., 2021). Inversion flux estimates derived from satellite data provide regional or even global top-down emission estimates and are therefore more directly comparable to bottom-up emission budgets. More recently, new satellite platforms have been launched that allow for targeted observation of facility-scale emission plumes at very high spatial resolution (e.g. GHGSat, Jervis et al., 2021). Observations from this new class of satellite closely follow aircraft emission quantification approaches outlined in this thesis, thus comparison between the two platforms would be a useful validation strategy.

In addition to expanded top-down emission estimation, improvement of bottom-up emission modelling is crucial for reducing GHG budget uncertainties and reconciling the discrepancies between top-down and bottom-up estimates. Process models are built upon underlying assumptions of biogeochemical GHG production processes and their sensitivity to environmental conditions (e.g. temperature, precipitation). Such processes and sensitivities must be fully characterised and understood accurately in order to yield accurate upscaled GHG emission estimates, as errors in these model parameterisations will propagate to significant systematic uncertainties in methane emission output. More detailed studies focused on soil ecology and microbial GHG production processes will help to improve the parameterisation of such processes within biogeochemical process models, resulting in improved bottom-up GHG estimation from biogenic sources (e.g. wetlands, agriculture). In conjunction with this, continued top-down emission studies are also needed to assess the constant development of process models.

In summary, this thesis presents a diverse range of in situ GHG measurement studies that, along with similar studies, will help to better represent the true variability of GHG emissions in global GHG emission budgets, and therefore reducing the uncertainty in these budgets. A more precise understanding of the contributions of all individual source categories to global budgets will help in providing more informed policy guidance on anthropogenic GHG emission abatement to limit the future impact of climate change.

6.4. Published work

6.4.1. Published

Shaw, J. T., Allen, G., Pitt, J., Mead, M. I., Purvis, R. M., Dunmore, R., Wilde, S., Shah, A., Barker, P., Bateson, P., Bacak, A., Lewis, A. C., Lowry, D., Fisher, R., Lanoisellé, M. and Ward, R. S.: A baseline of atmospheric greenhouse gases for prospective UK shale gas sites, *Sci. Total Environ.*, 684, 1–13, doi:10.1016/j.scitotenv.2019.05.266, 2019.

Candidate contribution: Calibration and maintenance of instrumentation at fracking monitoring site, data collection from instrumentation.

Shaw, J. T., Allen, G., Pitt, J., Shah, A., Wilde, S., Stamford, L., Fan, Z., Ricketts, H., Williams, P. I., Bateson, P., Barker, P., Purvis, R., Lowry, D., Fisher, R., France, J., Coleman, M., Lewis, A. C., Risk, D. A. and Ward, R. S.: Methane flux from flowback operations at a shale gas site, *J. Air Waste Manag. Assoc.*, 70(12), 1324–1339, doi:10.1080/10962247.2020.1811800, 2020.

Candidate contribution: Calibration and maintenance of instrumentation at fracking monitoring site, data collection from instrumentation.

Barker, P. A., Allen, G., Gallagher, M., Pitt, J. R., Fisher, R. E., Bannan, T., Nisbet, E. G., Bauguitte, S. J. B., Pasternak, D., Cliff, S., Schimpf, M. B., Mehra, A., Bower, K. N., Lee, J. D., Coe, H. and Percival, C. J.: Airborne measurements of fire emission factors for African biomass burning sampled during the MOYA campaign, *Atmos. Chem. Phys.*, 20(23), 15443–15459, doi:10.5194/acp-20-15443-2020, 2020.

Candidate contribution: Principal author (see Chapter 3).

Lee, J. D., Squires, F. A., Sherwen, T., Wilde, S. E., Cliff, S. J., Carpenter, L. J., Hopkins, J. R., Bauguitte, S. J., Reed, C., Barker, P., Allen, G., Bannan, T. J., Matthews, E., Mehra, A., Percival, C., Heard, D. E., Whalley, L. K., Ronnie, G. V., Seldon, S., Ingham, T., Keller, C. A., Knowland, K. E., Nisbet, E. G. and Andrews, S.: Ozone production and precursor emission from wildfires in Africa, *Environ. Sci. Atmos.*, 524–542, doi:10.1039/d1ea00041a, 2021.

Candidate contribution: Operation of ethane instrumentation aboard MOYA-II science flights in Uganda and Zambia, data collection, calibration, and processing.

Wu, H., Taylor, J. W., Langridge, J. M., Yu, C., Allan, J. D., Szpek, K., Cotterell, M. I., Williams, P. I., Flynn, M., Barker, P., Fox, C., Allen, G., Lee, J. and Coe, H.: Rapid transformation of ambient absorbing aerosols from West African biomass burning, *Atmos. Chem. Phys.*, 21(12), 9417–9440, doi:10.5194/acp-21-9417-2021, 2021.

Candidate contribution: emission ratio methodology used in this manuscript, emission factors calculated in Chapter 3 used in this manuscript.

Barker, P. A., Allen, G., Pitt, J. R., Bauguitte, S. J., Pasternak, D., Cliff, S., France, J. L., Fisher, R. E., Lee, J. D., Bower, K. N. and Nisbet, E. G.: Airborne quantification of net methane and carbon dioxide fluxes from European Arctic wetlands in Summer 2019, *Phil. Trans. R. Soc. A*, 380(20210192), 2021.

Candidate contribution: Principal author (see Chapter 4).

MOYA/ZWAMPS Team, Nisbet, E. G., Allen, G., Fisher, R. E., France, J. L., Lee, J. D., Lowry, D., Andrade, M. F., Bannan, T. J., Barker, P., Bateson, P., Bauguitte, S. J.-B., Bower, K. N., Broderick, T., Chibesakunda, F., Cain, M., Cozens, A. E., Daly, M. C., Ganesan, A. L., Jones, A. E., Lambakasa, M., Lunt, M. F., Mehra, A., Moreno, I., Pasternak, D., Palmer, P. I., Percival, C. J., Pitt, J. R., Rigby, M., Shaw, J. T., Stell, A. C., Vaughan, A. R., Warwick, N. J., Wilde, S.: Isotopic signatures of methane emissions from tropical fires and wetlands: the MOYA and ZWAMPS flights, *Philos. Trans. R. Soc. A*, 380(20210112), 2021.

Candidate contribution: Operation of trace gas instrumentation aboard MOYA and ZWAMPS flights in Uganda and Zambia, data collection, calibration, and processing. Emission factors calculated in Chapter 3 used in this study.

Ramsden, A. E., Ganesan, A. L., Western, L. M., Rigby, M., Manning, A. J., Foulds, A., France, J. L., Barker, P., Levy, P., Say, D., Wisher, A., Arnold, T., Rennick, C., Stanley, K. M., Young, D. and O'Doherty, S.: Quantifying fossil fuel methane emissions using observations of atmospheric ethane and an uncertain emission ratio, *Atmos. Chem. Phys.*, 22(6), 3911–3929, doi:10.5194/acp-22-3911-2022, 2022.

Candidate contribution: Operation of ethane instrumentation during FAAM flight C191 (MOYA-Arctic). Collection, processing, and calibration of ethane mole fraction data used in this study.

Foulds, A., Allen, G., Shaw, J. T., Bateson, P., Barker, P. A., Huang, L., Pitt, J. R., Lee, J. D., Wilde, S. E., Dominutti, P., Purvis, R. M., Lowry, D., France, J. L., Fisher, R. E., Fiehn, A., Pühl, M., Bauguitte, S. J. B., Conley, S. A., Smith, M. L., Lachlan-Cope, T., Pisso, I. and Schwietzke, S.: Quantification and assessment of methane emissions from offshore oil and gas facilities on the Norwegian continental shelf, *Atmos. Chem. Phys.*, 22(7), 4303–4322, doi:10.5194/acp-22-4303-2022, 2022.

Candidate contribution: Operation of ethane instrumentation during MOYA-Arctic oil and gas survey flights. Collection, processing, and calibration of ethane mole fraction data used in this study.

Barker, P. A., Allen, G., Flynn, M., Riddick, S. & Pitt, J. R.: Measurement of recreational N₂O emissions from an urban environment in Manchester, UK. *Urban Clim.* 46, 101282, doi:10.1016/j.uclim.2022.101282, 2022.

Candidate contribution: Principal author (see Chapter 5)

6.4.2. In review

Shaw, J. T., Foulds, A., Wilde, S., Barker, P., Squires, F., Lee, J., Purvis, R., Burton, R., Colfescu, I., Mobbs, S., Bauguitte, S. J.-B., Young, S., Schwietzke, S., and Allen, G.: Flaring efficiencies and NO_x emission ratios measured for offshore oil and gas facilities in the North Sea, *Atmos. Chem. Phys. Discuss.* [preprint], <https://doi.org/10.5194/acp-2022-679>, in review, 2022.

Candidate contribution: Operation of ethane instrumentation during MOYA-Arctic oil and gas survey flights. Collection, processing, and calibration of ethane mole fraction data used in this study. Assistance given on instrument calibration description and emission ratio calculation.

References

Akagi, S. K., Yokelson, R. J., Wiedinmyer, C., Alvarado, M. J., Reid, J. S., Karl, T., Crounse, J. D. and Wennberg, P. O.: Emission factors for open and domestic biomass burning for use in atmospheric models, *Atmos. Chem. Phys.*, 11(9), 4039–4072, doi:10.5194/acp-11-4039-2011, 2011.

Alam, S.A., Rintala, J.M., Ahlgren, K. and Juurola, E. (eds.), ICOS Handbook: Knowledge through observations. ©ICOS ERIC, 2019.

Allan, W., Struthers, H. and Lowe, D. C.: Methane carbon isotope effects caused by atomic chlorine in the marine boundary layer: Global model results compared with Southern Hemisphere measurements, *J. Geophys. Res. Atmos.*, 112(4), 1–10, doi:10.1029/2006JD007369, 2007.

Allen, M.R., O.P. Dube, W. Solecki, F. Aragón-Durand, W. Cramer, S. Humphreys, M. Kainuma, J. Kala, N. Mahowald, Y. Mulugetta, R. Perez, M. Wairiu, and K. Zickfeld: Framing and Context. In: Global Warming of 1.5°C. An IPCC Special Report on the impacts of global warming of 1.5°C above pre-industrial levels and related global greenhouse gas emission pathways, in the context of strengthening the global response to the threat of climate change, sustainable development, and efforts to eradicate poverty [Masson-Delmotte, V., P. Zhai, H.-O. Pörtner, D. Roberts, J. Skea, P.R. Shukla, A. Pirani, W. Moufouma-Okia, C. Péan, R. Pidcock, S. Connors, J.B.R. Matthews, Y. Chen, X. Zhou, M.I. Gomis, E. Lonnoy, T. Maycock, M. Tignor, and T. Waterfield (eds.)]. Cambridge University Press, Cambridge, UK and New York, NY, USA, pp. 49-92. doi:10.1017/9781009157940.003, 2018.

Ambus, P., Clayton, H., Arah, J. R. M., Smith, K. A. and Christensen, S.: Similar N₂O flux from soil measured with different chamber techniques, *Atmos. Environ. Part A, Gen. Top.*, 27(1), 121–123, doi:10.1016/0960-1686(93)90078-D, 1993.

Anderson, D. C., Duncan, B. N., Fiore, A. M., Baublitz, C. B., Follette-Cook, M. B., Nicely, J. M. and Wolfe, G. M.: Spatial and temporal variability in the hydroxyl (OH) radical: Understanding the role of large-scale climate features and their influence on OH through its dynamical and photochemical drivers. *Atmos. Chem. Phys.* 21, 6481–6508, doi:10.5194/acp-21-6481-2021, 2021.

Anderson, W., Seager, R., Baethgen, W. and Cane, M.: Life cycles of agriculturally relevant ENSO teleconnections in North and South America, *Int. J. Climatol.*, 37(8), 3297–3318, doi:10.1002/joc.4916, 2017.

Andreae, M.: Emission of trace gases and aerosols from biomass burning -- An updated assessment, *Atmos. Chem. Phys. Discuss.*, 19, 8523–8546, doi:10.5194/acp-19-8523-2019, 2019.

Angot, H., Davel, C., Wiedinmyer, C., Pétron, G., Chopra, J., Hueber, J., Blanchard, B., Bourgeois, I., Vimont, I., Montzka, S. A., Miller, B. R., Elkins, J. W. and Helmig, D.: Temporary pause in the growth of atmospheric ethane and propane in 2015-2018, *Atmos. Chem. Phys.*, 21(19), 15153–15170, doi:10.5194/acp-21-15153-2021, 2021. Archer, D.: Methane hydrate stability and anthropogenic climate change, *Biogeosciences*, 4(4), 521–544, doi:10.5194/bg-4-521-2007, 2007.

Aubinet, M. et al. (eds.), Eddy Covariance: A Practical Guide to Measurement and Data Analysis, Springer Atmospheric Sciences, DOI 10.1007/978-94-007-2351-1 1 1, ©Springer Science & Business Media B.V., 2012.

Babbin, A. R., Bianchi, D., Jayakumar, A. and Ward, B. B.: Rapid nitrous oxide cycling in the suboxic ocean, *Science*, 348(6239), 1127–1129, doi:10.1126/science.aaa8380, 2015.

Babbin, A. R., Boles, E. L., Mühle, J. and Weiss, R. F.: On the natural spatio-temporal heterogeneity of South Pacific nitrous oxide, *Nat. Commun.*, 11(1), 1–9, doi:10.1038/s41467-020-17509-6, 2020.

Baer, D. S., Paul, J. B., Gupta, M. and O’Keefe, A.: Sensitive absorption measurements in the near-infrared region using off-axis integrated-cavity-output spectroscopy, *Appl. Phys. B Lasers Opt.*, 75(2–3), 261–265, doi:10.1007/s00340-002-0971-z, 2002.

Bakun, A. and Broad, K.: Environmental “loopholes” and fish population dynamics: Comparative pattern recognition with focus on El Niño effects in the Pacific, *Fish. Oceanogr.*, 12(4–5), 458–473, doi:10.1046/j.1365-2419.2003.00258.x, 2003.

Baldocchi, D. D.: Assessing the Eddy Covariance Technique for Evaluating the Carbon Balance of Ecosystems, *Glob. Chang. Biol.*, 9(4), 1–41, 2003.

Baldocchi, D., Falge, E., Gu, L., Olson, R., Hollinger, D., Running, S., Anthoni, P., Bernhofer, C., Davis, K., Evans, R., Fuentes, J., Goldstein, A., Katul, G., Law, B., Lee, X., Malhi, Y., Meyers, T., Munger, W., Oechel, W., Paw, U. K. T., Pilegaard, K., Schmid, H. P., Valentini, R., Verma, S., Vesala, T., Wilson, K. and Wofsy, S.: FLUXNET: A New Tool to Study the Temporal and Spatial Variability of Ecosystem-Scale Carbon Dioxide, Water Vapor, and Energy Flux Densities, *Bull. Am. Meteorol. Soc.*, 82(11), 2415–2434, doi:10.1175/1520-0477(2001)082<2415:FANTTS>2.3.CO;2, 2001.

Battaglia, G. and Joos, F.: Marine N₂O Emissions from Nitrification and Denitrification Constrained by Modern Observations and Projected in Multimillennial Global Warming Simulations, *Global Biogeochem. Cycles*, 32(1), 92–121, doi:10.1002/2017GB005671, 2018.

Berger, A., Mélice, J. L. and Loutre, M. F.: On the origin of the 100-kyr cycles in the astronomical forcing, *Paleoceanography*, 20(4), doi:10.1029/2005PA001173, 2005.

Blake, G. A., Liang, M., Morgan, C. G. and Yung, Y. L.: Photolytic fractionation of stratospheric nitrous oxide, *Geophys. Res. Lett.*, 106(A6), 1–5, 2002.

Borsdorff, T., Aan De Brugh, J., Hu, H., Hasekamp, O., Sussmann, R., Rettinger, M., Hase, F., Gross, J., Schneider, M., Garcia, O., Stremme, W., Grutter, M., Feist, Di. G., Arnold, S. G., De Mazière, M., Kumar Sha, M., Pollard, D. F., Kiel, M., Roehl, C., Wennberg, P. O., Toon, G. C. and Landgraf, J.: Mapping carbon monoxide pollution from space down to city scales with daily global coverage, *Atmos. Meas. Tech.*, 11(10), 5507–5518, doi:10.5194/amt-11-5507-2018, 2018.

Bousquet, P., Ciais, P., Miller, J. B., Dlugokencky, E. J., Hauglustaine, D. A., Prigent, C., Van Der Werf, G. R., Peylin, P., Brunke, E. G., Carouge, C., Langenfelds, R. L., Lathière, J., Papa, F., Ramonet, M., Schmidt, M., Steele, L. P., Tyler, S. C. and White, J.: Contribution of anthropogenic and natural sources to atmospheric methane variability, *Nature*, 443(7110), 439–443, doi:10.1038/nature05132, 2006.

Bouwman, A.: Direct emission of nitrous oxide from agricultural soils, *Nutr. Cycl. Agroecosystems*, 46(1), 53–70, 1996.

Bowling, D. R., Turnipseed, A. A., Delany, A. C., Baldocchi, D. D., Greenberg, J. P. and Monson, R. K.: The use of relaxed eddy accumulation to measure biosphere-

atmosphere exchange of isoprene and other biological trace gases, *Oecologia*, 116(3), 306–315, doi:10.1007/s004420050592, 1998.

Bremner, J.: Sources of nitrous oxide in soils, *Nutr. Cycl. Agroecosystems*, 49(1–3), 7–16, 1997.

Bridgham, S. D., Cadillo-Quiroz, H., Keller, J. K. and Zhuang, Q.: Methane emissions from wetlands: Biogeochemical, microbial, and modeling perspectives from local to global scales, *Glob. Chang. Biol.*, 19(5), 1325–1346, doi:10.1111/gcb.12131, 2013.

Butterbach-Bahl, K., Baggs, E., Dannenmann, M., Kiese, R. and Zechmeister-Boltenstern, S.: Nitrous oxide emissions from soils: how well do we understand the processes and their controls?, *Phil. Trans. R. Soc. B*, 368(1621), 20130122, 2013.

Caccamo, M. T. and Magazù, S.: On the breaking of the Milankovitch cycles triggered by temperature increase: The stochastic resonance response, *Climate*, 9(4), doi:10.3390/cli9040067, 2021.

Cambaliza, M. O. L., Shepson, P. B., Caulton, D. R., Stirn, B., Samarov, D., Gurney, K. R., Turnbull, J., Davis, K. J., Possolo, A., Karion, A., Sweeney, C., Moser, B., Hendricks, A., Lauvaux, T., Mays, K., Whetstone, J., Huang, J., Razlivanov, I., Miles, N. L. and Richardson, S. J.: Assessment of uncertainties of an aircraft-based mass balance approach for quantifying urban greenhouse gas emissions, *Atmos. Chem. Phys.*, 14(17), 9029–9050, doi:10.5194/acp-14-9029-2014, 2014.

Canty, T. and Minschwaner, K.: Seasonal and solar cycle variability of OH in the middle atmosphere, *J. Geophys. Res. Atmos.*, 107(24), 1–6, doi:10.1029/2002JD002278, 2002.

Chandra, J. and Paul, R.: The current state of aerosol-radiation interactions: A mini review, *J. Aerosol Sci.*, 130(December 2018), 45–54, doi:10.1016/j.jaerosci.2018.12.010, 2019.

Chanton, J. P., Rutkowski, C. M., Schwartz, C. C., Ward, D. E. and Boring, L.: Factors influencing the stable carbon isotopic signature of methane from combustion and biomass burning, *J. Geophys. Res. Atmos.*, doi:10.1029/1999JD900909, 2000.

Chapuis-lardy, L., Wrage, N., Metay, A., Chotte, J. L. and Bernoux, M.: Soils, a sink for N₂O? A review, *Glob. Chang. Biol.*, 13(1), 1–17, doi:10.1111/j.1365-2486.2006.01280.x, 2007.

Chen, Y. H. and Prinn, R. G.: Estimation of atmospheric methane emissions between 1996 and 2001 using a three-dimensional global chemical transport model, *J. Geophys. Res. Atmos.*, 111(10), doi:10.1029/2005JD006058, 2006.

Chodur, G. M., Zhao, X., Biehl, E., Mitrani-Reiser, J. and Neff, R.: Assessing food system vulnerabilities: a fault tree modelling approach, *BMC Public Health*, 18, 1–11, doi:10.1186/s12889-018-5563-x, 2018.

Christensen, T. R., Johansson, T., Åkerman, H. J., Mastepanov, M., Malmer, N., Friborg, T. and Svensson, B. H.: Thawing sub-arctic permafrost: Effects on vegetation and methane emissions, *Geophys. Res. Lett.*, 31(4), L04501, doi:10.1029/2003GL018680, 2004.

Clark, D. B., Mercado, L. M., Sitch, S., Jones, C. D., Gedney, N., Best, M. J., Pryor, M., Rooney, G. G., Essery, R. L. H., Blyth, E., Boucher, O., Harding, R. J., Huntingford, C. and Cox, P. M.: The Joint UK Land Environment Simulator (JULES), model description – Part 2: Carbon fluxes and vegetation dynamics, *Geosci. Model Dev.*, 4(3), 701–722, doi:10.5194/gmd-4-701-2011, 2011.

Collier, S. M., Ruark, M. D., Oates, L. G., Jokela, W. E. and Dell, C. J.: Measurement of greenhouse gas flux from agricultural soils using static chambers, *J. Vis. Exp.*, (90), 1–8, doi:10.3791/52110, 2014.

Crevoisier, C., Nobileau, D., Armante, R., Crépeau, L., Machida, T., Sawa, Y., Matsueda, H., Schuck, T., Thonat, T., Pernin, J., Scott, N. A. and Chédin, A.: The 2007–2011 evolution of tropical methane in the mid-troposphere as seen from space by MetOp-A/IASI, *Atmos. Chem. Phys.*, 13(8), 4279–4289, doi:10.5194/acp-13-4279-2013, 2013.

Daelman, M. R. J., van Voorthuizen, E. M., van Dongen, U. G. J. M., Volcke, E. I. P. and van Loosdrecht, M. C. M.: Methane emission during municipal wastewater treatment, *Water Res.*, 46(11), 3657–3670, doi:10.1016/j.watres.2012.04.024, 2012.

Dai, A., Luo, D., Song, M. and Liu, J.: Arctic amplification is caused by sea-ice loss under increasing CO₂, *Nat. Commun.*, 10(1), 1–13, doi:10.1038/s41467-018-07954-9, 2019.

Davey, M. K., Brookshaw, A. and Ineson, S.: The probability of the impact of ENSO on precipitation and near-surface temperature, *Clim. Risk Manag.*, 1, 5–24, doi:10.1016/j.crm.2013.12.002, 2014.

Davidson, E. A., De Carvalho, C. J. R., Figueira, A. M., Ishida, F. Y., Ometto, J. P. H. B., Nardoto, G. B., Sabá, R. T., Hayashi, S. N., Leal, E. C., Vieira, I. C. G. and Martinelli, L. A.: Recuperation of nitrogen cycling in Amazonian forests following agricultural abandonment, *Nature*, 447(7147), 995–998, doi:10.1038/nature05900, 2007.

Desai, A. R., Xu, K., Tian, H., Weishampel, P., Thom, J., Baumann, D., Andrews, A. E., Cook, B. D., King, J. Y. and Kolka, R.: Landscape-level terrestrial methane flux observed from a very tall tower, *Agric. For. Meteorol.*, 201, 61–75, doi:10.1016/j.agrformet.2014.10.017, 2015.

Di Trapani, D., Di Bella, G. and Viviani, G.: Uncontrolled methane emissions from a MSW landfill surface: Influence of landfill features and side slopes, *Waste Manag.*, 33(10), 2108–2115, doi:10.1016/j.wasman.2013.01.032, 2013.

Dlugokencky, E. J., Bruhwiler, L., White, J. W. C., Emmons, L. K., Novelli, P. C., Montzka, S. A., Masarie, K. A., Lang, P. M., Crotwell, A. M., Miller, J. B. and Gatti, L. V.: Observational constraints on recent increases in the atmospheric CH₄ burden, *Geophys. Res. Lett.*, 36(18), 3–7, doi:10.1029/2009GL039780, 2009.

Dlugokencky, E. J., Masarie, K. A., Lang, P. M., Tans, P. P., Steele, L. P., and Nisbet, E. G.: A dramatic decrease in the growth rate of atmospheric methane in the northern hemisphere during 1992, *Geophys. Res. Lett.*, 21(1), 45–48, doi:10.1029/93GL03070, 1994.

Dlugokencky, E. J., Nisbet, E. G., Fisher, R. and Lowry, D.: Global atmospheric methane: Budget, changes and dangers, *Philos. Trans. R. Soc. A Math. Phys. Eng. Sci.*, 369(1943), 2058–2072, doi:10.1098/rsta.2010.0341, 2011.

Environmental Defense Fund: MethaneSAT, <https://www.methanesat.org/>, (Accessed 18 September 2022), 2022.

Ehhalt, D. and Prather, M.: Atmospheric Chemistry and Greenhouse Gases, in: Climate Change 2001; Working Group 1: The Scientific Basis, Houghton, J., Ding, Y., Griggs, D., Noguer, M., van der Linden, P., and Xiaosu, D (eds.), Cambridge University Press, doi:10.2753/JES1097-203X330403 2001.

Ehhalt, D. H.: The atmospheric cycle of methane, *Tellus*, 26(1–2), 58–70, doi:10.3402/tellusa.v26i1-2.9737, 1974.

Etiope, G. and Sherwood L. B.: Abiotic methane on earth, *Rev. Geophys.*, 51(2), 276–299, doi:10.1002/rog.20011, 2013.

Eyer, S., Tuzson, B., Popa, M. E., Van Der Veen, C., Röckmann, T., Rothe, M., Brand, W. A., Fisher, R., Lowry, D., Nisbet, E. G., Brennwald, M. S., Harris, E., Zellweger, C., Emmenegger, L., Fischer, H. and Mohn, J.: Real-time analysis of $\delta^{13}\text{C}$ - And $\delta\text{D-CH}_4$ in ambient air with laser spectroscopy: Method development and first intercomparison results, *Atmos. Meas. Tech.*, 9(1), 263–280, doi:10.5194/amt-9-263-2016, 2016.

Famulari, D., Nemitz, E., Di Marco, C., Phillips, G. J., Thomas, R., House, E. and Fowler, D.: Eddy-covariance measurements of nitrous oxide fluxes above a city, *Agric. For. Meteorol.*, 150(6), 786–793, doi:10.1016/j.agrformet.2009.08.003, 2010.

Firestone, M. K. and Davidson, E. A.: Microbiological Basis of NO and N₂O production and consumption in soil, *Exch. Trace Gases between Terr. Ecosyst. Atmos.*, 47, 7–21, 1989.

Fisher, R., Lowry, D., Wilkin, O., Sriskantharajah, S. and Nisbet, E. G.: High-precision, automated stable isotope analysis of atmospheric methane and carbon dioxide using continuous-flow isotope-ratio mass spectrometry. *Rapid Commun. Mass Spectrom.*, 20(2), 200–208, 2005.

Fishman, J. and Crutzen, P. J.: The origin of ozone in the troposphere, *Nature*, 274(5674), 855–858, doi:10.1038/274855a0, 1978.

Franco, B., Mahieu, E., Emmons, L. K., Tzompa-Sosa, Z. A., Fischer, E. V., Sudo, K., Bovy, B., Conway, S., Griffin, D., Hannigan, J. W., Strong, K. and Walker, K. A.: Evaluating ethane and methane emissions associated with the development of oil and natural gas extraction in North America, *Environ. Res. Lett.*, 11(4), doi:10.1088/1748-9326/11/4/044010, 2016.

Freing, A., Wallace, D. and Bange, H.: Global oceanic production of nitrous oxide, *Philos. Trans. R. Soc. London B Biol. Sci.*, 367(1593), 1245–1255, 2012.

Ganesan, A. L., Manning, A. J., Grant, A., Young, D., Oram, D. E., Sturges, W. T., Moncrieff, J. B. and O'Doherty, S.: Quantifying methane and nitrous oxide emissions

from the UK and Ireland using a national-scale monitoring network, *Atmos. Chem. Phys.*, 15(11), 6393–6406, doi:10.5194/acp-15-6393-2015, 2015.

Ganopolski, A., Winkelmann, R. and Schellnhuber, H. J.: Critical insolation-CO₂ relation for diagnosing past and future glacial inception, *Nature*, 529(7585), 200–203, doi:10.1038/nature16494, 2016.

Gedney, N., Cox, P. M. and Huntingford, C.: Climate feedback from wetland methane emissions, *Geophys. Res. Lett.*, 31(20), 1–4, doi:10.1029/2004GL020919, 2004.

Gergis, J. L. and Fowler, A. M.: A history of ENSO events since A.D. 1525: Implications for future climate change, *Clim. Change*, 92, 343–387, doi:10.1007/s10584-008-9476-z, 2009.

Goessling, H. F. and Bathiany, S.: Why CO₂ cools the middle atmosphere-a consolidating model perspective, *Earth Syst. Dyn.*, 7(3), 697–715, doi:10.5194/esd-7-697-2016, 2016.

Goulden, M. L., Munger, J. W., Fan, S. M., Daube, B. C. and Wofsy, S. C.: Measurements of carbon sequestration by long-term eddy covariance: Methods and a critical evaluation of accuracy, *Glob. Chang. Biol.*, 2(3), 169–182, doi:10.1111/j.1365-2486.1996.tb00070.x, 1996.

Gupta, M., Jiao, H. and O’Keefe, A.: Cavity-enhanced spectroscopy in optical fibers, *Opt. Lett.*, 27(21), 1878, doi:10.1364/ol.27.001878, 2002.

Gvakharia, A., Kort, E. A., Smith, M. L. and Conley, S.: Evaluating Cropland N₂O Emissions and Fertilizer Plant Greenhouse Gas Emissions With Airborne Observations, *J. Geophys. Res. Atmos.*, 125(16), 1–13, doi:10.1029/2020JD032815, 2020.

Hall, B. D., Dutton, G. S. and Elkins, J. W.: The NOAA nitrous oxide standard scale for atmospheric observations, *J. Geophys. Res. Atmos.*, 112(9), 1–9, doi:10.1029/2006JD007954, 2007.

Hargreaves, K. J., Fowler, D., Pitcairn, C. E. R. and Aurela, M.: Annual methane emission from Finnish mires estimated from eddy covariance campaign measurements, *Theor. Appl. Climatol.*, 70(1–4), 203–213, doi:10.1007/s007040170015, 2001.

Harley, J., W. Nel, and V. Pretorius.: Flame ionization detector for gas chromatography. *Nature*, 181(4603), 177–178, 1958.

Hays, J. D., Imbrie, J., Shackleton, N. J.: Variations in the Earth's Orbit: Pacemaker of the Ice Ages, *Science*, 194(4270), 1121–1132, 1976.

Heimbürger, A. M. F., Harvey, R. M., Shepson, P. B., Stirm, B. H., Gore, C., Turnbull, J., Cambaliza, M. O. L., Salmon, O. E., Kerlo, A. E. M., Lavoie, T. N., Davis, K. J., Lauvaux, T., Karion, A., Sweeney, C., Brewer, W. A., Hardesty, R. M. and Gurney, K. R.: Assessing the optimized precision of the aircraft mass balance method for measurement of urban greenhouse gas emission rates through averaging, *Elementa*, 5, doi:10.1525/elementa.134, 2017.

Heiskanen, J., Brümmer, C., Buchmann, N., Calfapietra, C., Chen, H., Gielen, B., Gkritzalis, T., Hammer, S., Hartman, S., Herbst, M., et al.: The integrated carbon observation system in Europe, *Bull. Am. Meteorol. Soc.*, 103(3), E855–E872, 2022.

Hoare, D., Jones, R. L., Harris, N. R. P., Ferracci, V., Carruthers, D., Stidworthy, A., Forsyth, E. and Rigby, M.: Development of an urban greenhouse gas modelling system to support a London monitoring network, *Weather*, 75(11), 353–359, doi:10.1002/wea.3795, 2020.

Hossaini, R., Chipperfield, M. P., Saiz-Lopez, A., Fernandez, R., Monks, S., Feng, W., Brauer, P. and Von Glasow, R.: A global model of tropospheric chlorine chemistry: Organic versus inorganic sources and impact on methane oxidation, *J. Geophys. Res.*, 121(23), 14,271–14,297, doi:10.1002/2016JD025756, 2016.

Hu, H., Landgraf, J., Detmers, R., Borsdorff, T., Aan de Brugh, J., Aben, I., Butz, A. and Hasekamp, O.: Toward Global Mapping of Methane With TROPOMI: First Results and Intersatellite Comparison to GOSAT, *Geophys. Res. Lett.*, 45(8), 3682–3689, doi:10.1002/2018GL077259, 2018.

IAGOS: In-service Aircraft for a Global Observing System, <https://iagos.aeris-data.fr/>, (Accessed 18 September 2022), 2022.

Imbrie, J., Berger, A., Boyle, E. A., Clemens, S. C., Duffy, A., Howard, W. R., and Toggweiler, J. R.: On the structure and origin of major glaciation cycles 2. The 100,000-year cycle. *Paleoceanography*, 8(6), 699–735, doi:10.1029/93PA02751, 1993.

IPCC: The Earth's Energy Budget, Climate Feedbacks, and Climate Sensitivity. In Climate Change 2021: The Physical Science Basis. Contribution of Working Group I to the Sixth Assessment Report of the Intergovernmental Panel on Climate Change.

Masson-Delmotte, V., P. Zhai, A. Pirani, S.L. Connors, C. Péan, S. Berger, N. Caud, Y. Chen, L. Goldfarb, M.I. Gomis, M. Huang, K. Leitzell, E. Lonnoy, J.B.R. Matthews, T.K. Maycock, T. Waterfield, O. Yelekçi, R. Yu, and B. Zhou (eds.). Cambridge University Press, 923 Cambridge, United Kingdom and New York, NY, USA, pp. 923–1054, doi:10.1017/9781009157896.009, 2021a.

IPCC: Global Carbon and other Biogeochemical Cycles and Feedbacks. In Climate Change 2021: The Physical Science Basis. Contribution of Working Group I to the Sixth Assessment Report of the Intergovernmental Panel on Climate Change. Masson-Delmotte, V., P. Zhai, A. Pirani, S.L. Connors, C. Péan, S. Berger, N. Caud, Y. Chen, L. Goldfarb, M.I. Gomis, M. Huang, K. Leitzell, E. Lonnoy, J.B.R. Matthews, T.K. Maycock, T. Waterfield, O. Yelekçi, R. Yu, and B. Zhou (eds.). Cambridge University Press, Cambridge, United Kingdom and New York, NY, USA, pp. 673–816, doi:10.1017/9781009157896.007, 2021b.

Ishijima, K., Sugawara, S., Kawamura, K., Hashida, G., Morimoto, S., Murayama, S., Aoki, S. and Nakazawa, T.: Temporal variations of the atmospheric nitrous oxide concentration and its $\delta^{15}\text{N}$ and $\delta^{18}\text{O}$ for the latter half of the 20th century reconstructed from firn air analyses, *J. Geophys. Res. Atmos.*, 112(3), doi:10.1029/2006JD007208, 2007.

Ishijima, K., Patra, P. K., Takigawa, M., Machida, T., Matsueda, H., Sawa, Y., Steele, L. P., Krummel, P. B., Langenfelds, R. L., Aoki, S. and Nakazawa, T.: Stratospheric influence on the seasonal cycle of nitrous oxide in the troposphere as deduced from aircraft observations and model simulations, *J. Geophys. Res. Atmos.*, 115(20), 1–15, doi:10.1029/2009JD013322, 2010.

Järvi, L., Nordbo, A., Rannik, Ü., Haapanala, S., Mammarella, I., Pihlatie, M., Vesala, T. and Riikonen, A.: Urban nitrous-oxide fluxes measured using the eddy-covariance technique in Helsinki, Finland, *Boreal Environ. Res.*, 19(B), 108–121, 2014.

Jiang, X., Ku, W. L., Shia, R. L., Li, Q., Elkins, J. W., Prinn, R. G. and Yung, Y. L.: Seasonal cycle of N_2O : Analysis of data, *Global Biogeochem. Cycles*, 21(1), doi:10.1029/2006GB002691, 2007.

Johnson, K. A., & Johnson, D. E.: Methane emissions from cattle. *J. Anim. Sci.*, 73(8), 2483–2492, doi:10.2527/1995.7382483x, 1995.

Jouzel, J., Masson-Delmotte, V., Cattani, O., Dreyfus, G., Falourd, S., Hoffmann, G., Minster, B., Nouet, J., Barnola, J. M., Chappellaz, J., Fischer, H., Gallet, J. C., Johnsen, S., Leuenberger, M., Loulergue, L., Luethi, D., Oerter, H., Parrenin, F., Raisbeck, G., Raynaud, D., Schilt, A., Schwander, J., Selmo, E., Souchez, R., Spahni, R., Stauffer, B., Steffensen, J. P., Stenni, B., Stocker, T. F., Tison, J. L., Werner, M. and Wolff, E. W.: Orbital and millennial Antarctic climate variability over the past 800,000 years, *Science*, 317(5839), 793–796, doi:10.1126/science.1141038, 2007.

Karion, A., Sweeney, C., Kort, E. A., Shepson, P. B., Brewer, A., Cambaliza, M., Conley, S. A., Davis, K., Deng, A., Hardesty, M., Herndon, S. C., Lauvaux, T., Lavoie, T., Lyon, D., Newberger, T., Pétron, G., Rella, C., Smith, M., Wolter, S., Yacovitch, T. I. and Tans, P.: Aircraft-Based Estimate of Total Methane Emissions from the Barnett Shale Region, *Environ. Sci. Technol.*, 49(13), 8124–8131, doi:10.1021/acs.est.5b00217, 2015.

Kaufman, D. S., Schneider, D. P., McKay, N. P., Ammann, C. M., Bradley, R. S., Briffa, K. R., Miller, G. H., Otto-bliesner, B. L., Overpeck, J. T. and Vinther, B. M.: Recent Warming Reverses Long-Term Arctic Cooling, *Science*, 325, 1236–1239, 2009.

Khalil, M. A. K. and Rasmussen, R. A.: Sources, sinks, and seasonal cycles of atmospheric methane, *J. Geophys. Res.*, 88(C9), 5131–5144, doi:10.1029/JC088iC09p05131, 1983.

Kirschke, S., Bousquet, P., Ciais, P., Saunio, M., Canadell, J., Dlugokencky, E., Bergamaschi, P., Bergmann, D., Blake, D., Bruhwiler, L. and others: Three decades of global methane sources and sinks, *Nat. Geosci.*, 6(10), 813, 2013.

Kortenkamp, S. J. and Dermott, S. F.: A 100,000-year periodicity in the accretion rate of interplanetary dust, *Science*, 280(5365), 874–876, doi:10.1126/science.280.5365.874, 1998.

Krautstrunk, M., Giez, A. The Transition From FALCON to HALO Era Airborne Atmospheric Research. In: Schumann, U. (eds.) Atmospheric Physics. Research Topics in Aerospace. Springer, Berlin, Heidelberg. doi:10.1007/978-3-642-30183-4_37, 2012.

Kvenvolden, K. A: Methane hydrates and global climate. *Glob. Biogeochem. Cycles*, 2(3), 221-229, doi:10.1029/GB002i003p00221 1988

Lambert, F., Delmonte, B., Petit, J. R., Bigler, M., Kaufmann, P. R., Hutterli, M. A., Stocker, T. F., Ruth, U., Steffensen, J. P. and Maggi, V.: Dust - Climate couplings over the past 800,000 years from the EPICA Dome C ice core, *Nature*, 452(7187), 616–619, doi:10.1038/nature06763, 2008.

Laris, P., Koné, M., Dembélé, F., Rodrigue, C. M., Yang, L., Jacobs, R., and Laris, Q.: Methane gas emissions from savanna fires: what analysis of local burning regimes in a working West African landscape tell us, *Biogeosciences*, 18, 6229–6244, <https://doi.org/10.5194/bg-18-6229-2021>, 2021.

Le Fevre, C.: Methane Emissions: from blind spot to spotlight. <https://www.oxfordenergy.org/wpcms/wp-content/uploads/2017/07/Methane-Emissions-from-blind-spot-to-spotlight-NG-122.pdf> (Accessed 13/11/2022), 2017.

Le Quéré, C., Andrew, R. M., Friedlingstein, P., Sitch, S., Pongratz, J., Manning, A. C., Korsbakken, J. I., Peters, G. P., Canadell, J. G., Jackson, R. B., Boden, T. A., Tans, P. P. et al.: Global Carbon Budget 2018, *Earth Syst. Sci. Data.*, 10(4), 2141-2194, doi:10.5194/essd-10-2141-2018, 2018.

Lear, C. H., Billups, K., Rickaby, R. E. M., Diester-Haass, L., Mawbey, E. M. and Soshian, S. M.: Breathing more deeply: Deep Ocean carbon storage during the mid-Pleistocene climate transition, *Geology*, 44(12), 1035–1038, doi:10.1130/G38636.1, 2016.

Lee, J. E., Shen, A., Fox-Kemper, B. and Ming, Y.: Hemispheric sea ice distribution sets the glacial tempo, *Geophys. Res. Lett.*, 44(2), 1008–1014, doi:10.1002/2016GL071307, 2017.

Levin, I., Ciais, P., Langenfelds, R., Schmidt, M., Ramonet, M., Sidorov, K., Tchepakova, N., Gloor, M., Heimann, M., Schulze, E.-D., Vygodskaya, N. N., Shibistova, O. and Lloyd, J.: Three years of trace gas observations over the EuroSiberian domain derived from aircraft sampling — a concerted action, *Tellus B Chem. Phys. Meteorol.*, 54(5), 696–712, doi:10.3402/tellusb.v54i5.16717, 2002.

Liang, S., Wang, J. (eds.). Estimate of vegetation production of terrestrial ecosystem. In: Advanced remote sensing: terrestrial information extraction and applications. ©Academic Press, 2019.

Liao, T., Camp, C. D. and Yung, Y. L.: The seasonal cycle of N₂O, *Geophys. Res. Lett.*, 31(17), 3–5, doi:10.1029/2004GL020345, 2004.

Lisiecki, L. E.: Links between eccentricity forcing and the 100,000-year glacial cycle, *Nat. Geosci.*, 3(5), 349–352, doi:10.1038/ngeo828, 2010.

Liu, M., van der A, R., van Weele, M., Eskes, H., Lu, X., Veefkind, P., de Laat, J., Kong, H., Wang, J., Sun, J., Ding, J., Zhao, Y. and Weng, H.: A New Divergence Method to Quantify Methane Emissions Using Observations of Sentinel-5P TROPOMI, *Geophys. Res. Lett.*, 48(18), 1–10, doi:10.1029/2021GL094151, 2021.

Lorente, A., Borsdorff, T., Butz, A., Hasekamp, O., Aan De Brugh, J., Schneider, A., Wu, L., Hase, F., Kivi, R., Wunch, D., Pollard, D. F., Shiomi, K., Deutscher, N. M., Velasco, V. A., Roehl, C. M., Wennberg, P. O., Warneke, T. and Landgraf, J.: Methane retrieved from TROPOMI: Improvement of the data product and validation of the first 2 years of measurements, *Atmos. Meas. Tech.*, 14(1), 665–684, doi:10.5194/amt-14-665-2021, 2021.

Lourens, L. J.: The variation of the Earth's movements (orbital, tilt, and precession) and climate change. In: *Climate Change: Observed Impacts on Planet Earth*, 583-606, ©Elsevier B.V., doi:10.1016/B978-0-12-821575-3.00028-1, 2021.

Lunt, M. F., Palmer, P. I., Lorente, A., Borsdorff, T., Landgraf, J., Parker, R. J. and Boesch, H.: Rain-fed pulses of methane from East Africa during 2018-2019 contributed to atmospheric growth rate, *Environ. Res. Lett.*, 16(2), 024021, doi:10.1088/1748-9326/abd8fa, 2021.

Maione, M., Graziosi, F., Arduini, J., Furlani, F., Giostra, U., Blake, D. R., Bonasoni, P., Fang, X., Montzka, S. A., O'Doherty, S. J., Reimann, S., Stohl, A. and Vollmer, M. K.: Estimates of European emissions of methyl chloroform using a Bayesian inversion method, *Atmos. Chem. Phys.*, 14(18), 9755–9770, doi:10.5194/acp-14-9755-2014, 2014.

Maithani, S. and Pradhan, M.: Cavity ring-down spectroscopy and its applications to environmental, chemical and biomedical systems, *J. Chem. Sci.*, 132(1), 1–19, doi:10.1007/s12039-020-01817-x, 2020.

Mann, M. E., Lloyd, E. A. and Oreskes, N.: Assessing climate change impacts on extreme weather events: the case for an alternative (Bayesian) approach, *Clim. Change*, 144, 131–142, doi:10.1007/s10584-017-2048-3, 2017.

Manning, A. J., O'Doherty, S., Jones, A. R., Simmonds, P. G. and Derwent, R. G.: Estimating UK methane and nitrous oxide emissions from 1990 to 2007 using an inversion modeling approach, *J. Geophys. Res. Atmos.*, 116(2), 1–19, doi:10.1029/2010JD014763, 2011.

Marsh, G. E.: Interglacials, Milankovitch Cycles, Solar Activity, and Carbon Dioxide, *J. Climatol.*, 1–7, doi:10.1155/2014/345482, 2014.

Matus, A. V. and L'Ecuyer, T. S.: The role of cloud phase in Earth's radiation budget, *J. Geophys. Res.*, 122(5), 2559–2578, doi:10.1002/2016JD025951, 2017.

Mays, K. L., Shepson, P. B., Stirm, B. H., Karion, A., Sweeney, C. and Gurney, K. R.: Aircraft-based measurements of the carbon footprint of Indianapolis, *Environ. Sci. Technol.*, 43(20), 7816–7823, doi:10.1021/es901326b, 2009.

McBeath, K.: The use of aircraft for meteorological research in the United Kingdom, *Meteorol. Appl.*, 21(1), 105–116, doi:10.1002/met.1448, 2014.

McGuire, A. D., Anderson, L. G., Christensen, T. R., Scott, D., Laodong, G., Hayes, D. J., Martin, H., Lorenson, T. D., Macdonald, R. W. and Nigel, R.: Sensitivity of the carbon cycle in the Arctic to climate change, *Ecol. Monogr.*, 79(4), 523–555, doi:10.1890/08-2025.1, 2009.

McInnes, K. J. and Heilman, J. L.: Relaxed eddy accumulation, *Micrometeorology Agric. Syst.*, (47), 437–453, doi:10.2134/agronmonogr47.c19, 2015.

McNorton, J., Gloor, E., Wilson, C., Hayman, G. D., Gedney, N., Comyn-Platt, E., Marthews, T., Parker, R. J., Boesch, H., and Chipperfield, M. P.: Role of regional wetland emissions in atmospheric methane variability, *Geophys. Res. Lett.*, 43, 11,433–11,444, doi:10.1002/2016GL070649, 2016.

McNorton, J., Wilson, C., Gloor, M., Parker, R. J., Boesch, H., Feng, W., Hossaini, R. and Chipperfield, M. P.: Attribution of recent increases in atmospheric methane through 3-D inverse modelling, *Atmos. Chem. Phys.*, 18(24), 18149–18168, doi:10.5194/acp-18-18149-2018, 2018.

Melton, J. R., Wania, R., Hodson, E. L., Poulter, B., Ringeval, B., Spahni, R., Bohn, T., Avis, C. A., Beerling, D. J., Chen, G., Eliseev, A. V., Denisov, S. N., Hopcroft, P. O., Lettenmaier, D. P., Riley, W. J., Singarayer, J. S., Subin, Z. M., Tian, H., Zürcher, S.,

Brovkin, V., Van Bodegom, P. M., Kleinen, T., Yu, Z. C. and Kaplan, J. O.: Present state of global wetland extent and wetland methane modelling: Conclusions from a model inter-comparison project (WETCHIMP), *Biogeosciences*, doi:10.5194/bg-10-753-2013, 2013.

Monteil, G., Houweling, S., Butz, A., Guerlet, S., Schepers, D., Hasekamp, O., Frankenberg, C., Scheepmaker, R., Aben, I. and Röckmann, T.: Comparison of CH₄ inversions based on 15 months of GOSAT and SCIAMACHY observations, *J. Geophys. Res. Atmos.*, 118(20), 11,807–11,823, doi:10.1002/2013JD019760, 2013.

Moore, T. R. and Roulet, N. T.: A comparison of dynamic and static chambers for methane emission measurements from subarctic fens, *Atmos. - Ocean*, 29(1), 102–109, doi:10.1080/07055900.1991.9649395, 1991.

Morin, T. H., Bohrer, G., Stefanik, K. C., Rey-Sanchez, A. C., Matheny, A. M. and Mitsch, W. J.: Combining eddy-covariance and chamber measurements to determine the methane budget from a small, heterogeneous urban floodplain wetland park, *Agric. For. Meteorol.*, 237–238, 160–170, doi:10.1016/j.agrformet.2017.01.022, 2017.

Muccio, Z. and Jackson, G. P.: Isotope ratio mass spectrometry, *Analyst*, 134(2), 213–222, doi:10.1039/b808232d, 2009.

Muller, R. A., and MacDonald, G. J.: Glacial cycles and orbital inclination, *Nature*, 377, 107–108, 1995.

NAEI/BEIS, National Atmospheric Emissions Inventory UK Emissions Data Selector, <https://naei.beis.gov.uk/data/data-selector>, (Accessed 05 January 2022), 2022

Nédélec, P., Blot, R., Boulanger, D., Athier, G., Cousin, J. M., Gautron, B., Petzold, A., Volz-Thomas, A. and Thouret, V.: Instrumentation on commercial aircraft for monitoring the atmospheric composition on a global scale: The IAGOS system, technical overview of ozone and carbon monoxide measurements, *Tellus, Ser. B Chem. Phys. Meteorol.*, 6(1), doi:10.3402/tellusb.v67.27791, 2015.

Nevison, C. D., Mahowald, N. M., Weiss, R. F. and Prinn, R. G.: Interannual and seasonal variability in atmospheric N₂O, *Global Biogeochem. Cycles*, 21(3), 1–13, doi:10.1029/2006GB002755, 2007.

Nevison, C., Kinnison, D. and Weiss, R.: Stratospheric influences on the tropospheric seasonal cycles of nitrous oxide and chlorofluorocarbons, *Geophys. Res. Lett.*, 31(20), 2004.

Nisbet, E., Dlugokencky, E., Manning, M., Lowry, D., Fisher, R., France, J., Michel, S., Miller, J., White, J., Vaughn, B. and others: Rising atmospheric methane: 2007–2014 growth and isotopic shift, *Global Biogeochem. Cycles*, 30(9), 1356–1370, 2016.

Nisbet, E. G., Manning, M. R., Dlugokencky, E. J., Fisher, R. E., Lowry, D., Michel, S. E., Myhre, C. L., Platt, S. M., Allen, G., Bousquet, P., Brownlow, R., Cain, M., France, J. L., Hermansen, O., Hossaini, R., Jones, A. E., Levin, I., Manning, A. C., Myhre, G., Pyle, J. A., Vaughn, B. H., Warwick, N. J. and White, J. W. C.: Very Strong Atmospheric Methane Growth in the 4 Years 2014–2017: Implications for the Paris Agreement, *Global Biogeochem. Cycles*, 33(3), 318–342, doi:10.1029/2018GB006009, 2019.

NOAA/GML, gml.noaa.gov/ccgg/trends_ch4/, (Accessed 07 July 2021), 2021a

NOAA/GML, gml.noaa.gov/ccgg/trends_n2o/, (Accessed 08 September 2021), 2021b

O’Keefe, A. and Deacon, D. A. G.: Cavity ring-down optical spectrometer for absorption measurements using pulsed laser sources, *Rev. Sci. Instrum.*, 59(12), 2544–2551, doi:10.1063/1.1139895, 1988.

O’Shea, S. J., Allen, G., Gallagher, M. W., Bower, K., Illingworth, S. M., Muller, J. B. A., Jones, B. T., Percival, C. J., Bauguitte, S. J. B., Cain, M., Warwick, N., Quiquet, A., Skiba, U., Drewer, J., Dinsmore, K., Nisbet, E. G., Lowry, D., Fisher, R. E., France, J. L., Aurela, M., Lohila, A., Hayman, G., George, C., Clark, D. B., Manning, A. J., Friend, A. D. and Pyle, J.: Methane and carbon dioxide fluxes and their regional scalability for the European Arctic wetlands during the MAMM project in summer 2012, *Atmos. Chem. Phys.*, 14(23), 13159–13174, doi:10.5194/acp-14-13159-2014, 2014.

Oh, Y., Zhuang, Q., Welp, L. R., Liu, L., Lan, X., Basu, S., Dlugokencky, E. J., Bruhwiler, L., Miller, J. B., Michel, S. E., Schwietzke, S., Tans, P., Ciais, P. and Chanton, J. P.: Improved global wetland carbon isotopic signatures support post-2006 microbial methane emission increase, *Commun. Earth Environ.*, 3(1), 1–12, doi:10.1038/s43247-022-00488-5, 2022.

Palmer, P. I., Feng, L., Lunt, M. F., Parker, R. J., Bösch, H., Lan, X., Lorente, A. and Borsdorff, T.: The added value of satellite observations of methane for understanding the

contemporary methane budget, *Philos. Trans. R. Soc. A Math. Phys. Eng. Sci.*, 379(2210), 20210106, doi:10.1098/rsta.2021.0106, 2021.

Pan, X., Ichoku, C., Chin, M., Bian, H., Darmenov, A., Colarco, P., Ellison, L., Kucsera, T., Da Silva, A., Wang, J., Oda, T. and Cui, G.: Six global biomass burning emission datasets: Intercomparison and application in one global aerosol model, *Atmos. Chem. Phys.*, 20(2), 969–994, doi:10.5194/acp-20-969-2020, 2020.

Parton, W. J., Mosier, A. R., Ojima, D. S., Valentine, D. W., Schime, D. S., Weier, K. and Kulmala, A. E.: Generalized model for N₂ and N₂O production from nitrification and denitrification, *Global Biogeochem. Cycles*, 10(3), 401–412, doi:10.1029/96GB01455, 1996.

Paul, J. B., Lapson, L. and Anderson, J. G.: Ultrasensitive absorption spectroscopy with a high-finesse optical cavity and off-axis alignment, *Appl. Opt.*, 40(27), 4904, doi:10.1364/ao.40.004904, 2001.

Pavelka, M., Acosta, M., Kiese, R., Altimir, N., Brümmer, C., Crill, P., Darenova, E., Fuß, R., Gielen, B., Graf, A., Klemetsson, L., Lohila, A., Longdoz, B., Lindroth, A., Nilsson, M., Jiménez, S. M., Merbold, L., Montagnani, L., Peichl, M., Pihlatie, M., Pumpanen, J., Ortiz, P. S., Silvennoinen, H., Skiba, U., Vestin, P., Weslien, P., Janous, D. and Kutsch, W.: Standardisation of chamber technique for CO₂, N₂O and CH₄ fluxes measurements from terrestrial ecosystems, *Int. Agrophysics*, 32(4), 569–587, doi:10.1515/intag-2017-0045, 2018.

Perez, T., Trumbore, S. E., Tyler, S. C., Matson, P. a., Ortiz-Monasterio, I., Rahn, T. and Griffith, D. W. T.: Identifying the agricultural imprint on the global N₂O budget using stable isotopes, *J. Geophys. Res.*, 106(D9), 9869–9878, 2001.

Philander, S. G. H.: El Nino southern oscillation phenomena. *Nature*, 302(5906), 295–301, 1983.

Pithan, F. and Mauritsen, T.: Arctic amplification dominated by temperature feedbacks in contemporary climate models, *Nat. Geosci.*, 7(3), 181–184, doi:10.1038/ngeo2071, 2014.

Pitt, J. R., Le Breton, M., Allen, G., Percival, C. J., Gallagher, M. W., J.-B. Bauguitte, S., O'Shea, S. J., Muller, J. B. A., Zahniser, M. S., Pyle, J. and Palmer, P. I.: The development and evaluation of airborne in situ N₂O and CH₄ sampling using a quantum

cascade laser absorption spectrometer (QCLAS), *Atmos. Meas. Tech.*, 9(1), 63–77, doi:10.5194/amt-9-63-2016, 2016.

Pitt, J. R., Allen, G., Bauguitte, S. J. B., Gallagher, M. W., Lee, J. D., Drysdale, W., Nelson, B., Manning, A. J. and Palmer, P. I.: Assessing London CO₂, CH₄ and CO emissions using aircraft measurements and dispersion modelling, *Atmos. Chem. Phys.*, doi:10.5194/acp-19-8931-2019, 2019.

Poulter, B., Bousquet, P., Canadell, J. G., Ciais, P., Peregon, A., Saunois, M., Arora, V. K., Beerling, D. J., Brovkin, V., Jones, C. D., Joos, F., Gedney, N., Ito, A., Kleinen, T., Koven, C. D., McDonald, K., Melton, J. R., Peng, C., Peng, S., Prigent, C., Schroeder, R., Riley, W. J., Saito, M., Spahni, R., Tian, H., Taylor, L., Viovy, N., Wilton, D., Wiltshire, A., Xu, X., Zhang, B., Zhang, Z. and Zhu, Q.: Global wetland contribution to 2000-2012 atmospheric methane growth rate dynamics, *Environ. Res. Lett.*, 12(9), doi:10.1088/1748-9326/aa8391, 2017.

Prather, M. J., Hsu, J., Deluca, N. M., Jackman, C. H., Oman, L. D., Douglass, A. R., Fleming, E. L., Strahan, S. E., Steenrod, S. D., Søvde, O. A., Isaksen, I. S. a, Froidevaux, L. and Funke, B.: Measuring and modelling the lifetime of nitrous oxide including its variability, *J. Geophys. Res. Atmos.*, 120(11), 5693–5705, doi:10.1002/2015JD023267, 2015.

Prather, M. J.: Lifetimes and time scales in atmospheric chemistry, *Philos. Trans. R. Soc. A Math. Phys. Eng. Sci.*, 365(1856), 1705–1726, doi:10.1098/rsta.2007.2040, 2007.

Prokopiou, M., Sapart, C. J., Rosen, J., Sperlich, P., Blunier, T., Brook, E., van de Wal, R. S. W. and Röckmann, T.: Changes in the Isotopic Signature of Atmospheric Nitrous Oxide and Its Global Average Source During the Last Three Millennia, *J. Geophys. Res. Atmos.*, 123(18), 10,757-10,773, doi:10.1029/2018JD029008, 2018.

Ramanathan, V., Cess, R. D., Harrison, E. F., Minnis, P., Barkstrom, B. R., Ahmad, E. and Hartmann, D.: Cloud-radiative forcing and climate: Results from the earth radiation budget experiment, *Science* (80), 243(4887), 57–63, doi:10.1126/science.243.4887.57, 1989.

Rasmussen, R. A. and Khalil, M. A. K.: Differences in the concentrations of atmospheric trace gases in and above the tropical boundary layer, *Pure Appl. Geophys.*, 119(5), 990–997, doi:10.1007/BF00878964, 1981.

Ravishankara, A., Daniel, J. and Portmann, R.: Nitrous oxide (N₂O): the dominant ozone-depleting substance emitted in the 21st century, *Science*, 326(5949), 123–125, 2009.

Reay, D. S., Davidson, E. A., Smith, K. A., Smith, P., Melillo, J. M., Dentener, F. and Crutzen, P. J.: Global agriculture and nitrous oxide emissions, *Nat. Clim. Chang.*, 2(6), 410–416, doi:10.1038/nclimate1458, 2012.

Reay, D. S., Smith, K. A., Edwards, A. C., Hiscock, K. M., Dong, L. F. and Nedwell, D. B.: Indirect nitrous oxide emissions: Revised emission factors, *Environ. Sci.*, 2(2–3), 153–158, doi:10.1080/15693430500415525, 2005.

Reinhart, D. R., Cooper, D. C. and Walker, B. L.: Flux chamber design and operation for the measurement of municipal solid waste landfill gas emission rates, *J. Air Waste Manag. Assoc.*, 42(8), 1067–1070, doi:10.1080/10473289.1992.10467053, 1992.

Rigby, M., Montzka, S., Prinn, R., White, J., Young, D., O'Doherty, S., Lunt, M., Ganesan, A., Manning, A., Simmonds, P. and others: Role of atmospheric oxidation in recent methane growth, *Proc. Natl. Acad. Sci.*, 114(21), 5373–5377, 2017.

Rigby, M., Manning, A. J. and Prinn, R. G.: Inversion of long-lived trace gas emissions using combined Eulerian and Lagrangian chemical transport models, *Atmos. Chem. Phys.*, 11(18), 9887–9898, doi:10.5194/acp-11-9887-2011, 2011.

Rigby, M., Prinn, R. G., Fraser, P. J., Simmonds, P. G., Langenfelds, R. L., Huang, J., Cunnold, D. M., Steele, L. P., Krummel, P. B., Weiss, R. F., O'Doherty, S., Salameh, P. K., Wang, H. J., Harth, C. M., Mühle, J. and Porter, L. W.: Renewed growth of atmospheric methane, *Geophys. Res. Lett.*, 35(22), 2–7, doi:10.1029/2008GL036037, 2008.

Rochette, P. and Eriksen-Hamel, N. S.: Chamber Measurements of Soil Nitrous Oxide Flux: Are Absolute Values Reliable?, *Soil Sci. Soc. Am. J.*, 72(2), 331–342, doi:10.2136/sssaj2007.0215, 2008.

Röckmann, T., Kaiser, J. and Brenninkmeijer, C. A. M.: The isotopic fingerprint of the pre-industrial and the anthropogenic N₂O source, *Atmos. Chem. Phys.*, 3, 315–323, doi:10.5194/acp-3-315-2003, 2003.

Ropelewski, Chester F., and Michael S. Halpert.: North American precipitation and temperature patterns associated with the El Niño/Southern Oscillation (ENSO). *Mon. Weather Rev.* 114(12) 2352-2362, 1986.

Rothman, L. S.: History of the HITRAN Database, *Nat. Rev. Phys.*, 3(5), 302–304, doi:10.1038/s42254-021-00309-2, 2021.

Ruppel, C. D. and Kessler, J. D.: The interaction of climate change and methane hydrates, *Rev. Geophys.*, 55(1), 126–168, doi:10.1002/2016RG000534, 2017.

Saikawa, E., Prinn, R. G., Dlugokencky, E., Ishijima, K., Dutton, G. S., Hall, B. D., Langenfelds, R., Tohjima, Y., Machida, T., Manizza, M., Rigby, M., O'Doherty, S., Patra, P. K., Harth, C. M., Weiss, R. F., Krummel, P. B., Van Der Schoot, M., Fraser, P. J., Steele, L. P., Aoki, S., Nakazawa, T. and Elkins, J. W.: Global and regional emissions estimates for N₂O, *Atmos. Chem. Phys.*, 14(9), 4617–4641, doi:10.5194/acp-14-4617-2014, 2014.

Saunio, M., R. Stavert, A., Poulter, B., Bousquet, P., G. Canadell, J., B. Jackson, R., A. Raymond, P., J. Dlugokencky, E., Houweling, S., K. Patra, P., Ciais, P. et al.: The global methane budget 2000-2017, *Earth Syst. Sci. Data*, doi:10.5194/essd-12-1561-2020, 2020.

Schaefer, H., Fletcher, S. E. M., Veidt, C., Lassey, K. R., Brailsford, G. W., Bromley, T. M., Dlugokencky, E. J., Michel, S. E., Miller, J. B., Levin, I., Lowe, D. C., Martin, R. J., Vaughn, B. H. and White, J. W. C.: A 21st-century shift from fossil-fuel to biogenic methane emissions indicated by ¹³CH₄, *Science.*, 352(6281), 80–84, doi:10.1126/science.aad2705, 2016.

Schmid, H. P.: Source areas for scalars and scalar fluxes, *Boundary-Layer Meteorol.*, 67(3), 293–318, doi:10.1007/BF00713146, 1994.

Schoell, M.: Multiple origins of methane in the *Earth*, *Chem. Geol.*, 71(1–3), 1–10, doi:10.1016/0009-2541(88)90101-5, 1988.

Serrano-Silva, N., Sarria-Guzmán, Y., Dendooven, L. and Luna-Guido, M. Methanogenesis and Methanotrophy in Soil: A Review. *Pedosphere*, 24, 291–307, doi:10.1016/S1002-0160(14)60016-3, 2014.

Serreze, M. C. and Barry, R. G.: Processes and impacts of Arctic amplification: A research synthesis, *Glob. Planet. Change*, 77(1–2), 85–96, doi:10.1016/j.gloplacha.2011.03.004, 2011.

Shackleton, N. J.: The 100,000-year ice-age cycle identified and found to lag temperature, carbon dioxide, and orbital eccentricity, *Science*, 289(5486), 1897–1902, doi:10.1126/science.289.5486.1897, 2000.

Shah, A., Pitt, J., Ricketts, H., Leen, J. B., Williams, P., Kabbabe, K., Gallagher, M. and Allen, G.: Testing the near-field Gaussian plume inversion flux quantification technique using unmanned aerial vehicle sampling, *Atmos. Meas. Tech.*, 13, 1467–1484, doi:10.5194/amt-13-1467-2020 2020.

Shaw, J. T., Shah, A., Yong, H. and Allen, G.: Methods for quantifying methane emissions using unmanned aerial vehicles: A review, *Philos. Trans. R. Soc. A*, 379(2210), doi:10.1098/rsta.2020.0450, 2021.

Sherwood, O. A., Schwietzke, S., Arling, V. A. and Etiope, G.: Global inventory of gas geochemistry data from fossil fuel, microbial and burning sources, version 2017, *Earth Syst. Sci. Data*, 9(2), 639–656, doi:10.5194/essd-9-639-2017, 2017.

Sigman, D. M. and Boyle, E. A.: Glacial/Interglacial changes in atmospheric carbon dioxide, *Nature*, 407, 859–869, 2000.

Sommer, B. and Schad, M.: Climate change and society: Possible impacts and prospective developments, *Meteorol. Zeitschrift*, 24(2), 137–145, doi:10.1127/metz/2014/0522, 2015.

Sowers, T., Rodebaugh, A., Yoshida, N. and Toyoda, S.: Extending records of the isotopic composition of atmospheric N₂O back to 1800 A.D. from air trapped in snow at the South Pole and the Greenland Ice Sheet Project II ice core, *Global Biogeochem. Cycles*, 16(4), 76-1-76–10, doi:10.1029/2002gb001911, 2002.

Stevenson, D. S., Zhao, A., Naik, V., O'Connor, F. M., Tilmes, S., Zeng, G., Murray, L. T., Collins, W. J., Griffiths, P. T., Shim, S., Horowitz, L. W., Sentman, L. T. and Emmons, L.: Trends in global tropospheric hydroxyl radical and methane lifetime since 1850 from AerChemMIP. *Atmos. Chem. Phys.* 20, 12905–12920, doi:10.5194/acp-20-12905-2020, 2020.

Stocker, J. H. C., Carruthers, D., McHugh, C.: ADMS-Urban: developments in modelling dispersion from the city scale to the local scale. *Int. J. Environ. Pollut.*, 50, 308–316, doi:10.1504/IJEP.2012.051202, 2012

Stone, D., Whalley, L. K. and Heard, D. E.: Tropospheric OH and HO₂ radicals: Field measurements and model comparisons, *Chem. Soc. Rev.*, 41(19), 6348–6404, doi:10.1039/c2cs35140d, 2012.

Strode, S. A., Wang, J. S., Manyin, M., Duncan, B., Hossaini, R., Keller, C. A., Michel, S. E. and White, J. W. C.: Strong sensitivity of the isotopic composition of methane to the plausible range of tropospheric chlorine, *Atmos. Chem. Phys.*, 20(14), 8405–8419, doi:10.5194/acp-20-8405-2020, 2020.

Suntharalingam, P., Buitenhuis, E., Le Quéré, C., Dentener, F., Nevison, C., Butler, J., Bange, H. and Forster, G.: Quantifying the impact of anthropogenic nitrogen deposition on oceanic nitrous oxide, *Geophys. Res. Lett.*, 39(7), 2012.

Susott, R. A., Olbu, G. J., Baker, S. P., Ward, D. E., Kauffman, J. B., and Shea, R.: Carbon, hydrogen, nitrogen, and thermogravimetric analysis of tropical ecosystem biomass, in *Biomass Burning and Global Change*, Levine, J. S. (eds.), 350–360, MIT Press, Cambridge, 1996.

Sutka, R. L., Ostrom, N. E., Ostrom, P. H., Breznak, J. A., Gandhi, H., Pitt, A. J. and Li, F.: Distinguishing nitrous oxide production from nitrification and denitrification on the basis of isotopomer abundances, *Appl. Environ. Microbiol.*, 72(1), 638–644, doi:10.1128/AEM.72.1.638-644.2006, 2006.

Swinehart, D. F.: The Beer-Lambert law, *J. Chem. Educ.*, 39(7), 333–335, doi:10.1021/ed039p333, 1962.

Thompson, R. L., Lassaletta, L., Patra, P. K., Wilson, C., Wells, K. C., Gressent, A., Koffi, E. N., Chipperfield, M. P., Winiwarter, W., Davidson, E. A., Tian, H. and Canadell, J. G.: Acceleration of global N₂O emissions seen from two decades of atmospheric inversion, *Nat. Clim. Chang.*, 9(12), 993–998, doi:10.1038/s41558-019-0613-7, 2019.

Thompson, R. L., Nisbet, E. G., Pisso, I., Stohl, A., Blake, D., Dlugokencky, E. J., Helmig, D. and White, J. W. C.: Variability in Atmospheric Methane From Fossil Fuel

and Microbial Sources Over the Last Three Decades, *Geophys. Res. Lett.*, 45(20), 11,499–11,508, doi:10.1029/2018GL078127, 2018.

Tian, H., Xu, R., Canadell, J. G., Thompson, R. L., Winiwarter, W., Suntharalingam, P., Davidson, E. A., Ciais, P., Jackson, R. B., Janssens-Maenhout, G. et al.: A comprehensive quantification of global nitrous oxide sources and sinks, *Nature*, 586(7828), 248–256, doi:10.1038/s41586-020-2780-0, 2020.

Timmermann, A., An, S. Il, Kug, J. S., Jin, F. F., Cai, W., Capotondi, A., Cobb, K., Lengaigne, M., McPhaden, M. J., Stuecker, M. F., Stein, K., Wittenberg, A. T., Yun, K. S., Bayr, T., Chen, H. C., Chikamoto, Y., Dewitte, B., Dommenges, D., Grothe, P., Guilyardi, E., Ham, Y. G., Hayashi, M., Ineson, S., Kang, D., Kim, S., Kim, W. M., Lee, J. Y., Li, T., Luo, J. J., McGregor, S., Planton, Y., Power, S., Rashid, H., Ren, H. L., Santoso, A., Takahashi, K., Todd, A., Wang, G., Wang, G., Xie, R., Yang, W. H., Yeh, S. W., Yoon, J., Zeller, E. and Zhang, X.: El Niño–Southern Oscillation complexity, *Nature*, 559(7715), 535–545, doi:10.1038/s41586-018-0252-6, 2018.

Tokida, T., Mizoguchi, M., Miyazaki, T., Kagemoto, A., Nagata, O. and Hatano, R.: Episodic release of methane bubbles from peatland during spring thaw, *Chemosphere*, 70(2), 165–171, doi:10.1016/j.chemosphere.2007.06.042, 2007.

Tollefson, J.: US environmental group wins millions to develop methane-monitoring satellite, *Nature*, 556(7701), 283–284. doi:10.1038/d41586-018-04478-6, 2018.

Topp, E. and Pattey, E.: Soils as sources and sinks for atmospheric methane, *Can. J. Soil. Sci.*, 77(2), 167–177, 1997.

Toyoda, S., Yamamoto, S. I., Arai, S., Nara, H., Yoshida, N., Kashiwakura, K. and Akiyama, K. I.: Isotopomeric characterization of N₂O produced, consumed, and emitted by automobiles, *Rapid Commun. Mass Spectrom.*, 22(5), 603–612, doi:10.1002/rcm.3400, 2008.

Trenberth, K. E., Fasullo, J. T., & Kiehl, J.: Earth's global energy budget. *Bull. Am. Met. Soc.*, 90(3), 311–324, doi.org/10.1175/2008BAMS2634.1, 2009.

Trenberth, K. E. and Shea, D. J.: On the evolution of the Southern Oscillation, *Mon. Weather Rev.*, 115(12), 3078–3096, doi:10.1175/1520-0493(1987)115<3078:OTEOTS>2.0.CO;2, 1987.

Turner, A. J., Frankenberg, C., Wennberg, P. O. and Jacob, D. J.: Ambiguity in the causes for decadal trends in atmospheric methane and hydroxyl, *Proc. Natl. Acad. Sci. U. S. A.*, 114(21), 5367–5372, doi:10.1073/pnas.1616020114, 2017.

UK Home Office: Drug Misuse: Findings from the 2017/18 Crime Survey for England and Wales. Available from: https://assets.publishing.service.gov.uk/government/uploads/system/uploads/attachment_data/file/729249/drug-misuse-2018-hosb1418.pdf (Accessed 07 December 2021), 2018.

Urban, F. E., Cole, J. E. and Overpeck, J. T.: Influence of mean climate change on climate variability from a 155-year tropical Pacific coral record, *Nature*, 407(6807), 989–993, doi:10.1038/35039597, 2000.

Van Der Werf, G. R., Randerson, J. T., Giglio, L., Van Leeuwen, T. T., Chen, Y., Rogers, B. M., Mu, M., Van Marle, M. J. E., Morton, D. C., Collatz, G. J., Yokelson, R. J. and Kasibhatla, P. S.: Global fire emissions estimates during 1997–2016, *Earth Syst. Sci. Data*, 9(2), 697–720, doi:10.5194/essd-9-697-2017, 2017.

Van Dijk, A. I. J. M. and Dolman, A. J.: Estimates of CO₂ uptake and release among European forests based on eddy covariance data, *Glob. Chang. Biol.*, 10(9), 1445–1459, doi:10.1111/j.1365-2486.2004.00831.x, 2004.

Verchot, L. V., Davidson, E. A., Cattânio, J. H., Ackerman, I. L., Erickson, H. E. and Keller, M.: Land use change and biogeochemical controls of nitrogen oxide emissions from soils in eastern Amazonia, *Global Biogeochem. Cycles*, 13(1), 31–46, doi:10.1029/1998GB900019, 1999.

Vernooij, R., Dusek, U., Popa, M. E., Yao, P., Shaikat, A., Qiu, C., Winiger, P., van der Veen, C., Eames, T., Ribeiro, N., and van der Werf, G.: Stable carbon isotopic composition of biomass burning emissions – implications for estimating the contribution of C₃ and C₄ plants, *Atmos. Chem. Phys. Discuss.* [preprint], <https://doi.org/10.5194/acp-2021-897>, in review, 2021.

Ward, P. J., Jongman, B., Kummu, M., Dettinger, M. D., Weiland, F. C. S. and Winsemius, H. C.: Strong influence of El Niño Southern Oscillation on flood risk around the world, *Proc. Natl. Acad. Sci. U. S. A.*, 111(44), 15659–15664, doi:10.1073/pnas.1409822111, 2014.

Wecht, K. J., Jacob, J. D., Frankenberg, C., Jiang, Z. and Blake R, D.: Mapping of North American methane emissions with high spatial resolution by inversion of SCIAMACHY satellite data, *J. Geophys. Res. Atmos. Res.*, 7741–7756, doi:10.1002/2014JD021551. Received, 2014.

Willeit, M. and Ganopolski, A.: The importance of snow albedo for ice sheet evolution over the last glacial cycle, *Clim. Past*, 14(5), 697–707, doi:10.5194/cp-14-697-2018, 2018.

WMO: World Meteorological Organisation – Global Atmospheric Watch Programme, <https://community.wmo.int/activity-areas/gaw>, (Accessed 18 September 2022), 2022a.

WMO: X2004A Methane (CH₄) WMO Scale, https://gml.noaa.gov/ccl/ch4_scale.html, (Accessed 18 September 2022), 2022b

Worden, J. R., Bloom, A. A., Pandey, S., Jiang, Z., Worden, H. M., Walker, T. W., Houweling, S. and Röckmann, T.: Reduced biomass burning emissions reconcile conflicting estimates of the post-2006 atmospheric methane budget, *Nat. Commun.*, 8(1), 1–11, doi:10.1038/s41467-017-02246-0, 2017.

Wunch, D., Toon, G. C., Blavier, J. F. L., Washenfelder, R. A., Notholt, J., Connor, B. J., Griffith, D. W. T., Sherlock, V. and Wennberg, P. O.: The total carbon column observing network, *Philos. Trans. R. Soc. A Math. Phys. Eng. Sci.*, 369(1943), 2087–2112, doi:10.1098/rsta.2010.0240, 2011.

Yang, S., Chang, B. X., Warner, M. J., Weber, T. S., Bourbonnais, A. M., Santoro, A. E., Kock, A., Sonnerup, R. E., Bullister, J. L., Wilson, S. T. and Bianchi, D.: Global reconstruction reduces the uncertainty of oceanic nitrous oxide emissions and reveals a vigorous seasonal cycle, *Proc. Natl. Acad. Sci. U. S. A.*, 117(22), doi:10.1073/pnas.1921914117, 2020.

Yang, Y., Liu, L., Zhang, F., Zhang, X., Xu, W., Liu, X., Wang, Z. and Xie, Y.: Soil Nitrous Oxide Emissions by Atmospheric Nitrogen Deposition over Global Agricultural Systems, *Environ. Sci. Technol.*, 55(8), 4420–4429, doi:10.1021/acs.est.0c08004, 2021.

Yokelson, R. J., Andreae, M. O. and Akagi, S. K.: Pitfalls with the use of enhancement ratios or normalized excess mixing ratios measured in plumes to characterize pollution sources and aging, *Atmos. Meas. Tech.*, 6(8), 2155–2158, doi:10.5194/amt-6-2155-2013, 2013.

Yokelson, R. J., Crounse, J. D., DeCarlo, P. F., Karl, T., Urbanski, S., Atlas, E., Campos, T., Shinozuka, Y., Kapustin, V., Clarke, A. D., Weinheimer, A., Knapp, D. J., Montzka, D. D., Holloway, J., Weibring, P., Flocke, F., Zheng, W., Toohey, D., Wennberg, P. O., Wiedinmyer, C., Mauldin, L., Fried, A., Richter, D., Walega, J., Jimenez, J. L., Adachi, K., Buseck, P. R., Hall, S. R. and Shetter, R.: Emissions from biomass burning in the Yucatan, *Atmos. Chem. Phys.*, 9(15), 5785–5812, doi:10.5194/acp-9-5785-2009, 2009.

Yokelson, R. J., Goode, J. G., Ward, D. E., Susott, R. A., Babbitt, R. E., Wade, D. D., Bertschi, I., Griffith, D. W. T., and Hao, W. M.: Emissions of formaldehyde, acetic acid, methanol, and other trace gases from biomass fires in North Carolina measured by airborne Fourier transform infrared spectroscopy, *J. Geophys. Res. Atmos.*, 104(D23), 30109–30125, doi:10.1029/1999JD900817, 1999.

Yu, X., Millet, D. B., Wells, K. C., Henze, D. K., Cao, H., Griffis, T. J., Kort, E. A., Plant, G., Deventer, M. J., Kolka, R. K., Tyler, R. D., Davis, K. J., Desai, A. R., Baier, B. C., McKain, K., Czarnetzki, A. C. and Bloom, A.: Aircraft-based inversions quantify the importance of wetlands and livestock for Upper Midwest methane emissions, *Atmos. Chem. Phys.*, 21(2), 951–971, doi:10.5194/acp-21-951-2021, 2021.

Zaehle, S., Ciais, P., Friend, A. D. and Prieur, V.: Carbon benefits of anthropogenic reactive nitrogen offset by nitrous oxide emissions, *Nat. Geosci.*, 4(9), 601–605, doi:10.1038/ngeo1207, 2011.

Zellweger, C., Emmenegger, L., Firdaus, M., Hatakka, J., Heimann, M., Kozlova, E., Gerard Spain, T., Steinbacher, M., Van Der Schoot, M. V. and Buchmann, B.: Assessment of recent advances in measurement techniques for atmospheric carbon dioxide and methane observations, *Atmos. Meas. Tech.*, 9(9), 4737–4757, doi:10.5194/amt-9-4737-2016, 2016.

Zhao, C., Andrews, A. E., Bianco, L., Eluszkiewicz, J., Hirsch, A., MacDonald, C., Nehr Korn, T. and Fischer, M. L.: Atmospheric inverse estimates of methane emissions from Central California, *J. Geophys. Res. Atmos.*, 114(16), 1–47, doi:10.1029/2008JD011671, 2009.

Zhao, Y., Saunio, M., Bousquet, P., Lin, X., Berchet, A., Hegglin, M. I., Canadell, J. G., Jackson, R. B., Deushi, M., Jöckel, P. et al.: On the role of trend and variability in the

hydroxyl radical (OH) in the global methane budget. *Atmos. Chem. Phys.* 20, 13011–13022, doi:10.5194/acp-20-13011-2020, 2020.

Appendix

A.1. Supplementary material to Manuscript 1

Supplementary Material – Airborne measurements of fire emission factors for African biomass burning sampled during the MOYA campaign

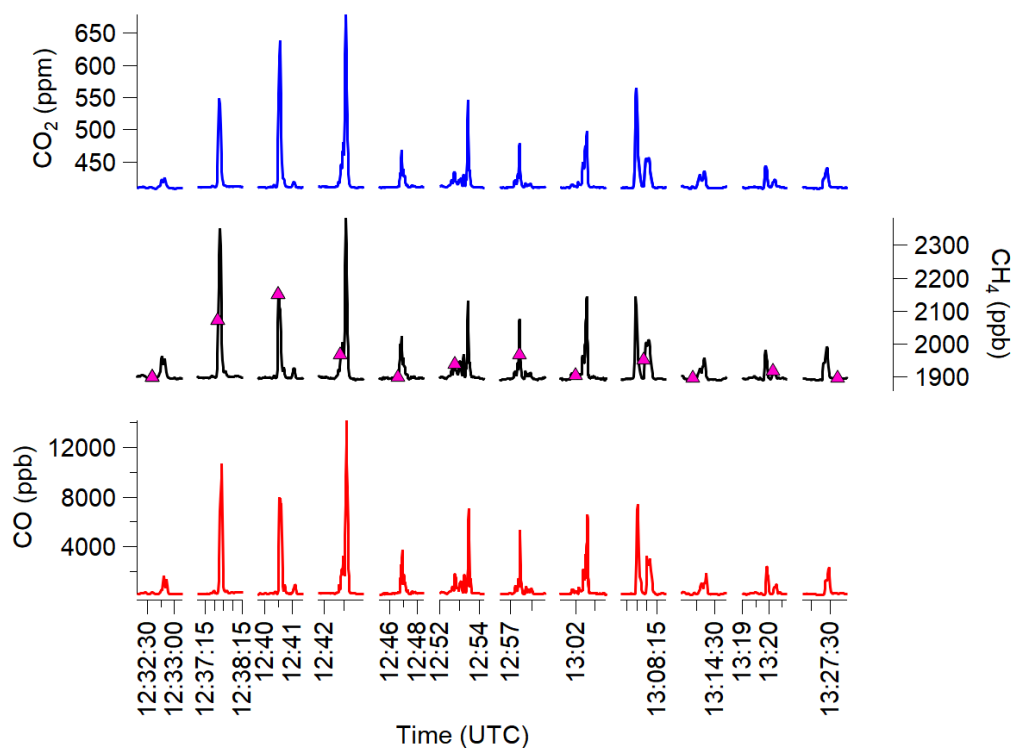


Figure S1: time series of CO (red), CH₄ (black), CO₂ (blue) and concentrations in the plumes analysed for flight C005. Median WAS canister fill times are marked on the CH₄ time series as pink triangles. Note that some WAS taken in background regions are not shown here.

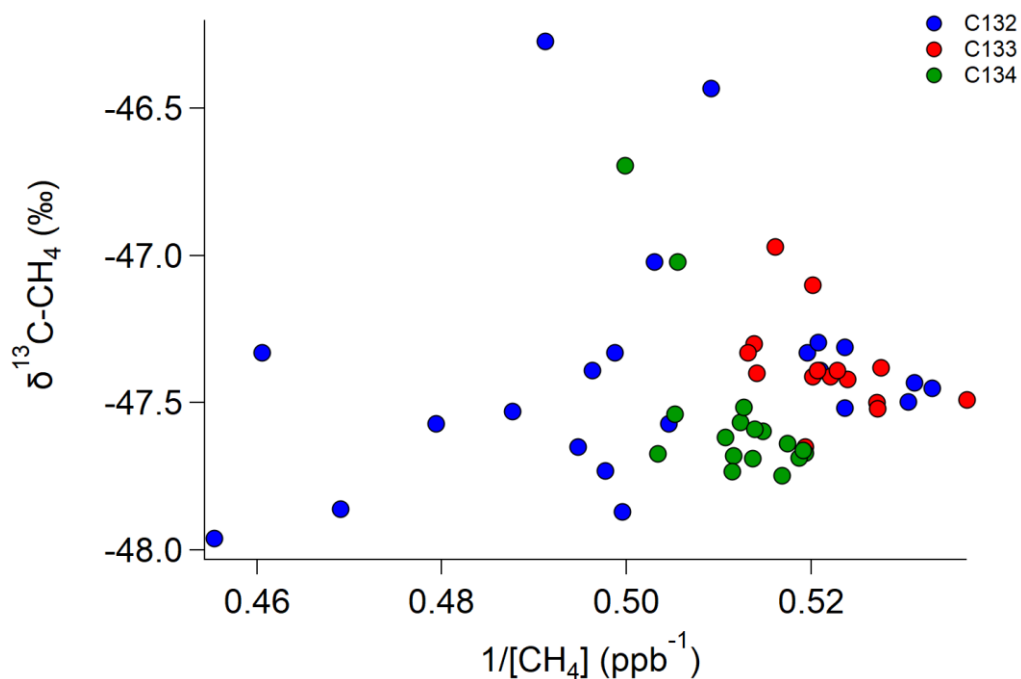


Figure S1.2: Keeling plot ($\delta^{13}\text{C-CH}_4$ vs inverse CH_4 mixing ratio) for all isotope samples taken during the MOYA-II (Uganda) flights C132 (blue), C133 (red) and C134 (green).

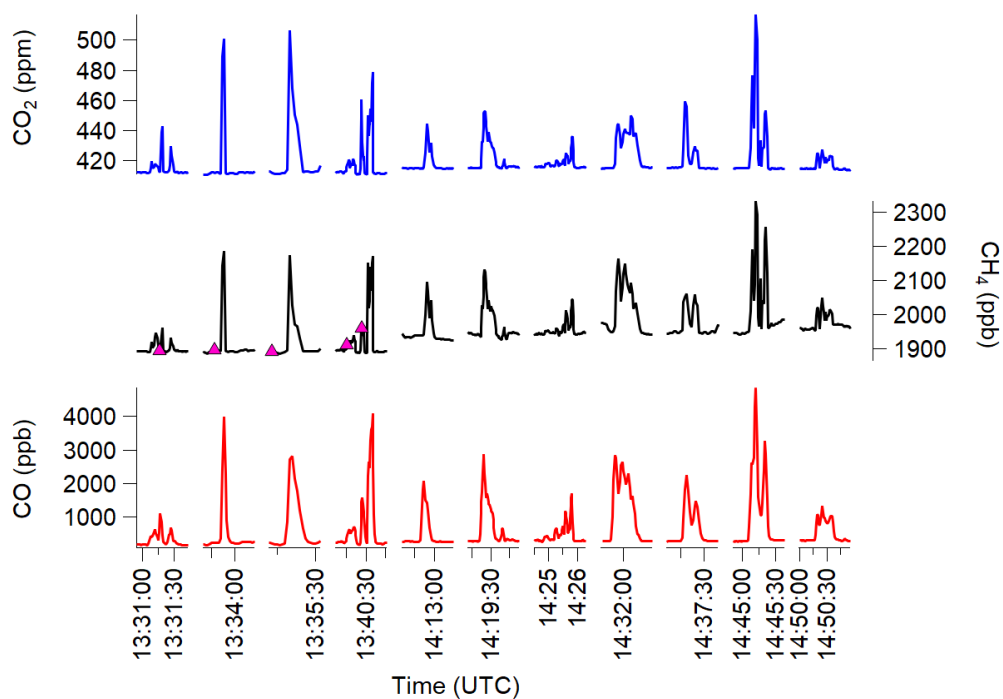


Figure S1.3: time series of CO (red), CH_4 (black), CO_2 (blue) and concentrations in the plumes analysed for flight C133. Median WAS canister fill times are marked on the CH_4 time series as pink triangles. Note that some WAS taken in background regions are not shown here.

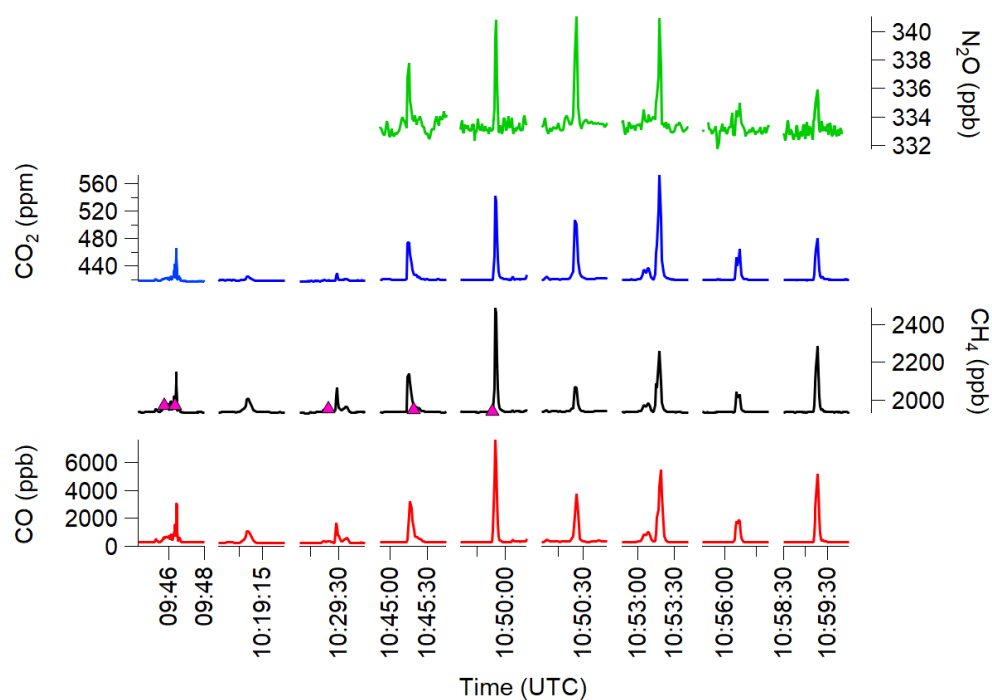


Figure S1.4: time series of CO (red), CH₄ (black), CO₂ (blue) and N₂O (green) concentrations in the nine plumes analysed for flight C134. N₂O data quality was insufficient for calculation of EF for the first three plumes, hence these are not shown. Median WAS canister fill times are marked on the CH₄ time series as pink triangles. Note that some WAS taken in background regions are not shown here.

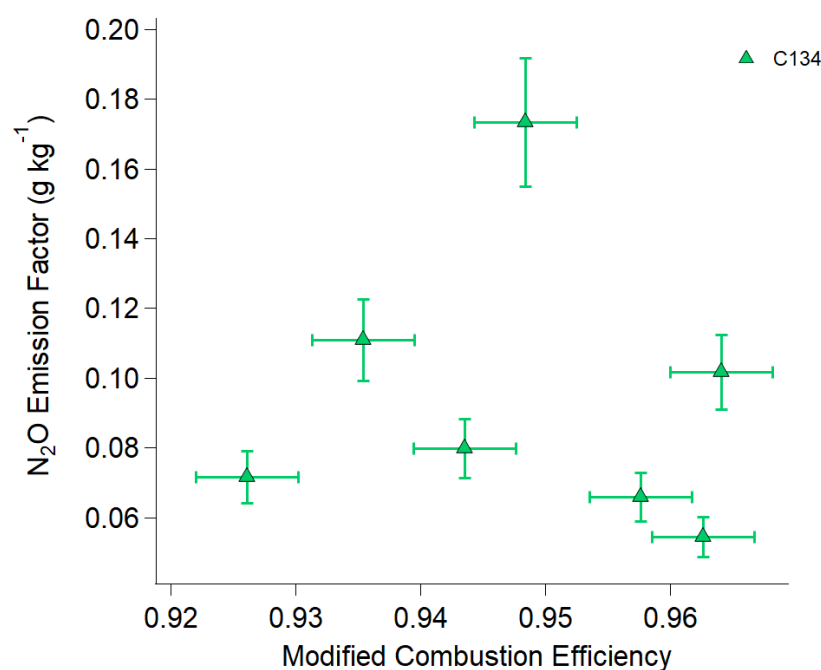


Figure S1.5: N₂O EF vs modified combustion efficiency for six biomass burning plumes sampled in flight C134 during MOYA-II.

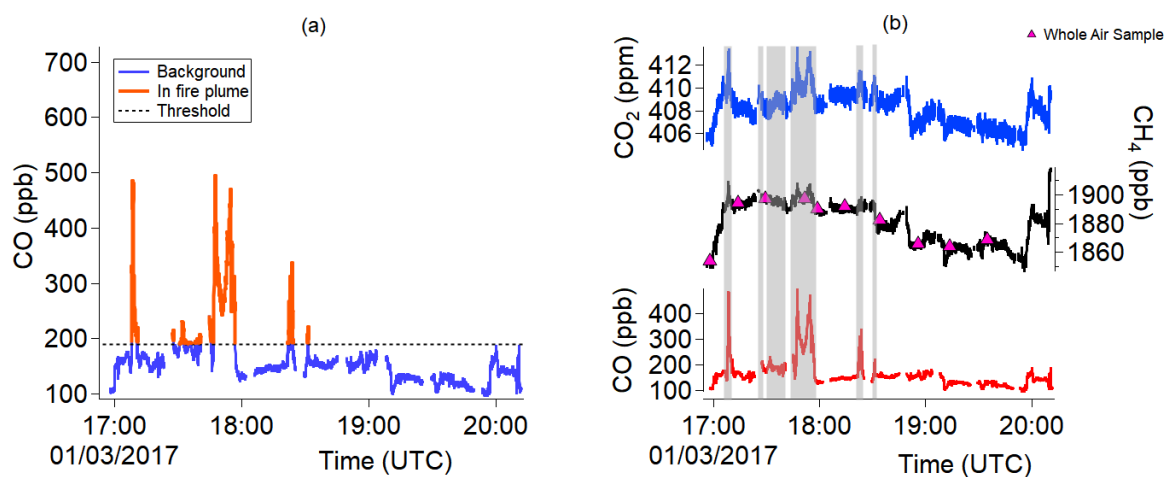


Figure S1.6: (a) CO mixing ratio time series over the course of flight C006, with the plumes exceeding the statistical threshold shown in orange and the background shown in purple. The plume selection threshold is also shown as a dashed line. (b) time series of CO (red), CH₄ (black) and CO₂ (blue) concentrations over flight C006, the biomass burning plumes chosen for analysis are highlighted in grey. Median WAS canister collection times are shown as pink triangles

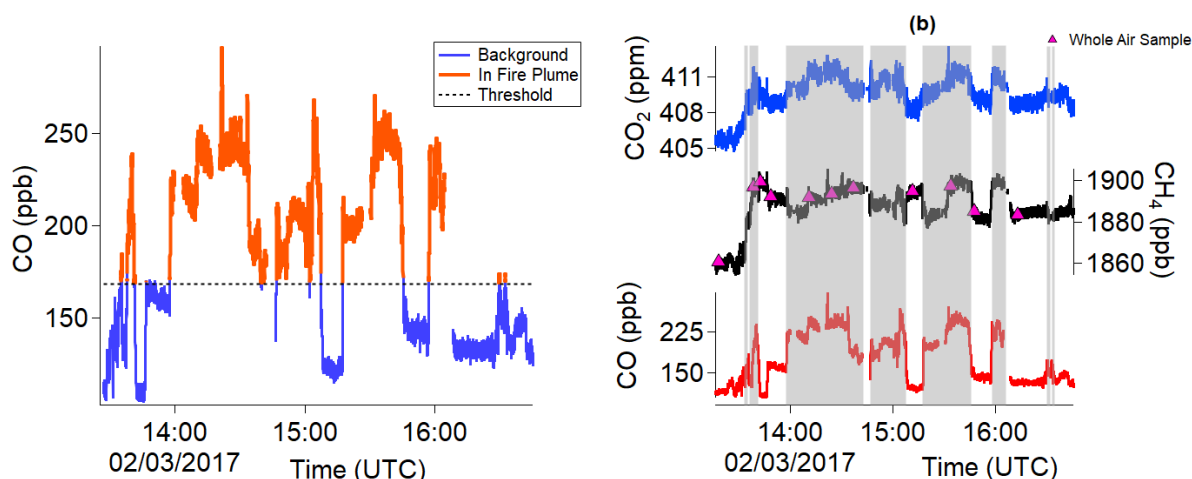


Figure S1.7: (a) CO mixing ratio time series over the course of flight C006, with the plumes exceeding the statistical threshold shown in orange and the background shown in purple. The plume selection threshold is also shown as a dashed line. (b) time series of CO (red), CH₄ (black) and CO₂ (blue) concentrations over flight C006, the biomass burning plumes chosen for analysis are highlighted in grey. Median WAS canister collection times are shown as pink triangles

A.1.1. Comparison of peak integration and regression method for emission factor calculation

During this work, two separate methods were used to calculate emission ratios (ER). The first method involves using the integrated plume area with background subtracted in the concentration time series for each plume, the second uses weighted regression analysis of in-plume species vs in-plume tracer CO from which ER with respect to CO is obtained from the gradient. Both analytical methods have been used to calculate ERs and emission factors (EF) for both the near-field and far-field fire emissions. The comparison between the two methods is presented here.

The regression analyses of the near-field flights are shown in Fig. S1.8 and S1.9. For the MOYA-II near-field flights where HCN was used as a biomass burning tracer, a seven standard deviation CO threshold above mean background was used to select in-plume data as is used for the MOYA-I near-field flights. For the integration analysis of the far-field flights, all enhanced in-plume data (Fig. S1.6 and S1.7) is treated as a single ‘plume’, and the averaged background subtracted from the integrated area under all in-plume data is used to calculate one ER per flight. The CH₄ and CO₂ EFs and their respective uncertainties calculated from each method are shown in Fig. S1.10.

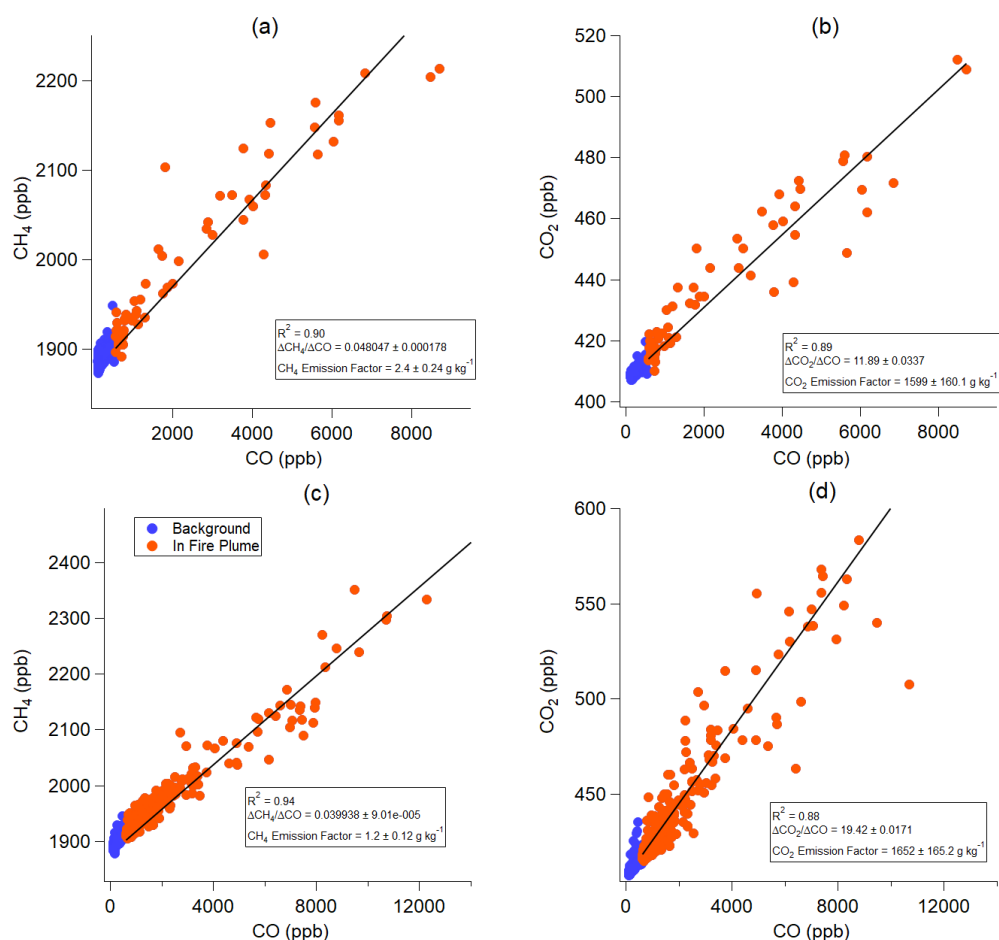


Figure S1.8: Linear regressions of in-plume (a) CH₄ and (b) CO₂ mixing ratio versus in-plume CO mixing ratio for flight C004 and (c) CH₄ and (d) CO₂ mixing ratio versus in-plume CO for flight C005. The linear regressions are calculated using the York regression method, and are weighted towards CO and CH₄/CO₂ measurement uncertainty (York et al. 2004). ERs obtained from the slope are also shown, as well as the calculated EFs.

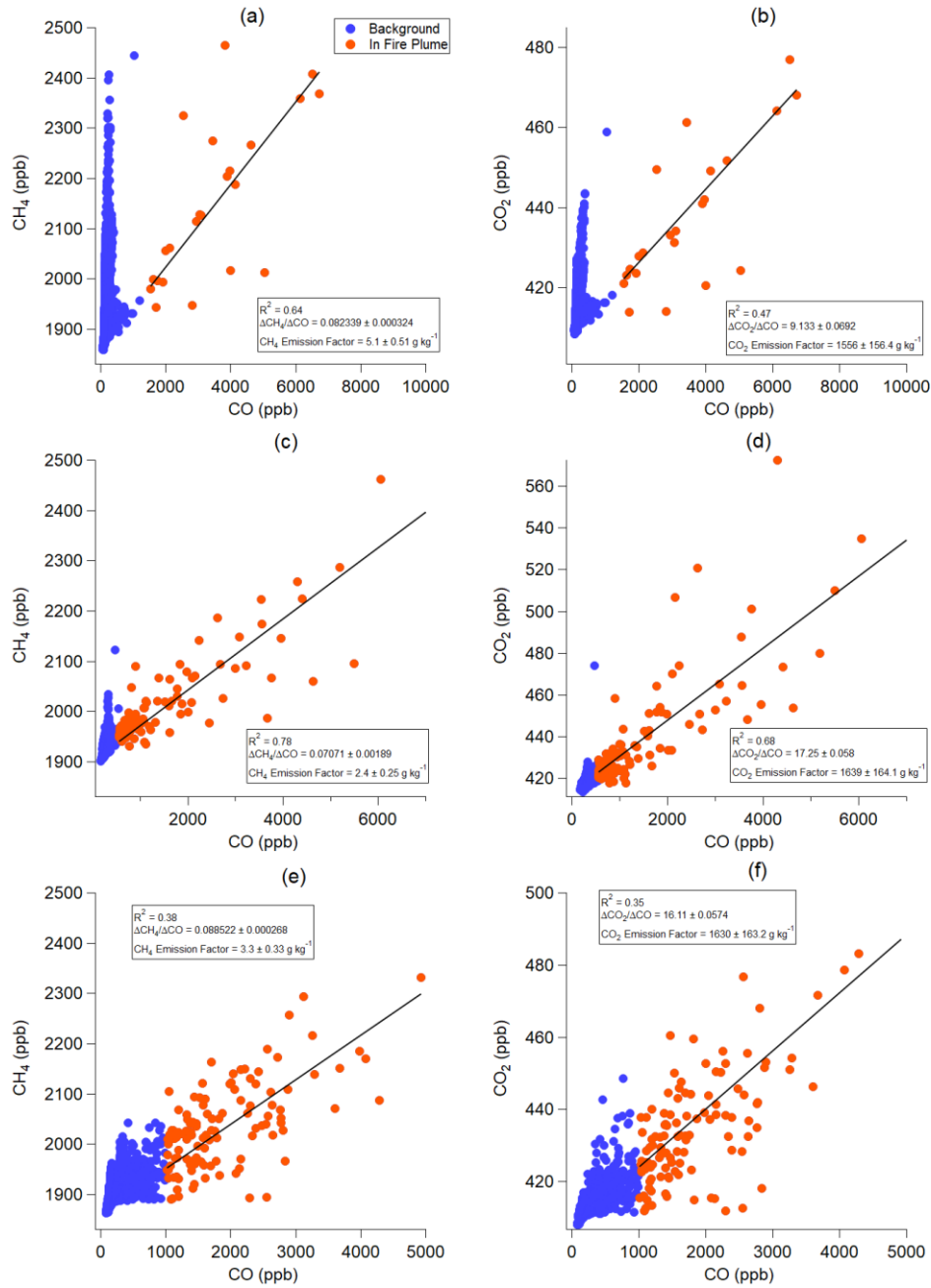


Figure S1.9: Linear regressions of in-plume (a) CH₄ and (b) CO₂ mixing ratio versus in-plume CO mixing ratio for flight C132 (c) CH₄ and (d) CO₂ versus in-plume CO for flight C133 and (e) CH₄ and (f) CO₂ versus in-plume CO for flight C134. The linear regressions are calculated using the York regression method, and are weighted towards CO and CH₄/CO₂ measurement uncertainty (York et al. 2004). ERs obtained from the slope are also shown, as well as the calculated EFs.

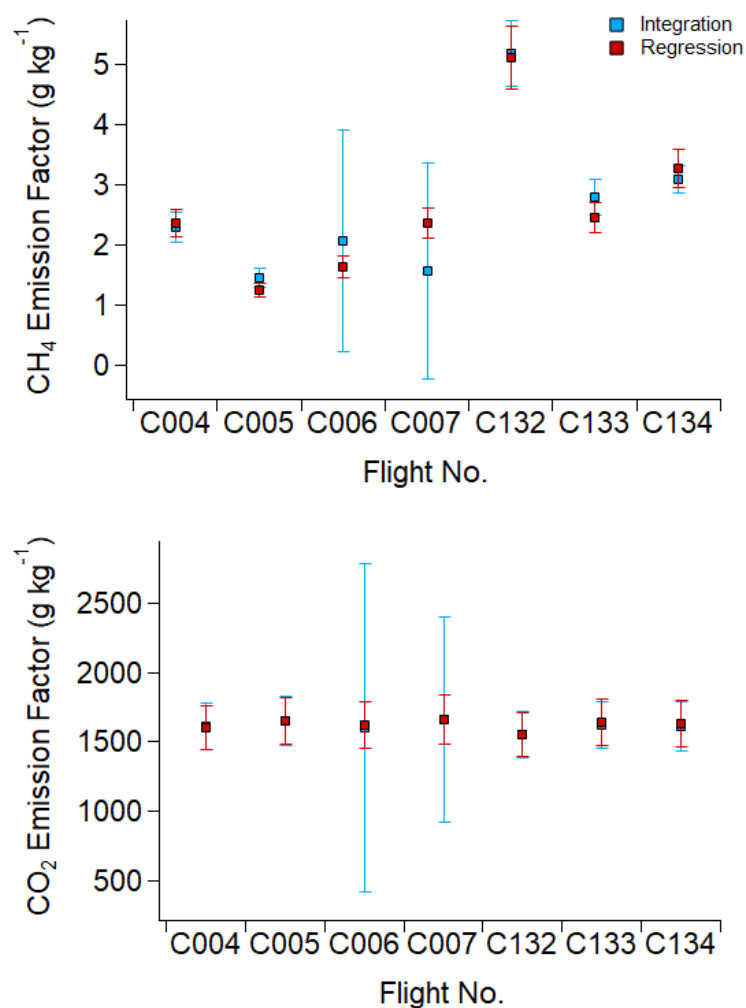


Figure S1.10: Comparison of CH₄ and CO₂ EFs and their respective uncertainties calculated using the integration method (blue) and regression analysis (red).

It can be seen from Fig. S1.10 that there is good agreement between the two methods of calculating ER for both CO₂ and CH₄. The uncertainties of C006 and C007 integration EF are notably larger than uncertainties for all other EF, this is due to the high variability in the background in the far-field flights and relatively small enhancement over the background in the plume compared to the near-field flights.

For the near-field flights C004, C005, C132, C133 and C134, the integration method is chosen as this allows calculation of specific EFs for each fire plume, whereas the regression analysis only yields one EF per flight in this case. Regression analysis is chosen for the far-field flights as the EF yielded from this method have a significantly smaller uncertainty than those determined via the integration method.

References

York, D., Evensen, N. M., Martínez, M. L., and De Basabe Delgado, J.: Unified equations for the slope, intercept, and standard errors of the best straight line, *Am. J. Phys.*, 72, 367–375, <https://doi.org/10.1119/1.1632486>, 2004.

A.2. Supplementary material to Manuscript 2

Supplementary Material - Airborne quantification of net methane and carbon dioxide fluxes from European Arctic wetlands in Summer 2019

A.2.1. CH₄ isotope analysis

In order to confirm the wetland origin of the methane emissions sampled during flight C195, $\delta^{13}\text{C}$ -CH₄ isotopic ratios were calculated from Whole air samples (WAS) collected from the aircraft across flights C195 and C196. Flight C196 also surveyed the same region of Fennoscandian wetland as C195, but CH₄/CO₂ mole fraction gradients were unsuitable for mass balance flux quantification. WAS were collected onboard the aircraft in 3L silica passivated stainless steel canisters (Thames Restek, UK). Sample collection was triggered manually to sample within the boundary layer, guided by the real time methane measurements from the FGGA onboard. Fill times ranged between 10 and 20 seconds depending on sampling altitude, representative of an integrated air sample over a 1 - 2 km track. Methane mole fraction in the WAS flasks was measured in the Royal Holloway greenhouse gas laboratory using a Picarro 1301 cavity ringdown spectroscopy analyser, and $\delta^{13}\text{C}$ ratio analysis was carried out by gas chromatography – isotope ratio mass spectrometry using a Trace Gas preconcentrator and Isoprime mass spectrometer (see Fisher et al. for details of the technique (1)).

A Keeling plot analysis of the WAS canister methane and $\delta^{13}\text{C}$ is shown in supplementary figure 1. The intercept and hence $\delta^{13}\text{C}$ source signature of $-73 \pm 6.6 \text{ ‰}$ is comparable to previous methane isotope measurements from similar study regions. Fisher et al. found a $\delta^{13}\text{C}$ source signature of $-71 \pm 1 \text{ ‰}$ for Finnish and Swedish peatlands compiled from aircraft samples, groundbased sampling, and chamber measurements (2). Sriskantharajah et al. conducted groundbased Tedlar bag sampling in Finnish subarctic peatlands and found a $\delta^{13}\text{C}$ source signature of $-68.5 \pm 0.7 \text{ ‰}$ (3). The $\delta^{13}\text{C}$ signature from WAS during this study therefore strongly indicates that the methane emissions originated from a wetland source.

A.2.2. CH₄ flux upscaling

The meridional gradient in fluxes with differing wetland area allows for tentative but limited upscaling the fluxes to a wider area of northern European wetlands for July 2019, assuming that they are representative of analogous land classifications. It is not possible to extrapolate for a longer time period as emissions would be expected to change much more significantly over an annual cycle. Supplementary fig. 4 shows a linear least-squares regression of bulk methane flux vs total wetland area within each of the three flux areas, forced through zero. It can be seen that the relationship between bulk flux and wetland area is broadly linear (R^2 of 0.85). Using this relationship fluxes obtained for this specific area have been extrapolated to a wider regional area.

A similar regression analysis was attempted for CO₂ sink vs total area of vegetated CORINE land-classes (see supplementary fig. 5). However the linear correlation coefficient was not as strong for the CO₂ regression ($R^2 = 0.33$). Furthermore, upscaling the CO₂ sink to a wider area would assume that all area-normalised vegetation land classes (e.g. forest and agricultural land) will represent the same CO₂ sink, which would be an inaccurate assumption, so CO₂ sink extrapolations are not reported in this work.

For CH₄, Barthelmes et al. provides an estimate of 249,066 km² total peatland area for multiple northern European countries, including Sweden, Finland, Norway, Denmark, Iceland, Greenland, Estonia, Latvia, Lithuania, and selected limited areas of northwest Russia. This comprises the land area approximately between 4° E and 32° E longitude and 54° N and 72° N latitude (4). Substituting the Barthelmes et al. peatland area value into the linear regression equation yields a total emission of 1.009 ± 0.052 Tg CH₄ emitted for the region in July 2019. The upscaling carried out here relies on a few key assumptions. Firstly, this method assumes that the area methane flux from all areas of peatland across the entirety of northern Europe are constant, and that there will be negligible variability in methane fluxes from different areas of peatland. This may be inaccurate as surface temperature will inevitably be different across the entire upscaled region, leading to likely differences in methane flux from areas of peatland. The second assumption is that peatland is the only land type that is emitting methane during this time. Despite peatland likely being the major methane-emitting land type, this may be oversimplified. However, this simple extrapolation provides a useful first order estimate of the regional flux in summer that may inform future model and measurement studies attempting to place Arctic terrestrial carbon sources in a global context.

A.2.3. N₂O flux threshold

A direct flux of N₂O could not be calculated in this work, as there was no observable concentration enhancement downwind of the wetland area. Despite this, an N₂O flux ‘limit of detection’ can be calculated using the mean concentration along the northernmost transect as a background, and knowledge of the instrument uncertainty which can prescribe a maximum possible enhancement within measurement error. This gives a limit of detection for flux that represents the lowest possible statistically significant N₂O flux that can be calculated using the in-flight QCLAS data with the current measurement uncertainty. This also represents a maximum possible upper limit on N₂O flux from the study region. This limit of detection for N₂O flux was calculated as 0.726 mg m⁻² h⁻¹, which is noted to be higher than N₂O fluxes in the range of 0.023 – 0.58 mg m⁻² h⁻¹ previously measured from arctic peatlands (5, 6). Hence it is unlikely that statistically significant Arctic fluxes of N₂O can be calculated using the aircraft mass balance method with the QCLAS instrument given its current N₂O measurement uncertainty. This limit

may be useful guidance to others attempting similar studies with analogous QCLAS aircraft systems.

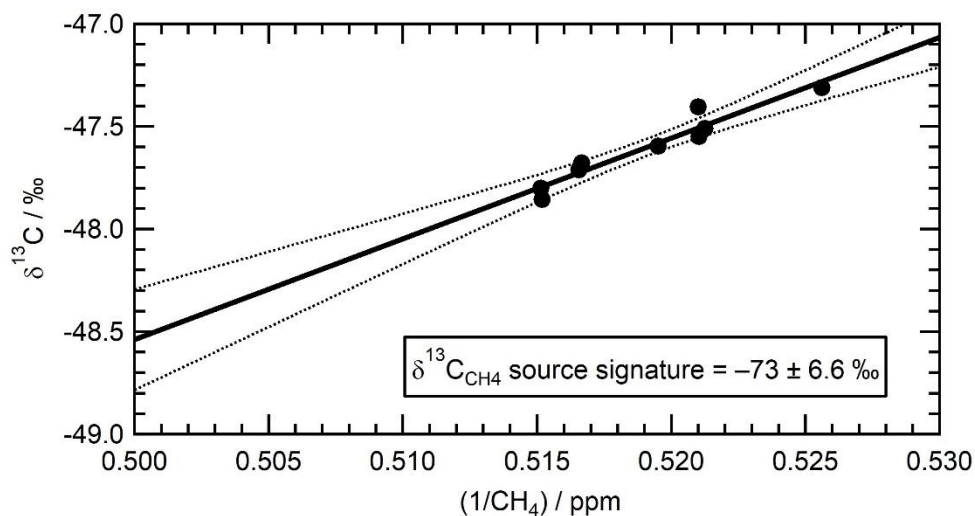


Figure S2.1: Keeling plot ($\delta^{13}\text{C}$ vs $1/\text{CH}_4$) for WAS taken over the course of flights C195 and C196 over the same area of Fennoscandian wetland. A linear regression is also shown (solid line) with 95% confidence interval (dotted lines). The Y-intercept is reported as the $\delta^{13}\text{C}_{\text{CH}_4}$ source signature.

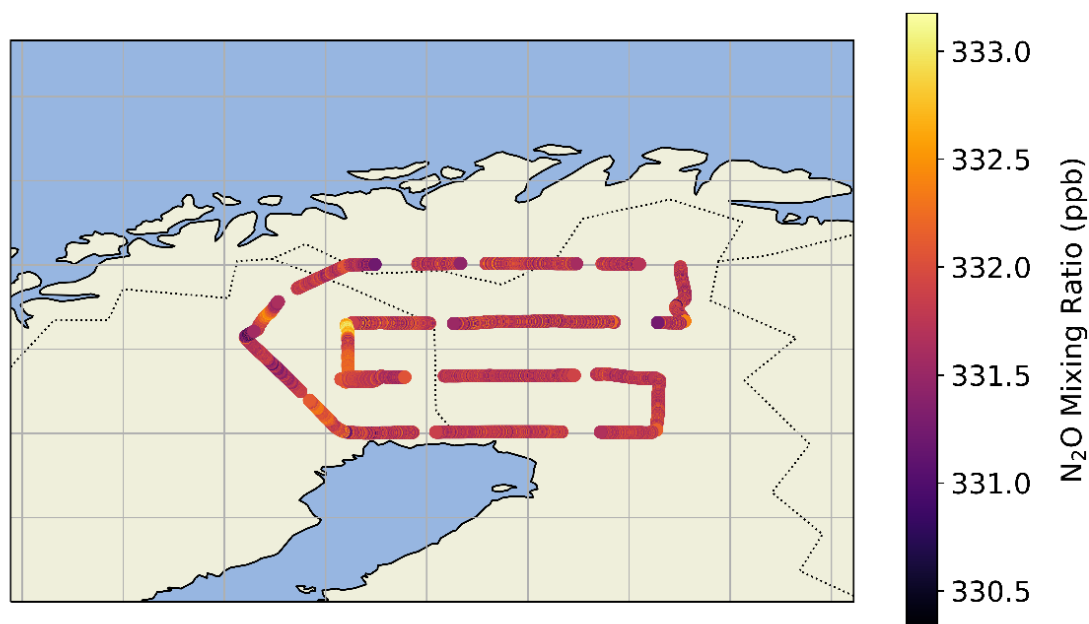


Figure S2.2: Flight track of FAAM flight C195 over northern Fennoscandian wetland areas coloured by N_2O mixing ratio.

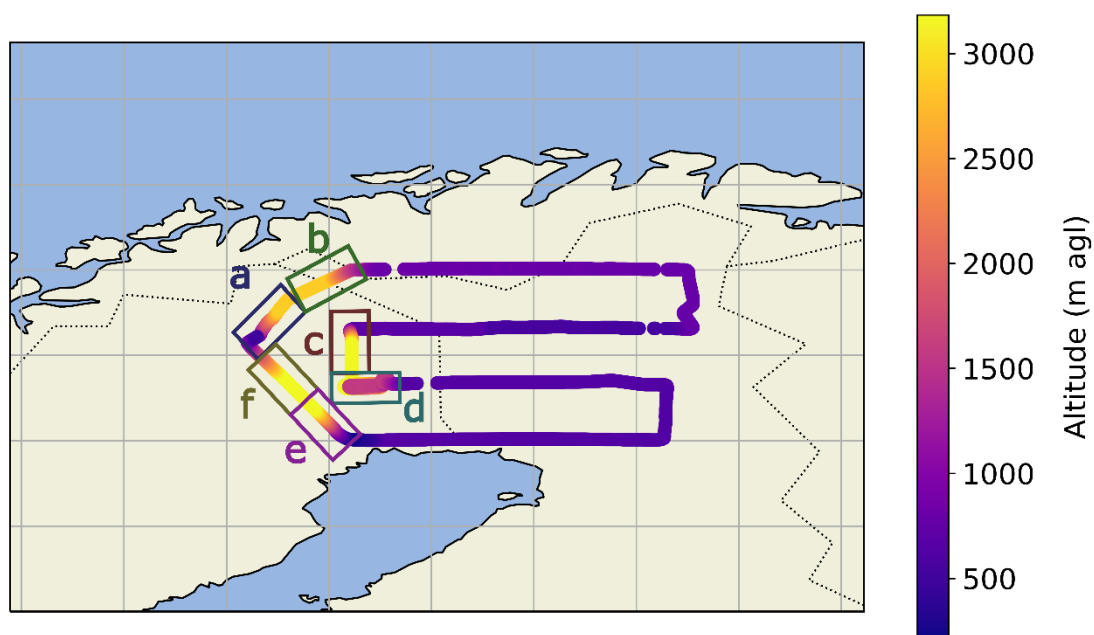


Figure S2.3: Flight track of FAAM flight C195 over northern Fennoscandian wetland areas coloured by altitude. The letters a-f and corresponding boxes highlight the profiles shown in figure 2a-f.

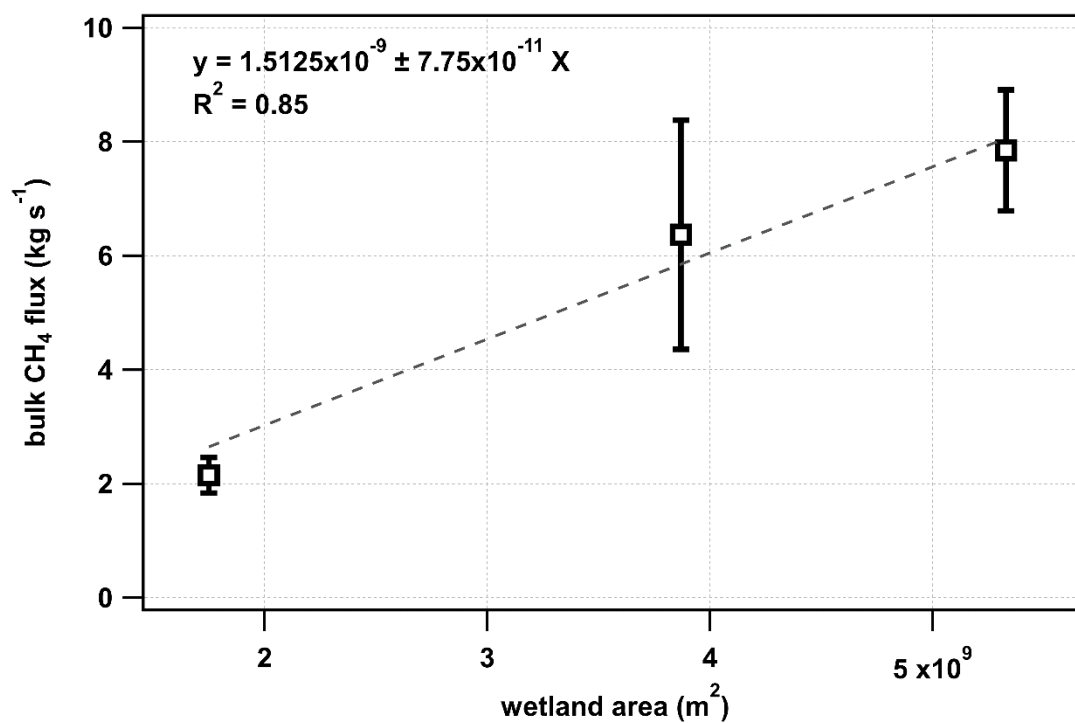


Figure S2.4: Plot of bulk methane flux versus wetland area for the three flux areas identified in section 3.1. A least-squares linear regression is fitted to these points and forced through zero, the equation of this regression is displayed, along with the correlation coefficient.

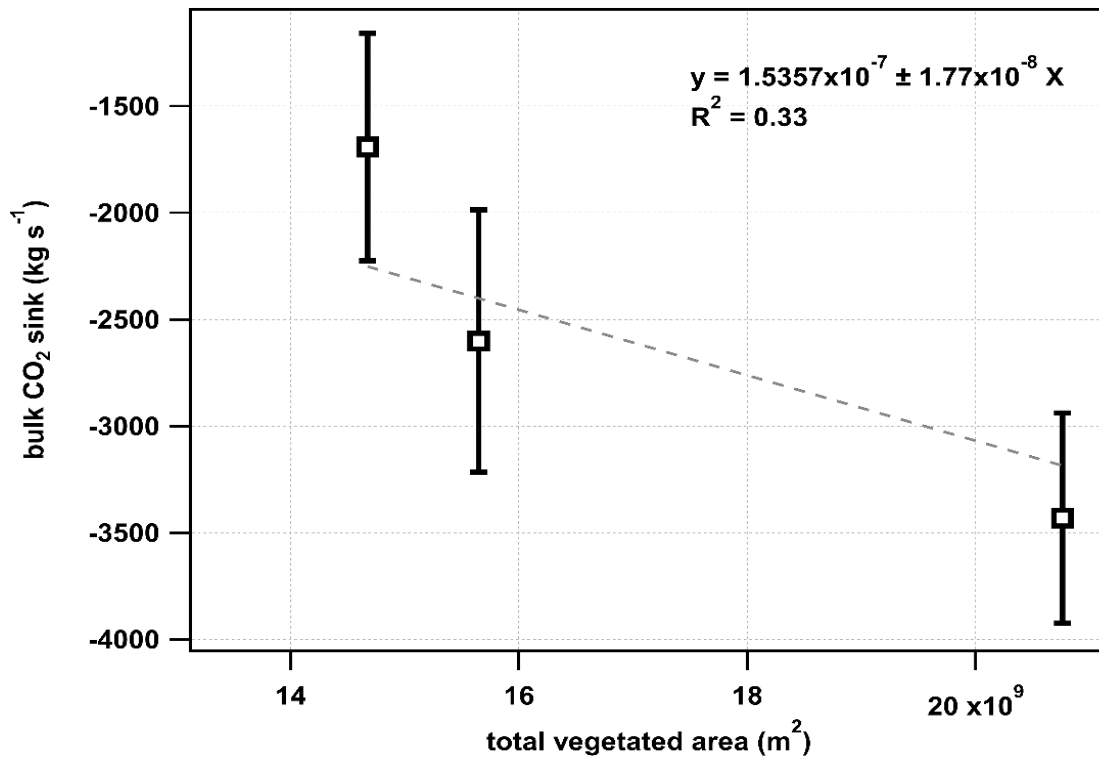


Figure S2.5: Plot of bulk CO₂ sink versus total CORINE vegetated area (non-irrigated arable, pasture, complex cultivation, agriculture, broadleafed forest, coniferous forest, mixed forest, grassland, moors, and woodland) for the three flux areas identified in section 3.1. A least-squares linear regression is fitted to these points and forced through zero, the equation of this regression is displayed, along with the correlation coefficient.

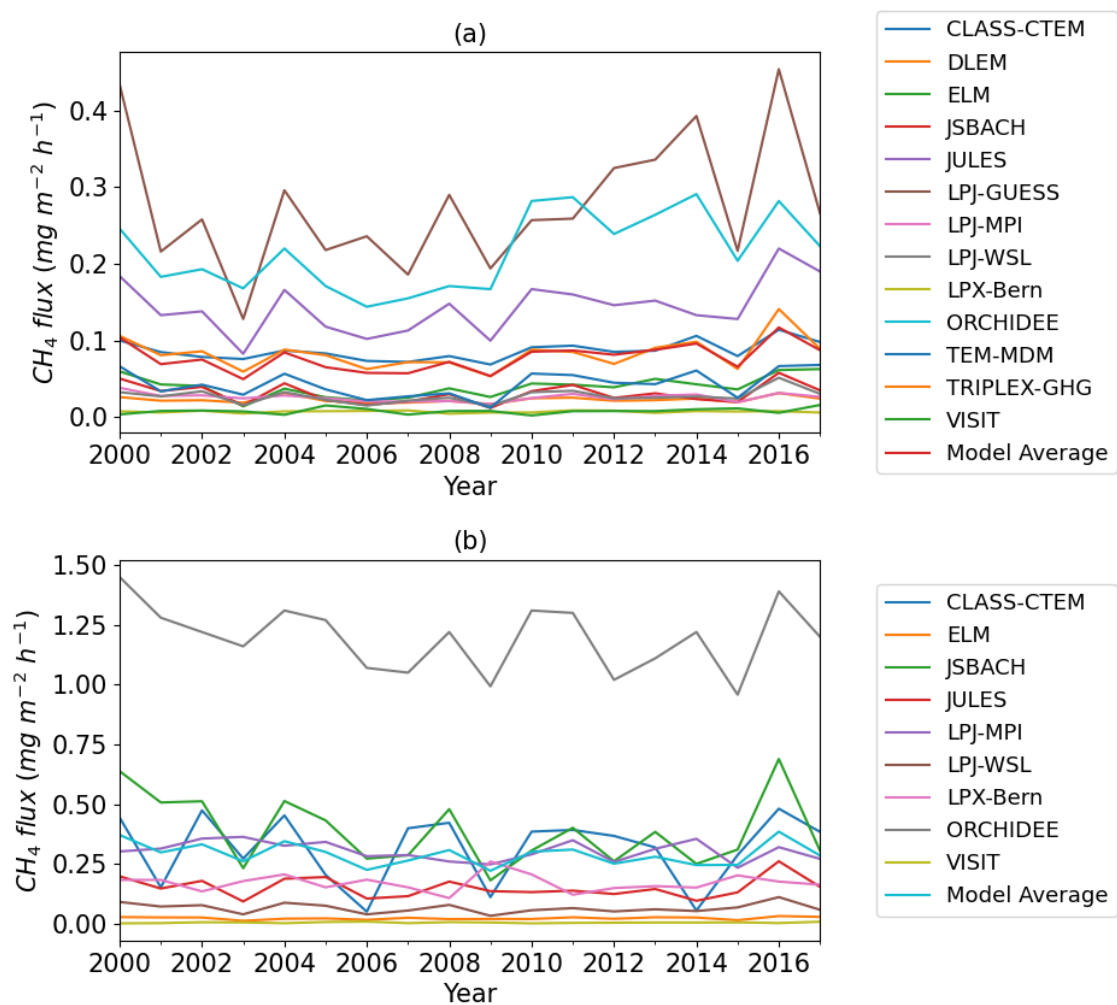


Figure S2.6: Time series of all GCP model CH_4 flux over the period 2000-2017 with (a) diagnostic wetland prescription and (b) prognostic wetland prescription. These area-normalised fluxes are for the entire study area of flight C195 (Areas 1, 2, and 3).

References

1. Fisher R, Lowry D, Wilkin O, Sriskantharajah S, Nisbet EG. 2006. High-precision, automated stable isotope analysis of atmospheric methane and carbon dioxide using continuous-flow isotope-ratio mass spectrometry. *Rapid Commun. Mass Spectrom.* **20(2)**, 200-208. (doi:10.1002/rcm.2300)
2. Fisher RE, France JL, Lowry D, Lanoisellé M, Brownlow R, Pyle JA, Cain M, Warwick N, Skiba UM, Drewer J, Dinsmore KJ. 2017. Measurement of the ¹³C isotopic signature of methane emissions from northern European wetlands. *Global Biogeochem. Cycles.* **31(3)**, 605-623. (<https://doi.org/10.1002/2016GB005504>)
3. Sriskantharajah S, Fisher RE, Lowry D, Aalto T, Hatakka J, Aurela M, Laurila T, Lohila A, Kuitunen E, Nisbet EG. *et al.* 2012. Stable carbon isotope signatures of methane from a Finnish subarctic wetland. *Tellus, Ser. B Chem. Phys. Meteorol.* **64**, 18818. (doi:10.3402/tellusb.v64i0.18818)
4. Barthelmes A, Couwenberg J, Risager M, Tegetmeyer C, Joosten H. 2015. *Peatlands and Climate in a Ramsar context. A Nordic-Baltic Perspective.*
5. Marushchak ME, Pitkämäki A, Koponen H, Biasi C, Seppälä M, Martikainen PJ. 2011. Hot spots for nitrous oxide emissions found in different types of permafrost peatlands. *Glob. Chang. Biol.* **17**, 2601–2614. (doi:10.1111/j.1365-2486.2011.02442.x)
6. Voigt C, Marushchak ME, Lamprecht RE, Jackowicz-Korczyński M, Lindgren A, Mastepanov M, Granlund L, Christensen TR, Tahvanainen T, Martikainen PJ, Biasi C. 2017. Increased nitrous oxide emissions from Arctic peatlands after permafrost thaw. *Proc. Natl. Acad.* **114(24)**, 6238–6243. (doi:10.1073/PNAS.1702902114)

A.3. Supplementary material to Manuscript 3

Supplementary Material - Measurement of recreational N₂O emissions from an urban environment in Manchester, UK

At the time of writing, Manuscript 3 has already been accepted for publication. Therefore the supplementary material presented here has not been included in the published journal article. This supplement is included solely in this thesis, and provides additional analysis of N₂O mole fractions observed at the MAQS.

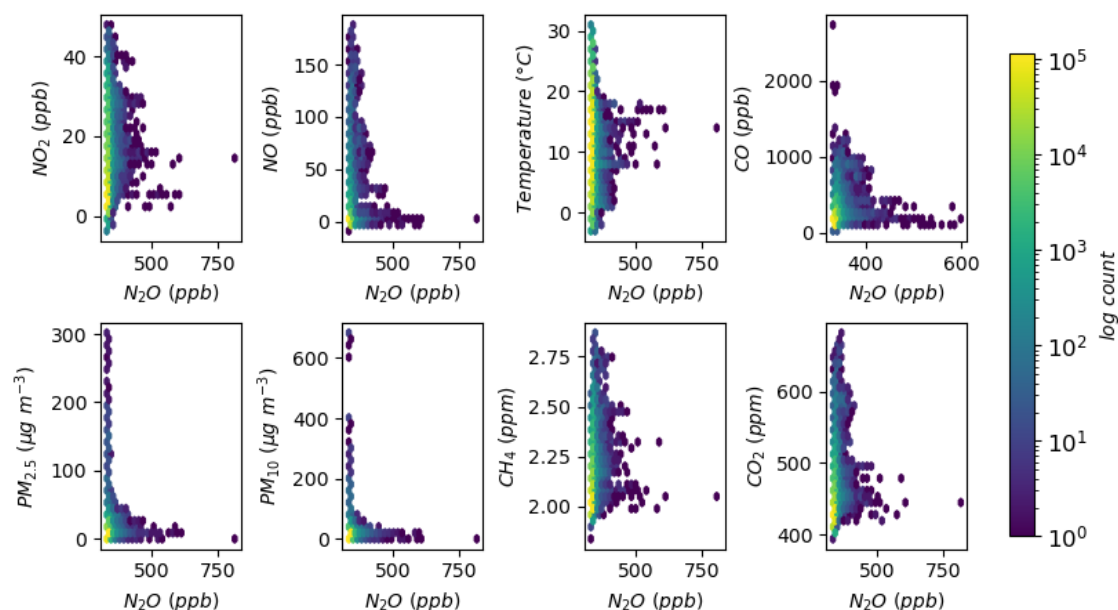


Figure S3.1: Density plot of pollutant concentrations vs N₂O measured at the MAQS between October 2020 and October 2021. Data are sorted into 50 bins per axis, and each point is coloured by the logarithmic count of points in each bin.

A.3.1. Extended temporal analysis

Fig. S3.2 shows the variability of mean nocturnal N₂O mole fraction over the course of the year-long study period. Maximum mean nocturnal N₂O concentrations were observed in June both for weekdays and weekends, whereas minima occurred in February/March and in August. There is a sharp decline in mole fraction enhancement from the June maximum to the August minimum which coincides with the onset of the University of Manchester Summer break. It is possible that the summertime decline in nocturnal N₂O enhancements is a result of lower student populations in the surrounding university accommodation blocks, and hence lessened N₂O emissions during this period. The lower nocturnal N₂O enhancements during February/March may also be a result of lessened recreational N₂O use during exam season.

Despite the observation of lower night-time N₂O enhancements during periods with lower student populations or during exam seasons, there are notable gaps in the N₂O dataset during these periods, especially January and February. Conclusive links between student activity and recreational N₂O use cannot be made with limited data availability for some months. An extended multi-year dataset would be required in order to further understand the variability of N₂O throughout a typical year, and to better characterise any correlations between student activity and local N₂O enhancements.

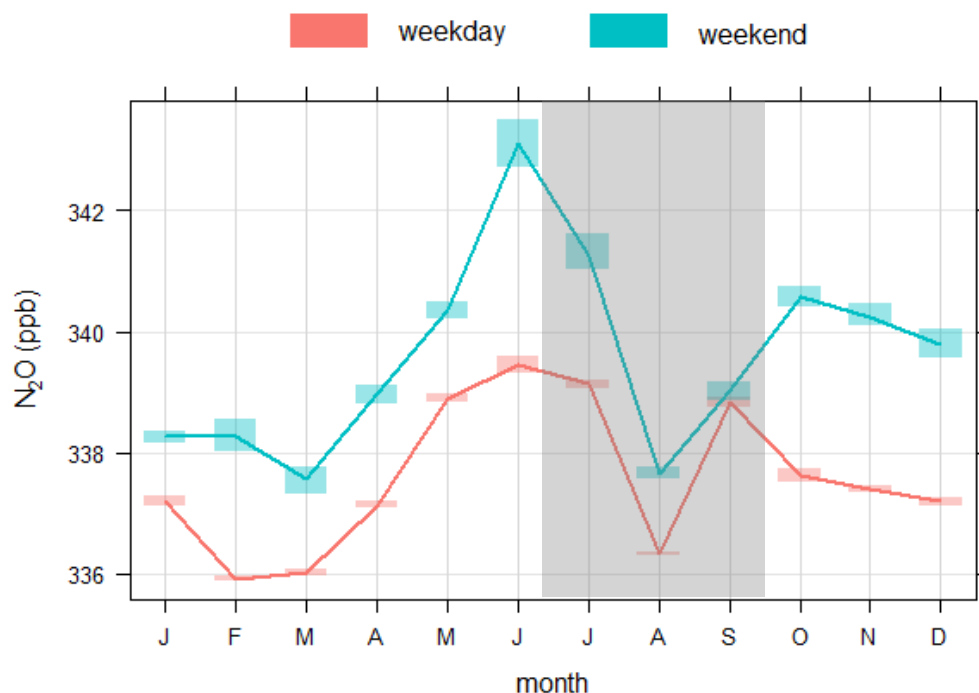


Figure S3.2: Mean night-time N_2O mole fraction observed from the MAQS during the study period. Both weekend and weekday mole fractions are shown in blue and red respectively. The shaded area depicts the duration of the University of Manchester Summer break (07 June 2021 – 13 September 2021).

A.3.2. Flux estimation using dispersion modelling

N_2O fluxes for the entire study period were determined using the Windtrax v2.0 modelling software (Windtrax, ThunderBeach Scientific). Windtrax is a stochastic Lagrangian dispersion model, which models the turbulent dispersion of thousands of particles from either a specified source location (forward mode) or backwards in time from a specified source to a concentration sensor (backwards mode). The modelled surface contact between released particles and source/receptor locations is used to determine local contribution to measured concentrations. Windtrax is designed for pollution dispersion modelling over short distances (<1 km) and features in-built utilities for surface emission flux inversions over these distances.

For flux quantification from the area surrounding the MAQS, the backwards mode was used with a network of student accommodation block area sources prescribed around the MAQS (see Fig. S3.3). Backwards dispersion models were run for the entire study period for 10 min averaged MAQS data, with 50,000 particles simulated for each data

point. A surface roughness length of 1 was used to account for the local building and vegetation topography. The flux results are shown in fig. S3.4.



Figure S3.3: Windtrax inverse model set up for N₂O flux estimation. The MAQS is shown as a yellow pin, and the manually assigned area sources are highlighted as green polygons.

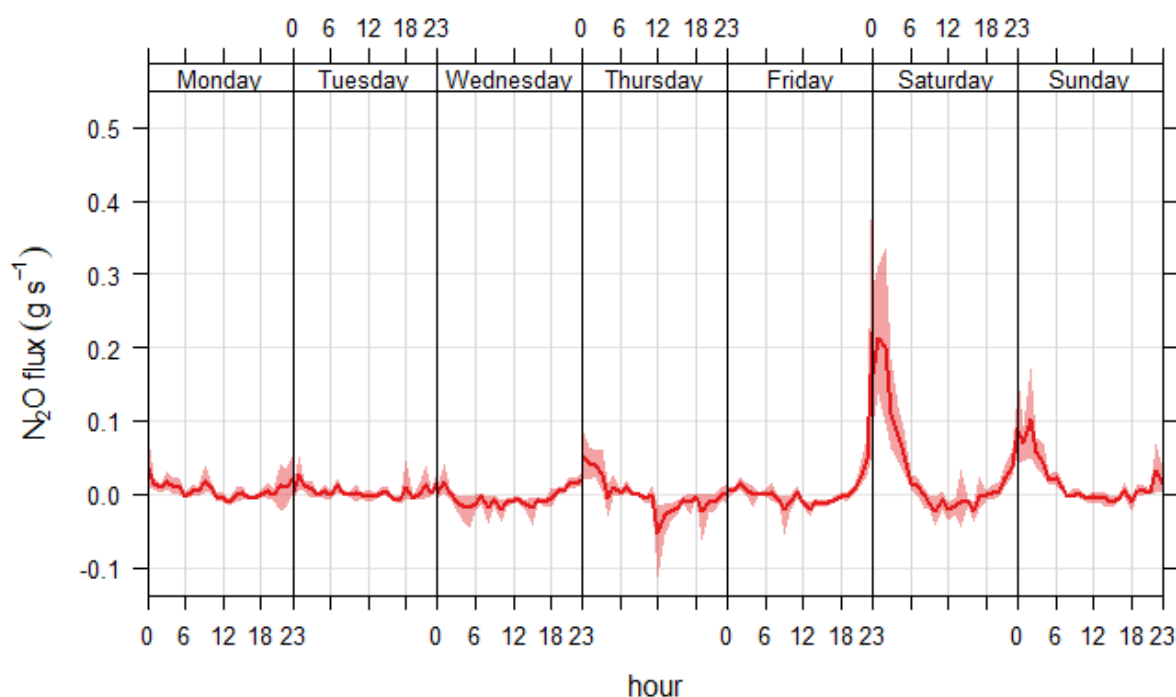


Figure S3.4: Weekly distribution of mean N_2O fluxes (in g s^{-1}) for the study period. The shaded area around the solid mean line indicates the 95% confidence interval.

The results in Fig. S3.4 show negligible fluxes during the week, with very little significant nocturnal flux increase above the daytime noise. There are significant positive N_2O fluxes during the Friday night-Saturday morning and Saturday night-Sunday morning periods, with peak mean values of $\sim 12 \mu\text{g m}^{-2} \text{s}^{-1}$ for Friday-Saturday, and $\sim 8 \mu\text{g m}^{-2} \text{s}^{-1}$ for Saturday-Sunday. These fluxes mirror the weekly trend in N_2O mole fraction enhancement shown in Fig. 8 of the main manuscript.

As there have been no previous studies investigating recreational N_2O emissions to date, comparison of these results remains difficult. However, previous studies into N_2O emissions from urban vegetation and roadways have reported mean fluxes significantly lower than those observed in this study (in the range $20 - 200 \text{ ng m}^{-2} \text{s}^{-1}$, Famulari et al., 2010; Järvi et al., 2014). It may therefore be the case that recreational N_2O emissions dominate other sources in certain urban environments, and increasing prevalence of recreational N_2O use may highlight the need for more widespread study and emission inventory validation.

A significant source of uncertainty in the observed fluxes originates from the prediction of area source locations. In this work, only student accommodation buildings

in the near vicinity of the MAQS are assigned as sources, whereas it is likely that recreational N₂O emissions may originate from wider areas of residential housing, parks, or streets that have not been included in the inversion model set up (Fig. S3.3). The choice of source areas could result in an overestimation of the area-normalised fluxes reported here. Further work to lessen the uncertainty in source area could involve tower eddy covariance flux quantification, which would yield an area-normalised flux from the footprint of the measurement tower.

References

Famulari, D., Nemitz, E., Di Marco, C., Phillips, G. J., Thomas, R., House, E. and Fowler, D.: Eddy-covariance measurements of nitrous oxide fluxes above a city, *Agric. For. Meteorol.*, 150(6), 786–793, doi:10.1016/j.agrformet.2009.08.003, 2010. Famulari, D., Nemitz, E., Di Marco, C., Phillips, G. J., Thomas, R., House, E. and Fowler, D.: Eddy-covariance measurements of nitrous oxide fluxes above a city, *Agric. For. Meteorol.*, 150(6), 786–793, doi:10.1016/j.agrformet.2009.08.003, 2010.

Järvi, L., Nordbo, A., Rannik, Ü., Haapanala, S., Mammarella, I., Pihlatie, M., Vesala, T. and Riikonen, A.: Urban nitrous-oxide fluxes measured using the eddy-covariance technique in Helsinki, Finland, *Boreal Environ. Res.*, 19(September), 108–121, 2014.